Oil & Natural Gas Technology

Detection and Production of Methane Hydrate

End of Phase 2 Topical Report

Reporting Period: June, 2007-June, 2008

Submitted by:
Rice University and University of Houston

George J. Hirasaki and Walter Chapman, Chemical and Biomolecular Engineering
Gerald R. Dickens, Colin A. Zelt, and Brandon E. Dugan, Earth Science
Kishore K. Mohanty, University of Houston

June, 2008

DOE Award No.: DE-FC26-06NT42960

Rice University – MS 362
6100 Main St.
Houston, TX 77251-1892
Phone: 713-348-5416; FAX: 713-348-5478; Email: gjh@rice.edu

University of Houston
Department of Chemical Engineering
4800 Calhoun Street
Houston, TX 77204-4004

Prepared for:
United States Department of Energy
National Energy Technology Laboratory

Office of Fossil Energy

Table of Contents

Disclaimer

Executive Summary

The results of Phase 2 are presented as Tasks 5 through 9. With the development of the numerical models, there have been increased interactions between group members. Several articles and presentations have multiple authors from both Chemical Engineering and Earth Science. Also Gangsheng Gu of Chemical Engineering has been collaborating with Jerry Dickens of Earth Science and Dr. Frederick S Colwell of Organ State University (Battelle Grant BEA 00054031) on the effect of seafloor temperature on hydrate accumulation.

Task 5: Carbon Inputs and Outputs to Gas Hydrate Systems

We have determined the amount of iodine in sediment and pore waters down boreholes at 10 locations, including 3 with gas hydrate. This work, when combined with disparate data sets scattered throughout the literature, clearly shows that iodine accumulates in marine sediment as a function of organic carbon input over time. Iodine profiles provide a crucial constraint on the organic carbon input to marine gas hydrate systems. We anticipate including iodine into our modeling as a means to evaluate certain parameters. We have examined carbon, sulfur and metal chemistry across the SMT at sites in the Japan Sea and the Peru Trench to assess whether sulfate profiles can, in fact, be used to determine the upward flux of methane. This appears to be a valid assumption in the Sea of Japan, but only after all carbon fluxes are accounted for. In particular, an upward flux of bicarbonate and carbonate precipitation impact geochemical interpretations across the SMT. We are assessing whether this holds true for the Peru Trench, and also, how this affects carbon isotopes. This information provides crucial constraints for modeling the out of methane from marine gas hydrate systems.

Task 6: Numerical Models for Quantification of Hydrate and Free Gas Accumulations

The development of the numerical models for hydrate and free gas accumulation has progressed to increase the fundamental understand of the accumulation phenomena.

Subtask 6.1: Model development. A numerical model has been developed for the simulation of the accumulation of hydrate and free gas over geological time and length scales in one or two dimensions. Work has continued towards extending the one-dimensional numerical model to two spatial dimensions.

Subtask 6.2: Conditions for existence of gas hydrate. The simulations delineate basic modes of gas hydrate distribution in marine sediment, including systems with no gas hydrate, gas hydrate without underlying free gas, and gas hydrate with underlying free gas below the gas hydrate stability zone, for various methane sources. The results are scaled using combinations of dimensionless variables, particularly the Peclet number and Damkohler number, such that the dependence of average hydrate saturation on numerous parameters can be summarized using two contour maps, one for a biogenic source and one for upward flux from a deeper source.

Our model presents a unified picture of hydrate accumulations that can be used to understand well-characterized gas hydrate systems or to predict steady-state average hydrate saturation and distribution at locations for which seismic or core data are not available.

Subtask 6.3. Compositional Effect on BSR The presence of methane hydrate is usually detected by a bottom simulating reflector (BSR). The BSR results from the sudden change in acoustic impedance as the formation changes from being hydrate saturated to free-gas saturated at the base of the hydrate stability zone. If other hydrocarbons in addition to methane are present, this transition may take place over a depth greater than the acoustic wavelength and the BSR may be attenuated or absent.

The result of an example saturation calculation of the CH_4 - C_3H_8 - H_2O hydrate system in the sediment is presented. It successfully demonstrated that continuous change of S_H and S_v over a long spatial distance (~300 m) is possible. A gradual change of saturations, may result in gradual change of acoustic properties, and induce weak BSR or even no BSR.

Subtask 6.5: Processes leading to overpressure. Work has continued through one-dimensional numerical modeling to ascertain the factors and dimensionless groups responsible for overpressure generation in gas hydrate systems. We had determined through numerical simulations that the ratio of sediment absolute permeability to the sedimentation rate was the key dimensionless group controlling overpressure generation. The effect of overpressure, in turn, limits the amount (thickness) of free gas that can accumulate below the GHSZ. Hydrostatic pore pressures allow a relatively long connected gas column to form. On the other hand, overpressure generation can significantly reduce the thickness of this connected gas column before gas pressure reaches the lithostatic limit at the BHSZ and causes sediments to fracture.

Subtask 6.8: Sulfate profile as indicator of methane flux. Numerical and analytical models have been developed for inferring gas hydrate saturation in marine sediments from pore water sulfate profiles. These models utilize the depth of the sulfate-methane transition (SMT) as the primary input variable and are valid for systems dominated by methane supply from deeper sources. Results from these models are in agreement with gas hydrate saturations estimated from resistivity logs/chloride data at several sites along Cascadia Margin.

Task 7: Analysis of Production Strategy

Our in-house simulator performs as well as the other simulators in the code comparison study. For Problem 3 with ice formation, our simulator, STOMP, and MH21 performed better than the other simulators. For warm water injection, production well pressure, injection temperature and pressure play an important role in the production of gas from hydrate deposits. For high injection temperature, the higher pressure increases the flow of warm water (heat) in the reservoir making the production rate faster, but if injection temperature is not high

then only depressurization is the best method of production. At intermediate injection temperature, the production rate changes non-monotonically with the injection pressure. These parameters should be chosen carefully to optimize recovery and recovery rate of gas. This paper addresses a very simple homogeneous domain. Realistic reservoirs would have heterogeneity in sediments as well as hydrate distribution, which need to be taken into account.

Task 8: Seafloor and Borehole Stability

We are moving forward on Task 8 as scheduled and as outlined by the Milestone Status. In conjunction with compiling published geomechanical and fluid flow properties we have identified a dearth of data for multi-phase flow in hydrate systems and for strength in low-to-moderate hydrate saturation in fine-grained materials. We are working with colleagues at MIT, GATech, the USGS, and LBNL to see what technology exists to fill these data gaps. We are integrating the sediment properties work (this task), the geologic hydrate accumulation work (Task 6), the hydrate production work (Task 7) and the DOE-sponsored JIP hydrate work in the Gulf of Mexico to develop forward models of hydrate accumulation to test the JIP predictions and to provide accurate and realistic sediment models for our hydrate production models. We have also measured permeability of samples to evaluate new techniques for getting permeability anisotropy and for getting robust permeability data from logging measurements. Lastly, through involvement in recent and upcoming conferences, we are staying appraised of the state of the art from the academic and industrial perspectives.

Task 9: Geophysical Imaging of Gas Hydrate and Free Gas Accumulations

Subtask 9.1: Preliminary processing and inversion of seismic data.

Seismic data has been identified and is currently being processed at NIO, India with Priyank Jaiswal's remote involvement. The identified seismic line has three inline wells all of which were drilled in 2001. The drilling was based on BSR signatures that appear to be similar at the well locations but the recovered hydrate concentration was found to be varying. A visit of NIO to Rice in July is being arranged.

Background

A. Objective

This project seeks to understand regional differences in gas hydrate systems from the perspective of as an energy resource, geohazard, and long-term climate influence. Specifically, the effort will: (1) collect data and conceptual models that targets causes of gas hydrate variance, (2) construct numerical models that explain and predict regional-scale gas hydrate differences in 2- and 3-dimensions with minimal "free parameters", (3) simulate hydrocarbon production from various gas hydrate systems to establish promising resource characteristics, (4) perturb different gas hydrate systems to assess potential impacts of hot fluids on seafloor stability and well stability, and (5) develop geophysical approaches that enable remote quantification of gas hydrate heterogeneities so that they can be characterized with minimial costly drilling. Our integrated program takes advantage of the fact that we have a close working team comprised of experts in distinct disciplines.

The expected outcomes of this project are improved exploration and production technology for production of natural gas from methane hydrates and improved safety through understanding of seafloor and well bore stability in the presence of hydrates.

B. Scope of Work

The scope of this project is to more fully characterize, understand, and appreciate fundamental differences in the amount and distribution of gas hydrate and how this affects the production potential of a hydrate accumulation in the marine environment. The effort will combine existing information from locations in the ocean that are dominated by low permeability sediments with small amounts of high permeability sediments, one permafrost location where extensive hydrates exist in reservoir quality rocks and other locations deemed by mutual agreement of DOE and Rice to be appropriate. The initial ocean locations are Blake Ridge, Hydrate Ridge, Peru Margin and GOM. The permafrost location is Mallik. Although the ultimate goal of the project is to understand processes that control production potential of hydrates in marine settings, Mallik will be included because of the extensive data collected in a producible hydrate accumulation. To date, such a location has not been studied in the oceanic environment. The project will work closely with ongoing projects (e.g. GOM JIP and offshore India) that are actively investigating potentially economic hydrate accumulations in marine settings.

The overall approach is fivefold: (1) collect key data concerning hydrocarbon fluxes which is currently missing at all locations to be included in the study, (2) use this and existing data to build numerical models that can explain gas hydrate variance at all four locations, (3) simulate how natural gas could be produced from each location with different production strategies, (4) collect new sediment property data at these locations that are required for constraining fluxes, production simulations and assessing sediment stability, and (5) develop a method for remotely quantifying heterogeneities in gas hydrate and free gas distributions. While we generally restrict our efforts to the locations where key parameters can be measured or constrained, our ultimate aim is to make our efforts universally applicable to any hydrate accumulation.

Task 5: Carbon Inputs and Outputs to Gas Hydrate Systems

Approach

The amount and distribution of gas hydrate in marine sediment depends on several factors. Our project-related modeling efforts [*Bhatnager et al.*, 2007a, 2008], as well as results from other studies [e.g., *Davie & Buffett*, 2001], indicate two particularly important factors: (1) the sedimentary input of labile organic carbon (C_{org}) over time, and (2) the output of gas via anaerobic oxidation of methane (AOM). We are constraining these factors by generating key chemical data sets using sediment and pore water obtained from present-day gas hydrate systems.

Subtask 5.1: Constrain organic carbon inputs using iodine

A large gas hydrate system was drilled in 1995 on outer Blake Ridge, offshore the southeast United States. An intriguing find was extremely high pore water iodide (I^-) concentrations at depth [*Egeberg & Dickens*, 1999]. These concentrations, exceeding 1 mol/m^3 and orders of magnitude greater than those in seawater (**Fig. 5.1**), suggest a crucial constraint on C_{org} inputs. Organic carbon landing on the seafloor carries significant amounts of I. Upon burial and decomposition, this I is released to pore waters as I^-. Since the concentration of I^- in seawater is very low, there is a concentration gradient and I^- diffuses up to the seafloor, where it is scavenged back to C_{org}. Over time, this recycling builds-up I in sediment and pore waters by an amount that should relate to the integrated flux of C_{org} over time, which would be fundamental to modeling efforts. To explore this concept, we proposed to measure iodine contents in sediment and water at several locations (with and without gas hydrate), to compare these contents to organic carbon inputs, and to eventually incorporate this work into numerical models for gas hydrate formation.

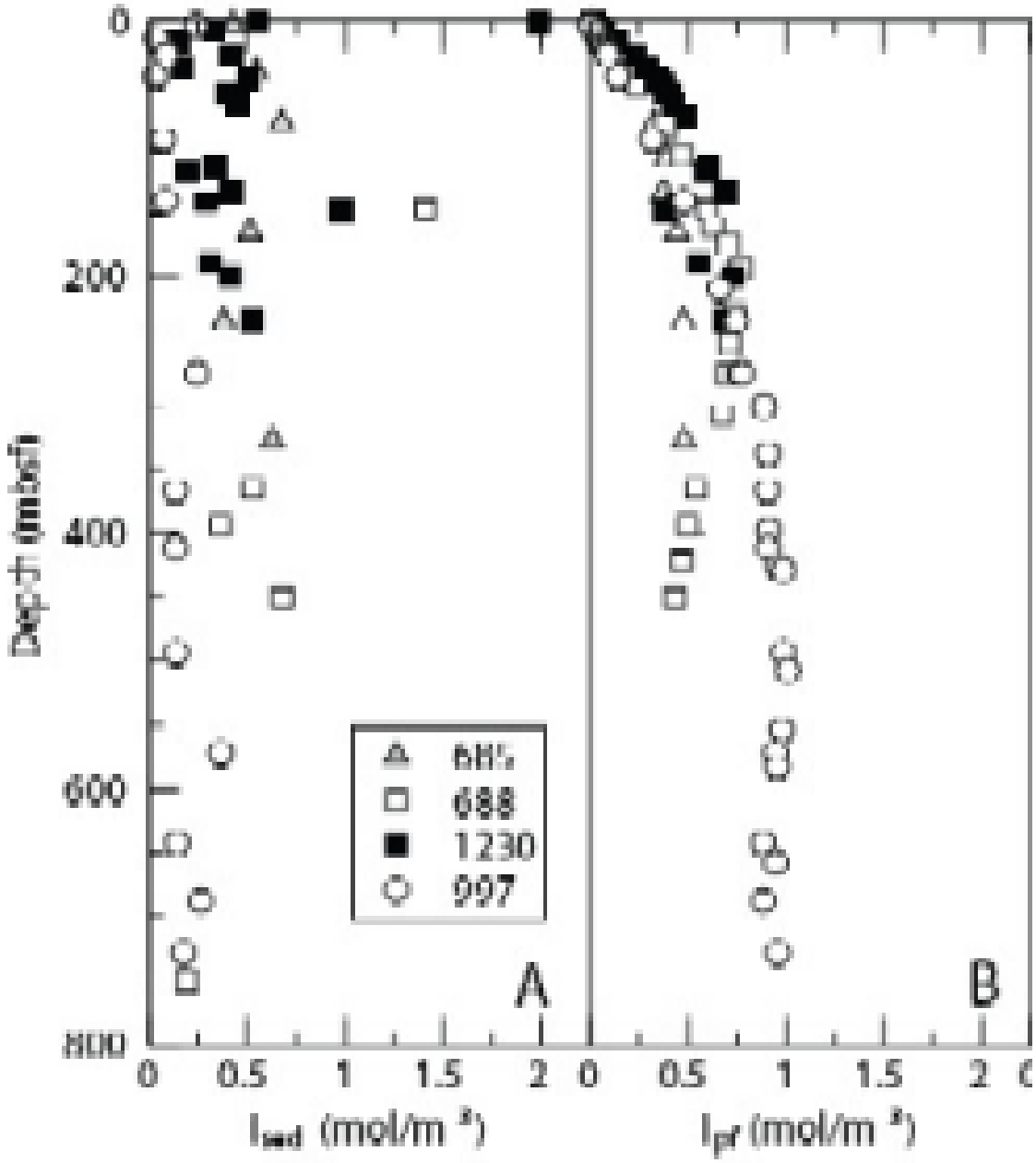

Figure 5.1: Sediment and pore water iodine concentrations in drill holes from gas hydrate systems on the Peru Margin (685, 688, 1230) and Blake Ridge (997).

Subtask 5.2: Constrain methane outputs using authigenic minerals

A major loss of methane from all gas hydrate systems is AOM in shallow sediment (**Fig. 5.2**). In fact, this may be the dominant methane output from most systems, and its flux may directly link to the abundance of underlying gas hydrate [*Bhatnagar et al.*, 2008]. In general, and at a sulfate-methane transition (SMT), upward moving methane reacts with downward diffusing sulfate, presumably in a 1:1 relationship: $CH_4 + SO_4^{2-} \dashrightarrow H_2O + HCO_3^- + HS^-$. Because *in situ* methane concentrations and fluxes can be difficult to measure, several workers have suggested that upward methane fluxes could be determined from dissolved sulfate (or bicarbonate) fluxes.

Several publications have provided data in support of this idea [*Borowski et al.*, 1999; *Niewöhner et al.*, 1998; *Luff and Wallmann*, 2003]. However, other publications have argued that sulfate and methane fluxes do not balance across the SMT [*Fossing et al.*, 2000; *Aharon and Fu*, 2003; *Joye et al.*, 2004; *Berelson et al.*, 2005]. In particular, downward sulfate fluxes appear much greater than upward methane fluxes. This has led to current debate as to whether pore water sulfate profiles actually can be used to constrain methane fluxes. Moreover, it is not obvious that present-day sulfate profiles above gas hydrate systems are legitimate for constraining methane fluxes over the time-scales of interest to modeling [e.g., *Dickens*, 2001]. These issues need clarification, as the sulfate profiles provide a crucial model parameter for understanding gas hydrate abundance [*Bhatnager et al.*, 2008].

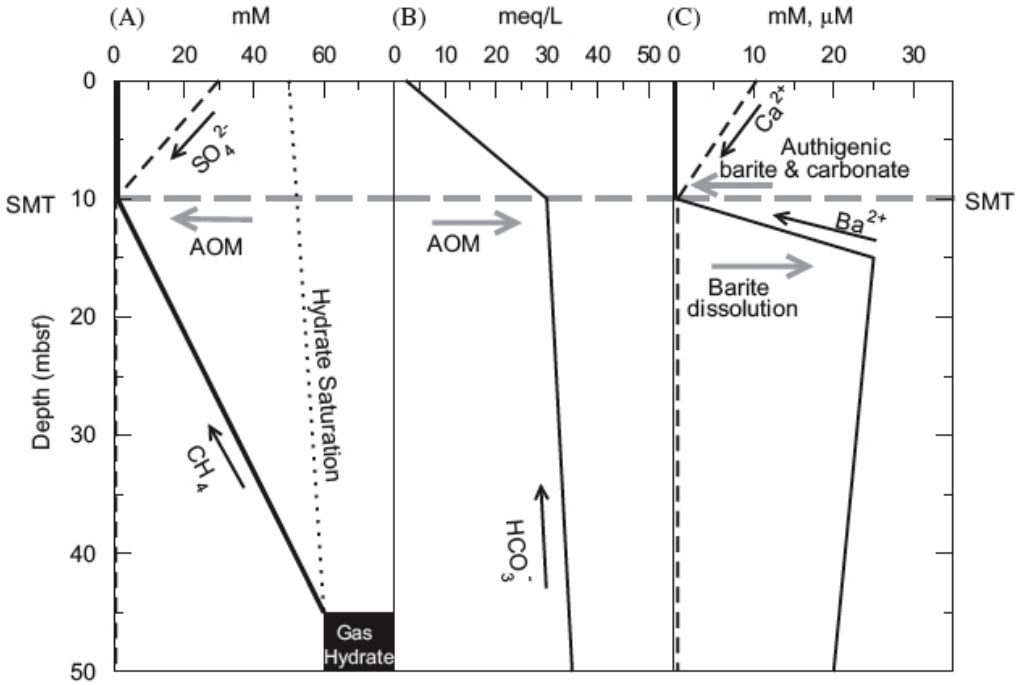

Figure 5.2: Schematic of dissolved solute behavior in shallow sediment above gas hydrate systems [from *Snyder et al.*, 2007]. Also shown are the sulfate-methane transition (SMT) and the location of authigenic mineral formation. AOM = anaerobic oxidation of methane.

We proposed to generate metal profiles in pore water and sediment across the SMT at several locations with underlying gas hydrate. Our goal is to evaluate the relationship between sulfate and methane profiles at present and in the past, and then use established methane fluxes to constrain our numerical models for gas hydrate formation. Previous work [e.g., *Dickens,* 2001; *Aloisi et al.*, 2003; *Luff and Wallmann*, 2003] has indicated that authigenic minerals (carbonate and barite), and their constiituent elements (Ca, Mg, Sr, Ba), can be used to constrain carbon and sulfur fluxes across the SMT.

Results and Discussion

Subtask 5.1: Constrain organic carbon inputs using iodine

We have generated a series of iodine profiles down holes at several locations with gas hydrate (outer Blake Ridge, Peru Trench, Gulf of Mexico, Japan Sea) as well as several "reference" locations without gas hydrate (e.g., Equatorial Pacific). Most of the limited work concerning iodine in marine sediment to date has focused on shallow sediment (the upper few meters) or pore waters in random deep boreholes. Consequently, much of our effort has been to "patch" existing information, generating sediment and pore water data at specific locations to maximize our understanding of the sedimentary iodine cycle.

Iodine contents of sediment samples were determined using an established technique. First, iodine was released from weighed aliquots of sediment to a trap solution by hydropyrolysis. Approximately 200 mg of powdered sample was placed in a porcelain boat, combined with vanadium pentoxide catalyst, and heated to 1100°C in a tube furnace using a quartz process tube while being exposed to a steady stream of wet oxygen gas. Vapors formed were passed through a reducing solution of 0.1% tetramethyammonium hydroxide trap solution. Solutions were analyzed for I concentration by inductively couple plasma mass spectrometry (ICP-MS), using mass 127 and rhodium (mass 103) as an internal standard. Pore fluids were diluted 1:500 wt % with 18MΩ water, to which tetramethylammonium hydroxide and the Rh internal standard were added. These were analyzed for I concentrations by ICP-MS as noted above.

When combined with previously published data, our results allow us to make generalizations regarding the distribution and accumulation of marine iodine across a variety of depositional environments. The extreme pore water iodide concentrations found on Blake Ridge are not unique (**Fig. 5.1**), but characterize large gas hydrate systems elsewhere (e.g., Hydrate Ridge, Peru Margin). On the other hand, sites with minimal organic carbon input over time have no appreciable iodine (**Fig. 5.3**). This is true for sites that do not receive high amounts of organic carbon, are too young, or both. Our work further shows that sedimentary iodine contents are only high near the seafloor. A somewhat amazing summary is that most of the iodine on Earth (>50%) occurs in methane-charged sediment along continental slopes, and much of this resides in pore fluids at sub-seafloor depths greater than 25 meters rather than in sediment. Clearly, iodine is accumulating over time and represents an integrated signal of organic input, likely because of the cycling hypothesized above.

We are writing these results and expect to have a paper submitted by the end of summer. We will then attempt to incorporate iodine into our numerical modeling. We note at this juncture, though, that some specific sites with gas hydrate, while conforming to our general views, are problematic because of external (deep) iodine sources. It may not be easy to use iodine at sites with high rates of fluid advection (e.g., Gulf of Mexico).

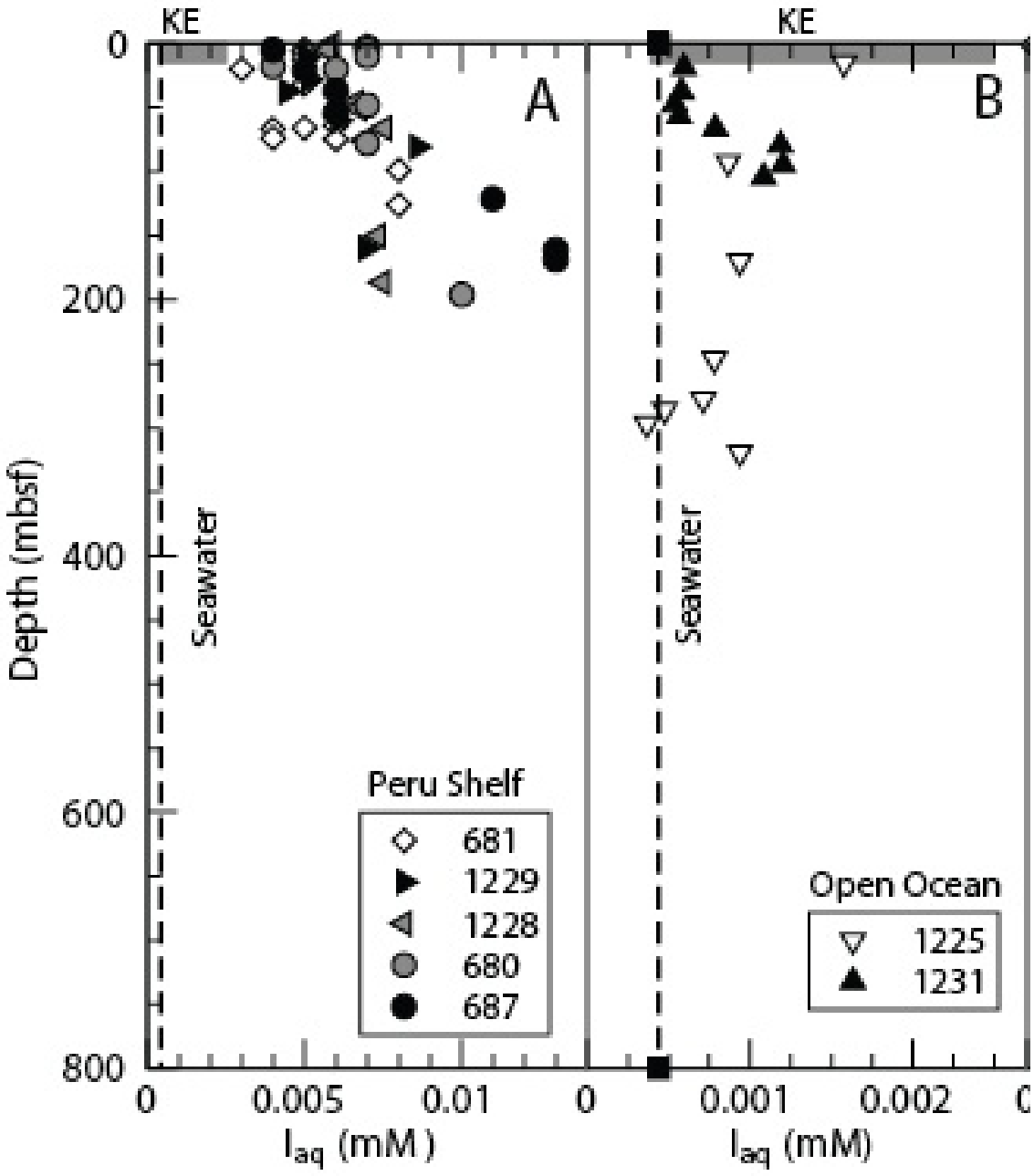

Figure 5.3: Pore water iodine concentrations in drill holes from the Peru Shelf and Equatorial Pacific where no gas hydrate occurs. Note scale change for the x-axis compared to Figure 5.1.

Subtask 5.2: Constrain methane outputs using authigenic minerals (and carbon isotopes)

We were tentatively awarded the grant at the end of 2006 but did not receive full confirmation or funding until late summer of 2007. To initiate Task 5 and to better understand methane outputs, therefore, we generated a suite of basic chemical data across the SMT using samples that we had already collected as part of a project with Japanese colleagues. These samples come from Umitaka Spur (Japan Sea), a location where shallow sediment contains abundant gas and gas hydrate. The data produced were Ca, Mg, Sr, S, and Ba concentrations in both pore water and sediment. These were determined using an Inductively Coupled Plasma Atomic Emission Spectrometer (ICP-AES) following procedures and extractions detailed by *Snyder et al.* [2007].

When combined with pore water HCO_3^- data generated on ship, problems and answers to carbon (and sulfur) cycling across the SMT become clear. A major issue is that very few studies have tried to constrain all relevant fluxes. In particular, across the SMT, AOM is not the only sink and source of carbon; there are three additional fluxes of interest: dissolved HCO_3^- rising into the SMT from below, excess dissolved HCO_3^- leaving the SMT to the seafloor, and precipitation of authigenic carbonate in sediment at (or near) the SMT. All five fluxes can be calculated for the Japan Sea cores (and in many cores) using our pore water data and standard diffusion equations (**Fig. 5.4**). These calculations indicate that sulfate and methane fluxes do balance across the SMT. However, some of the HCO_3^- entering and leaving the SMT comes from deep in the sediment column not from AOM (**Fig. 5.4**). Authigenic carbonate fronts were also identified at or near the SMT in all three cores. Given the dissolved fluxes of Ca, Mg, Sr and HCO_3^- into these fronts and the amounts of carbonate hosted by them further suggests that the SMT has been close to that at present-day for a long time (>20,000 years). These results have now been published [*Snyder et al.*, 2007].

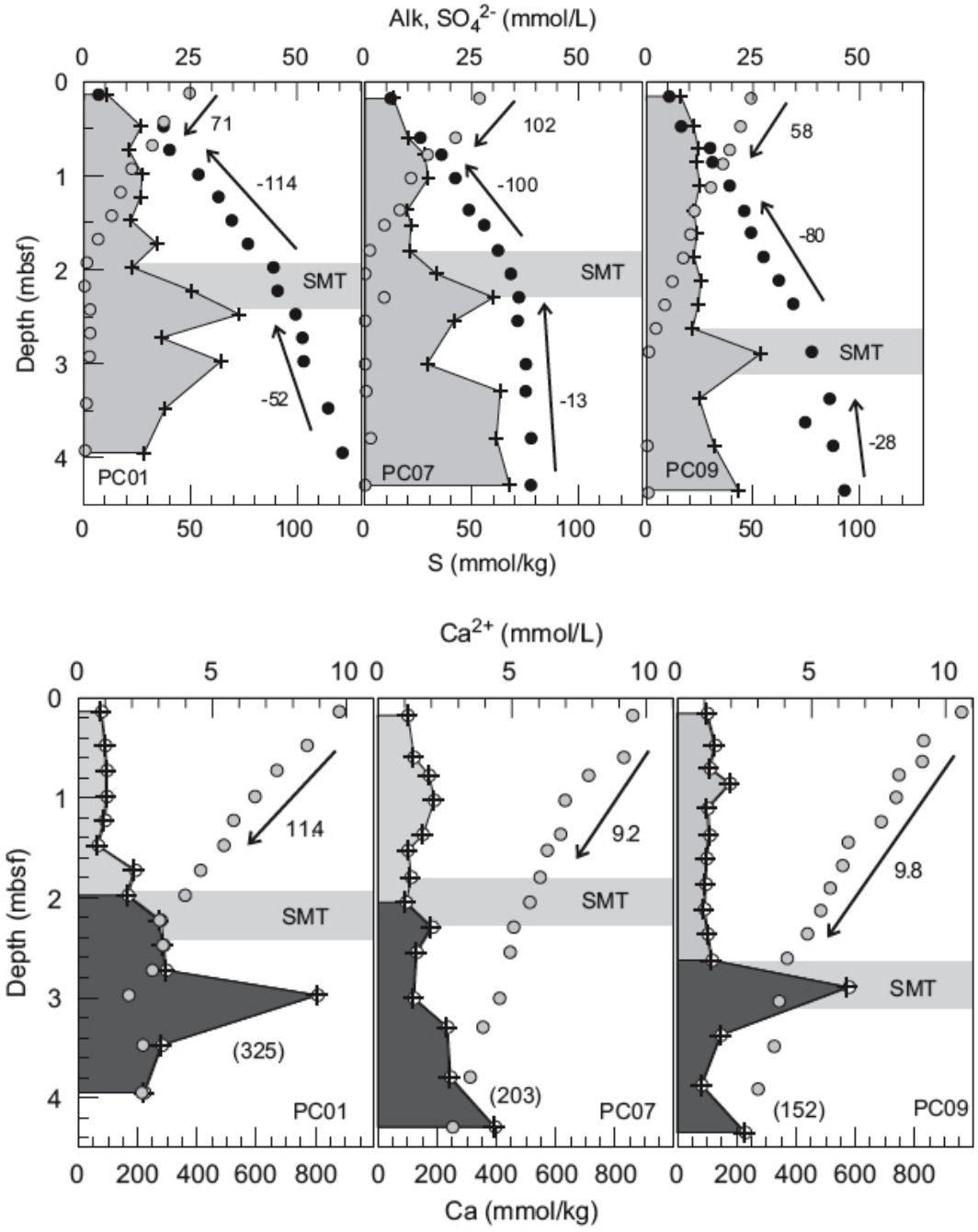

Figure 5.4: Pore water (points) and solid phase (shades) elemental profiles across the SMT in shallow sediment from three cores in the Japan Sea [*Snyder et al.*, 2007]. Also shown are fluxes in mol/m^2-kyr.

We have now collected and analyzed the sediment metals contents across a site with gas hydrate located in the Peru Trench (ODP Site 1230). This site was chosen because we have already published very detailed pore water records [*Donohue et al.*, 2006], because it is a very different environment from the Japan Sea, and because, being a deep borehole, it is amenable to our numerical modeling [*Bhatnager et al.*, 2007, 2008, in prep]. We have determined that there is a 2-m thick horizon with high amounts of authigenic carbonate (calcite) and barite across the SMT (**Fig. 5.5**). Similar to cores from the Japan Sea, this horizon attests to a methane output that has been similar to present-day over a long time interval (i.e., the system is close to steady-state, at least over the >10,000 yrs). We are presently modeling the fluxes of constituents into the SMT, to establish whether methane and sulfate fluxes balance here also, once other carbon and sulfur fluxes are considered. We plan on submitting this work for publication by the end of summer.

One argument that has been given for carbon balance inequity across the SMT concerns stable carbon isotopes of dissolved HCO_3^- and authigenic carbonate. It has been suggested that $d^{13}C$ values much "heavier" than methane (e.g., -25‰ instead of -60‰) at the SMT indicate consumption of sulfate by other processes. To test this, we have also collected and analyzed samples for carbon isotopes. These measurements give values of -12‰ to -5‰, much "heavier" than if all HCO_3^- was derived from AOM. However, we suspect that this is because there is a very large upward flux of HCO_3^- from depth, so that methane and sulfate fluxes may in fact still balance. We also plan on submitting this work for publication by the end of summer, either with the above manuscript or separately. Lastly, we have modeled the abundance of gas hydrate at this location [*Bhatnager et al.*, in preparation]. The results of our sediment chemistry work will enable us to evaluate whether key model parameters are reasonable.

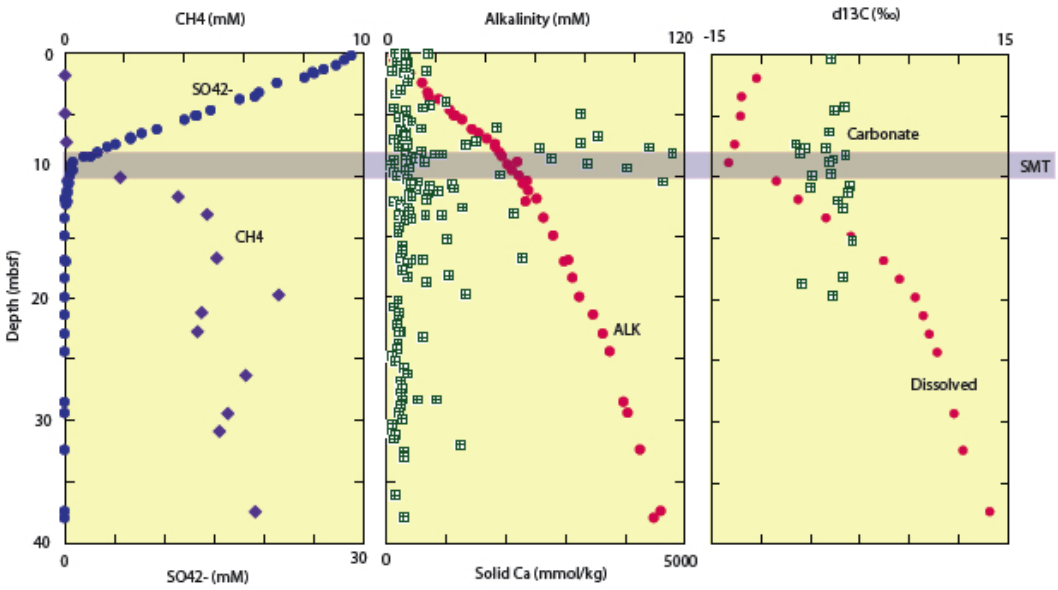

Figure 5.5. Pore water and solid phase chemistry across the SMT at ODP Site 1230, a borehole in the Peru Trench with gas hydrate.

Conclusions

Models concerning the abundance and distribution of gas hydrate in marine sediment require constraints on carbon inputs and outputs, fluid flow and temporal evolution. Iodine appears to be a proxy for the integrated flux of organic carbon over time, such that sites that have accumulated large amounts of organic carbon have extreme iodine abundance. Carbon, sulfur and metal profiles can be used to assess whether sulfate profiles are good proxies for upward methane fluxes, and whether these fluxes have changed over time. Our chemical analyses of sediment appear to be providing us reasonable constraints that we can use in our models.

References

Aloisi, G., K. Wallmann, S.M. Bollwerk, A. Derkachev, G. Bohrmann, & E. Suess, 2004. The effect of dissolved barium on biogeochemical processes at cold seeps. Geochimica et Cosmochimica Acta, 68: 1735-1748.

Aharon, P. & B. Fu, 2003. Sulfur and oxygen isotopes of coeval sulfate-sulfide in pore fluids of cold seep sediments with sharp redox gradients. Chemical Geology, 195: 201-218.

Berelson, W.M., M. Prokopenko, F.J. Sansone, A.W. Graham, J. McManus & J.M. Bernhard, 2005. Anaerobic diagenesis of silica and carbon incontinental margin sediments: discrete zone of TCO2 production. Geochimica et Cosmochimica Acta, 69: 4611-4629.

Borowski, W.S., C.K. Paull & W. Ussler III, 1999. Global and local variations of interstitial sulfate gradients in deep-water, continental margin sediments: Sensitivity to underlying methane and gas hydrates. Marine Geology, 159: 131-154.

Davie, M.K. & B.A. Buffett, 2001. A numerical model for the formation of gas hydrate below the seafloor. J. Geophysical Research, 106: 497-514.

Dickens, G.R., 2001. Sulfate profiles and barium fronts in sediment on the Blake Ridge: Present and past methane fluxes through a large gas hydrate reservoir. Geochimica et Cosmochimica Acta, 65: 529-543

Donohue, C.M., G.R. Dickens & G.T. Snyder, 2006. Data Report: Major cation concentrations of interstitial waters collected from deep subsurface microbial communities (ODP Leg 201). *Proceedings ODP, Scientific Reports*, *201*: available http://www-odp.tamu.edu/publications/201_SR/104/104.htm>

Egeberg, P.K. & G.R. Dickens, 1999. Thermodynamic and pore water halogen constraints on gas hydrate distribution at ODP site 997 (Blake Ridge). Chemical Geology, 153: 53-79.

Fossing, H., T.G. Ferdelman & P. Berg, 2000. Sulfate reduction and methane oxidation in continental margin sediments influenced by irrigation (South-East Atlantic off Namibia). Geochimica et Cosmochimica Acta, 64: 897-910.

Joye, S.B., A. Boetius, B.N. Orcutt, J.P. Montaya, H.N. Schulz, M.J. Erickson & S.K. Lugo, 2004. The anaerobic oxidation of methane and sulfate reduction in

sediments from Gulf of Mexico cold seeps. Chemical Geology, 205: 219-238.

Luff, R. & K. Wallmann, 2003. Fluid flow, methane fluxes, carbonate precipitation and biogeochemical turnover in gas hydrate-bearing sediments at Hydrate Ridge, Cascadia Margin: Numerical modeling and mass balances. Geochimica et Cosmochimica Acta, 67: 3403-3421.

Niewöhner, C., C. Hensen, S. Kasten, M. Zabel & Schulz, H.D., 1998. Deep sulfate reduction completely mediated by anaerobic methane oxidation in sediments of the upwelling area off Namibia. Geochimica et Cosmochimica Acta, 62: 455-464.

Snyder, G.T., A. Hiruta, R. Matsumoto, G.R. Dickens, H. Tomaru, R. Takeuchi, J. Komatsubara, Y. Ishida & H. Yu, 2007. Pore water profiles and authigenic mineralization in shallow marine sediments above the methane-charged system on Umitaka Spur, Japan Sea. Deep-Sea Research (II), 54: 1216-1239.

Task 6: Numerical Models for Quantification of Hydrate and Free Gas Accumulations

Subtask 6.1: Model development. A numerical model has been developed for the simulation of the accumulation of hydrate and free gas over geological time and length scales in one or two dimensions. The details of the model are described by the PhD thesis of Gaurav Bhatnagar, which is included in Appendix A of this report. The mechanism included in this model include methanogenesis, sedimentation and compaction, advection and diffusion, sulfate-methane transition, Darcy's law, and constitutive relations for porosity, permeability, relative permeability, and capillary pressure, and a thermodynamic model for the gas/liquid/hydrate equilibrium of methane and brine. The results of Task 6 are based on this model.

Work has continued towards extending the one-dimensional numerical model to two spatial dimensions. Upward free gas migration due to buoyancy has also been included in the model. We have also developed the capability to model the effect of heterogeneities in focusing fluid flow and concentrating gas hydrate/free gas in two dimensions. We present two simple test cases to illustrate how gas hydrate/free gas is concentrated along high permeability conduits.

The first case models a system with a single vertical fracture located along the center of the grid that extends from the seafloor down to the bottom of the simulation domain. The fracture permeability is assumed to be 100 times greater than that of the surrounding sediment. Over geologic time, this fracture gets buried away from the seafloor with the downward moving sediment. Figure 6.1-1 shows the position of the fracture at a later time and the effect of focused fluid flow on gas hydrate and free gas saturation contours. It can be clearly seen from Figure 6.1-1 that gas hydrate as well as free gas is concentrated within and around the fracture compared to the surrounding sediment.

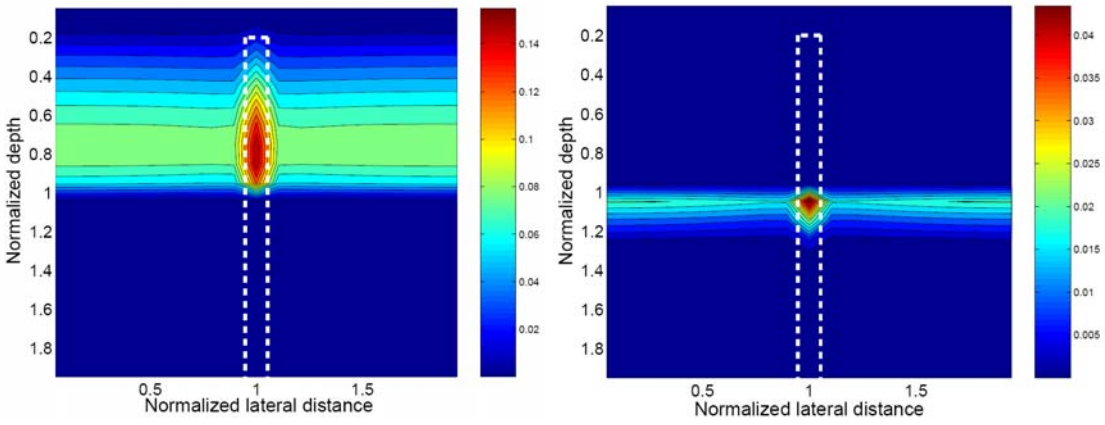

Figure 6.1-1: Gas hydrate (left) and free gas (right) saturation contours at dimensionless time $\tilde{t}$ = 0.1 after the fracture is introduced in the system. Dashed lines show the position of the fracture within the system.

Figure 6.1-2 shows the evolution of gas hydrate and free gas saturation at a later time ($\tilde{t}$ = 0.5). Peak gas hydrate saturation occurs within the fracture and close to the base of the GHSZ (~20%), which is almost twice the value in surrounding sediments at the same normalized depth. Free gas also accumulates in greater amount within the fracture, with peak saturation of about 50% beneath the GHSZ. Compared to Figure 6.1-1, the fracture has moved down to about half of the depth of the GHSZ. Consequently, the gas hydrate saturation in the upper half of the GHSZ becomes relatively homogeneous. At later times, the fracture gradually moves out of the GHSZ causing sediments to have a much more homogeneous hydrate distribution within the entire GHSZ.

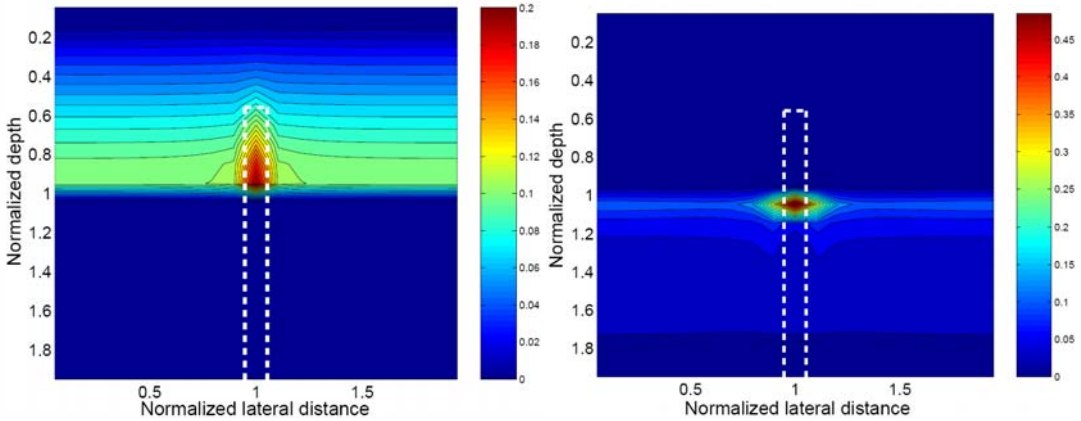

Figure 6.1-2**:** Gas hydrate (left) and free gas (right) saturation contours at dimensionless time $\tilde{t}$ = 0.5 after the fracture is introduced in the system. Dashed lines show the position of the fracture within the system.

We also study the effect of preferential gas hydrate accumulation in lithology of varying permeabilities. To model this scenario, we introduce a high permeability dipping sand layer within relatively low permeability clay sediments. The sand layer shown in simulations below has a dip of about 2.5 degrees and permeability 100 times greater than the clay permeability. Figure 6.1-3 shows the gas hydrate and free gas saturation contours at time $\tilde{t}$ = 0.25 after deposition. Continuous sedimentation buries the sand layer towards the base of the GHSZ, but the effect of fluid focusing in concentrating gas hydrate within the sand layer is clearly seen. The color axis for the hydrate saturation contour plot (Figure 6.1-3) is scaled to a maximum of 15% to show the hydrate distribution more clearly; otherwise the contour plot gets dominated by the high saturation gridblocks. Peak hydrate saturation increases to about 30% within the sand layer near the base of the GHSZ, while hydrate saturation at the same depth in neighboring clay sediments is only about 8%. The y-axis in the contour plots in Figure 6.1-3 has a vertical exaggeration (VE) of about 2:1, so that the sand layer appears to have a dip greater than the true dip of 2.5 deg.

At a later time ($\tilde{t}$ =0.75), the sand layer almost passes completely through the GHSZ (Figure 6.1-4). Consequently, hydrate saturation returns to a more homogeneous distribution within the GHSZ. Free gas saturation increase to about 60% within the sand layer just below the GHSZ and also migrates laterally to increase peak gas saturation in the lower permeability sediments to about 30% (Figure 6.1-4).

The above simulations were relatively simple test cases performed to validate our two-dimensional model and code. Effect of different system parameters, such as thickness of beds, permeability contrasts, dip angles, and combination of different permeability beds with fracture networks are planned as future work.

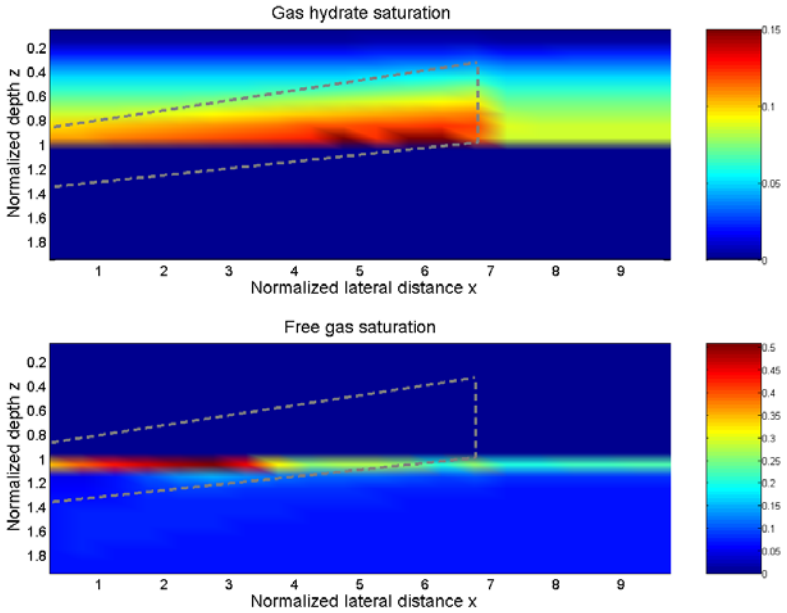

Figure 6.1-3**:** Gas hydrate and free gas saturation contours at dimensionless time $\tilde{t}$ =0.25 after deposition of the sand layer within low permeability clay sediments. Peak hydrate saturation within the sand layer increases to about 30%, but the color axis is scaled to a maximum of 15% to show the other contours more clearly. Vertical exaggeration is about 2:1.

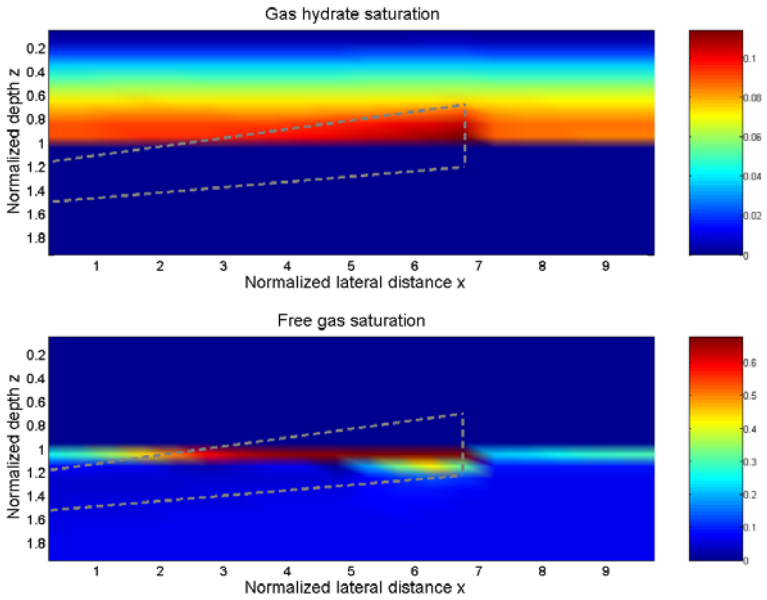

Figure 6.1-4**:** Gas hydrate and free gas saturation contours at dimensionless time $\tilde{t}$ =0.75. Sand layer almost passes through the GHSZ, causing hydrate saturation to become more homogeneous laterally within the GHSZ. Vertical exaggeration is about 2:1.

In conclusion, numerical models have been developed in 1-D and 2-D for the accumulation of hydrate and free-gas. The applications of this model are described in the following subtasks.

***Subtask 6.2: Conditions for existence of gas hydrate*.**

G. Bhatnagar, W. G. Chapman, G. R. Dickens, B. Dugan, and G. J. Hirasaki, "Generalization Of Gas Hydrate Distribution and Saturation In Marine Sediments by Scaling of Thermodynamic and Transport Processes," *American Journal of Science*, Vol. **307**, June, 2007, P. 861–900, DOI 10.2475/06.2007.01

ABSTRACT.

Gas hydrates dominated by methane naturally occur in deep marine sediment along continental margins. These compounds form in pore space between the seafloor and a sub-bottom depth where appropriate stability conditions prevail. However, the amount and distribution of gas hydrate within this zone, and free gas below, can vary significantly at different locations. To understand this variability, we develop a one-dimensional numerical model that simulates the accumulation of gas hydrates in marine sediments due to upward and downward fluxes of methane over time. The model contains rigorous thermodynamic and component mass balance equations that are solved using expressions for fluid flow in compacting sediments. The effect of salinity on gas hydrate distribution is also included.

The simulations delineate basic modes of gas hydrate distribution in marine sediment, including systems with no gas hydrate, gas hydrate without underlying free gas, and gas hydrate with underlying free gas below the gas hydrate stability zone, for various methane sources. The results are scaled using combinations of dimensionless variables, particularly the Peclet number and Damkohler number, such that the dependence of average hydrate saturation on numerous parameters can be summarized using two contour maps, one for a biogenic source and one for upward flux from a deeper source. Simulations also predict that for systems at steady state, large differences in parameters like seafloor depth, seafloor temperature and geothermal gradient cause only small differences in average hydrate saturation when examined with scaled variables, although important caveats exist. Our model presents a unified picture of hydrate accumulations that can be used to understand well-characterized gas hydrate systems or to predict steady-state average hydrate saturation and distribution at locations for which seismic or core data are not available.

(Only the abstract is presented here since the manuscript has been published.)

Subtask 6.3. Compositional Effect on BSR The presence of methane hydrate is usually detected by a bottom simulating reflector (BSR). The BSR results from the sudden change in acoustic impedance as the formation changes from being hydrate saturated to free-gas saturated at the base of the hydrate stability zone. If other hydrocarbons in addition to methane are present, this transition may take place over a depth greater than the acoustic wavelength and the BSR may be attenuated or absent.

Natural gas from thermogenetic sources may contain many hydrocarbons. Thus compositional effect should be considered when thermogenetic natural gas is present. In the following work, we focus on the CH_4-C_3H_8-H_2O hydrate system as an example. The effects of propane on the hydrate formation condition and on hydrate distribution, are studied. D. Sloan's CSMGem program is used to obtain the gas/liquid/hydrate equilibrium data.

An example saturation calculation will be presented in the end of the following work. The purpose of this example calculation is to demonstrate the possibility of gradual change of saturations with distance in sediment. The calculation is based on constant composition, whereas compositions will change during fluid migration in realistic cases.

Denote the overall molar fraction of species *i* as:

$$x_i = \frac{n_i}{n_{CH4} + n_{C3H8} + n_{H2O}}$$, *i* = CH_4, C_3H_8, H_2O.

where n_i is the amount of species *i* in the system (unit: mol), *i* = CH_4, C_3H_8, H_2O.

The water free molar fraction of species *i* is denoted as:

$$x_i^{wf} = \frac{n_i}{n_{CH4} + n_{C3H8}} = \frac{x_i}{x_{CH4} + x_{C3H8}}$$, *i* =C H_4, C_3H_8.

(1) Incipient Hydrate Formation Condition and Phase Regions

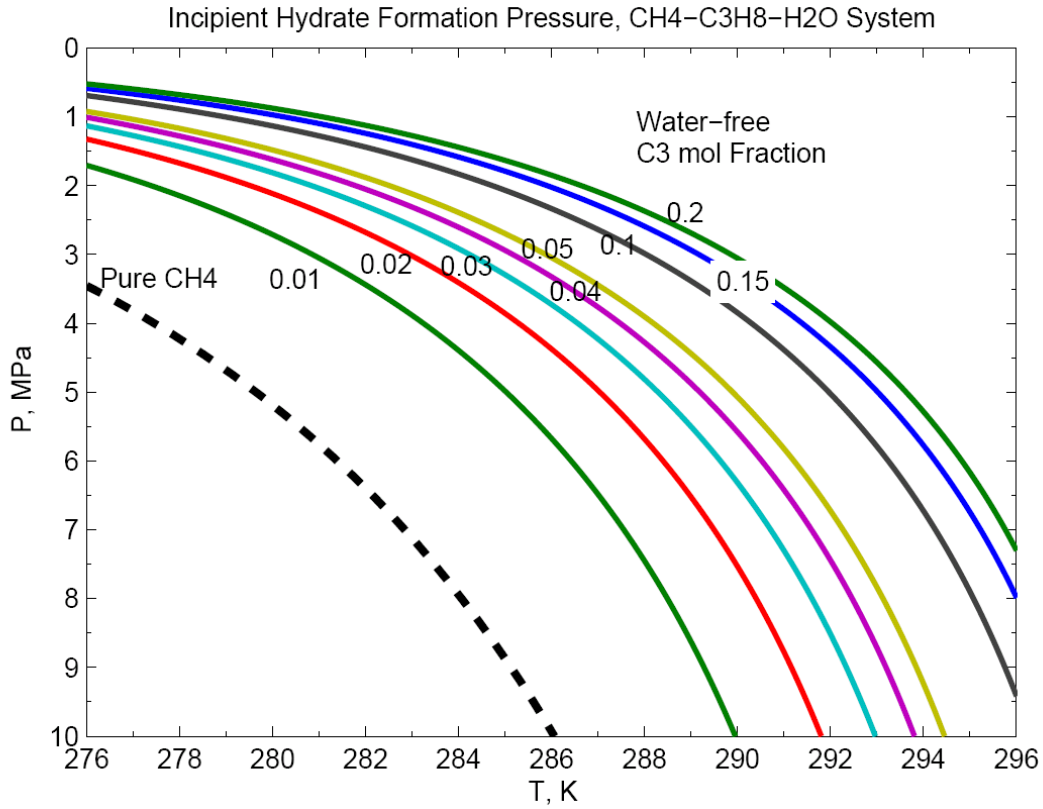

Fig. 6.3-1. Incipient Hydrate Formation Pressure of the CH_4-C_3H_8-H_2O System. Water is in excess. The data labeled for each curve, are the water-free propane molar fractions. The black dash curve, is for the pure CH_4-H_2O system (i.e. water-free propane molar fraction = 0).

Fig. 6.3-1 shows the incipient hydrate formation pressure of the CH_4-C_3H_8-H_2O System. For x_{C3H8}^{wf} = 0.01, the incipient hydrate formation pressure differs very much from that for the pure CH_4 system (i.e., x_i^{wf} = 0).

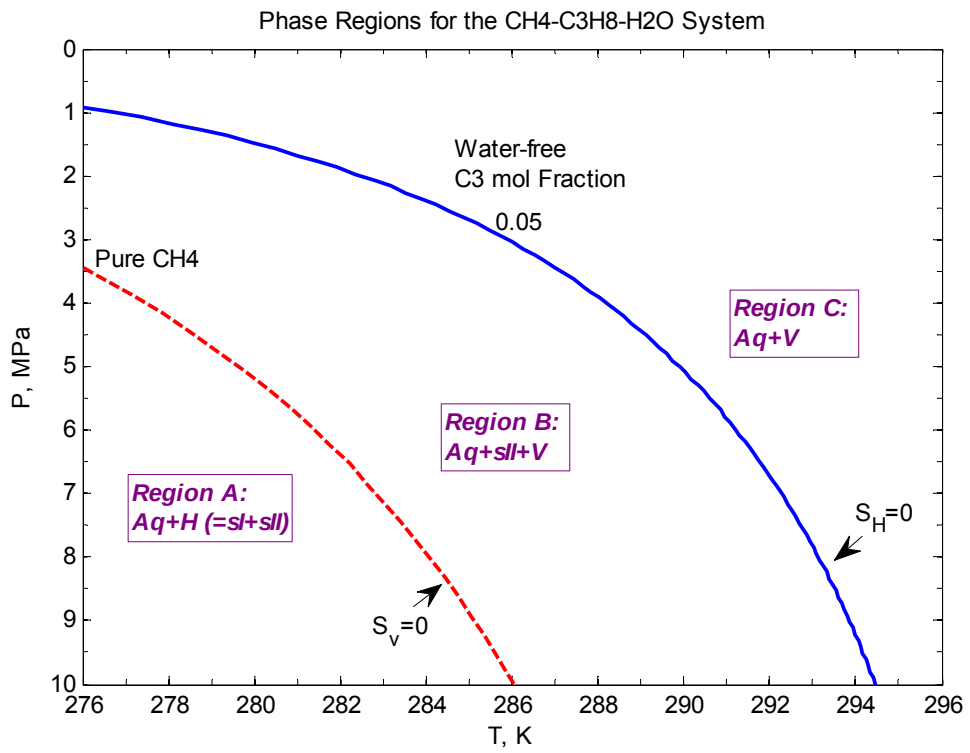

Fig. 6.3-2. Phase Regions of the CH_4-C_3H_8-H_2O System (water-free propane molar fraction is 0.05). Water is present in excess. The red dash curve is the incipient hydrate formation pressure for the pure CH_4-H_2O system. There are 3 regions: Region *A, B, C*. Region *A*: *Aq* + *Hydrate* (= *sI* + *sII*); Region *B*: *Aq* + *sII* + *V*; Region *C*: *Aq* + *V*. The red dash curve, and the blue solid curve, are boundaries for S_v=0 and S_H=0, respectively.

Fig. 6.3-2 presents the phase regions of the CH_4-C_3H_8-H_2O System (x_{C3H8}^{wf} is 0.05). 3 phase regions are marked in the figure. In Region A, both sI and sII hydrates are stable, while in Region B and C, sI is not stable. In Region B, sII is stable, while in Region C, sII hydrate is not stable. Therefore, in Region B, 3 phases can co-exist: Aq, H, and V. The boundaries for S_v=0 and S_H=0 are marked in the Fig. 6.3-2.

(2) Gradual Phase Transition (i.e. Saturation Change) in Sediment

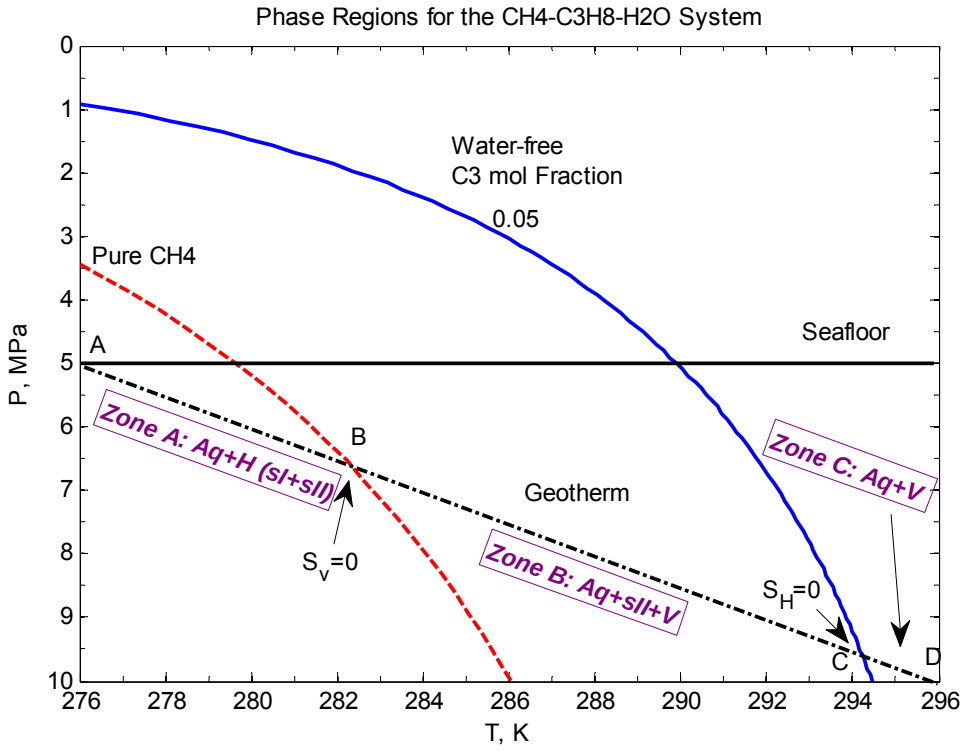

Fig. 6.3-3. Different zones of sediments of a CH_4-C_3H_8-H_2O System (water-free propane molar fraction is 0.05). The Geotherm curve is shown as the black dash-dot curve. There are 3 zones of sediments along the geotherm curve. Zone *A* (Line segment *AB*): *Aq + Hydrate* (= *sI + sII*); Zone *B* (Line segment *BC*): *Aq + sII + V*; Zone *C* (Line segment *CD*): *Aq + V*. Points *B* and *C*, are boundaries for S_v=0 and S_H=0 in the sediment, respectively.

In Fig. 6.3-3 an example geotherm curve in sediment is considered. Three different zones may exist in the sediment along the geotherm curve, due to the 3 different phase regions described in Fig. 6.3-2. Zone *B* is a special one: 3 phases, *Aq + H (sII) +V*, co-exist. The boundary for S_v=0 in the sediment is the point B in Fig. 6.3-3, while that for S_H=0 is the point C. It's obvious that Zone B (Line *BC*) is a phase-transition-zone corresponding to the boundary of S_v=0 to that of S_H=0. Line segment BC in Fig. 6.3-3, around 300 m in spatial distance, is definitely very long. Such a gradual change of saturations within a long distance, may result in gradual change of sediment acoustic properties, and further induce weak BSR or even absence of BSR. An example calculation can demonstrate the possibility of such kind of gradual saturation change, as shown in Fig 6.3-4.

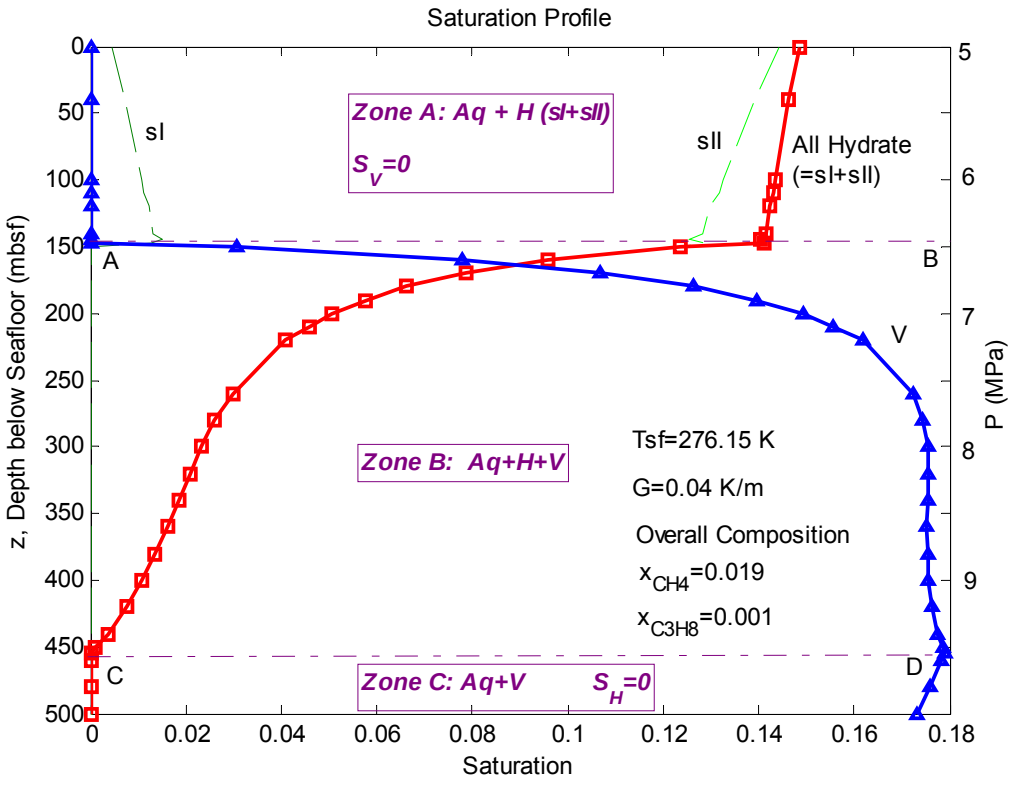

Fig. 6.3-4. An example calculation of a CH_4-C_3H_8-H_2O System (water-free propane molar fraction is 0.05; Overall composition x_{CH4}=0.019, x_{C3H8}=0.001, x_{H2O}=0.98). Assume: The overall composition is the same in the spatial domain. There are 3 zones of sediments in the domain. Zone A: *Aq + Hydrate* (= *sI + sII*); Zone B: *Aq + sII + V*; Zone C: *Aq + V*. Dash-dot line *AB* and *CD*, are boundaries for S_V=0 and S_H=0 in the sediment, respectively. Red solid curve and blue solid curve are saturation profiles for All Hydrate (=sI + sII), and for Vapor, respectively. Seafloor temperature T_{sf} = 276.15 K. Geothermal gradient G= 0.04 K/m. Pressure is marked on the right side.

An example calculation of a CH_4-C_3H_8-H_2O System is presented in Fig. 6.3-4. The following conditions and assumptions are applied:

(1) Water-free propane molar fraction is 0.05; Overall composition x_{CH4}=0.019, x_{C3H8}=0.001, x_{H2O}=0.98.
(2) Overall composition is constant in the spatial domain.
(3) Seafloor temperature T_{sf} = 276.15 K. Geothermal gradient G= 0.04 K/m.
(4) Seafloor Pressure P_{sf}=5 MPa.

As is well known, there is a sharp phase transition in the CH_4-H_2O hydrate system, which is the basis for BSR. However, for a CH_4-C_3H_8-H_2O System, in Zone *B* in Fig. 6.3-4, from z=147.5 mbsf (Line *AB*) to z= 450 mbsf (Line *CD*), the S_H decreases continually from 14.1% to 0%, while S_V increases continuously from 0% to 17.9%. Zone *B* is a phase transition zone, in which 3 phases (Aq+H+V) co-exist, and saturations change continuously.

A gradual saturation change will result in the gradual change of acoustic properties with increase in depth, and consequently, very possibly induce a weak BSR, or even absence of BSR.

Conclusion

(1) For the CH_4-C_3H_8-H_2O hydrate system, the incipient hydrate formation conditions are presented. There is a big difference for the incipient hydrate formation condition of the CH_4-C_3H_8-H_2O hydrate system, from that of the CH_4-H_2O hydrate system, even when the water-free-propane molar fraction is only 0.01.

(2) 3 different phase regions are described for different *P-T* conditions. As shown in Fig. 6.3-2. Region B is especially important, because Aq, H (sII), V can co-exist. Therefore, in the sediment, 3 zones can be present. Zone B, is the phase-transition-zone, because Aq, H (sII), V co-exist, and S_H and S_v change gradually.

(3) The result of an example saturation calculation of the CH_4-C_3H_8-H_2O hydrate system in the sediment is presented in Fig. 6.3-4. It successfully demonstrated that continuous change of S_H and S_v over a long spatial distance (~300 m) is possible. A gradual change of saturations, may result in gradual change of acoustic properties, and induce weak BSR or even no BSR.

Future Work

The work presented in this report is based on constant composition in sediment as an example. In real situations, the composition in spatial domain is not constant, but dependent on various kinds of factors, such as the fluid flow, diffusion, and phase transformation. Therefore, compositional fluid migration simulation with consideration of fluid flow, diffusion, phase transformation, will be carried out to compute realistic compositions and saturation profiles. The acoustic impedance and seismic reflection will be computed from the saturation profile.

Subtask 6.5: Processes leading to overpressure.

Work has continued through one-dimensional numerical modeling to ascertain the factors and dimensionless groups responsible for overpressure generation in gas hydrate systems. We had determined through numerical simulations that the ratio of sediment absolute permeability to the sedimentation rate was the key dimensionless group controlling overpressure generation. This group, N_{sc}, was defined as:

$$N_{sc} = \frac{k_0 \rho_w g}{\mu_w \dot{S}}$$

where k_0 is the sediment permeability, ρ_w is seawater density, μ_w is viscosity and $\dot{S}$ is sedimentation rate. Figure 6.5-1 shows that higher values of N_{sc} indicate high permeability and/or low sedimentation rate, leading to hydrostatic pore pressures. As N_{sc} decreases, pore pressure starts to increase towards lithostatic values.

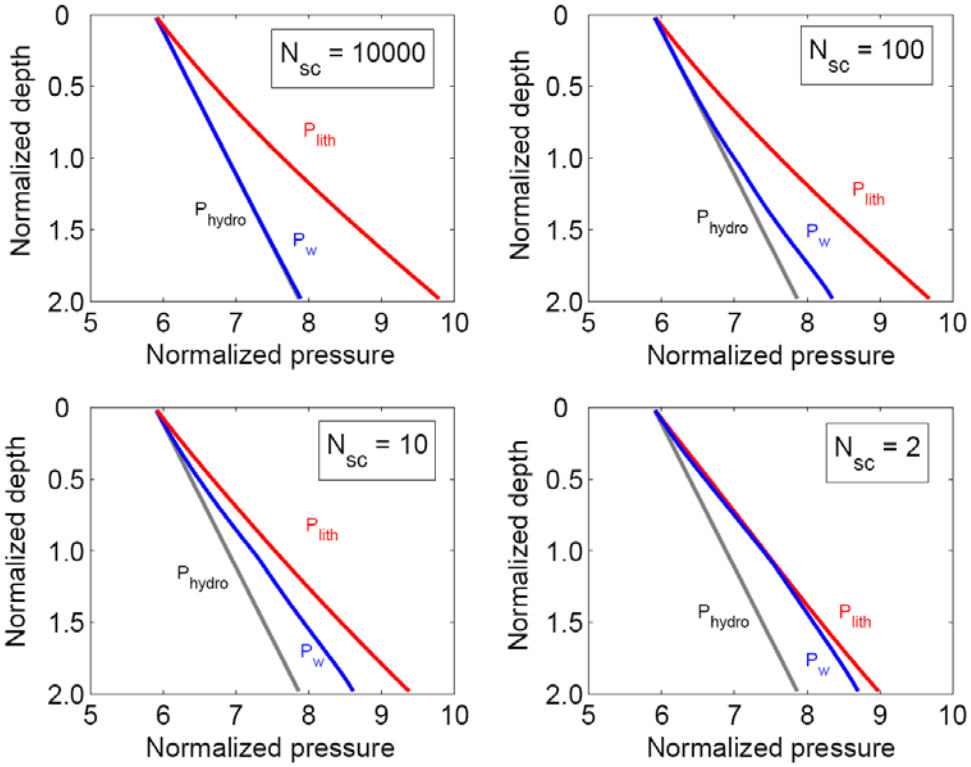

Figure 6.5-1**:** Effect of the dimensionless group N_{sc} on pore pressure evolution. P_{lith}, P_w and P_{hydro} denote lithostatic, pore pressure and hydrostatic pressure profiles, respectively. Relatively higher values of N_{sc} lead to almost hydrostatic pore pressure, while N_{sc} close to unity results in pore pressure that is very close to the lithostatic limit.

The effect of overpressure, in turn, limits the amount (thickness) of free gas that can accumulate below the GHSZ. This situation is depicted schematically in Figure 6.5-2a, where hydrostatic pore pressures allow a relatively long connected gas column to form. On the other hand, Figure 6.5-2b shows that overpressure generation can significantly reduce the thickness of this connected gas column before gas pressure reaches the lithostatic limit at the BHSZ and causes sediments to fracture.

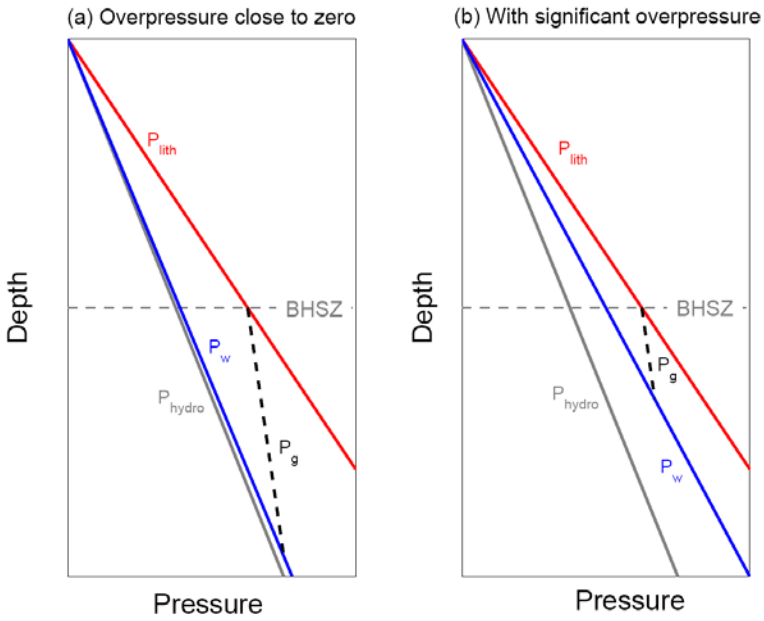

Figure 6.5-2**:** Schematic illustration of the effect of overpressure on the maximum thickness of the connected free gas column beneath the GHSZ. P_{lith}, P_w, P_{hydro} and P_g denote lithostatic, pore pressure, hydrostatic and gas pressure profiles, respectively. Development of overpressure can significantly reduce the thickness of the connected gas column before fracturing occurs.

We have now modeled this effect of N_{sc} on gas column thickness by allowing free gas to migrate buoyantly upwards when the critical gas saturation is exceeded. Two test cases are presented next. The first case (Figure 6.5-3), simulated for a relatively high value of N_{sc}, shows a thick connected gas column beneath the GHSZ due to low overpressure development. At the simulation time shown in Figure 6.5-3, gas pressure becomes equal to the lithostatic stress at the base of the GHSZ, causing sediments to fracture. Figure 6.5-4 shows a case simulated for N_{sc}=10, which shows that only a thin gas column develops before sediment fracturing is initiated. Thus, low values of this ratio N_{sc}, which physically translates to settings with low sediment permeability and/or fast sedimentation rates, will only allow thin gas columns to develop before sediment fracture occurs and vents the gas.

Conclusions A dimensionless has been identified to quantify the departure of the pressure profile from that of hydrostatic equilibrium. Departure of the pressure from hydrostatic reduces the maximum thickness of a gas column before sediment fracturing limits the free-gas accumulation.

This work has been accepted for a poster presentation at the 6th International Conference on Gas Hydrates, Vancouver, British Columbia, 2008. The abstract for this presentation is titled "***Effect of Overpressure on Gas Hydrate Distribution***". (Appendix B)

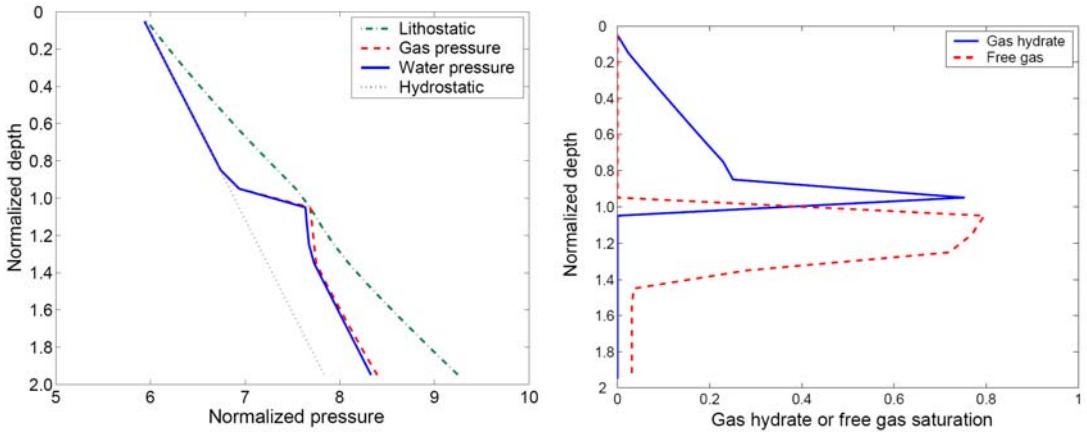

Figure 6.5-3**:** Normalized pressure profiles (left) and gas hydrate and free gas saturation profiles (right) for N_{sc}=1000. Gas pressure at this time is just equal to the lithostatic stress. A relatively thick connected gas column exists beneath the GHSZ at this state.

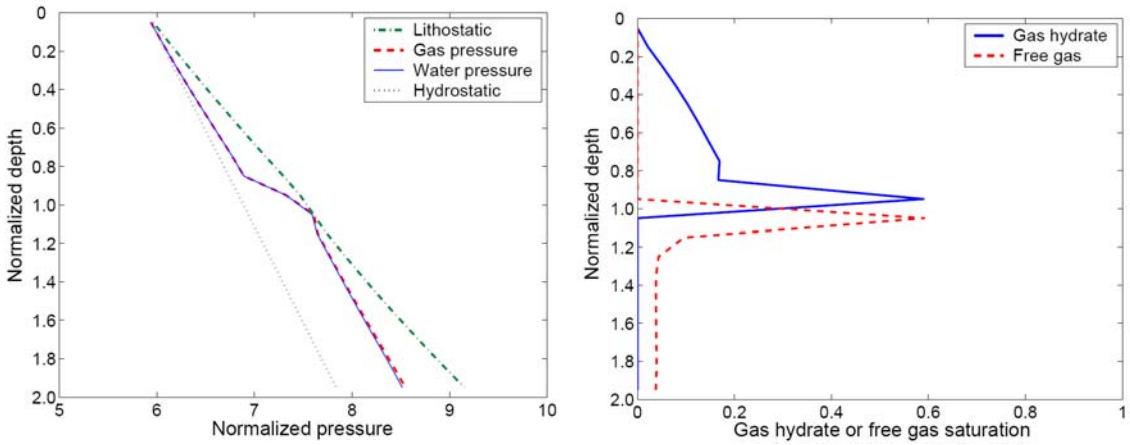

Figure 6.5-4**:** Normalized pressure profiles (left) and gas hydrate and free gas saturation profiles (right) for N_{sc}=10. Gas pressure at this time is just equal to the lithostatic stress. Compared to Figure 6.5-3, a relatively thin connected gas column exists beneath the GHSZ at this state.

Subtask 6.8: Sulfate profile as indicator of methane flux.

Numerical and analytical models have been developed for inferring gas hydrate saturation in marine sediments from pore water sulfate profiles. These models utilize the depth of the sulfate-methane transition (SMT) as the primary input variable and are valid for systems dominated by methane supply from deeper sources. Results from these models are in agreement with gas hydrate saturations estimated from resistivity logs/chloride data at several sites along Cascadia Margin.

The numerical model is explained in a short article in Geophysical Research Letters, titled "***Sulfate-methane transition as a proxy for average methane hydrate saturation in marine sediments***". *Geophysical Research Letters*, VOL. **35**, L03611, doi:10.1029/2007GL032500, 2008. The details are in the thesis in Appendix A.

Analytical theory has also been developed to predict steady-state gas hydrate saturation in deep-source systems using the depth of the SMT as the primary input. This theory allows calculation of the gas hydrate saturation profile, as well as the sulfate and methane concentration profiles, using simple analytical expressions. Figure 6.8-1 below shows gas hydrate saturation profiles as a function of scaled depth below the seafloor for different values of the SMT depth $\tilde{L}_s$**,** which is the ratio of the SMT depth to the depth to the base of the gas hydrate stability zone (GHSZ). Shallow SMT depths indicate higher methane flux and, consequently, higher gas hydrate saturation. Results from our numerical models (crosses) compare favorably with our analytical results (curves).

Several interesting aspects of gas hydrate systems can also be explained using our analytical theory. For example, we show why the depth to the first occurrence of gas hydrate below the seafloor is often 10-12 times the depth of the SMT (Figure 6.8-2) using our analytical theory. This "10 x SMT" relationship has been often hypothesized in the literature based on field observations. Figure 6.8-2 shows this ratio as a function of scaled SMT depth and demonstrates that the ratio is close to 10-12 for relatively large SMT depths, but increases to higher values for relatively shallower SMT depths.

Conclusions The depth of the sulfate-methane transition is an indicator of the average hydrate saturation when the accumulation is the result of steady-state accumulation from deeper sources.

This analytical theory has been written into a longer manuscript during this quarter and will be submitted shortly for publication in *Geochemistry, Geophysics, Geosystems*. This work has also been accepted for oral presentation at the 6th International Conference on Gas Hydrates, Vancouver, British Columbia, 2008. The abstract for this presentation is titled "***Relating Gas Hydrate Saturation to Depth of Sulfate-Methane Transition***". (Appendix C)

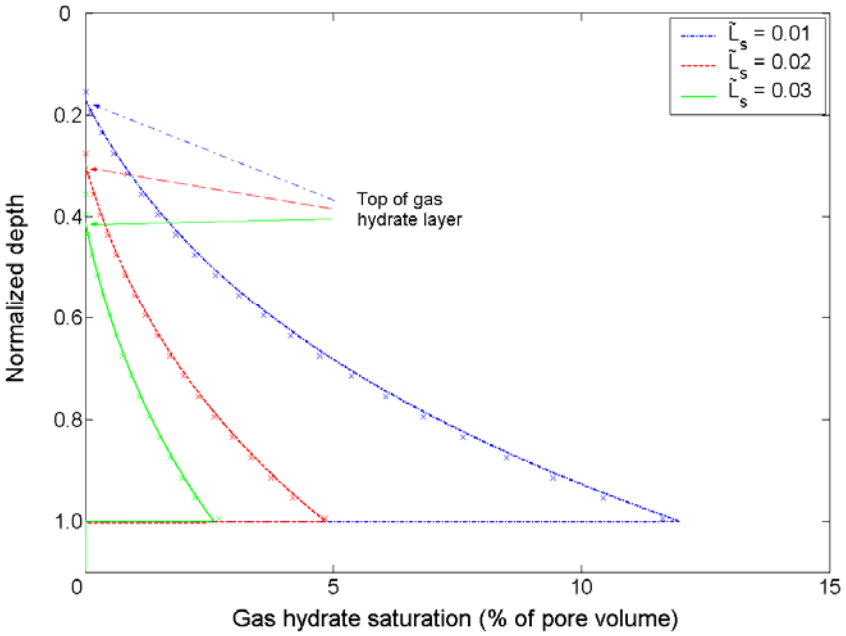

Figure 6.8-1**:** Steady-state gas hydrate saturation profiles for different scaled SMT depths $\tilde{L}_s$. Crosses denote numerical model results, while curves represent the analytical model.

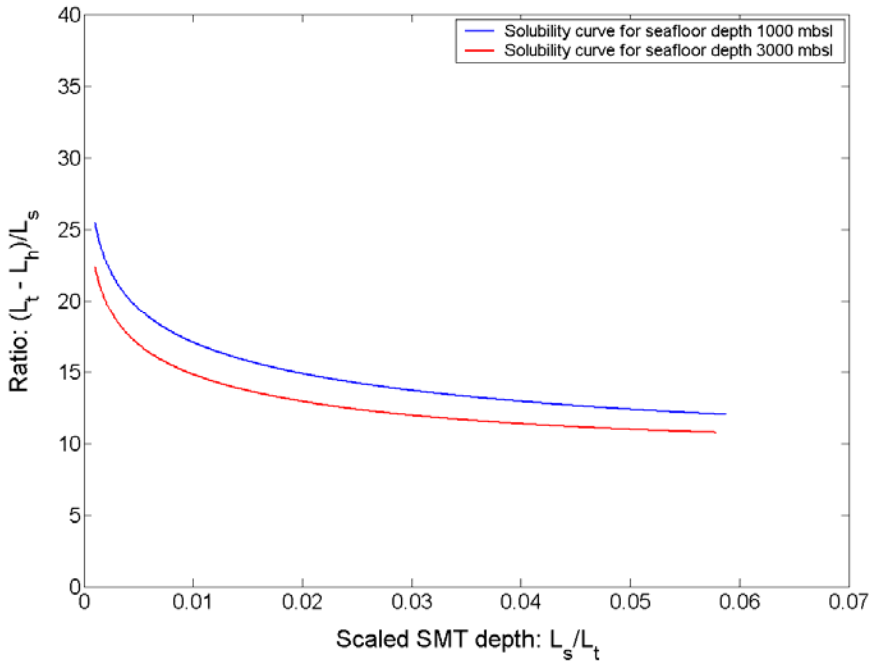

Figure 6.8-2**:** Relationship between the ratio of depth to the first occurrence of gas hydrate ($L_t - L_h$) to the SMT depth (L_s) as a function of the scaled SMT depth (L_s / L_t) for two different seafloor depths.

Task 6 Students

Gaurav Bhatnagar completed his Chemical Engineering PhD requirements and began employment in February 2008 with Shell Oil Company at the Westhollow Research Center.

Guangsheng Gu is continuing and Sayantan Chatterjee has been added as Chemical Engineering PhD students.

Task 7: Analysis of Production Strategy

We are moving forward on Task 7 as scheduled and as outlined by the Milestone Status. Task 7.1 involves code comparison and pore-scale development. Code comparison is complete and our results have been communicated Prof. Brian Anderson of University of West Virginia. Pore-scale modeling is expected to be completed in June. Petrophysical and thermophysical properties will be computed in the next 12 months. Task 7.2 involves modeling production strategies and incorporating reservoir heterogeneities. These subtasks would be executed in the following years. We are working with Prof. Hirasaki's group (Task 6) and Dr. Dugan's group (Task 8) to estimate the hetergeneities in reservoir properties. We are presenting a paper in the upcoming ICGH in Vancouver and staying appraised of the industrial and academic perspectives.

Subtask 7.1 Code Comparison

Overview

Task 7.1a includes code comparison and understanding of hydrate distribution at the pore-scale. We have conducted the following in the last year. We participated in the NETL methane hydrate code comparison study to evaluate the capabilities of the in-house (University of Houston) simulator with respect to other existing hydrate simulators participating in the code comparison study, we simulated warm water injection into simple homogeneous hydrate reservoirs and depressurization to identify the saturation history pores go through during hydrate dissociation. We performed simulations of hydrate formation in simple pores using the University of Houston in-house simulator.

Approach

We have completed simulation of the first four problems set up by the Code Comparison Study group by our in-house hydrate simulator. Our results have been communicated to Prof. Brian Anderson, the coordinator of the Code Comparison Study group. Warm water injection into a homogeneous hydrate reservoir has been modeled. Hydrate formation in simple cylindrical pores have been modeled.

Results & Discussion

Problem 1

This problem calculates transition to equilibrium in the absence of hydrates. The aqueous saturation, aqueous pressure and temperature calculated by our simulator are in complete agreement with the other results. There is a slight discrepancy in the mass fraction of methane in the aqueous phase. This may be due to different correlations used in different simulators for methane solubility. Our results are labeled UH in Figure 7-1.

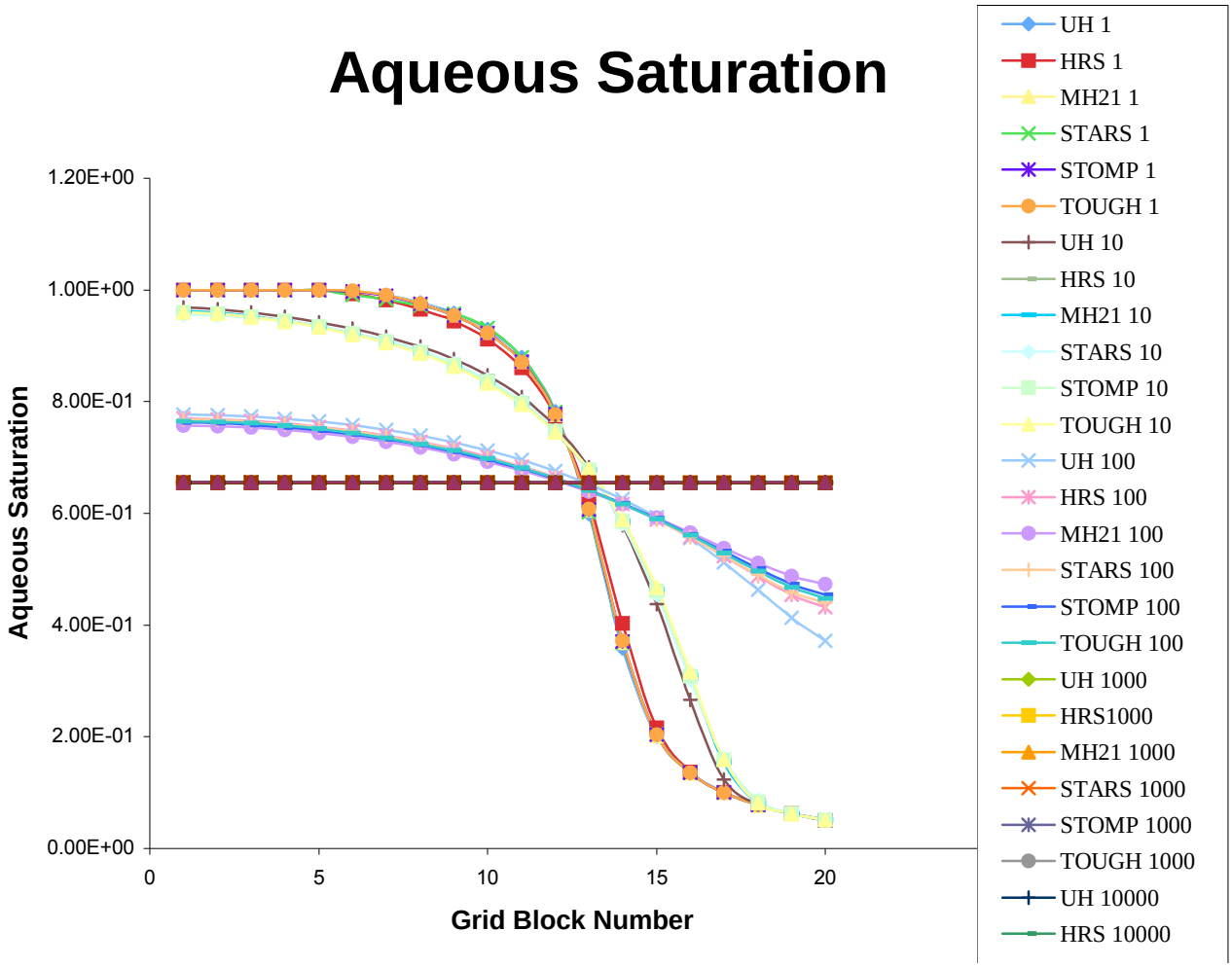

Figure 7-1. Water saturation (parameter is time in days) in Problem 1

Problem 2

This problem calculates transition to equilibrium in a closed domain with hydrate dissociation. There is a discrepancy in the position of the saturation front (Figure 7-2). We believe, that is due to the unspecified correlation of change of permeability with hydrate saturation. (This issue is present in all the problems except Problem 1). The sediment permeability changes with hydrate saturation; we have used a correlation. We do not know the correlations used by others. Heat conductivity of the hydrates is also not specified. It affects the heat flow and hence the slight deviation in the results. Our results are shown in yellow in the plots.

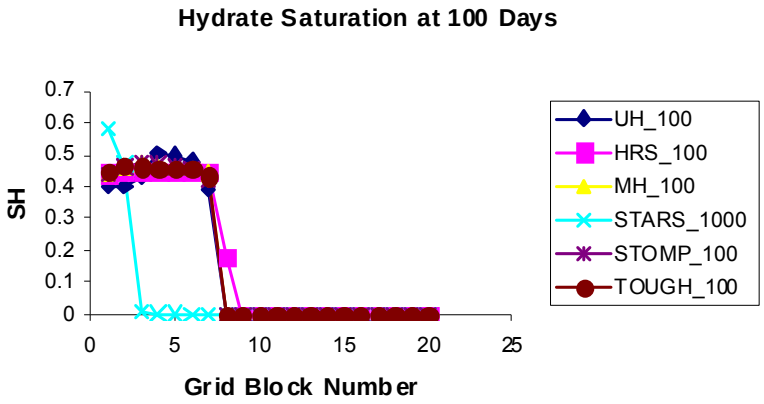

Figure 7-2. Comparison of hydrate saturation at 100 days in Problem 2

Problem 3

This problem calculates hydrate dissociation in an open 1-D domain. In the first part, hydrate is dissociated by thermal stimulation. In the second part, hydrate is dissociated by depressurization without ice formation. In the third part, hydrate is dissociated by depressurization with ice formation for a very low pressure.

Thermal Stimulation (3_1)

Most of the results match except for the gas saturation (Figure 7-3), which is high because permeability is low. The aqueous saturation does not deviate much because water is already present and gas is formed by dissociation of hydrates. The methane release curves are different because they depend on two processes: the increase in permeability due to hydrates melting and the amount of hydrates that melt.

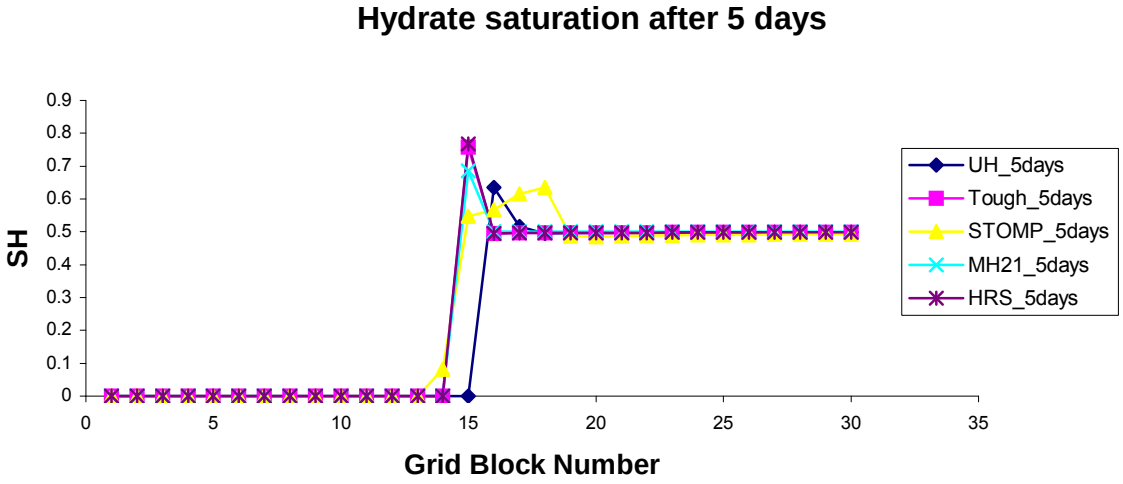

Figure 7-3. Comparison of hydrate saturation in Problem 3, part 1

Depressurization (3_2)
The results for all the simulators match except for a small difference in the shape of the hydrate front (Figure 7-4).

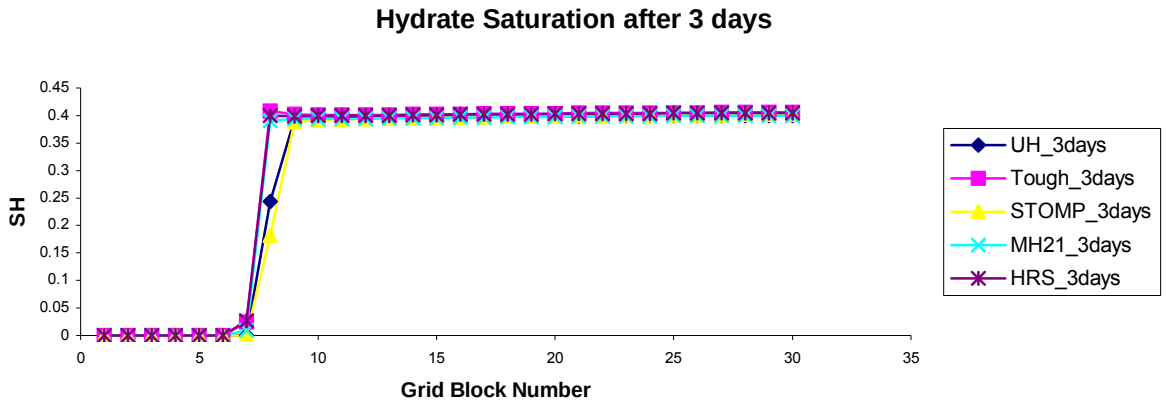

Figure 7-4. Comparison of hydrate saturation in Problem 3, part 2

Depressurization with ice formation (3_3)
Figure 7-5 shows the ice saturation at 5 days. Our, STOMP and MH21 results are stable, but the other results have oscillations.

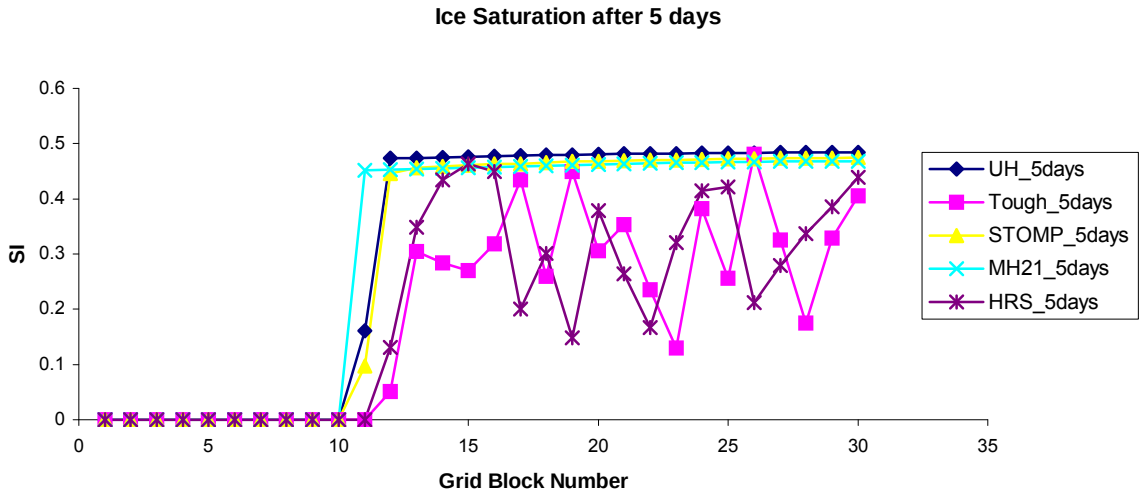

Figure 7-5. Comparison of hydrate saturation in Problem 3, part 3

Problem 4

Thermal Stimulation in Radial Coordinates

Problem 4 addresses thermal stimulation of a hydrate reservoir in 1-D radial coordinates. The radial hydrate saturation distribution at several times show that all the plots almost fall on each when plotted against r^2/t. The results from our simulator matched with those from other simulators (not shown).

Modeling of Warm Water Injection

In this work, we are considering injection of warm water and depressurization for production from Class 2 hydrate reservoirs. The source of warm water could be a nearby oil reservoir or an underlying water aquifer. Gas production from a hydrate reservoir is studied through numerical simulation.

The numerical model used is a finite-volume simulator that takes into account heat transfer, multiphase fluid flow and equilibrium thermodynamics of hydrates. Four components (hydrate, methane, water and salt) and five phases (hydrate, gas, aqueous-phase, ice and salt precipitate) are considered in the simulator. Water freezing and ice melting are tracked with primary variable switch method (PVSM) by assuming equilibrium phase transition. Equilibrium simulation method is used here because kinetics of hydrate formation and dissociation are relatively fast in the field-scale. This simulator has been validated against several other simulators for the problems in the code comparison study conducted by US DOE.

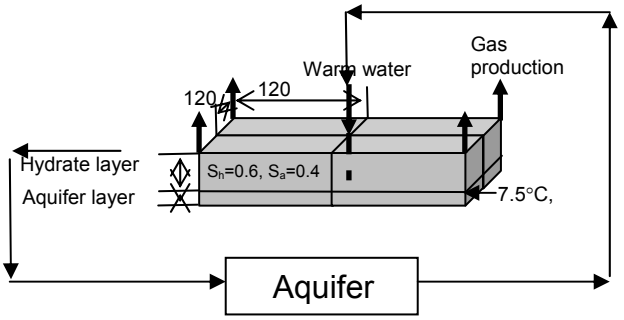

Figure 7-6: Domain considered for the base case

The objective of this study is to identify optimum production strategies for gas production from Class 2 hydrate reservoirs through numerical simulation. The domain selected as the base case is a quarter five-spot of size 120m x120m x10m (Figure 7-6). Initial temperature and pressure are assumed to be 7.5°C and 9MPa, respectively, which lie in the hydrate stable zone. The bottom 2m of the domain is an aquifer layer (S_A=1.0) and the top 8m is a hydrate layer with a hydrate saturation, S_H of 0.6 and aqueous saturation, S_A of 0.4. There is no heat and mass transfer though the side boundaries due to symmetry. There is only

heat transfer, but no mass flow through the top and bottom boundaries due to impermeable shale layers. The effect of injection temperature, injection pressure and production well pressure on gas and water production is studied. The saturation histories encountered in these simulations will be modeled at the pore scale for transport properties.

Simulations were run for different injection pressures, injection temperatures and production pressures for 3000 days and total production of gas was compared for the above parameters.

For the case of no injection, the dissociation is due to pressure falling below the hydrate stable pressure due to depressurization at the production well. The heat of dissociation comes from surroundings, decreasing the temperature of the reservoir. Ice starts forming if the pressure goes below quadruple point pressure. After all the hydrates dissociate, the temperature again starts rising by the heat from surroundings.

For the case of warm water injection, the pressure of injection has to be higher than the reservoir pressure for the hot water to go in. The temperature rise is higher for higher temperature and higher injection pressure (injection flow rate increases). But if injection pressure is high, the average pressure in the reservoir increases, slowing the dissociation of hydrates (and even formation of additional hydrates) before the warm water reaches a certain region. If production pressure and temperature are both high, the rate of production of gas increases. The total production of gas also depends on the production pressure, and for different production pressure the optimum injection conditions vary.

Figure 7-7 shows total production for the production well pressure of 2MPa. The injection temperature was kept constant at 20C and injection pressure was varied. The results were compared against the no injection or depressurization only case. When warm water is injected at a higher pressure but at a relatively low temperature (20C in the present case) the gas production rate decreases with increasing injection pressure. This is because the average pressure of the reservoir domain increases; dissociation of hydrate slows down. In case of 5MPa of injection pressure, the total production of gas increases because water occupies some pore space that would have been occupied by gas during depressurization. At higher injection pressure the hydrate dissociation is not complete in 3000 days. For low temperature water injection, only depressurization seems to be better than warm water injection.

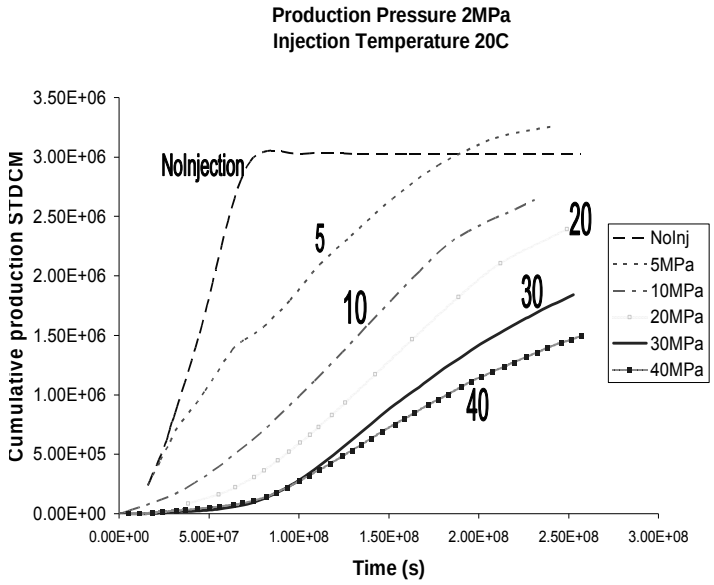

Figure 7-7: Cumulative production of gas with varying injection pressure, 20°C of injection temperature and 2MPa of production pressure

Figure 7-8 shows the cumulative production of gas when production well pressure is kept at 4MPa and injection temperature is 80°C. The injection pressure is varied. In this case, only depressurization is slow and does not dissociate all the hydrates present in 3000 days. With increasing injection pressure the gas production rate increases. With an injection water of 80°C, as the injection pressure increases more of the reservoir gets to this high temperature which helps hydrate dissociation.

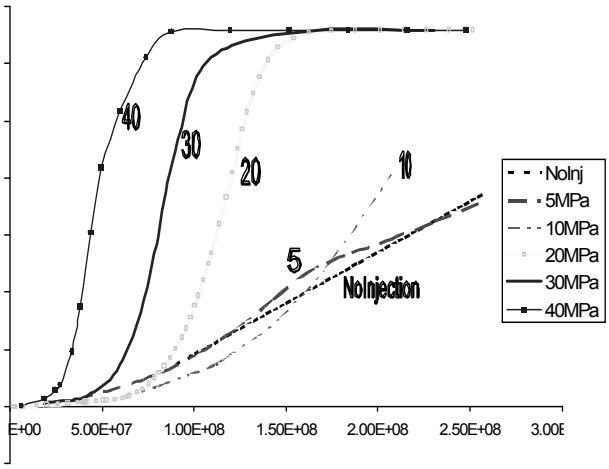

Figure 7-8: Cumulative production of gas with varying injection pressure at 80°C of injection temperature and 4MPa of production pressure.

If injection temperature is in medium range (50°C) then injection pressure and production pressure play an important role. Figure 7-9 and 7-10 are plots for 2MPa and 4MPa of production pressure, respectively, at 50°C of injection temperature with varying injection well pressures. If Injection pressure rises from 5MPa to 10MPa the production almost remains same for the case of production pressure 2MPa but decreases drastically in the case of production pressure 4MPa. This can be attributed to higher average pressure in the reservoir domain, which hinders hydrate dissociation. In case of injection pressure of 30MPa and 40MPa the total production and rate of production increases (Figure 7-9 and 7-10), though initial rate of production falls due to increase in average reservoir pressure, which assists hydrate formation while temperature is still not high. The gas production rate is non-monotonic with the increase in injection pressure.

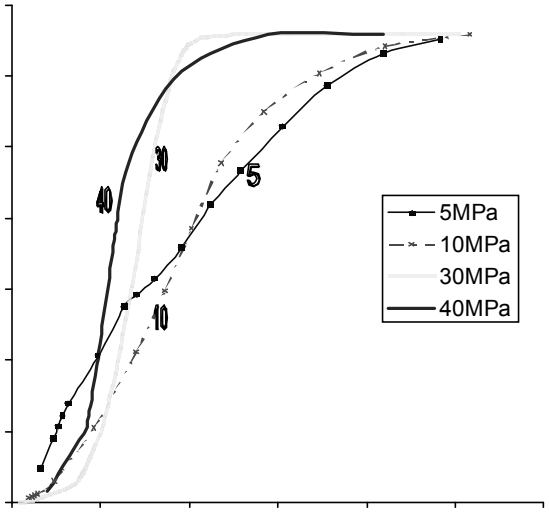

Figure 7-9: Cumulative gas production with varying injection pressure and 2MPa of production pressure and 50°C of injection temperature.

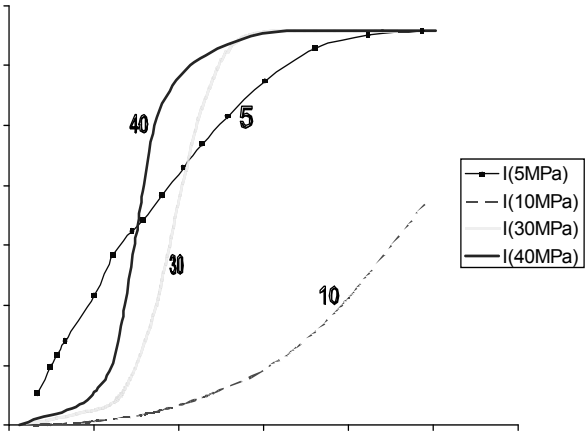

Figure 7-10: Cumulative gas production with varying injection pressure and 4MPa of production pressure and 50°C of injection temperature.

Pore-Scale Model

We have modeled the pore-level hydrate distribution in single-phase flow (no free gas phase) in order to estimate transport properties of hydrate bearing sediments. A basic element of porous media is a pore throat. We have assumed a simplified cylindrical geometry for a pore throat. We have also assumed that this cylindrical throat is at a temperature and pressure where hydrates can form if the methane content is high enough. Water saturated with methane at a higher temperature flows into this pore throat. As the water passes through this throat, temperature falls, hydrates can form at a low-enough temperature region. Characteristic times for diffusion, heat conduction, reaction and flow are compared.

Results from this study indicate that temperature is the coldest near the pore wall because heat is removed through the wall. Hydrate forms near on the wall and builds up. The rate at which hydrate layer builds up depend on the temperature gradient, flow rate etc. These observations will be used to build a model for hydrate deposition in a medium with distributed pore size distribution. As the cold water passes through a collection of pores, the hydrate saturation at the pore scale will vary from pore to pore. We will use these results to calculate permeability of porous media as a function of overall hydrate saturation. We will also develop models for multiphase flow during hydrate deposition.

CONCLUSIONS

Our in-house simulator performs as well as the other simulators in the code comparison study. For Problem 3 with ice formation, our simulator, STOMP, and MH21 performed better than the other simulators. For warm water injection, production well pressure, injection temperature and pressure play an important role in the production of gas from hydrate deposits. For high injection temperature, the higher pressure increases the flow of warm water (heat) in the reservoir making the production rate faster, but if injection temperature is not high then only depressurization is the best method of production. At intermediate injection temperature, the production rate changes non-monotonically with the injection pressure. These parameters should be chosen carefully to optimize recovery and recovery rate of gas. This paper addresses a very simple homogeneous domain. Realistic reservoirs would have heterogeneity in sediments as well as hydrate distribution, which need to be taken into account. Models are being developed in Dr. Hirasaki's group to address the variation in hydrate saturation in marine sediments.

Students

Jyoti Phirani [continuing Chemical Engineering PhD Thesis, 2010] Modeling of Gas Production from Marine Hydrate Deposits

Task 8: Seafloor and Borehole Stability

We are moving forward on Task 8 as scheduled and as outlined by the Milestone Status. In conjunction with compiling published geomechanical and fluid flow properties we have identified a dearth of data for multi-phase flow in hydrate systems and for strength in low-to-moderate hydrate saturation in fine-grained materials. We are working with colleagues at MIT, GATech, the USGS, and LBNL to see what technology exists to fill these data gaps. We are integrating the sediment properties work (this task), the geologic hydrate accumulation work (Task 6), the hydrate production work (Task 7) and the DOE-sponsored JIP hydrate work in the Gulf of Mexico to develop forward models of hydrate accumulation to test the JIP predictions and to provide accurate and realistic sediment models for our hydrate production models. We have also measured permeability of samples to evaluate new techniques for getting permeability anisotropy and for getting robust permeability data from logging measurements. Lastly, through involvement in recent and upcoming conferences, we are staying appraised of the state of the art from the academic and industrial perspectives.

Subtask 8.1: Sediment-Hydrate Properties

Overview

We have compiled an extensive literature database for flow, strength, and deformation properties of hydrate bearing sediments. We are cataloging the literature in EndNote. As part of the database construction we are cataloging the data, identifying the key datasets that exist, and highlighting the key measurements that are missing. We have made contact with other DOE-funded groups (USGS, GATech, LBNL) to address how key gaps might be filled with existing infrastructure and facilities. The final database will include a summary of existing data and a plan for filling data gaps.

In addition to compiling the existing physical properties, we are making measurements of permeability in fine-grained sediments from the 2005 JIP drilling project and correlating them with petrophysical data collected during logging-while-drilling. We hope to develop novel and versatile techniques for estimating permeability through hydrate systems with high resolution logs. This could greatly impact our ability to model these systems thus understand flow, hydrate accumulation, and gas production.

Approach

We have continued to expand our database on flow properties of fine-grained sediments from oceanic hydrate settings. We have interacted and collaborated with other hydrate researchers to make sure we have digital reprints of the papers and reports. We have reviewed the papers and compiled data sets. We are separating the references based on type of measurement (e.g., mechanical property, thermal property, flow property, etc.) and how the measurement was

made. It is critical to understand the measurement technique as it has a large impact on the application of the results to hydrate systems.

We have also made measurements of permeability of Keathley Canyon sediments (JIP Phase II drilling) with constant rate of strain consolidation experiments (ASTM International, 2006). Details of the samples and permeability measurement technique are provided in Dugan (in press). We have integrated those measurements with the NMR (nuclear magnetic resonance) log data from the field to develop a complete permeability profile for Keathley Canyon. Ultimately this approach should allow for better permeability assessment in the hydrate stability zone and thus better modeling of hydrate accumulation and distribution.

Based on exciting results pointing out the importance of flow and hydrate accumulation in heterogeneous and anisotropic porous media (Task 6), we have developed a new sample procedure for horizontal and vertical permeability measurements. The approach uses standard flow-through permeability techniques with existing laboratory equipment at Rice. We have adapted our permeability chamber to accommodate vertically and horizontally oriented cores.

Results and Discussion

Development of the physical properties database is moving along successfully. We have compiled field and laboratory measurements, but now are working on how to compare different measurement techniques. We are beginning to integrate these data sets with the modeling aspects of this project (Tasks 6 and 7) and are on target to complete a sorted database.

The correlation of permeability measurements and NMR log data (T_2 relaxation times) has allowed us to develop a permeability model for Keathley Canyon. We based our model on the Schlumberger-Doll Research (SDR) equation relating permeability and T_2 (Kenyon et al., 1989).

$$k = A\phi^4 T_{2LM}^2 \qquad \text{Equation 8.1}$$

k is permeability, ϕ is porosity, T_{2LM} is the geometric mean of the transverse relaxation times of the fluids in the pores and a proxy for mean pore size (Kleinberg, 1999), and A is an empirical constant. A is typically assigned a fixed value of 4 mD/ms^2 in sandstones or 0.1 mD/ms^2 in carbonates for conventional log analysis, but in fact the parameter varies with lithology (Kleinberg et al., 2003). A more accurate estimate of permeability could therefore be obtained by varying A with lithology throughout the well. In mudstones, lithological variations mainly result from differing volume fractions of clay; thus, establishing a relationship between A and clay volume fraction should provide a method for representing variations in grain shape, pore geometry, and fluid pathways due to the presence of clay. This in turn would extend the applicability and robustness of NMR data in hydrocarbon exploration. To investigate this we have compared

core-measured permeability with LWD measurements of T_{2LM} from the NMR log. From this we have developed a lithology-dependent A based on the response of the gamma ray log.

$$A = -2.5917 \times 10^{-18} GR + 2.2969 \times 10^{-16} \ (\text{m}^2/\text{ms}^2) \qquad \text{Equation 8.2}$$

Using Eqns. 8.1 and 8.2, we have developed a nearly-complete permeability profile for Keathley Canyon (Figure 8.1).

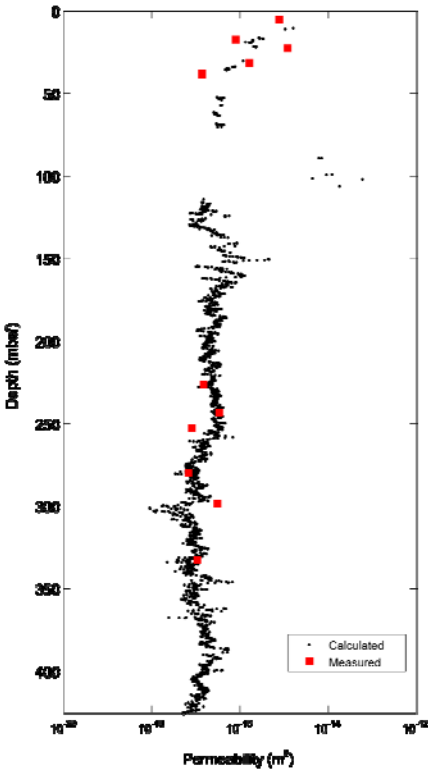

Figure 8.1: Measured permeability from Keathley Canyon (red squares) compared with the NMR-derived permeability with the modified SDR equation. The modified SDR equation allows high-resolution (<1m) estimates of permeability which can be incorporated in numerical models of flow through hydrate systems.

Conclusion

We are nearing completion of a physical properties database that will help advance our understanding of flow, strength, and compression in hydrate bearing sediments. Along with this, we are working with other hydrate researchers to establish how we can fix gaps in multi-phase flow properties in coarse-grained materials and strength properties in fine-grained sediments with low-to-moderate hydrate saturation.

Our permeability measurements and combination with LWD data has enhanced our knowledge on flow and transport properties in fine-grained sediments. We also feel it expands the use of NMR logs to get permeability in multiple

lithologies. Historically the SDR equation has been employed in reservoir systems; we have adapted it for marine hydrate settings.

Subtask 8.2: Modeling (In)stability

Overview

Numerous hazards have been related to gas hydrate systems. At the geologic scale, the accumulation of free gas can lead to critical state pressures, fractures and gas leakage (e.g., Flemings et al., 2003; Hornbach et al., 2004). Other studies have implicated hydrate and hydrate dissociation when looking at large seafloor failures (e.g., Dillon et al., 2000; Vogt and Jung, 2002). We are using standard stability analyses for sediments to understand the evolution of stable and unstable conditions in marine sediments without hydrate, as hydrate accumulates, as hydrate dissociates, and as gas is produced from hydrate. This work will help us better understand large scale failures associated with hydrates as well as potential production-related hazards. The stability models will be integrated with our geologic and production models (Tasks 6 and 7).

Approach

Our basin-scale models of fluid flow have been coupled to a slope stability calculation that we are testing in the absence of hydrate. Preliminary tests are able to predict when slope failures will exist under different pore pressure regimes and seafloor slopes. In summer 2008, I plan to have Justin Stigall (Earth Science graduate student, Task 8) work with Sayantan Chatterjee (Chemical & Biomolecular Engineering graduate student, Task 6) to implement the stability calculations in the two-dimensional models that couple sedimentation, consolidation, fluid flow, and hydrate accumulation. Currently we are looking at infinite slope analyses (Figure 8.2) which are computationally inexpensive and give quick assessment of stability. In future tests, we will look at more complex failure modes through more developed stability models (e.g., 2-D method of slices) applied to zones identified as potentially unstable in infinite slope analyses.

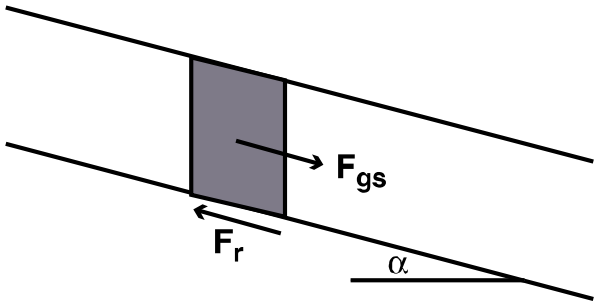

$$FS = \frac{F_r}{F_{gs}} = \frac{f(\gamma, \alpha, \phi, P)}{f(\gamma, \alpha)}$$

Figure 8.2: Schematic representation of slope stability calculations using the infinite slope approximation. The model compares the forces resisting failure (F_r) to those driving failure (F_{gs}) to calculate a factor of safety (FS). Failure, or slope instability, occurs when FS < 1.

The infinite slope analysis (Equation 8.3) assess stability by comparing the gravitational forces driving failure to the frictional forces resisting failure.

$$FS = \frac{c + \left[\left(S_v - \rho_w g z\right)\cos^2\alpha - P^*\right]\tan\phi}{\left(S_v - \rho_w g z\right)\sin\alpha\cos\alpha} \qquad \text{Equation 8.3}$$

Unstable condition exist when *FS* < 1. S_v is the overburden stress, ρ_w is the density of water, *g* is the acceleration due to gravity, *z* is the depth below sea level, α is the slope of the seafloor, *P** is fluid overpressure, *c* is cohesion, and ϕ is the angle of friction.

Results and Discussion

At this stage we are successfully modeling stability conditions and those that drive instability in water-saturated systems. The key parameters for marine slope settings similar to those where hydrate exists are the overpressure and the frictional strength. Frictional strength and cohesion are anticipated to change in hydrate bearing sediment as well as overpressure depending on the basin history and distribution of hydrate. We will incorporate Equation 8.3 into our hydrate models to look at the impacts of hydrate formation and dissociation on stability of continental slope sediments. Sensitivity studies and parameter tests will be the first phase of this research as we try to isolate the key driving forces for unstable conditions.

Conclusions

Modeling of stable and unstable conditions is complete with an infinite slope approximation in the absence of hydrate. We need to incorporate the same stability analyses into the hydrate models to continue working on addressing (in)stability in hydrate settings. This study is on target.

Subtask 8.3: Integrating geomechanical studies

Overview

This subtask involves assessing ongoing geomechanical studies to maximize our understanding of geomechanical properties of hydrate bearing sediments across DOE-funded projects. The goal is a comprehensive geomechanical database and modeling approach with a means to understand these properties at geologic and human time-scales.

Approach

We have worked directly with the USGS, MIT, GATech, and LBNL to integrate our data sets and address the best technology for estimating physical properties. This has included work I completed with the USGS to develop testing procedures and preparation techniques for working with pressurized hydrate cores from

India hydrates program (NGHP). I have also worked with W. Waite (USGS Woods Hole) to develop data processing stream and interface for working with data from the Gas Hydrate and Sediment Testing Laboratory Instrument (GHASTLI) such that it is available in near-real time. Last, I attended a DOE-sponsored workshop in Atlanta, GA to assess the current techniques used for hydrate physical properties measurements, identify the strengths in those measurements, and identify key data gaps.

Results and Discussion

After a three-day workshop in Atlanta, GA, three key gaps have been identified: (1) physical properties of fine-grained materials at low (<40%) hydrate saturation; (2) relative permeability measurements for gas and water in hydrate bearing sediments; and (3) consistent measurements of strength in hydrate bearing sediments. Rice is taking the lead in (1) and we are working with MIT to develop a technique to address this issue by working with ice-water-sediment systems in existing infrastructure. We will be submitting an external proposal to fund the experiments. Lawrence Berkeley National Laboratory is taking the lead on (2) with their experimental set-up. We hope to have some preliminary results by the OTC conference in May to include in our database. Issue (3) is of greater scale and we are working on the best way to solve it as it involves integrating data and methods from different labs; and the methods have a very large impact on the strength. We (Rice, LBNL, GATech, USGS) have started a physical properties review paper based on the existing data.

Conclusions

Collaboratively with other DOE-sponsored researchers, we are finishing a review paper of the existing data to capture the state of the art and the status of physical properties measurements in hydrate bearing sediments. Along with this, we have isolated the gaps and are pursuing options to fill these gaps.

Students

H. Daigle, PhD student, Earth Science

L. Ashley Hubbard [MS Earth Science Thesis, 2008] - Investigation of fluid relationships at diverse sites in the northern Gulf of Mexico using dissolved ion concentrations and strontium isotopes

Steinar Hustoft [visiting Ph.D. student from University of Tromso, Norway 2008] – Studied sediment properties and fluid flow history for the Norwegian margin

Hydrate Activities

Physical Properties of Hydrate Bearing Sediments participant [16-19 March 2008, Atlanta, GA]

Offshore Technology Conference participant [5-8 May 2008, Houston TX]

DOE/JIP Site Selection Working Group member [2007-present]

Geofluids Editorial Board member [2007-present]

Steering Committee Member for IODP Workshop "Addressing Geologic Hazards through Ocean Drilling" [26-30 August 2007, Portland, OR]

Reviewer for Basin Research; Geochemistry, Geophysics, and Geosystems; Journal of Geophysical Research; Marine and Petroleum Geology; Research Council of Norway [2007-present]

Earth Science Overview and Rice Lab Tour for Citizens School Students [28 September 2008]

Acronyms and Abbreviations

JIP – Joint Industry Project
NMR – Nuclear Magnetic Resonance
SDR – Schlumberger-Doll Research
MIT – Massachusetts Institute of Technology
USGS – United States Geological Survey
LBNL – Lawrence Berkeley National Laboratory
GATech – Georgia Institute of Technology
DOE – Department of Energy
IODP – Integrated Ocean Drilling Program

FS – factor of safety
F_r – forces resisting failure
F_{gs} – forces driving failure
γ – bulk unit weight of the sediment
α – angle of seafloor
ϕ – internal angle of friction
P – pore fluid pressure
c – cohesion
S_v – total vertical stress
P^* - fluid overpressure
ρ_w – density of water
g – acceleration due to gravity
z – depth below sea-level

References

ASTM International, 2006, Standard Test Method for One-Dimensional Consolidation Properties of Saturated Cohesive Soils Using Controlled-Strain Loading, Standard D4186-06.

Dillon, W.P., Nealon, J.W., Taylor, M.H., Lee, M.W., Drury, R.M., Anton, C.H., 2000, Seafloor collapse and methane venting associated with gas hydrate on the Blake Ridge; causes and implications to seafloor stability and methane release, in *Geophysical Monograph* **124**, Paull, C.K. and Dillon, W.P. (eds), 211-233.

Dugan, B., 2008, Fluid Flow in the Keathley Canyon 151 Mini-Basin, Northern Gulf of Mexico, Marine and *Petroleum Geology*, doi:10.1016/j.marpetgeo.2007.12.005.

Flemings, P.B., Liu, X., Winters, W.J., 2003, Critical pressure and multiphase flow in Blake Ridge gas hydrates, *Geology*, **31**(12), 1057-1060.

Hornbach, M.J., Saffer, D.M., Holbrook W.S., 2004, Critically pressured free-gas reservoirs below gas-hydrate provinces, *Nature*, **427**, 142-144.

Kenyon, W.E., Howard, J.J., Sezinger, A., Straley, C., Matteson, A., Horkowitz, K., Ehrlich, R., 1989, Pore-size distribution and NMR in Microporous Cherty Sandstones, Transactions of the SPWLA 30th Annual Logging Symposium, Denver CO (USA), 11-14 June 1989, paper LL.

Kleinberg, R.L., 1999, Nuclear magnetic resonance, In Wong, P.-Z. (ed), *Methods in the Physics of Porous Media*, 337-385, San Diego: Academic Press.

Kleinberg, R.L., Flaum, C., Straley, C., Brewer, P.G., Malby, G.E., Peltzer III, E.T., et al., 2003, Seafloor nuclear magnetic resonance assay of methane hydrate in sediment and rock. *Journal of Geophysical Research* **108**(B3), 2137, doi:10.1029/2001JB000919.

Vogt, P.R., and Jung, W., 2002, Holocene mass wasting on upper non-Polar continental slopes—due to post-Glacial ocean warming and hydrate dissociation?, *Geophysical Research Letters*, **29**(9), 1341, doi:10.1029/2001GL013488.

Task 9: Geophysical Imaging of Gas Hydrate and Free Gas Accumulations

For this task in particular, and others in general, we have successfully initiated collaboration with National Institute of Oceanography (NIO), India. We intend to demonstrate geophysical imaging with multichannel seismic data from the Krishna-Godavari (K-G) basin in the Indian east coast. NIO scientists are tentatively scheduled to visit Rice University in July.

Though Priyank Jaiswal has not started working on the gas hydrate project officially, he is helping NIO in preliminary processing of the selected seismic line and thus is working towards subtask 9.1. The results of the preliminary processing will be shown at Rice University by the NIO scientists during their scheduled visit.

It is estimated that Priyank Jaiswal will start working on the project directly as a Post Doc sometimes in summer.

Subtask 9.1: Preliminary processing and inversion of seismic data.

Seismic data has been identified and is currently being processed at NIO, India with Priyank's remote involvement. The identified seismic line (Figure attached) has three inline wells all of which were drilled in 2001. The drilling was based on BSR signatures that appear to be similar at the well locations but the recovered hydrate concentration was found to be varying.

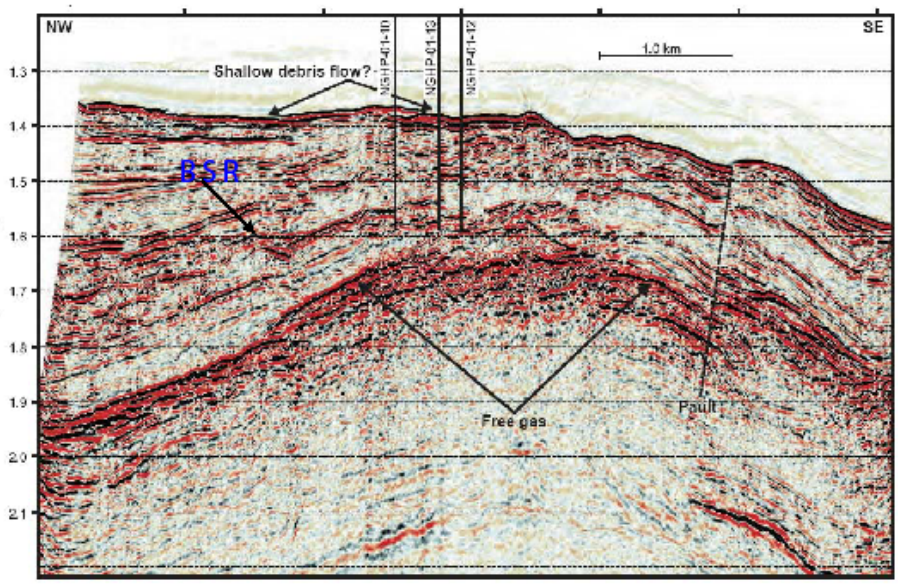

Seismic data from the K-G basin showing NGHP drill sites 10, 13, and 12. Site 12 had massive hydrate contents while 10 and 13 did not.

Task 10: Technology Transfer Activities

The members of the research team gave presentations at the NETI Hydrate Merit Review at Golden, Colorado on September 18-20, 2007. The group gave a briefing to Rick Baker on April 14, 2008 at Rice University.

Publication and Presentations by Tasks

Task 5

**Snyder, G.T., A. Hiruta, R. Matsumoto, **G.R. Dickens, H. Tomaru, R. Takeuchi, J. Komatsubara, Y. Ishida & **H. Yu, 2007. Pore water profiles and authigenic mineralization in shallow marine sediments above the methane-charged system on Umitaka Spur, Japan Sea. *Deep-Sea Research (II)*, *54*: 1216-1239.

Abstract. Umitaka Spur, situated on an unusual collisional plate boundary along the eastern margin of the Japan Sea, hosts gas seeps, pock-marks, collapse structures, and gas hydrates. Piston cores were recovered from this ridge to understand carbon cycling, pore fluid gradients and authigenic mineralization above a methane-charged system. We present the chemistry of fluids and solids from three cores adjacent to seep locations. High fluxes of CH_4 and alkalinity transport carbon from a deep zone of methanogenesis toward the seafloor. Methane, however, reacts with SO_4^{2-} across a shallow sulfate-methane transition (SMT), which generates additional alkalinity and HS^-. A fraction of these CH_4 oxidation products form authigenic carbonate and pyrite. These minerals are not readily apparent from visual inspection of split cores, because they exist as micritic coatings on microfossils or as framboidal pyrite. They are, however, readily observed as peaks of “labile” Ca, Sr, Ba or S in sediment at or near the SMT. Carbon inputs and outputs nicely balance across the SMT in all three cores if one considers the four relevant fluxes: loss of alkalinity to the seafloor, addition of methane from below, addition of alkalinity from below, and carbonate precipitation. Importantly, in all cores, the magnitude of the fluxes decreases in this order. Although some carbon rising from depth forms authigenic carbonate, most (>80%) escapes to the ocean as alkalinity. Nonetheless, authigenic fronts in sediment on Umitaka Spur are a significant reservoir of inorganic carbon. Given calculated pore fluid fluxes for Ca and Sr, the fronts require tens of thousands of years to form, suggesting that the present state and loss of carbon represent long-lived processes.

Task 6 Publications and Presentations

G. Bhatnagar, W. G. Chapman, G. R. Dickens, B. Dugan, and G. J. Hirasaki, “Generalization Of Gas Hydrate Distribution and Saturation In Marine Sediments by Scaling of Thermodynamic and Transport Processes,” *American Journal of Science*, Vol. **307**, June, 2007, P. 861–900, DOI 10.2475/06.2007.01

G. Bhatnagar, W. G. Chapman, G. R. Dickens, B. Dugan, and G. J. Hirasaki, "Sulfate-methane transition as a proxy for average methane hydrate saturation in marine sediments," *Geophysical Research Letters*, VOL. **35**, L03611, doi:10.1029/2007GL032500, 2008.

G. Bhatnager, G. J. Hirasaki, W. G. Chapman, B. Dugan, G. R. Dickens, "Quantifying methane hydrate saturation in different geologic settings," The University of Texas, November 26, 2007.

G. Gu, G. Bhatnager, G. Dickens, W. Chapman, G. J. Hirasaki, poster, "Effects of Seafloor Temperature on the Distribution of Methane Hydrate," American Geological Union, Fall Meeting, 10-14 December 2007, San Francisco.

G. J. Hirasaki, "Effect of Overpressure on Gas Hydrate Distribution," poster presentation at the 6th International Conference on Gas Hydrate, Vancouver, BC, July 6-10, 2008. (Appendix B)

G. J. Hirasaki, "Relating Gas Hydrate Saturation to Depth of Sulfate-Methane Transition," oral presentation at the 6th International Conference on Gas Hydrate, Vancouver, BC, July 6-10, 2008. (Appendix C)

March 2008, Rice University Consortium on Processes in Porous Media

Task 7 Presentations

July 2008 ICGH, Vancouver, Canada
March 2008 Rice University Consortium on Processes in Porous Media
Sept 2007 DOE-NETL Gas Hydrate Merit Review, Golden, CO

Hydrate Presentations

March 2008 Rice University Consortium on Processes in Porous Media
Sept 2007 DOE-NETL Gas Hydrate Merit Review, Golden, CO
Aug 2007 IODP Geohazards Workshop, Portland, OR

Task 8 Papers (journals)

Hutchinson, D.R., Hart, P.E., Ruppel, C.D., Snyder, F. and Dugan, B., in press, Seismic and thermal characterization of a Bottom Simulating Reflection in the northern Gulf of Mexico, in Collett, T.S., Johnson, A., Knapp, C., Boswell, R. (Eds.), Natural Gas Hydrates: Energy Resources, Potential and Associated Geologic Hazards. AAPG Special Publication.

Dugan, B., 2008, Fluid Flow in the Keathley Canyon 151 Mini-Basin, Northern Gulf of Mexico, Marine and Petroleum Geology, doi:10.1016/j.marpetgeo.2007.12.005.

Winters, W.J., B. Dugan, T.S. Collett, 2008, Physical Properties of Sediments from Keathley Canyon and Atwater Valley, JIP Gulf of Mexico Gas Hydrate Drilling Program, Marine and Petroleum Geology, doi:10.1016/j.marpetgeo.2008.01.018.

Bhatnagar, G., W.G. Chapman, G.R. Dickens, B. Dugan, G.J. Hirasaki, 2008, The sulfate-methane transition as a proxy for average methane hydrate saturation in marine sediments, Geophysical Research Letters, 35, L03611, doi:10.1029/2007GL032500.

Bhatnagar, G., W.G. Chapman, G.R. Dickens, B. Dugan, G.J. Hirasaki, 2007, Generalization of gas hydrate distribution and saturation in marine sediments by scaling of thermodynamic and transport processes, American Journal of Science, 307(6), 861-900, doi:10.2475/06.2007.01.

Task 8 Papers (conference proceedings)

Bhatnagar, G., Chapman, W.G., Dickens, G.R., Dugan, B., Hirasaki, G.J, 2008, Effects of Overpressure on Gas Hydrate Distribution, Sixth International Conference on Gas Hydrates, Vancouver, British Columbia, Canada.

Bhatnagar, G., Chapman, W.G., Dickens, G.R., Dugan, B., Hirasaki, G.J, 2008, Relating Gas Hydrate Saturation to Depth of Sulfate-Methane Transition, Sixth International Conference on Gas Hydrates, Vancouver, British Columbia, Canada.

Jones, E., T. Latham, D. McConnell, M. Frye, J. Hunt Jr., W. Shedd, D. Shelander, R. Boswell, K. Rose, C. Ruppel, D. Hutchinson, T. Collett, B. Dugan, W. Wood, 2008, Scientific Objectives of the Gulf of Mexico Gas Hydrate JIP Leg II Drilling, Paper OTC 19501, Offshore Technology Conference, Houston TX, 5-8 May 2008.

Task 8 Abstracts

Daigle, H., Dugan, B., in review, Extending Nuclear Magnetic Resonance Data for Permeability Estimation in Low-Permeability Sediments, 2008 Schlumberger Information Solutions Global Forum, Paris, France, 6-9 October 2008.

COST PLAN / STATUS					
	Phase 1	Phase 2: Year 1 (June 2007 - May 2008)			
Baseline Quarter Reporting		7/1/07 TO 9/30/07	10/1/07 TO 12/31/07	1/1/08 TO 3/31/08	4/1/08 TO 6/30/08
Baseline Cost Plan (SF-424A)					
Federal Share	$ 3,624	$ 80,003	$ 80,003	$ 80,003	$ 80,003
Non-Federal Share	$ 1,004	$ 28,653	$ 28,653	$ 28,653	$ 28,653
Total Planned	$ 4,628	$ 108,656	$ 108,656	$ 108,656	$ 108,656
Cumulative Baseline Cost	$ 4,628	$ 113,284	$ 221,940	$ 330,596	$ 439,252
Actual Incurred Cost					
Federal Share	$ 3,082	$ 59,364	$ 20,610	$ 55,903	$ 93,151 *
Non-Federal Share	$ 1,091	$ 18,616	$ 33,647	$ 52,085	$ 13,797 *
Total Incurred	$ 4,173	$ 77,980	$ 54,257	$ 107,988	$ 106,948 *
Cumulative Costs	$ 4,173	$ 82,153	$ 136,410	$ 244,398	$ 351,346 *
Variance (plan-actual)					
Federal Share	$ 542	$ 20,639	$ 59,393	$ 24,100	$ (13,148)*
Non-Federal Share	$ (87)	$ 10,037	$ (4,994)	$ (23,432)	$ 14,856 *
Total Variance	$ 455	$ 30,676	$ 54,399	$ 668	$ 1,708 *
Cumulative Variance	$ 455	$ 31,131	$ 85,530	$ 86,198	$ 87,906 *

***** These quantities are for the period April-May, 2008. Financial data for June has not yet been posted.

The cumulative variance at the end of the period has the appearance of the project being under spent. The financial data does not include the June 1-19 period. We expect by June 19, 2008 the cumulative variance will be close to zero. This period will include faculty summer salaries and a correction for the stipend of a graduate student (Gaurav Bhatnagar) who was paid from another account last fall.

Milestone Plan/Status

Task	Milestone: Status and Results	Date	Status
5. Carbon inputs and outputs to gas hydrate systems	5.1a Measure iodine in sediments We have measured iodine concentrations in pore waters from several gas hydrate systems. The analyses are completed and we are writing the results over the summer.	12/07	1/08
	5.1b Constrain C_{org} inputs from iodine We will measure the content and isotopic composition of organic carbon and carbonate in sediment from cores of several gas hydrate systems. We have collected most of the samples, although plan to visit the ODP repository (College Station) in late spring or early summer to collect additional samples. Some analyses have been completed; additional ones will be done over the summer.	10/08	
	5.2a Construct metal profiles in sediments We will measure metal contents in sediment from cores of several gas hydrate systems to constrain past hydrocarbon outputs via anaerobic oxidation of methane (AOM). Some work was published in the fall (Snyder et al., 2007). We plan on submitting a manuscript regarding profiles on the Peru Margin by the end of summer.	12/09	
	5.2b Modeling/integrating profiles We will use the metal and iodine profiles to constrain models for gas hydrate formation. We have discussed data and models but have not begun this work so far.	12/10	
6. Numerical models for quantification of hydrate and free gas accumulations	6.1 Model development. The recipient shall develop finite difference models for the accumulation of gas hydrate and free gas in natural sediment sequences on geologically relevant time scales.	9/07	1/08
	6.2: Conditions for existence of gas hydrate	3/07	done

	The recipient shall summarize, quantitatively, the conditions for the absence, presence, and distribution of gas hydrates and free gas in 1-D systems by expressing the conditions in terms of dimensionless groups that combine thermodynamic, biological and lithologic transformation, and transport parameters.		
	6.3 Compositional effect on BSR The recipient shall add to the numerical model, developed under this task, a chloride balance and multi-hydrocarbon capability specifically to investigate how hydrocarbon fractionation might affect Bottom Simulating Reflectors (BSRs).	7/07	12/08
	6.4: Amplitude Attenuation and chaotic zones due to hydrate distribution The recipient shall simulate preferential formation of gas hydrate in coarse-grained, porous sediment in 2-D by linking fluid flux to the permeability distribution.	3/09	
	6.5: Processes leading to overpressure The recipient shall quantify, by simulation and summarize by combination of responsible dimensionless groups, the conditions leading to overpressure to the point of sediment failure.	3/08	done
	6.6 Concentrated hydrate and free gas The recipient shall, using 2-D and 3-D models, simulate lateral migration and concentration of gas hydrate and free gas in structural and stratigraphic traps.	3/08	started
	6.7 Focused free gas, heat and salinity The recipient shall quantify, using 2-D and 3-D model simulations and comparisons to available observations, the factors controlling the process of localized upward migration of free gas along faults and lateral transfer to dipping strata that can lead to chaotic zones and possible accumulations of concentrated hydrate.	9/09	
	6.8 Sulfate profile as indicator of methane flux	7/07	done

	The recipient shall compute, for systems where data on the sulfate profile is available, the oxidation of methane by sulfate and shall indicate the perceived level of effect on gas hydrate accumulation and the data's value as an indicator of methane flux.		
	6.9 Application of models to interpretation of case studies. The models developed in Task 6 will be applied to case studies in the interpretation of each of the other tasks.	6/10	6/10
7. Analysis of production strategy	7.1a Pore scale model development and Hydrate code comparison For this milestone, we will develop pore-scale models of hydrate accumulation by simulation. Our hydrate code will be used to solve a set of problems formulated by the Code Comparison Study group. Our results will be compared with those of other hydrate codes. Should be changed to: 6/08 Reason: The starting date was moved to 6/07 Status: Code comparison study is 80% complete.	1/08	6/08 Code comparison is done.
	7.1b Petrophysical and thermophysical properties of hydrate sediments from pore-scale model For this milestone, we will assume the pore-scale models of hydrate accumulation developed in the last milestone and estimate transport properties as a function of hydrate and gas saturations. Should be changed to: 6/09 Reason: The starting date was moved to 6/07 Status: Have not started	1/09	6/09
	7.2a Modeling of several production strategies to recover gas from marine hydrates Several production strategies would be modelled using the transport property correlations developed in the previous milestone. Optimal strategies will be identified. Should be changed to: 6/10	1/10	6/10

	Reason: The starting date was moved to 6/07 Status: Have not started		
	7.2b Effect of marine reservoir heterogeneities on production of methane Reservoir heterogeneity anticipated in marine environments (known or determined through other tasks) would be incorporated. Appropriate hydrate distributions, either constrained from experimental data or mechanistic simulations (Task 5) would be used. Sensitivity of gas production to the heterogeneities would be calculated. Should be changed to: 6/11 Reason: The starting date was moved to 6/07 Status: Have not started	12/10	6/10
8. Seafloor and borehole stability	8.1a Collection of data We have collected the published data and are working it into a data base. We are also working on a review paper summarizing the state of the art settings. This will include laboratory experiments, field data, published results, and unpublished data.	05/08	Completed
	8.1c Complete database We are organizing the data from task 8.1a into a format that can be searched and used by researchers trying to understand mechanical behavior of hydrate-bearing sediment. We will also identify key gaps in the database for focusing future hydrate research endeavors. We have started exchanging these data with the modeling components of this project.	10/09	On target
	8.2a Link database with models We have started passing data along to the modeling groups so they can use sediment properties from hydrate provinces as they simulate hydrate accumulation and production.	08/08	On target
	8.2b Add sediment stability to models Standard stability calculations have been implemented in a standard basin model. Now that it is functional we will work with the hydrate accumulation model to add a stability calculation to the 2-D models.	10/08	On target

	8.2c Conditions for (in)stability After implementing the stability model in the hydrate accumulation code, we can explore the conditions (e.g., hydrate dissociation, sea-level fall) that could drive slope failure and hydrate/methane release or lead to borehole failures during production.	9/09	On target
9 Geophysical imaging of hydrate and free gas	9.1 Preliminary processing and inversion of seismic data. Perform conventional seismic reflection processing, velocity analysis, travel time tomography, and other analyses as deemed appropriate and necessary.	8/08	
	9.2: Final 1-D elastic and 2-D acoustic waveform inversion. Apply 1-D elastic and 2D acoustic inversions on data obtained from subtask 9.1 to derive determine high-resolution elastic and acoustic properties.	8/09	
	9.3: Rock physics modeling. Apply rock physics models to the developed seismic models to estimate hydrate saturation and lithology through application of well log data in conjunction with data from subtask 9.2. For this subtask we shall seek to collaborate with research being conducted under separately funded DOE-NETL projects (DE-FC26-05NT42663 with Stanford University, "Seismic-Scale Rock Physics of Methane Hydrate" and others as applicable).	8/10	

RICE UNIVERSITY

Accumulation of gas hydrates in marine sediments

by

Gaurav Bhatnagar

A THESIS SUBMITTED
IN PARTIAL FULFILLMENT OF THE
REQUIREMENTS FOR THE DEGREE

Doctor of Philosophy

APPROVED, THESIS COMMITTEE:

George J. Hirasaki, Chair
A. J. Hartsook Professor in Chemical
and Biomolecular Engineering

Walter G. Chapman, co-Chair
William W. Akers Professor in Chemical
and Biomolecular Engineering

Clarence A. Miller
Louis Calder Professor in Chemical and
Biomolecular Engineering

Brandon Dugan
Assistant Professor in Earth Science

Houston, Texas

February, 2008

ABSTRACT

Accumulation of gas hydrates in marine sediments

by

Gaurav Bhatnagar

Generalized numerical models for simulating gas hydrate and free gas accumulation in marine sediments have been developed. These models include several physical processes such as phase equilibrium of gas hydrates, multiphase fluid flow in porous media, biogenic methane production, and sedimentation-compaction of sediments over geologic timescales. Non-dimensionalization of the models lead to the emergence of important dimensionless groups controlling these dynamic systems, such as the Peclet number, Damkohler number, and a sedimentation-compaction group that compares permeability to sedimentation rate. Exploring the entire parameter space of these dimensionless groups helps in delineating different modes of gas hydrate and free gas occurrence, e.g., no hydrate and hydrate with or without underlying free gas. Scaling schemes developed for these systems help in summarizing average gas hydrate saturation for hundreds of simulation results into two simple contour plots. The utility of these contour plots in predicting average hydrate saturation is shown through application to different geologic settings.

The depth to the sulfate-methane transition (SMT) is also developed as an in-

dependent proxy for gas hydrate saturation for deep-source systems. It is shown through numerical modeling that scaled depth to the SMT correlates with the average gas hydrate flux through the gas hydrate stability zone (GHSZ). Later, analytical theory is developed for calculating steady-state concentration profiles as well as the complete gas hydrate saturation profile from the SMT depth. Application of this theory to several sites along Cascadia Margin indicates that SMT depth can be used as a fast and inexpensive proxy to get a first-order estimate of gas hydrate saturation, compared to expensive deep-drilling methods.

The effect of overpressure development in low permeability gas hydrate systems is shown to have an important effect on gas hydrate and free gas saturations. Specifically, overpressure development decreases the net amount of gas hydrate and free gas in the system, in addition to extending the base of the hydrate stability zone below the seafloor by a relatively small depth. We also study the role of upward free gas migration in producing long, connected free gas columns beneath the gas hydrate layer. Finally, two-dimensional models are developed to study the effect of heterogeneities on gas hydrate and free gas distribution. Simulation results show that hydrate as well as free gas accumulates in relatively high saturations within these high permeability sediments, such as faults/fracture networks, dipping sand layers, and combinations of both, due to focused fluid flow.

Acknowledgements

I would like to express my sincere gratitude to the following persons:

Dr. George J. Hirasaki for being my thesis advisor and a great mentor. His knowledge and infectious enthusiasm towards research have contributed immensely towards the completion of this thesis. In addition, his work ethics and dedication always motivated me to move out of my comfort zone and work on a challenging and very interesting multidisciplinary project. I will be forever grateful to him for all the things he has taught me over the course of this thesis.

Dr. Walter G. Chapman for being my co-advisor and for his guidance and support throughout the last four years.

Dr. Clarence A. Miller for serving on my thesis committee.

Dr. Brandon Dugan for serving on my thesis committee and always providing valuable suggestions and comments on my thesis work. I learnt a lot about hydrogeology from him through numerous discussions and paper revisions, and thank him for his enthusiasm and motivation.

Dr. Gerald R. Dickens for teaching me the subtleties of marine geology, and earth science in general. His ideas and suggestions helped me appreciate research problems from a very different perspective. I also thank him for several stimulating discussions on gas hydrate systems and for greatly improving my technical writing skills.

I thank the Shell Center for Sustainability, the Kobayashi Graduate Fellowship, and the Department of Energy for financial support.

I also thank all my friends and colleagues at Rice University for their help and making these last four years memorable.

Lastly, I would like to acknowledge my parents and family in India for their continued love and support. This thesis would not have been made possible without their encouragement and sacrifices. I thank them for everything.

Gaurav Bhatnagar

Contents

Glossary

AGHS: Average Gas Hydrate Saturation

AOM: Anaerobic Oxidation of Methane

BHSZ: Base of Hydrate Stability Zone

BSR: Bottom Simulating Reflector

CSMHYD: Colorado School of Mines Hydrate code

GHOZ: Gas Hydrate Occurrence Zone

GHSZ: Gas Hydrate Stability Zone

IODP: Integrated Ocean Drilling Program

L-H zone: Region of liquid water and hydrate stability

LPTM: Late Paleocene Thermal Maximum

L-V zone: Region of liquid water and vapor stability

LWD: Logging While Drilling

ODP: Ocean Drilling Program

SMI: Sulfate-Methane Interface

SMT: Sulfate-Methane Transition

SRZ: Sulfate Reduction Zone

TOC: Total Organic Carbon

VE: Vertical Exaggeration

VSP: Vertical Seismic Profiling

Illustrations

Tables

Chapter 1

Introduction

Gas hydrates are inclusion compounds formed by the encapsulation of low molecular weight gases (guest molecule) in hydrogen bonded cages formed by water (host molecule) (Figure 1.1) (Kvenvolden, 1993; Sloan and Koh, 2007). This clathrate structure is stabilized by weak van der Waals interactions between the guest and host molecules. Depending on the gas (guest) composition, hydrates can form one of three primary crystal structures: Structure I (sI), Structure II (sII) or Structure H (sH) (Figure 1.1). However, natural gas hydrates have methane as their main guest component which causes them to occur mostly as sI hydrates. Small amounts of heavier hydrocarbons such as ethane and propane or other gases like carbon dioxide and hydrogen sulfide have also been found to be present as hydrate formers (Kastner et al., 1998; Milkov and Sassen, 2000; Milkov et al., 2005). Mixtures of different hydrate formers, for example methane and ethane, can result in sII hydrate formation (Subramanian et al., 2000).

Hydrate formation is thermodynamically favored at high pressures, low temperatures and low salt concentrations (Sloan and Koh, 2007). Gas hydrates, thus, occur abundantly in nature beneath seafloor sediments along continental margins and permafrost regions, often accompanied by an underlying free gas layer (Kven-

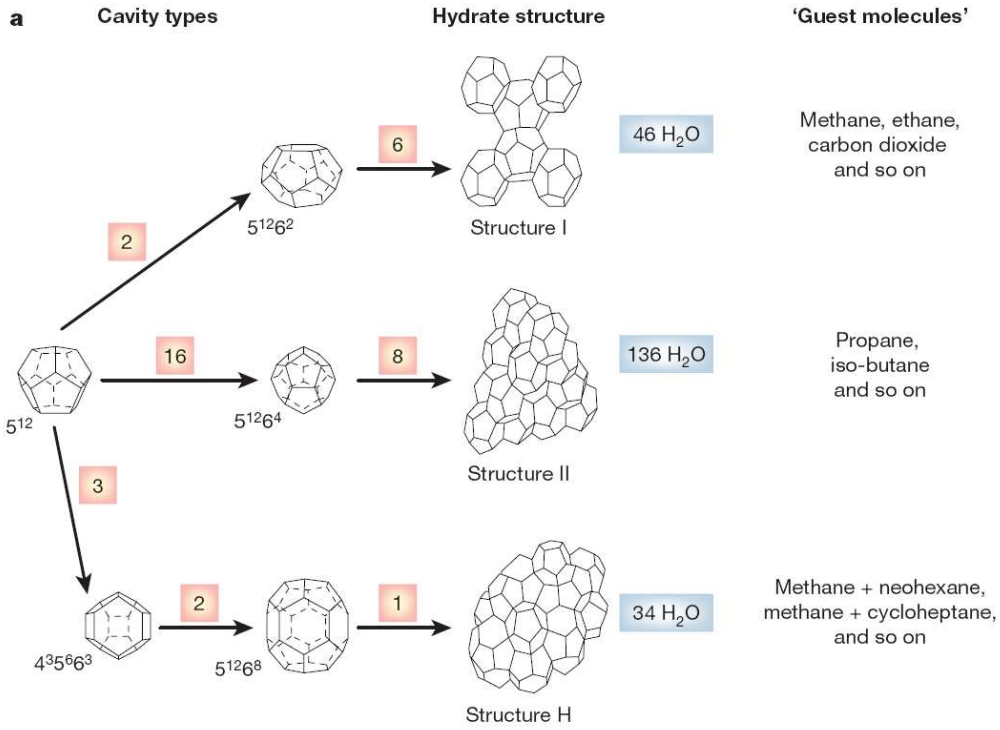

b

Hydrate crystal structure	I		II		H		
Cavity	Small	Large	Small	Large	Small	Medium	Large
Description	5^{12}	$5^{12}6^2$	5^{12}	$5^{12}6^4$	5^{12}	$4^35^66^3$	$5^{12}6^8$
Number of cavities per unit cell	2	6	16	8	3	2	1
Average cavity radius (Å)	3.95	4.33	3.91	4.73	3.91†	4.06†	5.71†
Coordination number*	20	24	20	28	20	20	36
Number of waters per unit cell	46		136		34		

*Number of oxygens at the periphery of each cavity.
†Estimates of structure H cavities from geometric models.

Figure 1.1: The three primary unit crystal structures of gas hydrates: Structure I, Structure II and Structure H. Pure methane and ethane form Structure I hydrate, but certain compositions of their mixtures undergo phase transition to form Structure II hydrates. The notation $5^{12}6^2$ indicates that a particular water cage consists of 12 pentagonal faces and 2 hexagonal faces [*Taken from Sloan (2003)*].

volden, 1988, 1993). In addition to temperature, pressure and salinity, gas hydrate stability in marine settings is also influenced by gas composition and sediment pore size distribution (Henry et al., 1999).

The amount of methane trapped in worldwide deposits of hydrate, along with the associated free gas, is enormous and various global estimates have been reported in the literature (Kvenvolden, 1993; Dickens, 2001; Buffett and Archer, 2004; Milkov, 2004; Klauda and Sandler, 2005). However, due to their sensitive dependence on seafloor temperature and pressure, gas hydrates also represent a geohazard, possibly destabilizing shallow sediments and causing slope failures, slumps and submarine slides (Borowski and Paull, 1997; Sultan et al., 2004). Hydrates have also been believed to affect past climate change. During the Late Paleocene Thermal Maximum (LPTM), isotopic records indicate that ocean bottom water temperature increased by more than 4°C within a short time interval ($<$ 10^4years), along with a -2 to -3 $^{o}/_{oo}$ excursion in the δ^{13}C of the ocean/atmospheric inorganic carbon reservoir (Dickens et al., 1995; Katz et al., 1999; Kennett et al., 2003). This event has been hypothesized to be a result of massive dissociation of oceanic methane hydrates caused by warming of oceanic sediments (Dickens et al., 1995).

Thus, understanding the factors responsible for the accumulation and distribution of gas hydrates in submarine sediments becomes imperative to study their potential as a possible energy resource, a submarine geohazard or an agent of climate change. The overall objective of this thesis is to develop general numerical models to characterize the spatial and temporal distribution of gas hydrates in sedi-

ments due to different sources of methane. Apart from developing these numerical models, the different modes of gas hydrate occurrence are also characterized on the basis of a few dimensionless groups. This makes our model results applicable to several distinct geologic settings, as opposed to the site-specific studies currently reported in the literature. A new method for directly evaluating gas hydrate distribution from pore water sulfate profile as the main proxy is also developed. This method can be used to predict gas hydrate saturation in a relatively fast and inexpensive manner, compared to conventional pressure coring methods that can be expensive, spatially limited and difficult to interpret.

1.1 Organization

This thesis is divided into twelve chapters. Chapter 2 provides a brief background of natural gas hydrate systems and motivation to study them in a generalized manner. Current state of the art models of marine gas hydrate systems and their shortcomings are also reviewed. Chapter 3 discusses the phase equilibrium of fresh water-methane and sea water-methane systems and explains the emergence of the zone of gas hydrate stability in marine sediments in a thermodynamically consistent fashion. Chapter 4 is devoted to modeling porosity loss of shallow marine sediments as a result of sedimentation and compaction over geologic timescales and its role in driving fluid flow in the sediments. Chapter 5 describes various component balances and modeling of gas hydrate formation and accumulation in one-dimension. Generalization of results of this model using appropriate scaling

schemes is also discussed. In Chapter 6 we apply this generalized dimensionless numerical model to various sites and compare our predictions with inferences from proxy data at these sites. Chapter 7 develops a numerical model to estimate average gas hydrate saturation using depth of the sulfate-methane transition as a proxy. In Chapter 8 we develop analytical theory and expressions relating gas hydrate saturation profile to sulfate-methane transition depth and apply it to several Cascadia Margin sites. Chapter 9 discusses the effect of overpressure on gas hydrate and free gas saturations due to fast sedimentation and/or low permeability of the sediments. Chapter 10 develops a two-dimensional numerical model for simulating gas hydrate and free gas (mobile) accumulation. Chapter 11 summarizes the conclusions of this thesis and discusses future research directions arising from this study.

Chapter 2

Motivation and Background

2.1 Motivation

Natural gas hydrates are known to occur worldwide in sediments on offshore continental margins as well as in permafrost regions where favorable temperature and pressure conditions along with sufficient amounts of methane result in accumulation of large hydrate deposits (Kvenvolden, 1993; Sloan and Koh, 2007). This thesis focuses only on marine gas hydrate systems, because they are estimated to be much greater in amount than onshore deposits (Kvenvolden, 1993, 1998). Current interest in natural gas hydrates stems from three main areas:

Potential energy source: It is well known that huge amounts of methane hydrates are sequestered both in oceanic and onshore sediments (Kvenvolden, 1988). Estimates range from early consensus values of about 10,000 Gt (Kvenvolden, 1988) of carbon to recent estimates of 3,000 Gt (Buffett and Archer, 2004), 500-2,500 Gt (Milkov, 2004) and 74,400 Gt (Klauda and Sandler, 2005). Such figures make methane hydrates a very promising energy resource. However, the challenge is to identify concentrated gas hydrate accumulations that might be economically feasible for production, because most marine sites explored to date contain gas hydrate dispersed in relatively low

saturations in the sediments. Developing economical methods of producing such gas hydrate systems has also been an area of active research (Moridis, 2003; Moridis and Collett, 2003; Sun et al., 2005).

Deep water geohazard: Natural gas hydrates concentrated along continental margins represent a potential geohazard in the form of slope failures. Theoretically, sustained decreases in pressure or increase in temperature can dissociate large amounts of hydrate and possibly cause sediment failure. Towards this end, research has been done to understand how much free gas can accumulate before sediment fracturing occurs (Flemings et al., 2003; Hornbach et al., 2004). The effect of thermodynamic destabilization of gas hydrates on triggering slope failures has also been recently studied (Xu et al., 2001; Sultan et al., 2004). These models are relatively simple and, in general, do not have any coupled geomechanical models to predict the effect of overpressure and free gas generation on sediment strength and stability.

Global climate change: Rapid changes in past climate have been attributed to carbon influx from methane hydrate dissociation. Dickens et al. (1995, 1997) hypothesized that huge quantities of methane were released during the LPTM, due to thermal dissociation of oceanic hydrates, causing a negative shift in the heavier carbon isotope within a relatively short time interval ($< 10^4$years). Kennett et al. (2003) recently proposed the clathrate gun hypothesis, which relates climate change during the Late Quaternary to global warming caused by hydrate dissociation. Present day hydrate reservoirs are dynamic systems

(Dickens, 2003), with large carbon fluxes to and from the ocean, and could affect present day climate if perturbed over large time periods. Studies of gas hydrate dissociation in response to sealevel and seafloor temperature fluctuations conclude that the effect of seafloor temperature perturbations is more significant than sealevel perturbations (Xu et al., 2001).

2.2 Background of marine hydrate systems

Thermodynamically, gas hydrates are stable at relatively higher pressures and lower temperatures (Sloan and Koh, 2007). However, both pressure and temperature usually increase as a function of depth below the seafloor due to increasing overburden and geothermal heat, respectively. This implies that the temperature at some sub-bottom depth below the seafloor will exceed the three-phase stability limit, thereby constraining the actual zone of hydrate occurrence to some finite region below the seafloor (Figure 2.1). This finite zone is known as the gas hydrate stability zone (GHSZ) and its emergence from the three-phase equilibrium curve is explained in detail in Chapter 3. The depth at which the geothermal gradient causes the temperature to rise above the stability limit marks the base of the hydrate stability zone (BHSZ) (Figure 2.1).

Submarine gas hydrates are often found with a free gas layer below the BHSZ. This free gas can be produced by the dissociation of hydrate (due to burial with the sediment) beyond the GHSZ over geologic time scales (Davie and Buffett, 2001). Alternatively, free gas can also be supplied from depth and can get sealed by

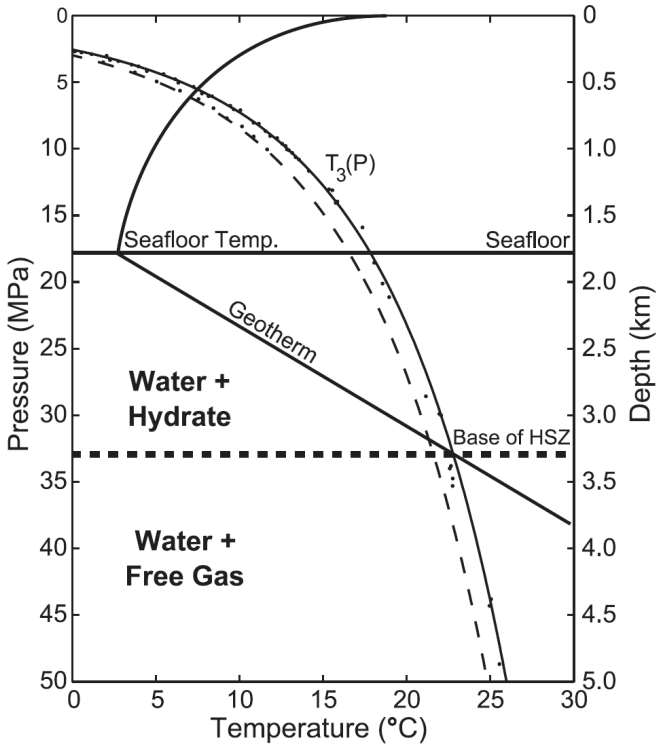

Figure 2.1: Schematic representation of temperature profile through the ocean and marine sediments illustrating that hydrates are stable at depths where temperature is less than T_3(P). The curve T_3(P) denotes the three-phase hydrate-water-gas stability boundary [*Taken from Buffett and Archer (2004)*].

the low permeability hydrate layer at the BHSZ (Xu and Ruppel, 1999; Liu and Flemings, 2007). Free gas can also migrate upwards back into the GHSZ to further concentrate the hydrate layer. Natural gas hydrates are often identified by the presence of a strong seismic reflection that parallels the seafloor, known as the bottom simulating reflection (BSR). This reflection is believed to be caused by the differences in acoustic impedances across the BHSZ (MacKay et al., 1994).

Results of the Ocean Drilling Program (ODP), particularly Legs 164 and 204, have greatly enhanced our understanding of gas hydrate distribution along active and passive margins (Paull et al., 1996; Tréhu et al., 2003). Unquestionably, at

many locations, lithology dictates gas hydrate distribution at the local scale (Kraemer et al., 2000; Weinberger et al., 2005). More important, however, are regional-scale variations in gas hydrate distribution between and within different geologic settings. For example, outer Blake Ridge (Leg 164) offshore South Carolina (USA) has modest quantities of gas hydrate dispersed over immense volumes of sediment, but locations with and without free gas beneath the GHSZ (Paull et al., 2000). By contrast, Hydrate Ridge (Leg 204) on the Cascadia Margin offshore Oregon (USA) has widely varying gas hydrate contents distributed across small volumes of sediment usually underlain by free gas (Tréhu et al., 2004).

Marine gas hydrates are components of complex systems with dynamic inputs and outputs of methane over time (Dickens, 2003). Excepting at select sites (for example, some seeps in the Gulf of Mexico), most gas within marine gas hydrates is methane (Kvenvolden, 1993; Milkov et al., 2005). However, this methane may derive from two general reactions, and gas hydrates may form through two general processes. At relatively low temperatures, characteristic of sediments at shallow burial depths, methanogenic archaea form biogenic methane; at relatively high temperatures, such as found deep within sediment sequences, thermo-catalytic reactions produce thermogenic methane (Claypool and Kvenvolden, 1983; Whiticar et al., 1986). Gas hydrates have been recovered from marine sediment with constituent methane principally derived from biogenic or thermogenic reactions (Kvenvolden, 1993; Milkov et al., 2005). More crucially, biogenic methane can be supplied within the GHSZ during burial of organic carbon (in situ methane) or to the GHSZ through upward migration of methane bearing fluids (deep methane). The

first input appears to dominate some gas hydrate systems, such as on outer Blake Ridge (Paull et al., 1994; Egeberg and Dickens, 1999), while the second appears to dominate other systems, such as along Cascadia Margin (Hyndman and Davis, 1992; Haeckel et al., 2004; Torres et al., 2004). Outputs of methane from gas hydrate systems include advection, diffusion or anaerobic oxidation through pore water sulfate (Xu and Ruppel, 1999; Borowski et al., 1996). Given the known variations in natural gas hydrate systems, an important issue is whether relatively simple and straightforward numerical models can explain general features of all systems. In particular, can changes in a few basic factors encompass a wide range of observations?

Previous numerical models for the accumulation of gas hydrate in marine sediment have focused mainly on simulating the distribution of gas hydrate at specific sites using parameters relevant to those locations. Blake Ridge (Egeberg and Dickens, 1999; Davie and Buffett, 2001, 2003a; Gering, 2003) and Hydrate Ridge (Luff and Wallman, 2003; Haeckel et al., 2004; Torres et al., 2004; Liu and Flemings, 2006) have been the subject of most studies. These models yield hydrate profiles fairly consistent with proxy evidence, but give little insight as to how changes in basic parameters alter the dynamics and distribution of gas hydrate. Studying effects of parameter changes in these models through sensitivity analysis requires new simulations to be performed for the perturbed parameter around its base case value. Thus, separate hydrate provinces are studied as isolated examples without common processes connecting them. We acknowledge that heterogeneous gas hydrate distribution at the local scale necessitates modeling that accounts for de-

tailed geology and structure, probably in two or three spatial dimensions. However, first-order modeling in one-dimension has the advantage of providing a simple understanding for how various processes affect natural gas hydrate systems.

We first develop a simple 1-D numerical model for gas hydrate accumulation in marine sediments over geologic time-scales. Using this model, we show that gas hydrate distributions in various locations can be described in terms of a few dimensionless groups or variables. This allows different gas hydrate systems to be classified and linked from a mechanistic perspective. The model is later extended to two-dimensions to simulate more complex and heterogeneous gas hydrate settings.

2.3 Quantitative studies of natural gas hydrates

The amount and distribution of gas hydrate within the GHSZ at a given location can be quantified by several indirect techniques (Paull et al., 2000; Tréhu et al., 2004). These include analyses of pressurized sediment cores, pore fluid geochemistry, sediment thermal anomalies, well-log velocity and resistivity, NMR and density-porosity logs, and seismic profiles. In concert, such methods can provide a current ”snapshot” for the presence and abundance of gas hydrate (Paull et al., 2000; Tréhu et al., 2004). However, they give no insight as to how the gas hydrate formed or the processes governing the accumulation.

The other main approach is to study these systems using coupled transport models, thereby explicitly accounting for the different methane sources. Rempel

and Buffett (1997) modeled hydrate formation as a Stefan problem and obtained analytical solutions for hydrate growth in a porous half-space that is cooled on its boundary. Xu and Ruppel (1999) extended the model by including coupled mass, momentum and energy equations to derive analytical solutions for hydrate distribution in marine sediments. Based on their results, they defined a critical methane flux required for the hydrate layer to extend to the BHSZ. However, methane was only supplied in their model from depth, i.e. sedimentation and biogenic in situ generation to methane were not considered. Davie and Buffett (2001) proposed a 1-D numerical model for hydrate accumulation due to biogenic sources of methane. They used the model to predict hydrate distribution in the Blake Ridge sediments as a case study and constrained the simulation parameters using pore water chloride anomalies from core data. Pore water sulfate gradients were used to further constrain the different sources of methane in the Blake Ridge hydrates (Davie and Buffett, 2003a). Gering (2003) focused on the effect of sediment compaction rates on hydrate accumulations.

A basic problem with the aforementioned models is that they do not incorporate both sources of methane (i.e., biogenic in situ production or methane from depth) in a systematic manner. This causes them to be valid only at specific hydrate locations, e.g. Blake Ridge (Davie and Buffett, 2003a) or Cascadia Margin (Haeckel et al., 2004; Torres et al., 2004). Moreover, most of these transport models use a first-order rate law to model the kinetics of hydrate formation, the driving force being the difference between pore water methane concentration and the local solubility (Davie and Buffett, 2001). Thermodynamic equilibrium is then approximately

enforced by arbitrarily choosing a large value of the rate constant, with no physical basis. Porosity loss and compaction driven fluid flow is also modeled using empirical relationships and not as an intrinsic process common to most sedimentary basins. Our approach aims to give a more general understanding of hydrate systems without these limiting assumptions.

It is also known that marine hydrates are often distributed in heterogeneous patterns in sediments. None of the current models have the capability to incorporate this heterogeneity on any length-scale using a physically consistent and non-empirical approach. Effects such as focused fluid flow or lateral gas migration can also result in heterogeneous hydrate accumulations and will need at least two spatial dimensions to model.

Our model differs from existing models in using component balances so that the system is in thermodynamic equilibrium over geologic time-scales, which avoids the use of a kinetic model for hydrate formation. Further, we systematically incorporate both local and deeper sources of methane. The main difference, however, lies in the way we non-dimensionalize our system, which leads to the characterization of different hydrate distributions using a few dimensionless groups. This enables depiction of average hydrate saturations in different geological settings with just two contour plots, which are valid for a wide range of model parameters. We also include the effect of salinity on gas hydrate distributions so they are pertinent to marine environments.

Chapter 3

Phase Equilibrium of Gas Hydrates

3.1 Introduction

Gas hydrates can coexist with aqueous and vapor phases at specific conditions defined by a three-phase equilibrium curve (Sloan and Koh, 2007). At temperatures lower than and pressures higher than the three-phase equilibrium curve, gas hydrate is stable. In sediment sequences, increasing temperature with depth limits the GHSZ to some finite sub-bottom depth (Figure 2.1). In this region, gas hydrates can coexist with the aqueous phase; we call this region as the L-H zone. Below this region, free gas can coexist with the aqueous phase; we call this the L-V zone.

The thickness of this GHSZ is primarily governed by the seafloor depth, seafloor temperature, geothermal gradient and pore water salinity (Dickens et al., 1997). Capillary inhibition due to fine-grained sediments (Clennell et al., 1999) and gas composition have lesser impact on the GHSZ thickness. Because methane dominates naturally occurring gas hydrates, we focus on the phase diagram and modeling of structure I hydrates.

3.2 Three Phase Equilibrium Curve

The three-phase equilibrium curve of gas hydrates is predicted using the statistical thermodynamic model of van der Waals and Platteeuw (1959). The condition for three phase stability comes from the equality of the chemical potential of water in the hydrate and aqueous phases:

$$\mu_w^H = \mu_w^L \Longrightarrow \mu_w^\beta - \mu_w^H = \mu_w^\beta - \mu_w^L \tag{3.1}$$

where μ_w^H, μ_w^L and μ_w^β are the chemical potentials of water in the hydrate phase, the aqueous phase and a reference hypothetical empty gas hydrate lattice, respectively. The difference in chemical potential between the reference state and the liquid phase can be calculated using a simplified relationship first proposed by Holder et al. (1980):

$$\frac{\mu_w^\beta - \mu_w^L}{RT} = \frac{\Delta\mu_w^{L,0}}{RT_0} - \int_{T_0}^{T} \frac{\Delta h_w}{RT^2} dT + \int_0^P \frac{\Delta\nu_w}{RT} dP - \ln(\gamma_w x_w) \tag{3.2}$$

where $\Delta\mu_w^{L,0}$ is an experimentally determined chemical potential difference between the empty reference state and pure water at the reference temperature (T_0) and zero absolute pressure, Δh_w and $\Delta\nu_w$ are the enthalpy difference and volume difference between the empty hydrate lattice and pure water, respectively, γ_w is the activity coefficient of water, and x_w is the mole fraction of water in the aqueous phase. Due to the low solubilities of methane in water, the activity coefficient γ_w is assumed to be unity, unless salinity is included. The equation of state for methane

proposed by Duan et al. (1992) is used to find the solubility of methane in water.

The enthalpy difference, Δh_w, can be written as (Holder et al., 1980):

$$\Delta h_w = \Delta h_w^0 + \int_{T_0}^{T} \Delta C_{p,w} dT \tag{3.3}$$

where ΔC_{pw} is the heat capacity difference between the empty hydrate reference state and pure water, and is expressed as a function of temperature as (Holder et al., 1980):

$$\Delta C_{p,w} = \Delta C_{p,w}^0(T_0) + b\,(T - T_0) \tag{3.4}$$

The difference in chemical potential between the reference hydrate lattice and the filled structure can be written as (Parrish and Prausnitz, 1972):

$$\frac{\mu_w^\beta - \mu_w^H}{RT} = -\sum_{i=1}^{2} v_i \ln(1 - \theta_i) \tag{3.5}$$

where the summation is done over both cages of structure I hydrate, v_i is the ratio of the number of type i cavities to the number of water molecules in the hydrate structure and θ_i is the fractional occupancy of type i cavity by the gas molecules. The dependence of cage occupancies on gas fugacity is given by the following Langmuir type relation:

$$\theta_i = \frac{C_i f_{CH_4}}{1 + C_i f_{CH_4}} \tag{3.6}$$

where f_{CH_4} is the fugacity of methane in the gas phase, calculated using the Peng-Robinson equation of state (Peng and Robinson, 1976), and C_i corresponds to

the Langmuir constant of adsorption for the small and large cages of structure I hydrate. Calculation of Langmuir constants involves the integration of interaction potentials between the guest and host molecules over the cell volume, which after applying the Lennard-Jones-Devonshire approximation, reduces to the following:

$$C_i(T) = \frac{4\pi}{kT} \int_0^{R_i - a} r^2 exp\left[\frac{-w_i(r)}{kT}\right] dr \tag{3.7}$$

where k is Boltzmann's constant, R_i is the cell radius, a is the core radius of the guest and $w_i(r)$ is the spherically symmetric cell potential.

The cell potential term $w_i(r)$ can be approximated by a Kihara potential, which is known to model the three-phase equilibrium of hydrates accurately. The expressions relating $w_i(r)$ to the Kihara potential and different cell parameters are standard (Parrish and Prausnitz, 1972; Sloan and Koh, 2007). The one-dimensional integral in equation (3.7) can be evaluated numerically but the integrand becomes singular at both the upper and lower integration limits. To avoid this problem we use the Gauss-Kronrod quadrature rule (Piessens et al., 1983), which uses an adaptive scheme to evaluate functions with endpoint singularities. After evaluating these constants at any given temperature, the equality of chemical potentials can be recast into the following residual form, as a function of pressure:

$$g(P) = \frac{\Delta\mu_w^{L,0}}{RT_0} - \int_{T_0}^{T} \frac{\Delta h_w}{RT^2} dT + \int_0^P \frac{\Delta\nu_w}{RT} dP - \ln(\gamma_w x_w) + \sum_{i=1}^{2} v_i \ln\left(1 - \frac{C_i f_{CH_4}}{1 + C_i f_{CH_4}}\right) = 0 \tag{3.8}$$

The parameters used in this formulation are listed in Table 3.1. The root of this function $g(P)$ is the three-phase equilibrium pressure and it is evaluated using the Newton-Raphson method. The addition of dissolved ions changes the activity of water ($\gamma_w x_w$) in solution and this effect can be incorporated in the model. We use the Pitzer equations (Pitzer and Mayorga, 1973) to calculate water activity for different dissolved ion concentrations. These equations can be included in equation (3.8) to predict the phase equilibrium for brines.

Table 3.1: Parameters for thermodynamic model

Thermodynamic properties	Value	Reference
$\Delta\mu_w^{L,0}$	1236 J/mol	1
Δh_w^0	-4303.5 J/mol	1
$\Delta C_{p,w}^0$	-38.12 J/mol K	1
b	0.141 J/mol K^2	1
$\Delta\nu_w$	4.598 cm^3/mol	1
T_0	273.15 K	1

1) Cao et al. (2002)

The three-phase equilibrium curve obtained from the solution of equation (3.8) for pure water-methane system is shown in Figure 3.1 along with experimental data (McLeod and Campbell, 1961; Marshall et al., 1964; Adisasmito et al., 1991; Yang et al., 2001) and predictions from CSMHYD (Sloan and Koh, 2007). The

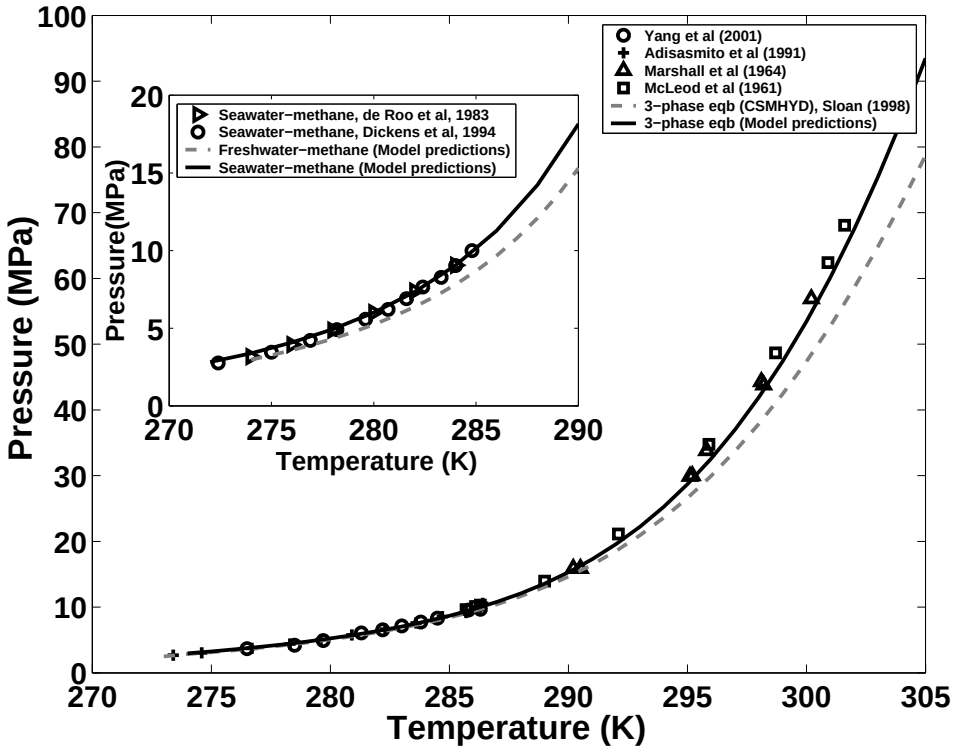

Figure 3.1: Three-phase equilibrium curves for the methane-pure water system compared with results from CSMHYD (dashed curve) and experimental data. Inset shows experimental and calculated equilibrium curves for the methane-seawater (0.6m NaCl solution) system.

CSMHYD program gives a good fit to experimental data at relatively low temperature/pressure conditions, but the deviation between experimental data and CSMHYD results increases significantly at relatively higher temperature/pressure conditions. In comparison, our model gives much better agreement with experimental data at high temperature/pressure conditions (Figure 3.1).

The addition of dissolved ions shifts the equilibrium curve towards higher pressures and lower temperatures (Figure 3.1, inset). The results are shown for 0.6m NaCl solution, which has water activity approximately equal to that of seawater (33.5 salinity). The results are in good agreement with the experimental values

(de Roo et al., 1983; Dickens and Quinby-Hunt, 1994) for three-phase equilibrium conditions of saline solutions.

The detailed modeling of the three-phase equilibrium allows us to calculate the cage occupancies of the small and large cages of structure I hydrate, which are later used to calculate the solubility of methane in the aqueous phase in equilibrium with the hydrate phase (L-H zone). This helps to build an accurate and thermodynamically rigorous methane solubility model compared to the approximate empirical relationships used in other transport models for hydrate accumulation (Xu and Ruppel, 1999; Davie and Buffett, 2001).

3.3 Methane Solubility

Methane solubility within the GHSZ corresponds to the concentration of methane required to precipitate a hydrate phase, in equilibrium with the aqueous phase. Thus, the calculation of solubility in the (L-H) region is most critical to the hydrate distribution in the GHSZ. It is known from experimental results (Yang et al., 2001; Seo et al., 2002; Servio and Englezos, 2002) and theoretical work (Handa, 1990; Zatsepina and Buffett, 1998) that methane solubility in equilibrium with gas hydrate increases with increasing temperature and decreases with increasing pressure. Approximate models for computing methane solubility in the L-H region have been reported (Servio and Englezos, 2002; Davie et al., 2004). However, we compute the solubility by using an accurate and thermodynamically rigorous formulation

proposed by Handa (1990). The final equations derived from the model are:

$$\left(\frac{\partial \ln(x_{CH_4})}{\partial P}\right)_T = \frac{1}{RT}\frac{V_e - \overline{V}_w - \overline{V}_{CH_4}\sum_{i=1}^{2} v_i\theta_i}{\sum_{i=1}^{2} v_i\theta_i - \frac{x_{CH_4}}{1-x_{CH_4}}} \tag{3.9}$$

$$\ln\left(\frac{\theta_i}{1-\theta_i}\right)_P = \ln\left(\frac{\theta_i}{1-\theta_i}\right)_{P_e} + \ln\left(\frac{(x_{CH_4})_P}{(x_{CH_4})_{P_e}}\right) + \frac{\overline{V}_{CH_4}}{RT}(P - P_e) \tag{3.10}$$

where V_e is the molar volume of the empty hydrate lattice per mole of water, $\overline{V}_w$ is the partial molar volume of water, $\overline{V}_{CH_4}$ is the partial molar volume of methane in the aqueous phase and P_e is the three-phase equilibrium pressure at the temperature T. The values for V_e and $\overline{V}_w$ are taken to be 22.5 cm^3/mol and 18.02 cm^3/mol (Handa, 1990), respectively, while $\overline{V}_{CH_4}$ is calculated using the relation reported by Duan et al. (1992).

The above equations allow methane solubility to be determined at any pressure greater than the equilibrium pressure. However, they form a set of coupled, non-linear equations that have to be solved iteratively. Our computational approach is summarized below:

- For a given temperature T, calculate the three-phase equilibrium pressure P_e using the numerical scheme outlined before. This calculation will also yield the cage occupancies (θ_i) at pressure P_e.
- Use the equation of state (Duan et al., 1992) to compute the solubility of methane $(x_{CH_4})_{P_e}$ in equilibrium with vapor at the three-phase point (P_e,T).
- Simultaneously solve equations (3.9) and (3.10) to advance to the pressure P.

As two examples, we show the relationship between methane solubility and pressure at constant temperatures of 278.15 K and 290 K (Figure 3.2). Experimental data from Seo et al. (2002) is also shown for comparison. The peak in methane solubility occurs at the three-phase equilibrium pressure P_e. At pressures lower than P_e, methane solubility increases with increasing pressure. However, at pressures exceeding P_e, this behavior is reversed and methane solubility slightly decreases as pressure is increased.

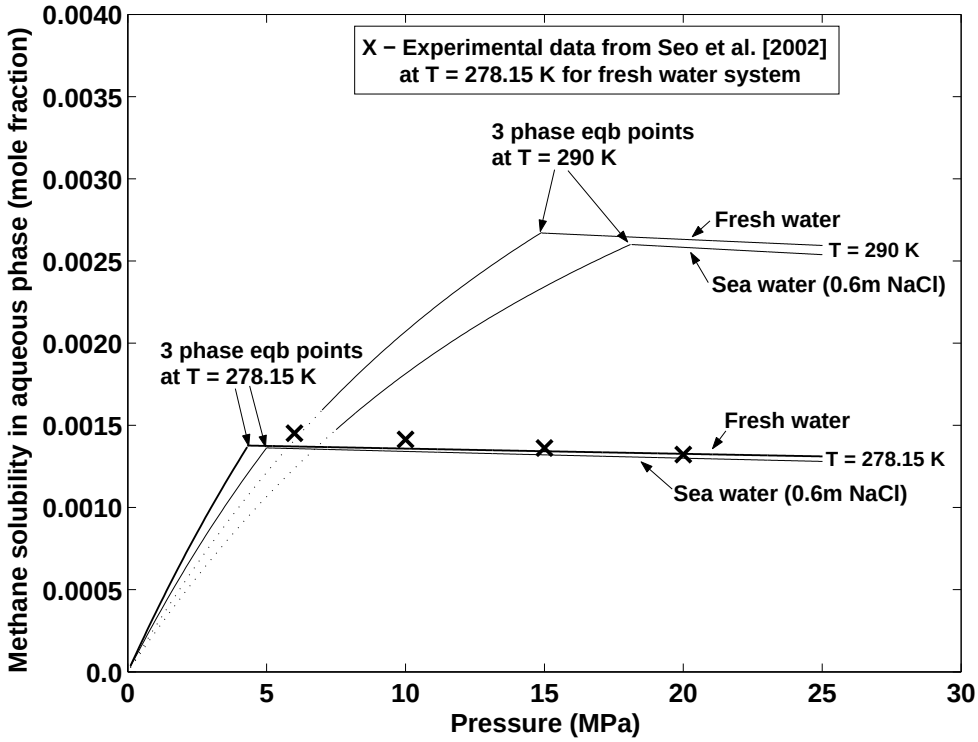

Figure 3.2: Variation of methane solubility in aqueous phase with pressure in the L-V and L-H regions of the phase diagram at $T = 278.15$ K and $T = 290$ K, for methane-pure water and methane-seawater (0.6m NaCl solution) systems.

3.4 Methane Solubility Curve

The final objective of the phase equilibrium calculations is to construct a composite curve that delineates methane solubility in water as a function of depth. Unless otherwise stated, all results shown henceforth are for water with a constant water activity equivalent to that of a 0.6m NaCl solution.

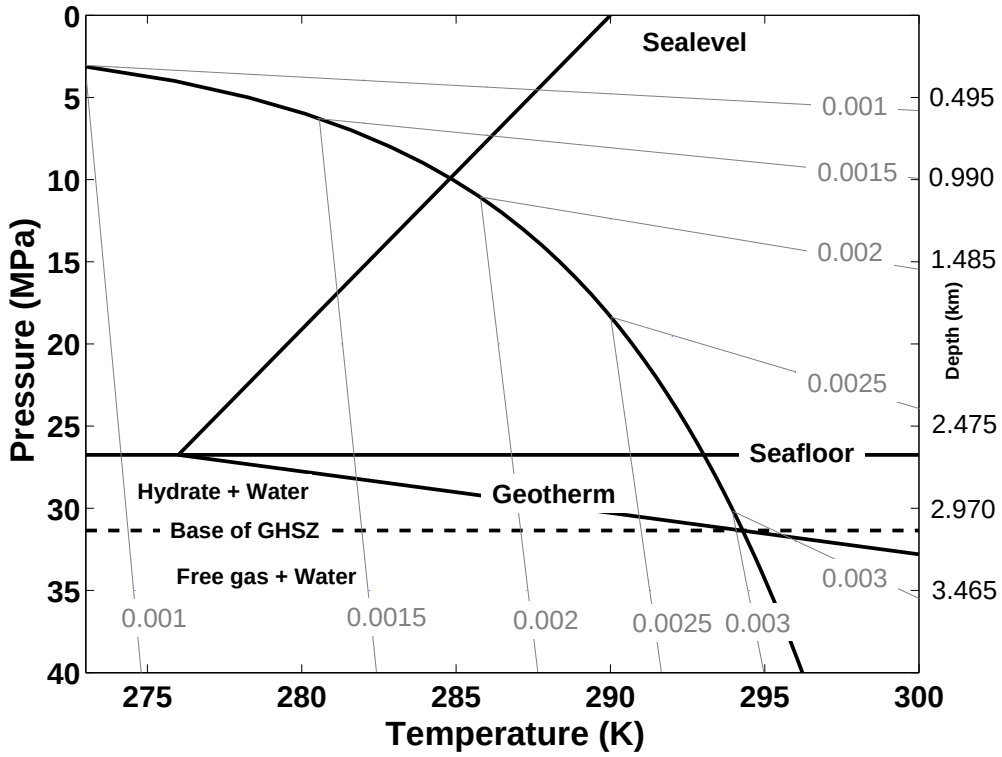

Figure 3.3: Emergence of the GHSZ by imposing a seafloor depth, seafloor temperature and geothermal gradient on the solubility contour plot (mole fraction). The curve represents the three-phase seawater-methane equilibrium profile. A depth scale corresponding to hydrostatic pressure (assuming constant seawater density of 1030 kg/m^3) is plotted on the right axis to apply this phase diagram to a marine environment.

We now plot the contours of constant methane solubilities in the L-V and L-H regions along with the three-phase equilibrium curve (Figure 3.3), using the mod-

els explained in the previous sections. In this example we assume the seafloor is located at 2700 m below sea level, the seafloor temperature is 276 K, and the geothermal gradient in the sedimentary section is about 0.016 K/m. This diagram also shows the point where the temperature profile within the sediments intersects the three-phase equilibrium curve at the depth marking the phase boundary, also referred to as the base of the GHSZ. Thus, the region extending from the seafloor down to the base of the GHSZ becomes the zone of hydrate stability (dissolved methane and gas hydrate can coexist), whereas free gas can coexist with the aqueous phases below the GHSZ, provided methane in excess of the local solubility is present.

Results from the contour plot can be combined into a single solubility curve (Figure 3.4) that forms the foundation for accumulating gas hydrates in sediments. In general, methane solubility increases with depth within the GHSZ, reaches a local maximum at the base of the GHSZ and then slightly decreases below. The specifics of the solubility curve, however, depend on water depth, seafloor temperature, geothermal gradient and pore water salinity.

The vertical depth below the seafloor (Figure 3.4) is normalized by depth to the base of the GHSZ, denoted as L_t. The methane solubility is also scaled with the peak concentration at this depth ($c^w_{m,eqb}$). This scaling fixes the base of the GHSZ at unit normalized depth with unit normalized methane solubility. The importance of this normalization will be evident when we later show that this scaling makes our final saturation plots relatively insensitive to changes in seafloor depth, seafloor temperature and geothermal gradient.

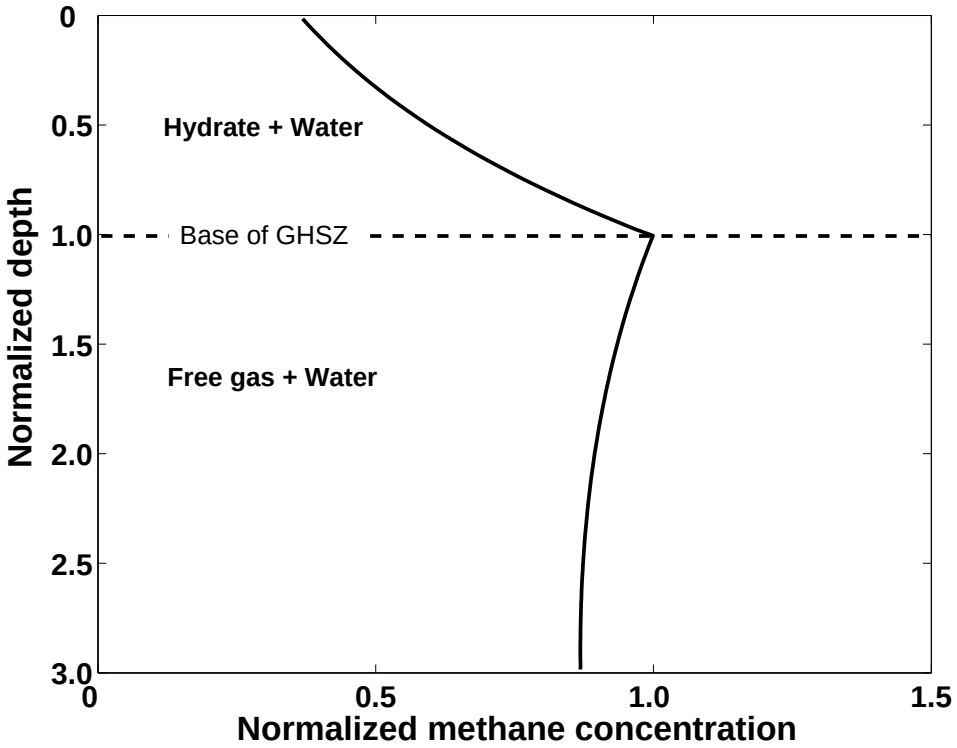

Figure 3.4: Final methane solubility curve in a submarine setting obtained from the phase equilibrium and methane solubility calculations. The depth scale is scaled with respect to the depth of the base of the GHSZ and the methane concentration is scaled with the peak solubility at the base of the GHSZ.

The phase stability and methane solubility curves are later used to predict hydrate saturations in a dynamic framework with respect to time. We acknowledge, up front, that this becomes a problem with our assumption of constant pore water salinity during the simulations. Precipitation and dissociation of gas hydrate changes the salinity, which, in turn, changes the phase boundaries and solubilities. We discuss the possible effects of these changes later.

Chapter 4

Sedimentation and Compaction in Sedimentary Basins

4.1 Introduction

For studying regional accumulation of gas hydrates, compaction-driven fluid flow in the upper few hundred meters of sediments assumes significance. It is believed that in situ (biogenic) generation of methane can contribute towards hydrate formation on all continental margins and may be the principal source of methane on passive margins (Kvenvolden, 1993). In the absence of upward external fluid fluxes, continuous sedimentation and associated compaction can be the primary source of fluid flow. Freshly deposited sediments are unconsolidated, have high porosity, low bulk density and high water content. However, with gradual burial under younger sediments, the sediments lose their porosity, become denser and get consolidated. The processes that bring about this change in sediment properties are collectively grouped under the term *diagenesis*, which can be broadly divided into the following categories (Einsele, 1992):

Mechanical diagenesis - Originates from the vertical and accompanying lateral stresses caused by the the overburden of young sediments, resulting in mechanical arrangement and compression of grains.

Chemical diagenesis - Includes dissolution and recrystallization of sediment grains, as well as precipitation of dissolved minerals as cement in the pore space.

These diagenetic processes generally lead to the reduction of porosity and permeability, causing the bulk density to increase. This loss in porosity and sediment thickness is called compaction (Berner, 1980). Compaction of water-saturated sediment is associated with the expulsion of pore water, resulting in compaction-driven fluid flow. The resulting porosity profiles are referred to as porosity-loss or compaction curves and are an indication of the sediment burial and subsidence histories (Berner, 1980; Giles, 1997).

In the absence of external fluxes, fluid flow in our system is assumed to originate from mechanical diagenesis only. This is assumed because the flux of compaction-driven fluid in a sedimentary basin is greatest in the upper few kilometers (Galloway, 1984), which overlaps with the region where gas hydrates are normally present. Chemical diagenesis usually assumes significance at temperature and pressure conditions that are high enough to be excluded from our physical domain of interest.

4.2 Mathematical Modeling of Compaction

The theory of primary consolidation was first developed by Terzaghi (1943) by relating the compaction and pore water expulsion to excess pore-pressures. Based on this theory, Gibson (1958) proposed a one-dimensional model for consolidation of a clay layer over time. Rubey and Hubbert (1959) explained the role of fluid pres-

sure in overthrust faulting by deriving a constitutive relationship between porosity and effective stress. The combined effect of vertical compaction-driven flow and heat transfer was studied by Sharp (1976) for modeling rapidly subsiding basins.

The first attempt at a two-dimensional compaction model was published by Bethke (1985) for anisotropic and accreting domains by using a Lagrangian frame of reference. Aquathermal pressuring was found to contribute negligibly to the excess flow potentials developed during compaction. Further, fluids in shallow sediments were reported to move upward toward the seafloor, whereas deeper fluids tend to move laterally. A mathematical model for non-linear compaction was proposed by Audet and Fowler (1992) in which different pore pressure regimes were predicted based on a single dimensionless parameter defined as the ratio of the Darcy flux to the sedimentation rate. Recent numerical models have been able to incorporate the complex effects of viscoelastic deformation of sediments, pressure dissolution at grain contacts and multiple mineral reactions in this hydro-mechanical problem (Luo et al., 1998; Yang and Fowler, 1998; Suetnova and Vasseur, 2000; Yang, 2001).

Most of the advanced models used to study compaction consider sedimentation on an impermeable basin-floor or basement in which the height of the seafloor above this datum becomes a dependent variable (Bethke, 1985; Wangen, 1992; Dugan and Flemings, 2000; Yang, 2001). As stated previously, we are interested in modeling compaction-driven flow in the top most layer of the sediments. Hence, a full basin-scale numerical model would not be a good choice for our problem, as it will make the computations unnecessarily expensive. To further simplify the

problem, we fix our reference frame at the seafloor and assume that the seafloor level stays constant over time. This assumption is commonly used in modeling early (shallow) diagenesis (Berner, 1980) and helps us in writing the formulation as a fixed boundary problem. We now present a simple 1-D compaction model in which pore-pressure is maintained hydrostatic. A more general compaction model where pore pressure is allowed to deviate form hydrostatic pressures is presented in Chapter 9.

4.3 Compaction with hydrostatic pressure gradient

Continuous sedimentation, compaction and associated fluid flow is modeled in one-dimension in this section to obtain porosity-loss curves, sediment velocity and fluid velocity profiles in the sediment. Porosity-loss can be empirically modeled using Athy's law (Athy, 1930), which assumes an exponential decay of porosity with sediment depth. However, it is well known that the driving force for porosity-loss is effective stress and not sediment depth (Bear, 1988). A simple model for compaction based porosity-loss can then be obtained by understanding the stresses acting on the sediments. Following assumptions are made in this model:

- Densities of the components (sediment and water) remain constant
- Sedimentation rate is constant in time and in equilibrium with the subsidence rate
- Porosity profile is independent of time

- No external upward fluid flow occurs in this system
- Fluid and solid velocities become equal as a minimum porosity is achieved
- Generation of water through diagenetic reactions is neglected

As explained before, the second assumption helps us to fix our reference frame at the seafloor level, which stays constant in time. The depth co-ordinate is assumed to be positive downwards. For one-dimensional compaction only (i.e., zero lateral strain) and incompressible solid and fluid phases, the gradient of the total vertical stress or overburden pressure (σ_v) acting on the sediments is:

$$\frac{\partial \sigma_v}{\partial z} = \rho_b g \tag{4.1}$$

where ρ_b is the bulk density of the sediments given by:

$$\rho_b = \rho_s(1-\phi) + \rho_f \phi \tag{4.2}$$

where ρ_s is the sediment density, ρ_f is the fluid density and ϕ is the porosity. Additionally we assume that the pore fluid pressure, p_w, is hydrostatic so that the pore pressure gradient is given by:

$$\frac{\partial p_w}{\partial z} = \rho_f g \tag{4.3}$$

Further, the mechanical compaction of sediments is governed by the effective stress, σ_e, which is defined according to Terzaghi's effective stress principle (Bear and Bachmat, 1990) as the difference between the total vertical stress σ_v and the

pore pressure p:

$$\sigma_e = \sigma_v - p \tag{4.4}$$

One of the common relationships linking the porosity-loss to effective stress is (Rubey and Hubbert, 1959):

$$\phi = \phi_\infty + (\phi_o - \phi_\infty)e^{-\frac{\sigma_e}{\sigma_\phi}} = \phi_\infty + (\phi_o - \phi_\infty)e^{-\frac{\sigma_v - p}{\sigma_\phi}} \tag{4.5}$$

where σ_ϕ is a characteristic constant having units of stress, ϕ_o is the porosity of the freshly deposited sediments and ϕ_∞ is the minimum porosity achieved at great depths. The original relation has been modified to account for a non-zero minimum porosity. Rearranging the above equation yields:

$$\ln\left(\frac{\phi - \phi_\infty}{\phi_o - \phi_\infty}\right) = -\frac{\sigma_e}{\sigma_\phi} \tag{4.6}$$

Differentiating (4.4) with respect to z and using (4.1) and (4.3), we get:

$$\frac{\partial \sigma_e}{\partial z} = (\rho_s - \rho_f)(1 - \phi)g \tag{4.7}$$

Differentiating (4.6) with respect to z gives:

$$\frac{\partial \sigma_e}{\partial z} = -\sigma_\phi \left(\frac{\phi_o - \phi_\infty}{\phi - \phi_\infty}\right) \frac{\partial}{\partial z}\left(\frac{\phi - \phi_\infty}{\phi_o - \phi_\infty}\right) \tag{4.8}$$

Eliminating the gradient of effective stress between (4.7) and (4.8) gives the following equation for porosity gradient:

$$-\sigma_\phi \left(\frac{\phi_o - \phi_\infty}{\phi - \phi_\infty}\right) \frac{\partial}{\partial z} \left(\frac{\phi - \phi_\infty}{\phi_o - \phi_\infty}\right) = (\rho_s - \rho_f)(1-\phi)g \tag{4.9}$$

4.3.1 Non-dimensionalization

It can be seen from equation (4.9) that the term $\sigma_\phi/[(1-\phi_\infty)(\rho_s - \rho_f)g]$ has units of length and is used to non-dimensionalize the depth z. We define this characteristic length by L_ϕ and the dimensionless depth by $\tilde{z}$, as below:

$$L_\phi = \frac{\sigma_\phi}{(1-\phi_\infty)(\rho_s - \rho_f)g} \tag{4.10}$$

$$\tilde{z} = \frac{z}{L_\phi} = \frac{z}{\sigma_\phi/[(1-\phi_\infty)(\rho_s - \rho_f)g]} \tag{4.11}$$

The actual porosity along with the initial and final porosities are also rewritten as reduced variables in the following form:

$$\tilde{\phi} = \frac{\phi - \phi_\infty}{1 - \phi_\infty}\,, \quad \eta = \frac{\phi_o - \phi_\infty}{1 - \phi_\infty} \tag{4.12}$$

In terms of these variables, (4.9) along with the boundary condition becomes:

$$\frac{1}{\tilde{\phi}} \frac{\partial \tilde{\phi}}{\partial z} = -(1 - \tilde{\phi}) \quad , \quad \text{B.C.}: \ \text{At } \tilde{z} = 0, \ \tilde{\phi} = \eta \tag{4.13}$$

Integration of the above equation leads to the following porosity profile along the dimensionless depth:

$$\tilde{\phi} = \frac{\eta}{\eta + (1-\eta)e^{\tilde{z}}} \tag{4.14}$$

4.3.2 Sediment and fluid velocities

Sediment and fluid velocities can be easily obtained from the porosity-loss curves, assuming no separate phase formation occurs. As a closure for this system of equations, it is generally assumed that the fluid and sediment velocities approach a common asymptotic value as the minimum porosity is achieved (Berner, 1980; Hutchison, 1985; Davie and Buffett, 2001). This is tantamount to saying that at very low porosities, there is no relative motion between the sediment and pore-fluid. The material balance for the sediment particles and fluid for this system can be written as:

$$\frac{\partial((1-\phi)\rho_s)}{\partial t} + \nabla \cdot (v_s \rho_s (1-\phi)) = 0 \tag{4.15}$$

$$\frac{\partial(\phi\rho_f)}{\partial t} + \nabla \cdot (v_f \rho_f \phi) = 0 \tag{4.16}$$

where v_s is the sediment velocity and v_f is the fluid velocity. For time independent densities and porosity profile $\phi(z)$, equations (4.15) and (4.16) become:

$$\nabla \cdot (v_s \rho_s (1-\phi)) = 0 \tag{4.17}$$

$$\nabla \cdot (v_f \rho_f \phi) = 0 \tag{4.18}$$

which simply states that the flux of sediment and fluid each remains constant in the system. The invariance of the sediment flux can be used to get the sediment velocity profile by knowing the rate of sedimentation at the seafloor:

$$v_s(z)\,(1-\phi(z)) = [v_s(z)\,(1-\phi(z))]_{\tilde{z}=0} = \dot{S}(1-\phi_o) \tag{4.19}$$

The assumption of solid and fluid velocities becoming equal at greater depths can be used to deduce the fluid velocity as follows:

$$v_f(z)\phi(z) = v_{f,\infty}\phi_\infty = v_{s,\infty}\phi_\infty \tag{4.20}$$

Utilizing relation (4.19) to get the sediment velocity $v_{s,\infty}$, the fluid velocity is given by:

$$v_f(z) = \frac{\dot{S}(1-\phi_o)\phi_\infty}{\phi(1-\phi_\infty)} \tag{4.21}$$

Non-dimensionalizing the velocities with respect to the sedimentation rate and reduced porosities, the final expressions for the velocities are given by:

$$\tilde{v}_s = \frac{1-\eta}{1-\tilde{\phi}} \tag{4.22}$$

$$\tilde{v}_f = \frac{1-\eta}{1+\gamma\tilde{\phi}}\ ,\ \text{where}\ \gamma = \frac{1-\phi_\infty}{\phi_\infty} \tag{4.23}$$

The above fluid balance is only performed for pore water in a compacting medium, i.e. it assumes no gas hydrate or free gas formation and their effects on the fluid flux. The complete water balance is presented in the next chapter.

4.3.3 Results and discussion

Porosity and velocity profiles are computed for $\eta = 6/9$ and $\gamma = 9$, which correspond to seafloor and minimum porosities of $\phi_0 = 0.7$ and $\phi_\infty = 0.1$, respectively. Figure 4.1 shows how the porosity decreases monotonously from the maximum value at the seafloor to an asymptotic value corresponding to the minimum over the normalized depth $\tilde{z}$. Figure 4.2 shows sediment and fluid velocity profiles

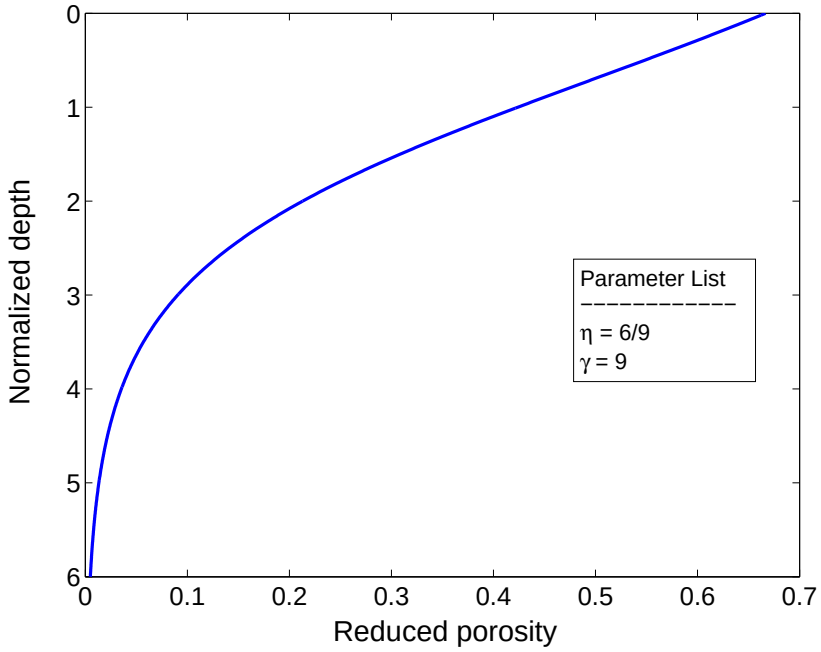

Figure 4.1: Porosity - depth profile for hydrostatic pore pressure

along the normalized depth. It can be seen that the sediment velocity is maximum at the seafloor, where it is initially deposited, and then steadily decreases. The fluid velocity, on the other hand, increases from its minimum at the seafloor and, together with the sediment velocity, approaches a common asymptote.

It is important to note that the fluid velocity is positive throughout the depth,

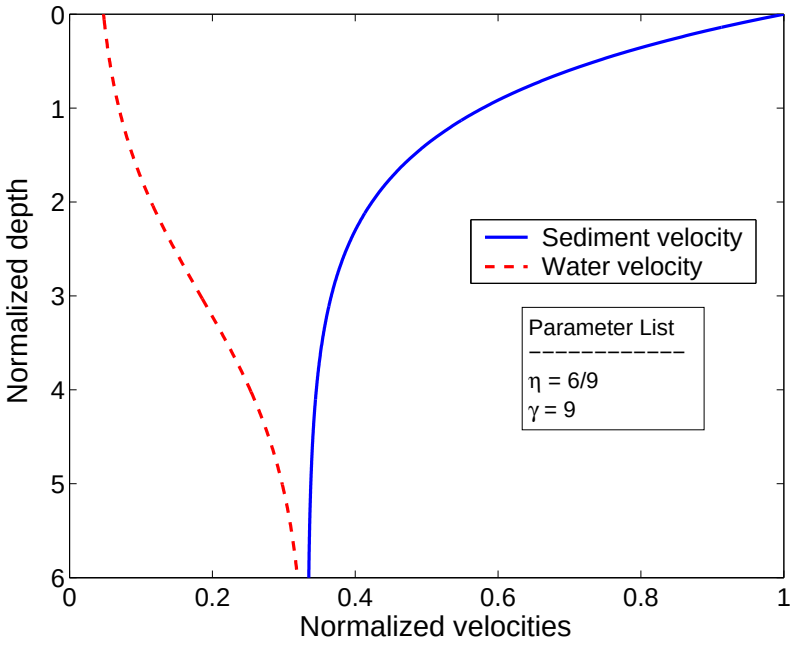

Figure 4.2: Velocity - depth profiles for hydrostatic pore pressure

which means that the fluid always moves downwards relative to the seafloor. This behavior is better understood by realizing that each new sedimentary layer being deposited has generally more pore volume than the volume of water squeezed out of the underlying layers, thus allowing some water into the system (de Caritat, 1989). Hence, although both water and sediment are carried into the subsurface on the escalator of basin subsidence, the sediment in general moves faster, resulting in the pore fluid moving upward relative to the sediment.

4.4 Conclusions

We started with a simple model of sedimentation-compaction by utilizing a constitutive porosity-effective stress relationship. Using steady-state mass balances,

analytical expressions for sediment and fluid velocities were derived for the case of hydrostatic pore pressures. The velocity profiles show that both fluid and sediment always moves downwards with respect to the seafloor and upwards with respect to the sediment. This fact is important in gas hydrate dynamics because it means that dissolved methane cannot be advectively transported up into the zone of hydrate stability without a source of external flux.

Chapter 5

Component Balances and Gas Hydrate Accumulation in 1-D

5.1 Introduction

Naturally occurring gas hydrates can derive their methane through two processes (Kvenvolden, 1993; Milkov et al., 2005). Decomposition of organic carbon buried with sediment can generate methane significantly faster than diffusion can remove it toward the seafloor. This could lead to in situ precipitation of gas hydrate within the GHSZ (Paull et al., 1994; Egeberg and Dickens, 1999; Davie and Buffett, 2001). Advection of methane, either biogenic or thermogenic, from deeper sources can supply methane into the GHSZ from below (Xu and Ruppel, 1999; Haeckel et al., 2004; Torres et al., 2004; Liu and Flemings, 2006). The progressive decrease of methane solubility with shoaling depth across the GHSZ (Figure 3.4) implies that gas hydrate can precipitate from methane charged fluids without requiring free gas (Hyndman and Davis, 1992). The development of a general model needs to consider gas hydrate accumulation from either of the two methane sources and from mixtures of both.

For in situ methanogenesis, solid organic carbon buried with sediments ultimately provides the methane. Complete conversion of organic matter to methane

proceeds via a series of complex reactions and pathways involving myriad compounds (Berner, 1980; Claypool and Kvenvolden, 1983; Whiticar et al., 1986; Wallman et al., 2006). To simplify this process, we combine possible pathways for biogenic methane into a single first-order reaction (Martens and Berner, 1977; Davie and Buffett, 2001). The rate of methane generation is assumed to be proportional to the available organic carbon present in the sediments and linked to it through a first-order rate law. We acknowledge that in constructing a relatively general first-order model, we have neglected the complications arising from using such simple kinetics for organic decay. More advanced models for simulating organic decay and other coupled reactions have been recently published (Wallman et al., 2006), but these introduce new parameters in the system, which makes our simulation results difficult to scale into simple plots.

5.2 Biogenic Methane Formation

Biogenic methane originates from the microbially mediated decomposition of organic matter accumulated in anaerobic conditions. Aerobic oxidation of organic matter is actually the most efficient energy yielding metabolic process, but in the absence of molecular oxygen, other oxidized substances can act as terminal electron acceptors to continue the degradation (Claypool and Kaplan, 1974). The bacterial group, methanogens, performs this anaerobic breakdown through two primary metabolic pathways, i.e. via reduction of carbon dioxide (respiratory processes) and fermentation of acetate (Claypool and Kvenvolden, 1983; Whiticar

et al., 1986). These methanogens can form methane from a limited number of substrates, the most important of which are $CO_2 + H_2$, acetate, formate, methanol and methylamines. The relative importance of $CO_2 + H_2$ vs. acetate as substrate for methanogenesis depends on the environmental conditions. In deeper water marine sediments, the evidence favors CO_2 reduction as the dominant pathway where acetate fermentation is an energetically less favorable process (Claypool and Kvenvolden, 1983).

Many species of methanogens can generate methane by CO_2 (present in dissolved form as HCO_3^-) reduction, with the following reaction pathway (Floodgate and Judd, 1992)

$$CO_2 + H_2O \longrightarrow HCO_3^- + H^+$$

$$HCO_3^- + H^+ + 4H_2 \longrightarrow CH_4 + 3H_2O$$

Formate is also metabolized by most methanogens, first being oxidized to carbon dioxide and hydrogen, followed by the reduction of CO_2 to methane. When acetate is the substrate, methane comes from the reduction of the methyl group, releasing carbon dioxide from the carboxyl end.

It was stated earlier that a variety of bacterial populations can metabolize the organic substrate using different electron acceptors. When two or more types of organisms compete for the same substrate supply, the one deriving the greatest metabolic energy will dominate. Bacterial populations utilizing dissolved sulfate as their electron acceptor can compete so favorably with CO_2 reducing bacteria

that methane production can be inhibited in the presence of dissolved sulfate ions. This creates a succession of microbial ecosystems, each characterized by their dominant form of respiratory metabolism. The main zones that result from this succession are:

Aerobic zone : Utilizes molecular oxygen as the electron acceptor, lying at the top layer of the sediments and is usually a few millimeters thick.

Anaerobic sulfate reduction zone (SRZ) : Dissolved sulfate is used for oxidation and can be tens of meters in thickness.

Anaerobic methane producing zone : Lies below the SRZ and contains the microbially derived methane using dissolved carbonate for metabolism. The boundary between the overlying SRZ is marked by the sulfate-methane interface (SMI), where the methane concentration goes to zero due to oxidation by sulfate.

Due to this zonation, methane can only be present below the SRZ and consequently hydrate cannot accumulate in the topmost sediment layers corresponding to the first two zones.

5.3 Organic Material Balance for in situ Production

The amount of organic carbon available to methanogens (α) is expressed as a mass fraction of total sediment. We note that represents only a fraction of the total organic carbon (TOC) because not all can be converted to methane. The following

assumptions are also made:

- sedimentation rate and the amount of degradable organic carbon at the seafloor (α_0) remain constant over time;
- microbial methanogenesis begins at the seafloor;
- solid organic material advects with sediment velocity v_s;
- sediment density is not altered by microbial degradation of organic carbon.

The first two assumptions warrant brief discussion. Constant sedimentation rate and organic carbon supply are not valid over geologic time-scales. This issue is addressed later. A sulfate reduction zone (SRZ) is present in shallow sediment above all gas hydrate systems examined to date (Borowski et al., 1999). The SRZ reduces the amount of TOC available for methanogenesis. More crucially, sulfate in pore water severely curtails methane production. Consequently, inclusion of the SRZ in our model shifts the zero methane boundary condition below the seafloor, often by 5-20 meters, but only causes a small change in average hydrate saturation. We therefore neglect the SRZ in the model and simulations presented in this chapter. However, the utility of the depth of SRZ as a proxy for predicting gas hydrate saturation is discussed in detail in Chapters 7 and 8.

With the above assumptions, the material balance for degradable organic carbon in one-dimension is (Berner, 1980; Davie and Buffett, 2001):

$$\frac{\partial}{\partial t}\left(\rho_s \alpha (1-\phi)\right) + \frac{\partial}{\partial z}\left(\rho_s v_s (1-\phi)\alpha\right) = -\rho_s \lambda \alpha (1-\phi) \tag{5.1}$$

where v_s is the sediment velocity, and λ is the first-order rate constant.

The initial condition and boundary condition for this system are

$$I.C. : \quad \alpha(z,0) = 0 \tag{5.2}$$

$$B.C. : \quad \alpha(0,t) = \alpha_0 \tag{5.3}$$

The equations and variables are now rewritten in dimensionless form to reduce the number of parameters describing the system. Defining dimensionless groups also helps to distinguish gas hydrate systems into separate categories, such as diffusion- or advection-dominated. The characteristic length of a gas hydrate system is better represented by the thickness of the GHSZ (L_t), rather than the length-scale used in the sedimentation-compaction model. This depth, L_t, can be used to normalize the vertical depth in equation (5.1):

$$\tilde{z} = \frac{z}{L_t} \tag{5.4}$$

Further, the material balance can be written in terms of sediment and fluid fluxes instead of velocities. The degradable content of organic matter in the sediments is normalized with respect to its initial concentration at the seafloor (α_0). Time is non-dimensionalized by a combination of L_t and the methane diffusivity (D_m). The sediment flux (U_s) is non-dimensionalized with respect to the fluid flux caused by sedimentation ($U_{f,sed}$), which causes it to be equal to a constant, γ. The resulting non-dimensional variables are expressed as follows:

$$\tilde{\alpha} = \frac{\alpha}{\alpha_o} \tag{5.5}$$

$$\tilde{t} = \frac{t}{L_t^2/D_m} \tag{5.6}$$

$$\tilde{U}_s = \frac{U_s}{U_{f,sed}} = \frac{\dot{S}(1-\phi_0)}{U_{f,sed}} = \frac{\left(\frac{1-\phi_\infty}{\phi_\infty}\right) U_{f,sed}}{U_{f,sed}} = \frac{1-\phi_\infty}{\phi_\infty} = \gamma \tag{5.7}$$

The following important dimensionless groups can also be defined:

$$\mathrm{Da} = \frac{\lambda L_t^2}{D_m} \tag{5.8}$$

$$\mathrm{Pe}_1 = \frac{U_{f,sed} L_t}{D_m} \tag{5.9}$$

The Damkohler number (Da) represents the ratio of methanogenesis rate to methane diffusion. Higher values of Da imply higher methane production and/or lower methane diffusivity. The first Peclet number (Pe_1) is the ratio of fluid advection to methane diffusion. The fluid flux used in defining Pe_1 denotes the contribution from sedimentation-compaction effects and will be supplemented by a second Peclet number, defined later, that will quantify the effect of upward external flow from deeper sources.

Using these dimensionless scalings, the organic mass balance (5.1) can be rewritten as:

$$\frac{\partial}{\partial \tilde{t}}\left(\tilde{\alpha}(\gamma-\tilde{\phi})\right)+\mathrm{Pe}_1\frac{\partial}{\partial \tilde{z}}\left(\frac{1+\gamma}{\gamma}\tilde{U}_s\tilde{\alpha}\right)=-\mathrm{Da}(1-\tilde{\phi})\tilde{\alpha} \tag{5.10}$$

The initial and boundary conditions for the dimensionless organic material balance are:

$$I.C.\ :\quad \tilde{\alpha}(\tilde{z},0)=0 \tag{5.11}$$

$$B.C.\ :\quad \tilde{\alpha}(0,\tilde{t})=1 \tag{5.12}$$

The porosity equation (4.14) was non-dimensionalized by a characteristic length L_ϕ, whereas the organic material balance equation (5.10) uses the GHSZ as a characteristic length. To use the same expression for porosity in the organic balance equation, we have to define another dimensionless group ($N_{t\phi}$) which is the ratio of these two characteristic lengths:

$$N_{t\phi}=\frac{L_t}{L_\phi} \tag{5.13}$$

The new porosity relation becomes:

$$\tilde{\phi}=\frac{\eta}{\eta+(1-\eta)e^{N_{t\phi}\tilde{z}}} \tag{5.14}$$

5.4 Methane Balance and Gas Hydrate Formation

We now develop equations for simulating gas hydrate and free gas accumulation at thermodynamic equilibrium by imposing methane solubility curves on methane concentration profiles. The basic assumption is that gas hydrate accumulates when dissolved methane concentration exceeds local solubility. In making this assumption, though, it is worth commenting on the morphology and local distribution of gas hydrate within marine sediments. Macroscopic specimens ($>$1 cm) of gas hydrate have been recovered from drill cores in many locations (Kvenvolden, 1993; Paull et al., 1996; Tréhu et al., 2003). However, analyses of pore water chemistry, sediment temperature and downhole logs suggest that most gas hydrate in marine sediment is disseminated between sediment grains, especially in systems where diffusion dominates, but that it dissociates during core recovery (Paull et al., 1996; Tréhu et al., 2003). We assume in our model that gas hydrate is disseminated within pore space and does not deform surrounding sediments.

The following assumptions are made in formulating the methane material balance:

- dissolved methane does not alter the fluid density, ρ_f;
- a sulfate reduction zone is not present;
- mass fraction of water in aqueous phase is unity due to low solubility of methane in pore water;
- hydrate and free gas phases move with sediment velocity, v_s;

- water density is the same in gas hydrate and aqueous phases;
- free gas phase contains no water.

We denote methane mass fraction in pore fluid by c_m^w, in hydrate phase by c_m^h and in gas phase by c_m^g. The three-phase material balance can be written in one-dimension as:

$$\frac{\partial}{\partial t}\left[\phi(1-S_h-S_g)c_m^w\rho_f+\phi S_h c_m^h\rho_h+\phi S_g c_m^g\rho_g\right]+\frac{\partial}{\partial z}\Big[U_f c_m^w\rho_f+U_s\frac{\phi}{1-\phi}S_h c_m^h\rho_h$$
$$+U_s\frac{\phi}{1-\phi}S_g c_m^g\rho_g\Big]=\frac{\partial}{\partial z}\left[\phi(1-S_h-S_g)D_m\rho_f\frac{\partial c_m^w}{\partial z}\right]+\frac{M_{CH_4}}{M_{org}}\rho_s\lambda\alpha_o(1-\phi)\tilde{\alpha} \quad (5.15)$$

where ρ_f, ρ_h and ρ_g are densities of the water, gas hydrate and free gas, respectively, S_h is the hydrate saturation in the pore space, S_g is the free gas saturation in the pore space, and M_{CH_4} and M_{org} are the molecular weights of methane and organic matter, respectively. The first expression on the left side gives the rate of accumulation of methane in the aqueous, gas hydrate and free gas phases. The second term on the left side represents the flux of methane in the aqueous, gas hydrate and free gas phases. The first term on the right side characterizes the diffusion of methane in the pore fluid. The last term corresponds to the generation of methane through the first-order organic reaction, and couples the methane mass balance to the organic mass balance in equation (5.10).

An initial condition and two boundary conditions are required to solve this partial differential equation. We specify zero initial methane concentration in the pore fluid, consistent with zero initial organic matter in sediment. A Dirichlet bound-

ary condition corresponding to zero methane concentration at the seafloor is used along with a Neumann boundary condition of zero diffusive flux of methane at the bottom of the model (depth D). These conditions can be written as:

$$I.C. \; : \quad c_m^w(z,0) = 0 \tag{5.16}$$

$$B.C.(1) \; : \quad c_m^w(0,t) = 0 \tag{5.17}$$

$$B.C.(2) \; : \quad \frac{\partial c_m^w}{\partial z}(D,t) = 0 \tag{5.18}$$

We non-dimensionalize equation (5.15) using the same dimensionless groups and scalings for depth, organic content and time as defined previously (equations 5.4-5.6). The methane mass fractions in the pore fluid (c_m^w), gas hydrate (c_m^h) and free gas phase (c_m^g) are normalized with the methane solubility at the base of the GHSZ. This value, denoted by $c_{m,eqb}^w$, is calculated from the phase equilibrium results for a given seafloor depth, temperature, geothermal gradient and pore water salinity. The scaled methane mass fractions are defined as:

$$\tilde{c}_m^w = \frac{c_m^w}{c_{m,eqb}^w} \quad , \quad \tilde{c}_m^h = \frac{c_m^h}{c_{m,eqb}^w} \quad , \quad \tilde{c}_m^g = \frac{c_m^g}{c_{m,eqb}^w} \tag{5.19}$$

The dimensionless form of the three-phase methane balance can be written as:

$$\frac{\partial}{\partial \tilde{t}}\left[\frac{1+\gamma\tilde{\phi}}{\gamma}\left((1-S_h-S_g)\tilde{c}_m^w + S_h\tilde{c}_m^h\tilde{\rho}_h + S_g\tilde{c}_m^g\tilde{\rho}_g\right)\right]$$
$$+\frac{1+\gamma}{\gamma}\frac{\partial}{\partial \tilde{z}}\Big[\left(\mathrm{Pe}_1 + |\mathrm{Pe}_2|\right)\tilde{U}_f\tilde{c}_m^w + \mathrm{Pe}_1\tilde{U}_s\frac{1+\gamma\tilde{\phi}}{\gamma\left(1-\tilde{\phi}\right)}(S_h$$

$$\tilde{c}_m^h \tilde{\rho}_h + S_g \tilde{c}_m^g \tilde{\rho}_g)\Big] = \frac{\partial}{\partial \tilde{z}} \left[\frac{1+\gamma\tilde{\phi}}{\gamma} S_w \frac{\partial \tilde{c}_m^w}{\partial \tilde{z}} \right] + \left(\frac{M_{CH_4}\rho_s}{M_{org}\rho_f} \right) \beta \mathrm{Da}(1-\tilde{\phi})\tilde{\alpha} \tag{5.20}$$

where Pe_2 is defined in the next section, $\tilde{\rho}_h$ is the ratio of hydrate to fluid density, $\tilde{\rho}_h$ is the ratio of free gas and fluid density, and β is the normalized initial organic carbon content at the time of deposition, defined as:

$$\tilde{\rho}_h = \frac{\rho_h}{\rho_f} \quad , \quad \tilde{\rho}_g = \frac{\rho_g}{\rho_f} \tag{5.21}$$

$$\beta = \frac{\alpha_o}{c^l_{m,eqb}} \tag{5.22}$$

The values of c_m^h and $\tilde{\rho}_h$ are assumed to be constant and equal to 0.134 and 0.9, respectively (Sloan and Koh, 2007; Davie and Buffett, 2001). Free gas density ($\tilde{\rho}_g$) is computed from the ideal gas law. Molecular weights M_{CH_4} and M_{org} are taken to be 16 and 30, respectively, while the ratio (ρ_s/ρ_f) is set to 2.65/1.03 = 2.57. The dimensionless initial and boundary conditions become:

$$I.C. \ : \quad \tilde{c}_m^w(\tilde{z},0) = 0 \tag{5.23}$$

$$B.C.(1) \ : \quad \tilde{c}_m^w(0,\tilde{t}) = 0 \tag{5.24}$$

$$B.C.(2) \ : \quad \frac{\partial \tilde{c}_m^w}{\partial \tilde{z}}(D,\tilde{t}) = 0 \tag{5.25}$$

5.4.1 External Upward Fluid Flow and Water Balance

In gas hydrate settings where in situ methanogenesis provides all methane, the fluid flux will be dominated by that resulting from compaction ($U_{f,sed}$). However, to incorporate the possibility of a deep methane source, an external fluid flux is required. We thus superimpose an external flux ($U_{f,ext}$) on the flux caused by compaction ($U_{f,sed}$) to get a total flux (U_f), as described by Davie and Buffett (2003b):

$$U_f = U_{f,sed} + U_{ext} \tag{5.26}$$

Since the depth variable is taken to be positive downwards, the flux due to sedimentation remains positive. However, the external flux $U_{f,ext}$ is directed upwards and will have a negative value. If $U_{f,ext}$ exceeds $U_{f,sed}$ in magnitude, the net flux will be negative, and fluid flow will be toward the seafloor. Alternatively, if the magnitude of $U_{f,ext}$ is less than $U_{f,sed}$, the net flux will be positive and fluid flow will be down. In case of equal magnitudes, U_f will be zero and methane transport will occur through diffusion only.

The total fluid flux is used as a boundary condition when solving the water mass balance, which can be written as:

$$\frac{\partial}{\partial t}\left[\phi S_w c_w^w \rho_f + \phi S_h c_w^h \rho_h\right] + \frac{\partial}{\partial z}\left[U_f c_w^w \rho_f + U_s \frac{\phi}{1-\phi} S_h c_w^h \rho_h\right] = 0 \tag{5.27}$$

where c_w^w and c_w^h are water mass fractions in the aqueous and hydrate phases, respectively, and S_w is water saturation ($S_w = 1 - S_h - S_g$). The assumption of small

methane solubility in water makes c_w^w approximately equal to unity. Further, the assumption of constant water density in the aqueous and hydrate phases makes the term $\left[\phi S_w c_w^w \rho_f + \phi S_h c_w^h \rho_h\right]$ invariant over time and drives the first term on the left side of equation (5.27) to zero. This assumption helps to decouple the water and methane mass balances, so that they do not have to be solved simultaneously. Equation (5.27) can be rewritten as:

$$\frac{\partial}{\partial z}\left[U_f + U_s \frac{\phi}{1-\phi} S_h c_w^h \tilde{\rho}_h\right] = 0 \Longrightarrow U_f + U_s \frac{\phi}{1-\phi} S_h c_w^h \tilde{\rho}_h = \text{const} \tag{5.28}$$

As long as no hydrate forms in the system, the flux of water in the aqueous phase is constant and equal to the total fluid flux. Once hydrate starts to accumulate in pore space, water moves into the hydrate phase and the flux of water in the aqueous phase decreases. We make use of the total flux at $\tilde{z} = 0$ as a boundary condition by rewriting equation (5.28) as:

$$U_f + U_s \frac{\phi}{1-\phi} S_h c_w^h \tilde{\rho}_h = \left(U_f + U_s \frac{\phi}{1-\phi} S_h c_w^h \tilde{\rho}_h\right)_{\tilde{z}=0} \tag{5.29}$$

The hydrate saturation at $\tilde{z} = 0$ is always zero due to the boundary condition on dissolved methane (equation 5.23). This enables us to rewrite equation (5.29) as:

$$U_f + U_s \frac{\phi}{1-\phi} S_h c_w^h \tilde{\rho}_h = (U_f)_{\tilde{z}=0} = U_{f,sed} + U_{f,ext} \tag{5.30}$$

which can be rearranged to:

$$U_f = U_{f,sed} + U_{f,ext} - U_s \frac{\phi}{1-\phi} S_h c_w^h \tilde{\rho}_h \tag{5.31}$$

To develop the most general model applicable for all cases, such as zero sedimentation, zero external flux or zero net flux ($|U_{f,sed}| = |U_{f,ext}|$), we normalize equation (5.31) by the sum ($U_{f,sed} + |U_{f,ext}|$). Equation (5.31) can then be cast as:

$$\tilde{U}_f = \frac{U_f}{U_{f,sed} + |U_{f,ext}|} = \frac{U_{f,sed} + U_{f,ext}}{U_{f,sed} + |U_{f,ext}|} - \frac{U_s}{U_{f,sed} + |U_{f,ext}|} \frac{\phi}{1-\phi} S_h c_w^h \tilde{\rho}_h \tag{5.32}$$

Multiplying numerators and denominators by the term (L_t/D_m), and making use of the definition of Peclet numbers, the fluid flux in dimensionless form is given by:

$$\tilde{U}_f = \left[\frac{\mathrm{Pe}_1 + \mathrm{Pe}_2}{\mathrm{Pe}_1 + |\mathrm{Pe}_2|}\right] - \frac{\mathrm{Pe}_1 \tilde{U}_s}{\mathrm{Pe}_1 + |\mathrm{Pe}_2|} \frac{(1+\gamma\tilde{\phi})}{\gamma(1-\tilde{\phi})} S_h c_w^h \tilde{\rho}_h \tag{5.33}$$

$$\mathrm{Pe}_2 = \frac{U_{f,ext} L_t}{D_m} \tag{5.34}$$

where Pe_2 is a second Peclet number corresponding to the ratio of external flux to diffusion. Thus, our numerical model has two independent Peclet numbers that characterize the compaction-driven and external fluxes with respect to methane diffusion. Importantly, Pe_1 will be positive, whereas Pe_2 will be negative so that fluid flux due to sedimentation dominates when $|\mathrm{Pe}_2| < |\mathrm{Pe}_1|$ and external flux dominates when $|\mathrm{Pe}_2| > |\mathrm{Pe}_1|$. For cases where external fluid flux dominates, the methane concentration in rising fluids needs specification. This methane concen-

tration, denoted by $c^w_{m,ext}$, is imposed as a Dirichlet boundary condition at the bottom of the domain, replacing the Neumann boundary condition in equation (5.25). It is normalized as:

$$\tilde{c}^w_{m,ext} = \frac{c^w_{m,ext}}{c^w_{m,eqb}} \tag{5.35}$$

$$B.C.(2) \; : \; \tilde{c}^w_m(D, \tilde{t}) = \tilde{c}^w_{m,ext} \tag{5.36}$$

5.5 Numerical Solution

5.5.1 Organic Carbon Balance

We first show the evolution of organic content within sediments (Figure 5.1) by numerically solving the organic mass balance (equation 5.10). This hyperbolic partial differential equation can be solved independently of the methane material balance (equation 5.20). We compute the numerical solution in conservative form using an implicit block-centered, finite-difference scheme. A single-point upstream weighting was used for the advection term. All results shown henceforth are for the following parameters: $\eta = 6/9$, $\gamma = 9$, $N_{t\phi} = 1$. These values correspond to seafloor porosity $\phi_0 = 0.7$ and minimum porosity $\phi_\infty = 0.1$.

The profile of available organic matter in sediment depends on the ratio $\mathrm{Pe}_1/\mathrm{Da}$, which given above (equations 5.8 and 5.9), signifies the ratio of sedimentation to methanogenesis. In general, the organic content decreases with depth because of microbial decomposition during burial (Figure 5.1). Moreover, as the ratio $\mathrm{Pe}_1/\mathrm{Da}$ increases, sedimentation increases with respect to methanogenesis, which means

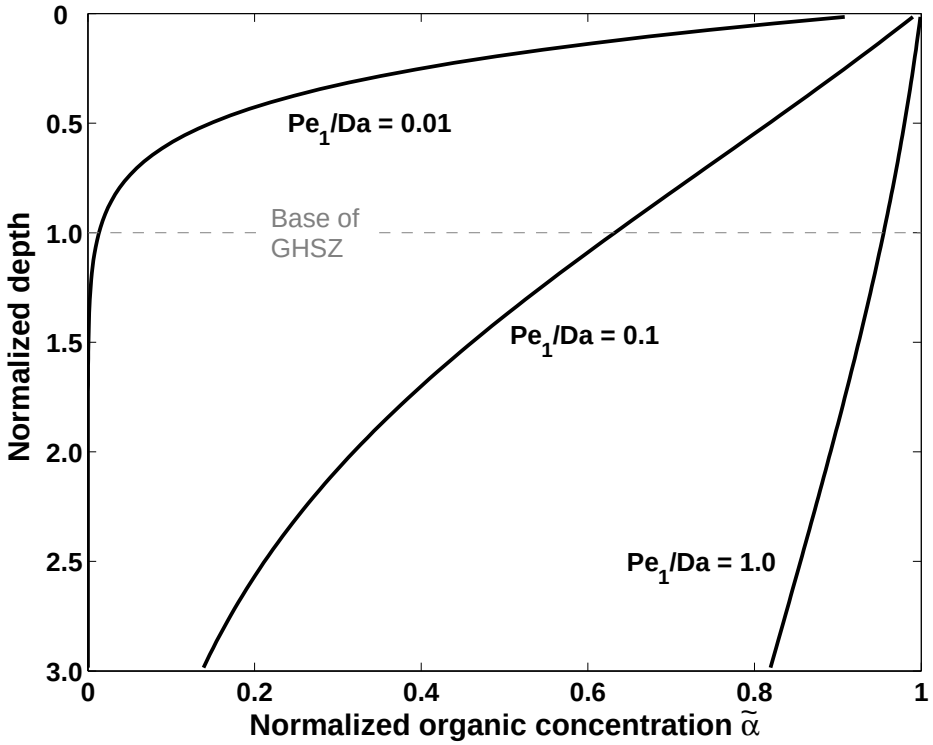

Figure 5.1: Normalized organic concentration profiles at steady-state as a function of the ratio $\mathrm{Pe}_1/\mathrm{Da}$. Lower values of $\mathrm{Pe}_1/\mathrm{Da}$ lead to lesser organic content leaving the GHSZ, resulting in higher methane generation within the GHSZ.

a higher carbon input at the seafloor or a lower reaction rate. Solid organic carbon available for methanogenesis reaches greater sediment depths with higher $\mathrm{Pe}_1/\mathrm{Da}$.

5.5.2 Methane Mass Balance

To simulate gas hydrate accumulation in marine sediment, mass balances for methane and water are solved numerically. The solution to the methane balance partial differential equation (5.20) is computed in finite-difference form after updating the organic content profile in time. Solution of the equations in conservative form ensures that there are no local material balance errors (all simulations had

material balance errors less than 10^{-12}).

The methane mass balance equation contains three unknowns: $\tilde{c}_m^w$, S_h and S_g, which must be solved at each time step. This apparently under-determined system can be solved, however, by realizing that all three cannot be the primary dependent variable at any given time. As long as the methane concentration in pore fluid is lower than the local solubility, $\tilde{c}_m^w$ is the primary variable and the saturations S_h and S_g are zero. Once dissolved methane exceeds solubility conditions within the GHSZ, $\tilde{c}_m^w$ is set equal to the solubility, and excess methane goes into the hydrate phase. In this case, S_g is set to zero, and S_h becomes the primary dependent variable. Alternatively, when dissolved methane exceeds solubility conditions below the GHSZ, $\tilde{c}_m^w$ is again set equal to the solubility, but excess methane goes into free gas. In this case, S_h is set equal to zero, and S_g becomes the primary dependent variable. Importantly, any gas hydrate crossing the base of GHSZ dissociates to dissolved methane, which can become free gas provided pore fluid is already saturated with methane. These checks for switching among $\tilde{c}_m^w$, S_h and S_g as the primary dependent variable are done at each grid-block for each time-step of the simulations.

5.6 Results and Discussion

5.6.1 In situ Methanogenesis

The simplest case of methane accumulation to consider is in situ methane generation with no external fluid flux. Transient profiles of dissolved methane concen-

tration and gas hydrate and free gas saturation can be obtained from numerical simulations (Figure 5.2). Most simulations reach steady-state within 2-3 units of dimensionless time ($\tilde{t}$). For $L_t \approx 450$ mbsf (similar to Blake Ridge; (Paull et al., 1996)) and $D_m = 10^{-9}$ m2/s (Davie and Buffett, 2001), steady-state is achieved within approximately 12 Myr. This residence time is similar to that predicted from other mass balance calculations (Davie and Buffett, 2001; Dickens, 2003).

Simulations (Figure 5.2) follow a common path toward steady state. Initially, there is no gas hydrate in pore space because dissolved methane concentrations are less than local solubility. When methane concentrations reach the solubility curve, gas hydrate starts to precipitate. With additional methane supply and sediment burial, the fraction of gas hydrate in sediment increases, and the lowermost occurrence of gas hydrate progressively moves down. In most cases, gas hydrate, when formed, reaches the base of the GHSZ at steady-state. Gas hydrate dissociates upon crossing this horizon, generating free gas. Hence, at steady-state there is a free gas layer immediately below gas hydrate (Davie and Buffett, 2001).

For both transient and steady-state simulations, a series of gas zones can exist (Figure 5.2): an uppermost zone with dissolved methane; an intermediate zone with dissolved methane and gas hydrate; and a lower zone with dissolved methane and free gas. However, the presence and thickness of these gas zones can vary. A more interesting case occurs with a modest reduction in the initial organic content of the sediments (β). At relatively low β, depending on values for other parameters, a steady-state can develop where gas hydrate does not extend to the base of the GHSZ, and free gas does not form below the GHSZ (Figure 5.3). Essentially,

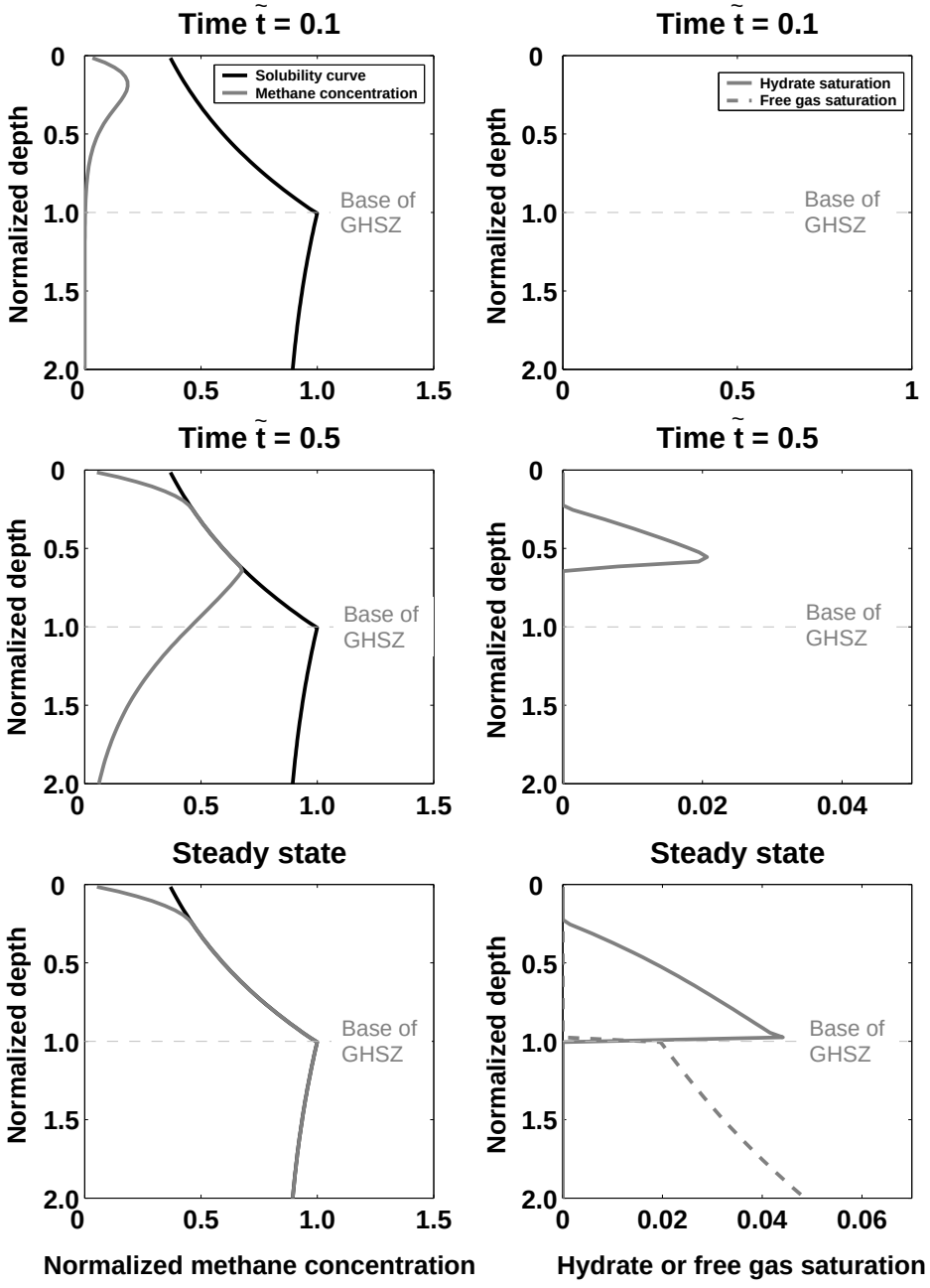

Figure 5.2: Simulations showing the time evolution of the dissolved methane concentration (left column) and the gas hydrate and free gas saturation in the sediments (right column). The results shown above are for methane generated from biogenic in situ sources only. A finite gas hydrate layer along with a free gas layer exists at steady state. The following model parameters were used for this simulation: $\mathrm{Pe}_1 = 0.1$, $\mathrm{Da} = 10$, $\beta = 3$, $\mathrm{Pe}_2 = 0$, $\eta = 6/9$, $\gamma = 9$. The seafloor parameters used are for the Blake Ridge area: Seafloor depth = 2700 m, seafloor temperature = 3°C and geothermal gradient = 0.04°C /m. We refer to these seafloor parameters as the base-case values.

methane concentrations are less than the solubility curve starting at some depth above the base of the GHSZ.

Xu and Ruppel (1999) have suggested that this case arises when methane supply from depth does not exceed a critical flux. Our simulations show that this situation can also occur when modest organic carbon input does not furnish enough methane to saturate pore waters. Hence, in case of in situ methanogenesis, a critical β has to be exceeded, analogous to the critical flux defined by Xu and Ruppel (1999), for hydrate and gas to coexist at the base of GHSZ.

5.6.2 Upward Methane Flux

Gas hydrate accumulation can also be simulated for systems where all methane is supplied from deeper sources and β is zero (Figure 5.4). As seen from transient profiles, methane enters the system from below and forms gas hydrate within the GHSZ when methane concentrations exceed solubility conditions. The gas hydrate layer then grows downwards because of sedimentation. At steady-state, gas hydrate extends to the base of the GHSZ and free gas forms below.

A certain minimum methane flux is required to form gas hydrate in this case. However, a critical methane flux from below is not required for gas hydrate to contact free gas at the base of the GHSZ. Assuming constant methane supply and sufficient time, once hydrate has precipitated, a gas hydrate/free gas interface will occur even at relatively low methane fluxes because sedimentation moves gas hydrate towards the base of the GHSZ. If we do not include sedimentation effects in our model by setting Pe_1 to zero, as done by Xu and Ruppel (1999), the hydrate

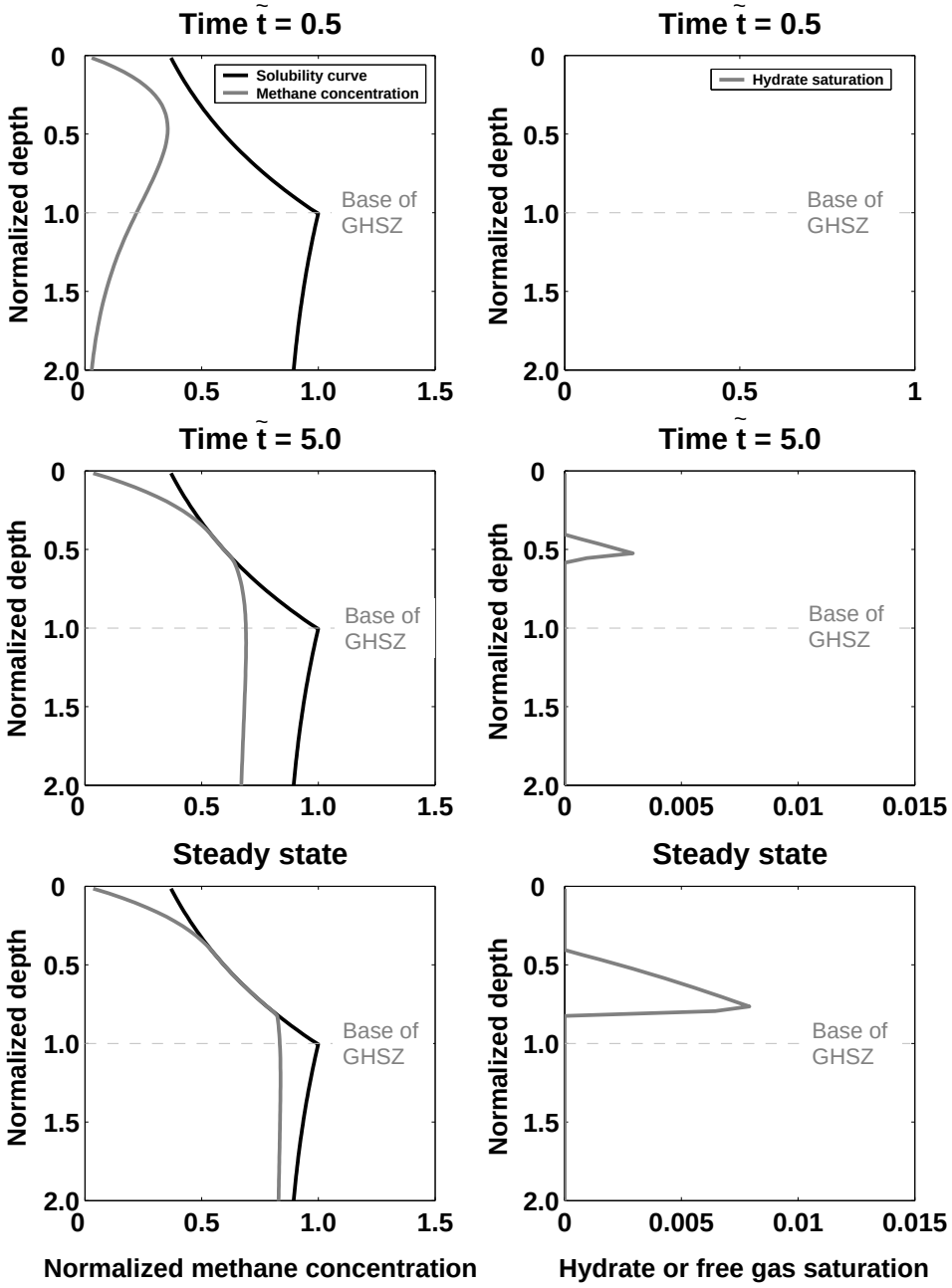

Figure 5.3: Simulations showing the time evolution of methane concentration and gas hydrate saturation (similar to Figure 5.2), except that this system has a smaller value of β, resulting in lesser carbon input. This causes an isolated hydrate layer to exist at steady state, without any free gas below. The following model parameters were used for this simulation: $\mathrm{Pe}_1 = 0.1$, $\mathrm{Da} = 10$, $\beta = 1.4$, $\mathrm{Pe}_2 = 0$, $\eta = 6/9$, $\gamma = 9$. Base-case seafloor parameters were used for this simulation.

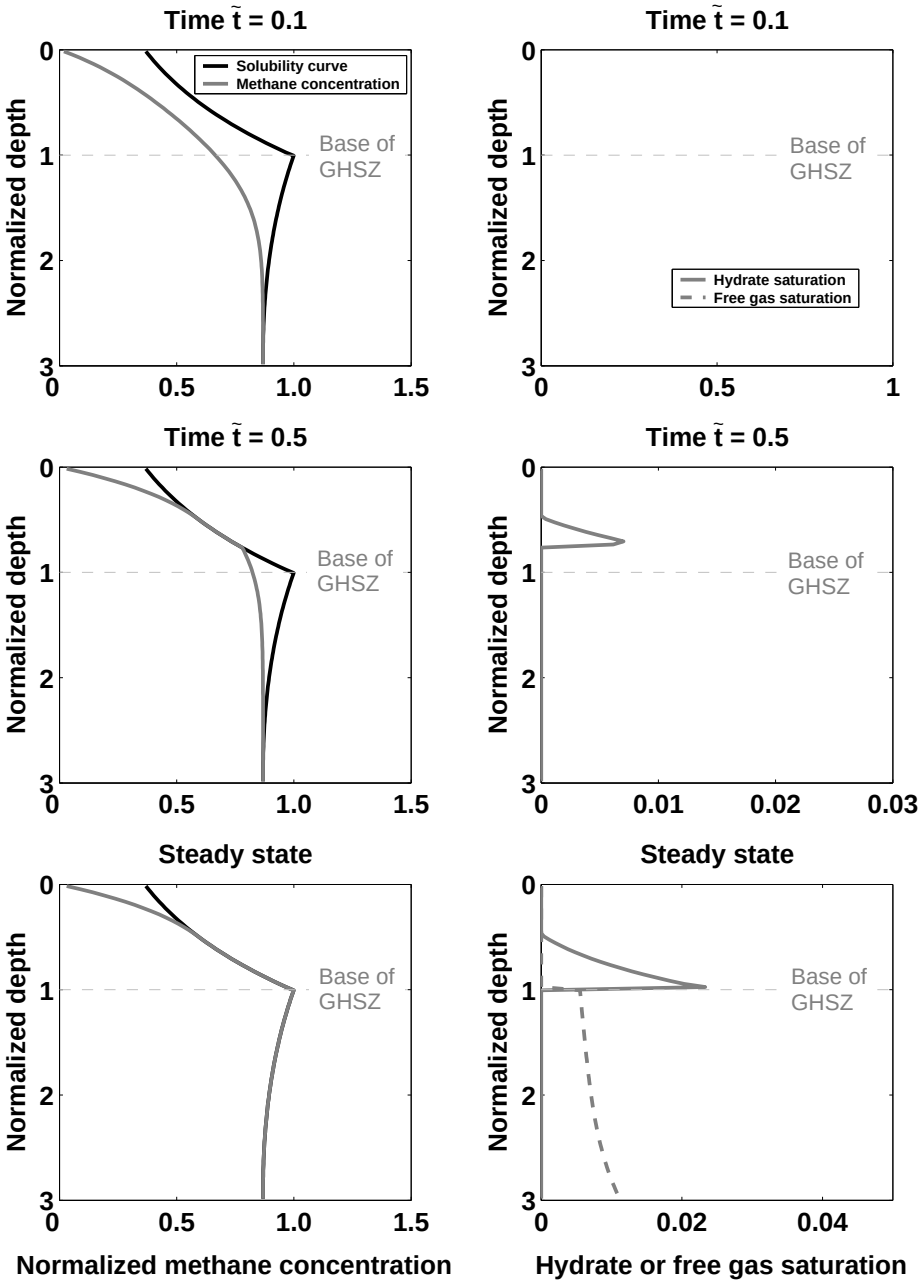

Figure 5.4: Simulations showing the time evolution of methane concentration and gas hydrate and free gas saturation (similar to Figures 5.2 and 5.3), except that the methane in this case is transported by an upward external flux from a deeper source. A gas hydrate layer exists at steady state, with free gas below. The following model parameters were used for this simulation: $\mathrm{Pe}_1 = 0.1$, $\mathrm{Da} = 0$, $\beta = 0$, $\mathrm{Pe}_2 = -2.0$, $\eta = 6/9$, $\gamma = 9$. Base-case seafloor parameters were used for this simulation.

phase becomes immobile within the sediments and we also observe the emergence of a critical flux required to bring the hydrate and free gas layers together at the base of the GHSZ (Figure 5.5). The methane solubility below the GHSZ was assumed to be constant for comparison with the results of Xu and Ruppel (1999). It can be seen that the critical flux needed for the hydrate and free gas phases to coexist at the base of the GHSZ is $\mathrm{Pe}_2 = -5$.

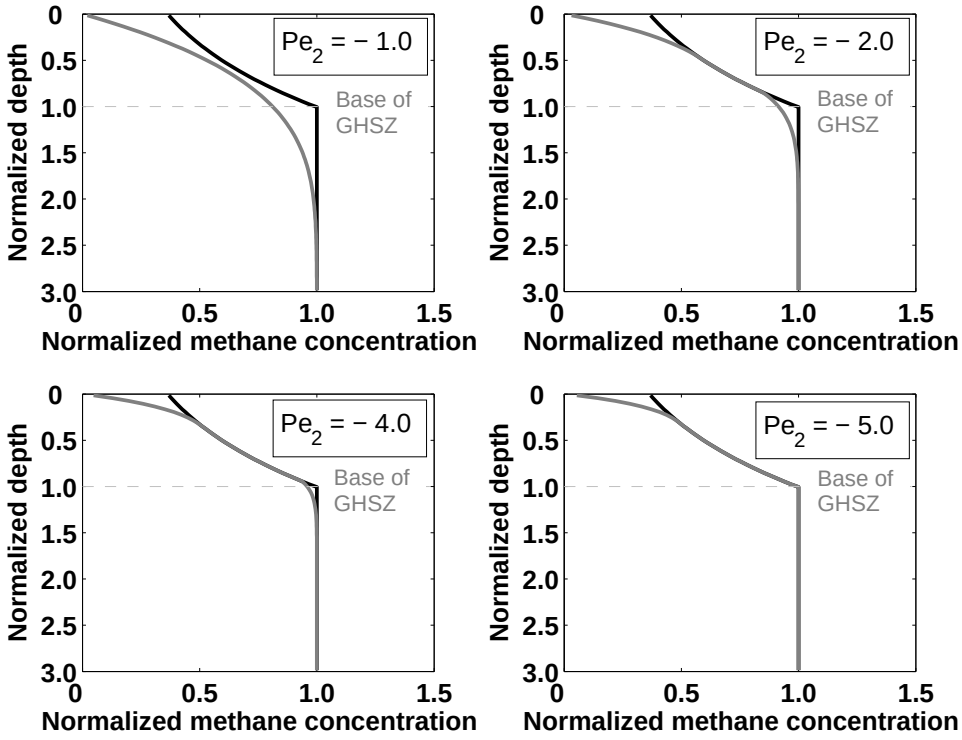

Figure 5.5: Steady state dissolved methane concentration profiles for the case of methane supplied from deeper sources and without the effect of sedimentation ($\mathrm{Pe}_1 = 0$). As Pe_2 increases in magnitude (that is, upward external flux becomes more important), the gas hydrate and free gas layers approach each other and co-exist at the base of the GHSZ only if the critical flux $\mathrm{Pe}_2 = -5$ is exceeded. Parameters used for these simulations are: $\mathrm{Pe}_1 = 0$, $\tilde{c}^w_{m,ext} = 1.0$, Pe_2 varies for the four plots. Base-case seafloor parameters were used for this simulation.

5.6.3 Combined Systems (Both Sources)

Gas hydrate systems with in situ methanogenesis providing all methane can be simulated by setting $\mathrm{Pe}_2 = 0$; those where rising fluids supply all methane can be studied by setting $\beta = 0$. Gas hydrate systems with mixed sources of methane can be simulated by assuming non-zero values of these parameters. General analysis of these systems, however, is complicated due to the large number of independent parameters. Thus, in the following two sections, we examine how changes in various parameters affect the behavior of these two end member systems.

5.6.4 Generalized Methanogenic Systems

The simulations of gas hydrate systems considered so far (Figures 5.2, 5.3 and 5.4) pertain to particular sets of parameter values. To obtain a more general understanding, numerous simulations can be performed for a range of parameters. For systems dominated by in situ methanogenesis, sensitivity analyses reveal that Pe_1, Da and β dominantly affect the distribution of gas hydrate and free gas (Davie and Buffett, 2001; Buffett and Archer, 2004).

If Da is constant, the general distribution of hydrate at steady-state in terms of β and Pe_1 can be divided into three fields (Figure 5.6). These fields define conditions where gas hydrate will occur, and with or without free gas at the base of the GHSZ. Paths can be followed across the fields to understand how parameters affect gas hydrate systems. For example, consider a path of constant Pe_1 (Figure 5.6): there is no gas hydrate at low β, gas hydrate without underlying free gas at

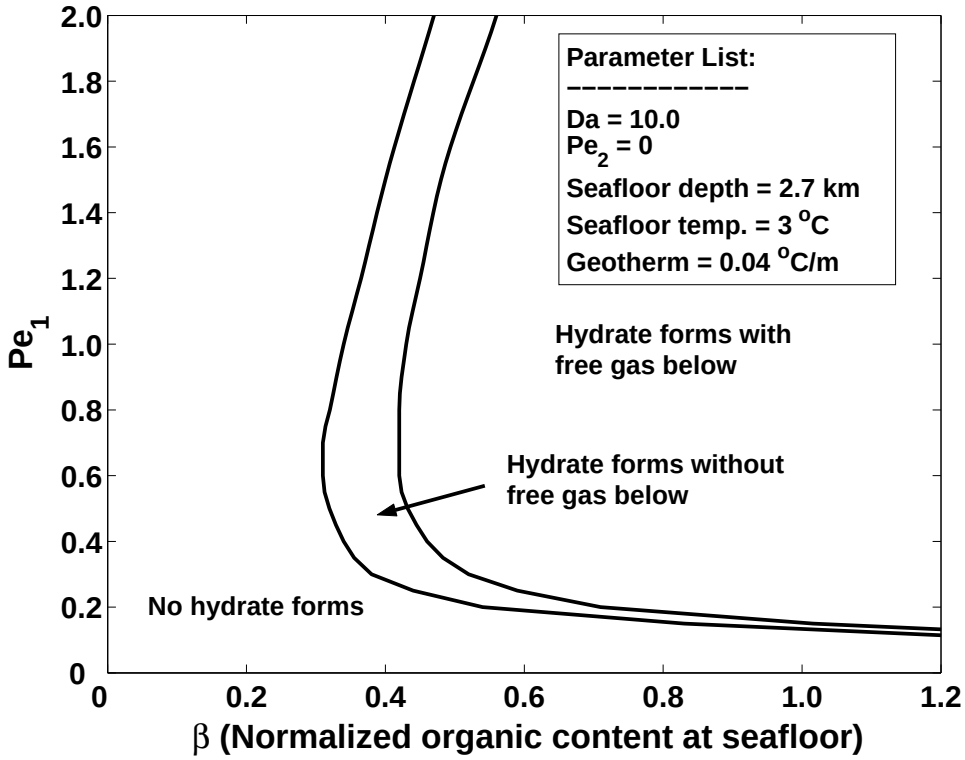

Figure 5.6: Parameter space of Pe_1 and β showing three different fields of gas hydrate distribution. As β increases, with Pe_1 held constant, the system moves from the state of no gas hydrate to gas hydrate without free gas below and finally to gas hydrate with free gas below.

intermediate β, and gas hydrate with free gas below the GHSZ at high β. The separation of these three fields at relatively low Pe_1 can be understood by realizing that, at low Pe_1, the system is dominated by high rates of diffusion, which causes loss of methane from the seafloor. To compensate for this loss, the burial of organic carbon at the seafloor and production of methane has to increase to accumulate gas hydrates.

As Pe_1 increases, one might expect gas hydrates to form at progressively lower values of β. However, this inverse relationship does not occur when Pe_1 exceeds

about 0.6. Instead, the system requires more organic carbon (higher β) to form gas hydrates (Figure 5.6). This effect results from the increase in sediment velocity associated with the increase in Pe_1. Essentially, organic carbon moves through the GHSZ faster, and because the Damkohler number is fixed, greater amounts of organic carbon leave the GHSZ unreacted (Figure 5.1).

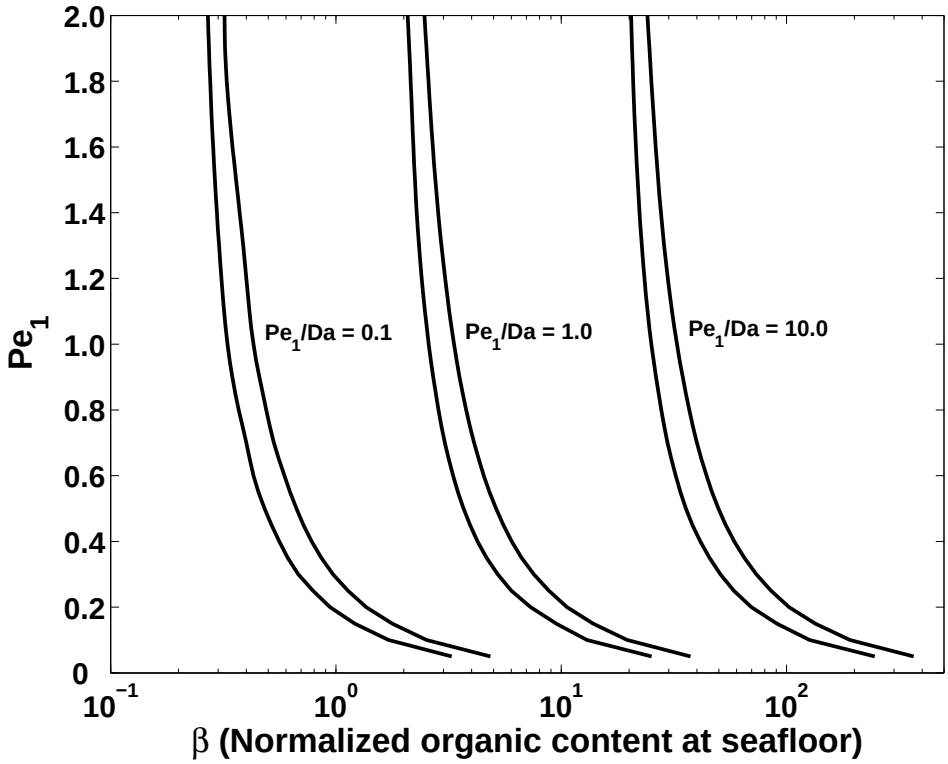

Figure 5.7: Different gas hydrate regimes simulated for various ratios of $\mathrm{Pe}_1/\mathrm{Da}$. The region to the left of each pair of curves represents no gas hydrate formation, the narrow central region bounds the part where gas hydrate occurs without free gas below, and to the right of each pair is the region where gas hydrates occur with free gas below. Base-case seafloor parameters were used for this simulation and $\mathrm{Pe}_2 = 0$.

The relationship between Pe_1, β and Da can be explored further by realizing that the ratio $\mathrm{Pe}_1/\mathrm{Da}$ controls organic decay and subsequent methane generation.

Instead of keeping Da constant, therefore, the three distinct regions of gas hydrate distribution can be examined for constant $\mathrm{Pe}_1/\mathrm{Da}$ (Figure 5.7). Again, there are three regions: there is a region of no hydrate formation at low β, a narrow central region of hydrate without associated free gas at moderate β, and a region corresponding to hydrate with free gas below at high β. This representation serves two purposes. First, curves representing gas hydrate formation and accumulation steadily decrease in Pe_1 as β gradually increases. The parameter space is, therefore, divided into two main regions: diffusion dominated at low Pe_1 and advection dominated at higher Pe_1. Second, the dependence of hydrate distribution on the Damkohler number can be included in the results explicitly.

Ideally, single plots can summarize the dependence of gas hydrate systems upon all relevant parameters. For in situ methanogenesis, this can be achieved by realizing that each set of curves (Figure 5.7) represents different amounts of organic carbon conversion; that is, the quantity that binds different curves together is the net amount of methane generated within the GHSZ. At steady-state, this quantity can be obtained from the normalized organic content at the base of the GHSZ. The analytical solution to the organic mass balance equation (equation 5.10, at $\tilde{z} = 1$) is:

$$\tilde{\alpha}|_{\tilde{z}=1} = \left[\eta + (1-\eta)e^{N_{t\phi}}\right]^{\frac{-1}{N_{t\phi}(1+\gamma)\mathrm{Pe}_1/\mathrm{Da}}} \tag{5.37}$$

The net amount of methane generated within the GHSZ can be computed from this

value and the carbon input at the seafloor (β):

$$\text{Organic carbon converted within GHSZ} = (1 - \tilde{\alpha}|_{\tilde{z}=1})\beta \tag{5.38}$$

If the curves shown in Figure 5.7 for different values of $\mathrm{Pe}_1/\mathrm{Da}$ are rescaled and plotted in Figure 5.8, with the x-axis now representing the methane generated within the GHSZ (equation 5.38), we see that the different set of curves collapse into one single pair of curves. The curves in Figure 5.7 covered ratios of $\mathrm{Pe}_1/\mathrm{Da}$ that were two orders of magnitude different. We are now able to summarize the dependence of gas hydrate distribution over a wide range of the relevant parameters (Pe_1,Da,β) with just one plot. This clearly highlights the importance of scaling the system by choosing appropriate dimensionless groups and variables.

5.6.5 Generalized Deeper Methane Systems

A simple, generalized plot can also be constructed for systems where all methane derives from deeper sources. The most important parameters in this case are the methane concentration in the upward migrating fluid ($\tilde{c}^w_{m,ext}$), Pe_1 and Pe_2. Deeper methane sources come into effect only when $|\mathrm{Pe}_2| > |\mathrm{Pe}_1|$.

We first examine results for different values of Pe_2 in the parameter space of Pe_1 and $\tilde{c}^w_{m,ext}$ (Figure 5.9). As mentioned before, we do not see the emergence of a zone of gas hydrate formation without free gas below at steady-state for this type of source. Hence, there is only one curve for each value of Pe_2, which separates parameters defining no gas hydrate formation from parameters defining gas hy-

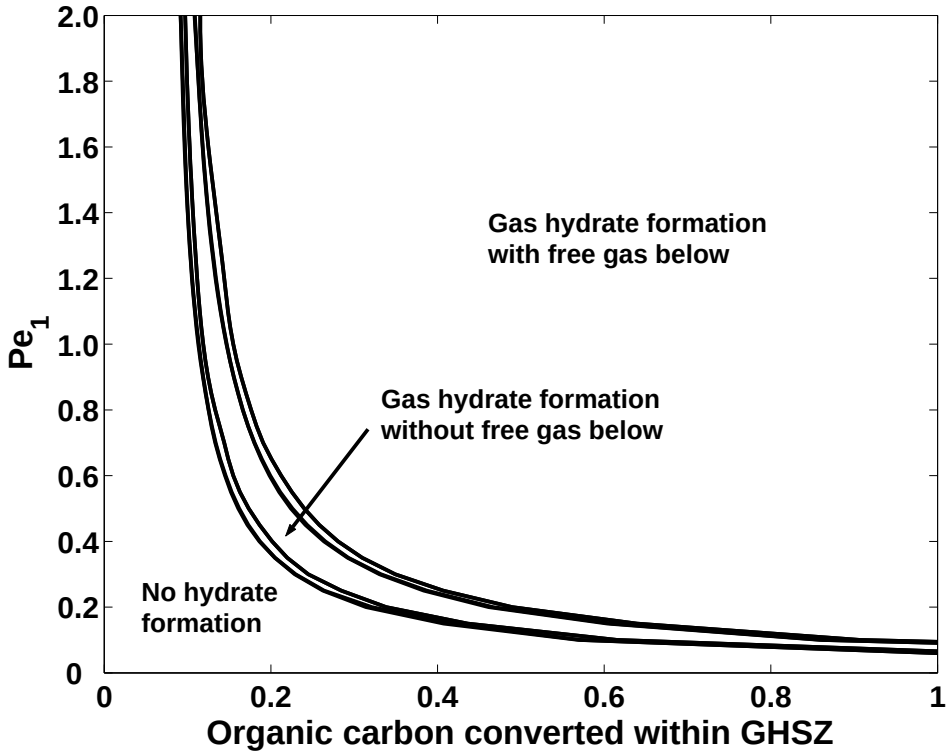

Figure 5.8: Collapse of the curves shown in Figure 5.7 into one single pair of curves achieved by rescaling and plotting them in a manner such that the x-axis represents the total methane generated within the GHSZ (equation 5.38). Base-case seafloor parameters were used for this simulation and $\mathrm{Pe}_2 = 0$.

drate with underlying free gas. Lower values of Pe_1 represent diffusion-dominated systems, whereas higher values of Pe_1 describe systems dominated by advection. In the latter case, diffusive losses of methane are reduced, requiring less dissolved methane in the external flux. Increasing the external fluid flux $|\mathrm{Pe}_2|$, keeping Pe_1 constant, implies greater net methane input to the system, thus requiring less $\tilde{c}^{w}_{m,ext}$ in the external flux to form gas hydrates.

To combine these multiple curves, we realize that net fluid flux is the controlling factor. If we rescale the parameter space so that the y-axis represents the net fluid

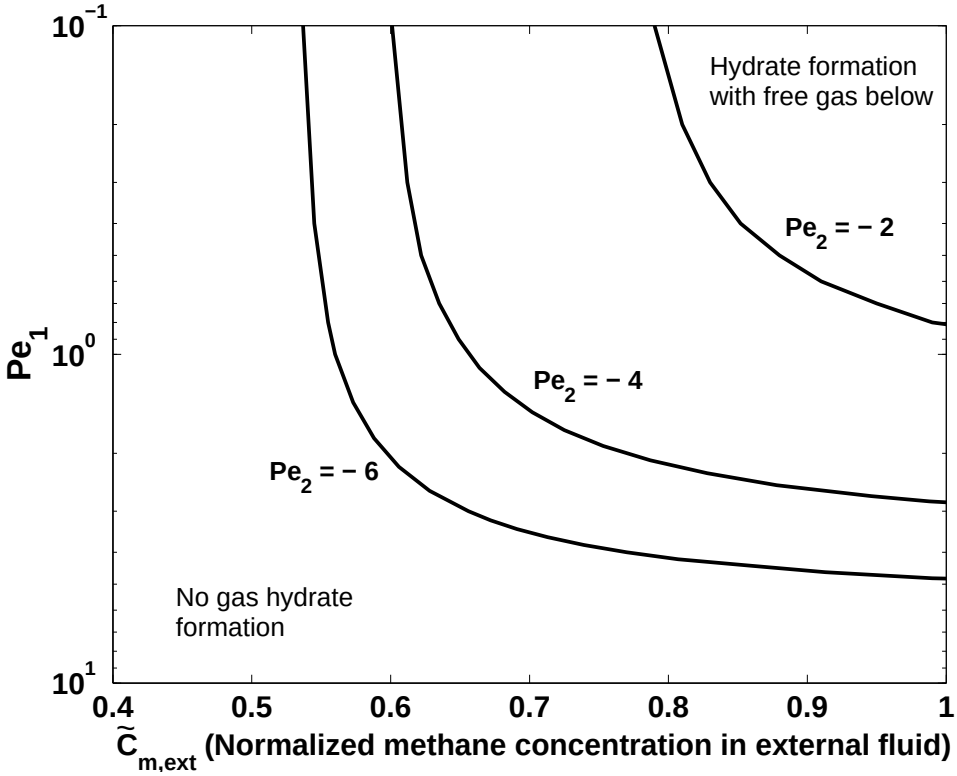

Figure 5.9: Parameter space showing curves separating the region of no gas hydrate formation from hydrate formation with free gas below, for methane supplied from deeper sources only ($\beta = 0$, $\mathrm{Da} = 0$ and $|\mathrm{Pe}_1| < |\mathrm{Pe}_2|$). Base-case seafloor parameters were used for this simulation.

flux in the system (algebraic sum of Pe_1 and Pe_2), the multiple curves for different Pe_2 collapse into a single curve (Figure 5.10). Thus, the entire parameter space for methane supplied from deeper sources can also be defined in a single plot.

5.6.6 Gas Hydrate Saturation Contours

Different gas hydrate regimes can be delineated in two plots (Figure 5.8 and 5.10) using appropriately scaled dimensionless groups. These plots, however, do not give any quantitative information about gas hydrate saturation (S_h), the volume

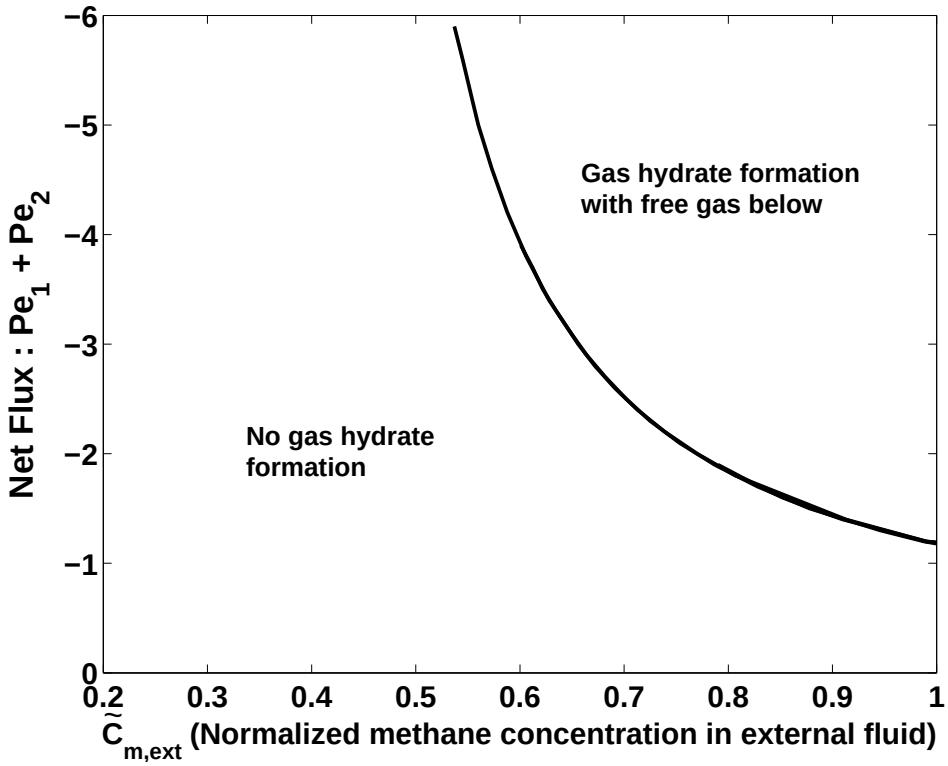

Figure 5.10: Single curve separating region of no gas hydrate formation from gas hydrate formation with free gas below by rescaling the y-axis of Figure 5.9, such that it represents the net flux of fluid in the system. The curves corresponding to different $|\mathrm{Pe}_2|$ in Figure 5.9 come together to yield a single curve for methane supplied from deeper sources ($\beta = 0$, $\mathrm{Da} = 0$ and $|\mathrm{Pe}_1| < |\mathrm{Pe}_2|$). Base-case seafloor parameters were used for this simulation.

fraction of gas hydrate within sediment pore space. The parameter space containing gas hydrate in Figures 5.8 and 5.10 represent steady-state conditions. Thus, each point inside these fields corresponds to a unique depth profile of gas hydrate saturation. Most profiles (for example, Figures 5.2, 5.3 and 5.4) exhibit variable gas hydrate saturation with depth. To get average gas hydrate saturation, we nu-

merically integrate the saturation profile over the depth of the GHSZ:

$$\langle S_h \rangle = \frac{1}{L_t} \int_0^{L_t} S_h(z) dz \tag{5.39}$$

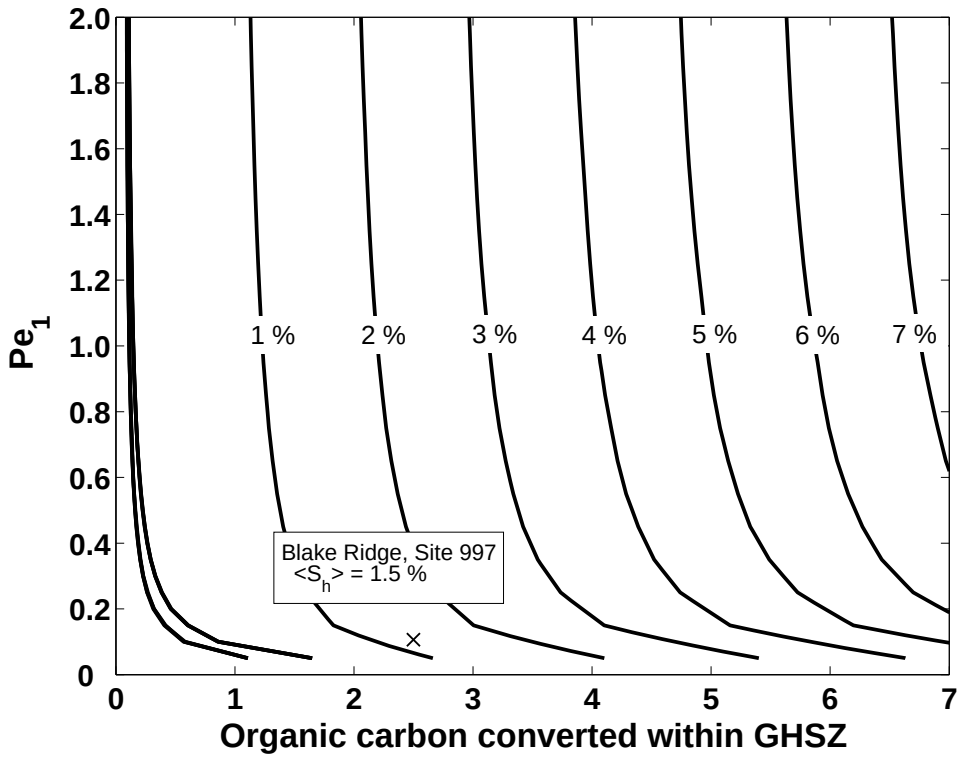

Figure 5.11: Average gas hydrate saturation (equation 5.38) contours plotted for the case of biogenic methane generated in situ ($\mathrm{Pe}_2 = 0$). The set of curves plotted in Figure 5.8 are also shown on the left side of the diagram. Base-case seafloor parameters were used for this simulation.

Average gas hydrate saturations were evaluated for several simulations in the gas hydrate forming region of Figures 5.8 and 5.10. The scaling schemes outlined in previous sections assume even more importance when we observe that average gas hydrate saturation also scales with the dimensionless groups and their combinations. We plot these saturation contours in Figure 5.11, for methane from in

situ sources, along with the set of curves defining the boundaries of the regions in Figure 5.8. The average gas hydrate saturation within the GHSZ increases as Pe_1 or the amount of methane entering the system is increased. It should be emphasized that this single plot of average hydrate saturation suffices for all values of the parameters Pe_1, Da and β.

Average gas hydrate saturations can also be evaluated for cases of external methane supplied from deep sources. The average saturation contours, however, do not scale if we apply the same scaling used to combine different curves in Figure 5.10. This happens because the y-axis in Figure 5.10 represents the total fluid flux into the system, whereas hydrate saturation also depends on the rate at which the sediments are moving. Higher sedimentation rate, characterized by large Pe_1, implies that the gas hydrate layer spends less time in the GHSZ, resulting in lower average hydrate saturation. This causes the average saturation to be strongly dependent on Pe_1, which gets neglected if we take the y-axis to be the sum of Pe_1 and Pe_2. For example, if we simulate a case where $\mathrm{Pe}_1 + \mathrm{Pe}_1 = -10$, then the average hydrate saturation will be different for the cases [$\mathrm{Pe}_1 = 1$,$\mathrm{Pe}_2 = -11$], [$\mathrm{Pe}_1 = 0.5$,$\mathrm{Pe}_2 = -10.5$] and [$\mathrm{Pe}_1 = 0.1$,$\mathrm{Pe}_2 = -10.1$], although their sum remains the same. The average gas hydrate saturations from the simulations for these cases are 0.4%, 0.8% and 4%, respectively. Although the average gas hydrate saturation is different for each case, we observe that the product of Pe_1 and average saturation remains constant. This means that the quantity that remains invariant is the flux of the gas hydrate, which is simply the product of Pe_1 and the average gas hydrate saturation. Thus, the term $\mathrm{Pe}_1\langle S_h \rangle$ remains constant and scales with the

y-axis of Figure 5.10. The average saturation simulated for several parameters is plotted as contours of constant $\mathrm{Pe}_1\langle S_h\rangle$ in Figure 5.12. The average saturation can be calculated from these contours by dividing the contour value by Pe_1. It should be noted that we always include the effects of sedimentation when modeling methane from deeper sources. Thus, the results shown in Figure 5.12 hold for the case of finite sedimentation and the problem of singularity when $\mathrm{Pe}_1 = 0$ is avoided. We also observe a lower limit to the values of Pe_1 for which the average gas hydrate saturation scales with Pe_1. For very low values of Pe_1, the gas hydrate saturation might approach 100% of the pore space, at which point the assumptions of our model do not hold. The contours shown in Figure 5.12 are valid for $\mathrm{Pe}_1 > 0.01$ and $\langle S_h\rangle < 1$. At steady-state, average gas hydrate saturation is independent of $\tilde{c}^w_{m,ext}$ in the external pore fluid. If the external methane concentration is slightly more than the minimum required to precipitate gas hydrate, it takes much longer integration times to achieve the steady-state saturation value.

5.6.7 Sensitivity to Seafloor Parameters

All simulations discussed so far have been for constant seafloor depth, bottom water temperature and geothermal gradient. Values of these parameters were taken to be close to those for the crest of Blake Ridge (Paull et al., 1996). We refer to these as the standard or base-case values, which are: seafloor depth of 2700 m, seafloor temperature of 3°C and geothermal gradient of 0.04°C/m.

We now show that significant changes in these three parameters cause very small changes to the average hydrate saturation contours shown in Figures 5.11

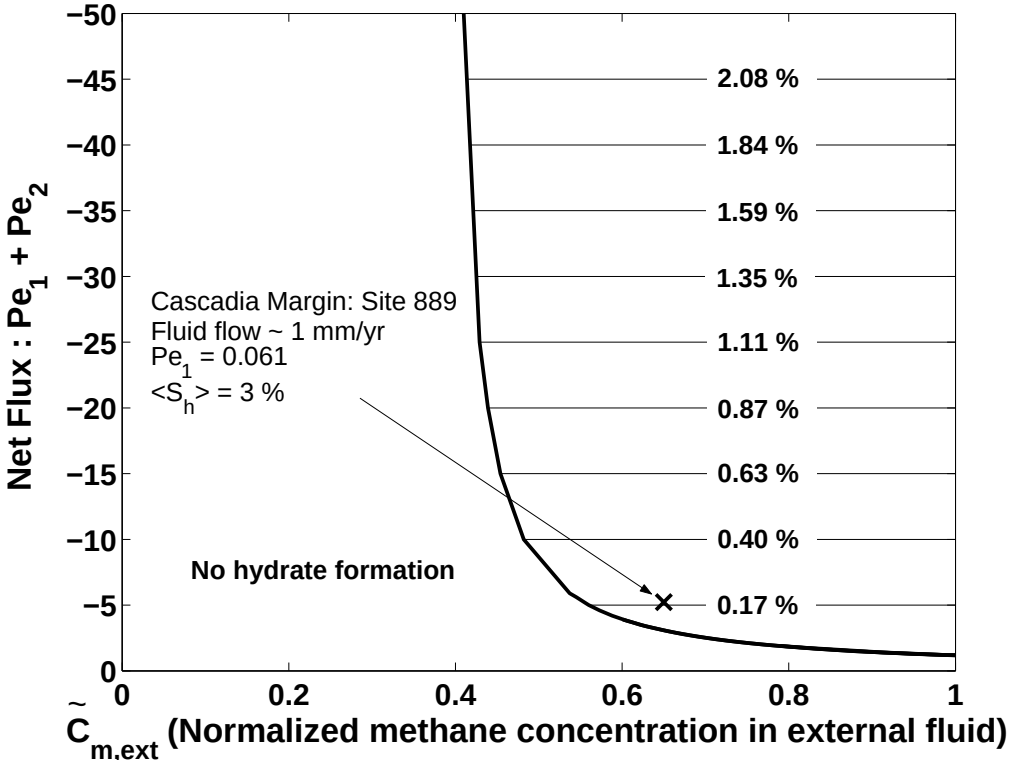

Figure 5.12: Contours of gas hydrate flux $\mathrm{Pe}_1\langle S_h\rangle$ plotted along with the curves separating the two regions of gas hydrate occurrence in Figure 5.10 for the case of non-zero sedimentation and $|\mathrm{Pe}_1| < |\mathrm{Pe}_2|$. Gas hydrate saturation can be calculated by dividing the contour values with . For example, if $\mathrm{Pe}_1 = 1$, these contours directly represent the average gas hydrate saturation in the pore space. Base-case seafloor parameters were used for this simulation.

and 5.12 for different methane sources. The reason for this behavior is the manner in which we non-dimensionalize the vertical depth in our model using the depth to the GHSZ (L_t) and methane concentration using the peak solubility at the base of the GHSZ. Changes in seafloor parameters can cause a big change in the depth of the GHSZ and peak methane solubility, thus causing a marked change in the methane inputs required to form hydrates. But our scaling scheme transforms these different methane solubility curves into curves that are very similar to each

other in the normalized form.

Figure 5.13 (left column) shows the small change in average saturation contours for biogenic in situ sources caused by large changes in seafloor temperature, geothermal gradient and seafloor depth. The solid curves in each plot represent the base case saturation contours while the dashed curves depict average saturation contours for the perturbed system. It can be seen that average hydrate saturation decreases on increasing seafloor temperature and geothermal gradient, while average hydrate saturation increases on increasing seafloor depth.

Figure 5.13 (right column) also shows the similar effect of perturbations in seafloor parameters on the saturation contours for methane supplied from deeper sources only. For this case, the three subplots show the boundary separating the region of hydrate with free gas below from the region of no hydrate for the base case (solid) and the perturbed case (dashed). The change in the product $\mathrm{Pe}_1\langle S_h\rangle$ from the base case is listed on the contours, where positive implies an increase in value of $\mathrm{Pe}_1\langle S_h\rangle$ after applying the perturbation and negative indicates a decrease in $\mathrm{Pe}_1\langle S_h\rangle$. Thus, because of the small magnitude of these changes, our simulation results shown in Figures 5.11 and 5.12 represent very good base cases, with the parameters for any given geological setting acting as small perturbations to the base case.

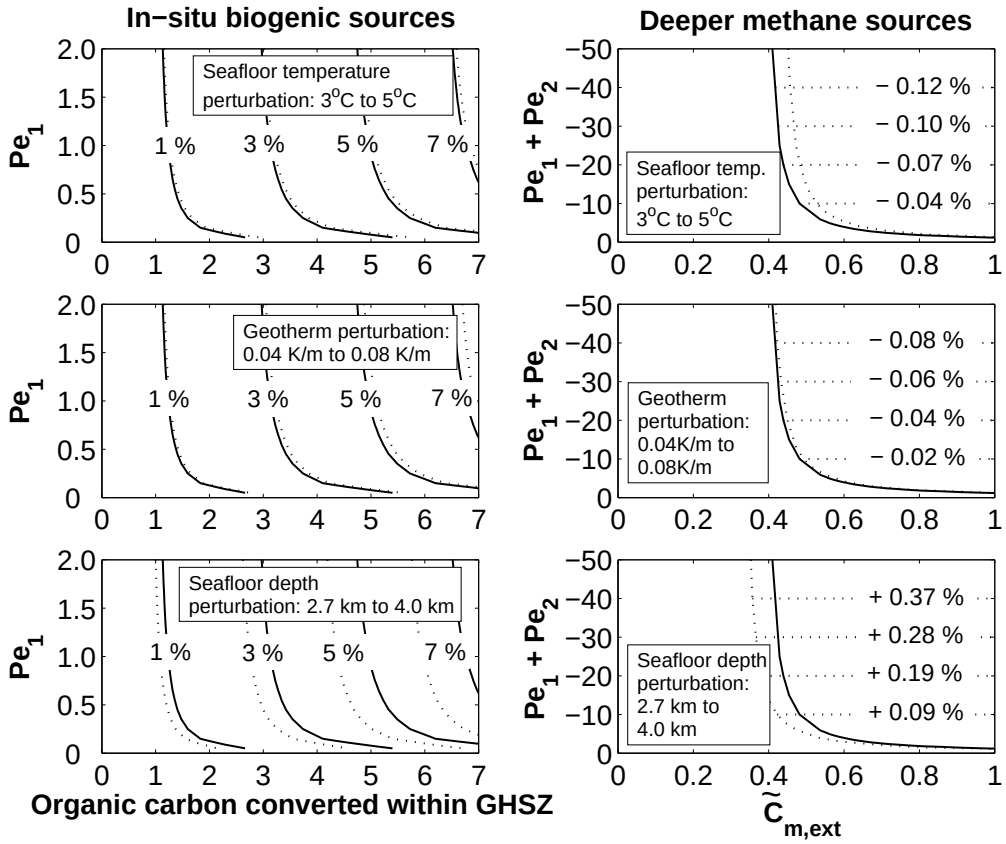

Figure 5.13: Sensitivity of the average gas hydrate saturation contours to perturbations in seafloor temperature, geothermal gradient and seafloor depth. The top plot in each column shows the temperature perturbation, the middle represents geotherm perturbation and the bottom represents seafloor depth perturbation. The left column shows contour plots depicting base case saturation contours (solid) and those obtained after applying the perturbation (dotted) for biogenic in situ sources only. The right column shows changes in $\mathrm{Pe}_1\langle S_h\rangle$ in response to these perturbations for deeper methane sources. The solid curve represents the boundary between the region of hydrate with free gas and no hydrate for the base case, while the dotted curve is the boundary after applying the perturbation. Change in values of $\mathrm{Pe}_1\langle S_h\rangle$ compared to those shown in Figure 5.12 are also listed.

5.7 Implications

By sampling the entire parameter space for each type of methane source, our simulations reveal why natural gas hydrate systems can be so variable. Depending on the methane inputs and outputs, there can be methane-charged sediment sequences containing no gas hydrate, gas hydrate but no free gas below the GHSZ, or gas hydrate with free gas below the GHSZ. The saturations of gas hydrate and free gas are also a function of the dimensionless parameters (Figures 5.11 and 5.12).

Some non-intuitive aspects of natural gas hydrate systems can also be understood from our numerical modeling. For example, gas hydrates can precipitate within the GHSZ from in situ sources of methane without a free gas layer below even with continuous sedimentation. Previous modeling had simulated this scenario, but only during the transient part of the simulations (Davie and Buffett, 2001). This happens at steady-state conditions, however, when the amount of methane produced is greater than the minimum needed to precipitate gas hydrates but less than the amount required to extend the gas hydrate layer to the base of the GHSZ. This finding has important implications because it suggests that gas hydrate systems can lack a gas hydrate/free gas contact, and hence a BSR on seismic profiles. ODP Site 994 on outer Blake Ridge (Paull et al., 2000) may be an example of this situation.

We have also shown that higher sedimentation rates do not necessarily imply higher gas hydrate saturations, at least in the case of in situ methane sources.

With the initial TOC context fixed at the seafloor, and the reaction rate fixed with time, increasing sedimentation rates can mean that a higher fraction of organic carbon passes through the GHSZ. This could yield lower gas hydrate saturation at steady-state.

Sedimentation rates and TOC input are not constant over geologic time-scales. The saturation contour plots (Figures 5.11 and 5.12) provide a convenient way to quantitatively examine variations in average gas hydrate saturation resulting from such changes. For example, if the sedimentation rate and TOC input over time are known, one can plot points corresponding to different values of these parameters to see how a particular gas hydrate system would evolve. This procedure, of course, assumes that the gas hydrate system achieved steady-state after each change in sedimentation rate and/or TOC input.

5.8 Conclusions

We have developed a numerical model for predicting gas hydrate formulation and accumulation over geologic time-scales from methane generated either from biogenic in situ sources, methane from upward external fluxes or both. The following conclusions can be drawn from our simulation results:

- At steady-state conditions, marine sequences where all methane comes from in situ microbial activity can be divided into three categories: no gas hydrate, gas hydrate without free gas below and gas hydrate with an underlying free gas layer. The first Peclet number (Pe_1), the Damkohler number (Da) and the

organic input at the seafloor control the category.

- For systems where methane derives from an external, deep source, the category of gas hydrate without free gas below is not observed at steady-state conditions when sedimentation occurs. Decreasing Pe_1 to low values delays the time it takes to achieve steady state, but the steady-state system either has no gas hydrate or gas hydrate directly underlain by a free gas layer at the base of the GHSZ.

- Disconnected gas hydrate and free gas layers are observed in our external flux simulations if we set sedimentation to zero ($\mathrm{Pe}_1 = 0$), because this causes the gas hydrate and free gas layers to become immobile. Consistent with the results of Xu and Ruppel (1999), a critical external flux has to be exceeded to extend the gas hydrate and free gas layers to the base of the GHSZ.

- Gas hydrate distribution depends on various parameters but can be summarized in two plots, one each for in situ and deeper methane sources, by appropriately combining dimensionless groups. For biogenic in situ sources, this happens when Pe_1 is plotted against the amount of methane generated within the GHSZ (equation 5.38). For deeper methane sources, this happens when the net flux ($\mathrm{Pe}_1 + \mathrm{Pe}_2$) is plotted against the methane concentration of the external flux.

- Average gas hydrate saturation contours also scale with dimensionless groups,

so that two contour maps provide gas hydrate saturation values for a large range of parameters. These dimensionless contour maps are relatively insensitive to changes in seafloor temperature, depth and geothermal gradients, and are thus applicable to a wide variety of geological settings. Site-specific simulations done by other investigators (Davie and Buffett, 2001, 2003a) become single points on these saturation maps. Our scaling schemes make these plots ideal base cases for providing quantitative information about the possible types of hydrate accumulation at any given location without performing any numerical simulations. This turns out to be a big improvement over most of the site-specific results available from hydrate modeling in the literature, which are valid only for the numerous parameters relevant to a particular gas hydrate province.

Chapter 6

Application to Geologic Sites

6.1 Introduction

The majority of natural gas hydrate accumulations are found in oceanic sediments along continental margins where sufficient methane is available for gas hydrate formation. Numerical models for gas hydrate accumulation in such settings have been developed (Xu and Ruppel, 1999; Davie and Buffett, 2001; Gering, 2003; Haeckel et al., 2004; Torres et al., 2004; Wallman et al., 2006), but their dependence on a number of transport and geologic parameters make them applicable only to specific sites. Hence, most of these numerical models have been applied to well studied sites, such as Blake Ridge or Hydrate Ridge (Cascadia Margin) (Davie and Buffett, 2003a; Gering, 2003; Haeckel et al., 2004; Torres et al., 2004).

Perturbations in these site-specific parameters, like seafloor depth or geothermal gradient, will result in different depths of the GHSZ and methane solubilities within the GHSZ. This can lead to a different gas hydrate and free gas distribution at steady state, requiring numerical simulations for each parameter perturbations. Further, this approach of parameter-specific simulations gives little insight into the physics governing these complex systems. For example, change in the depth of the GHSZ by altering the seafloor depth, temperature, geothermal gradi-

ent or seawater salinity can change the gas hydrate system from being advection to diffusion-dominated.

The previous chapters detailed the development of a general dimensionless numerical model for simulating gas hydrate formation and accumulation over geologic time-scales. More importantly, it was shown that appropriate scalings of dimensionless groups condense information of gas hydrate distribution and saturation for a wide range of parameters into simple contour plots. One of these plots corresponds to methane generated in situ through biogenic reactions within the GHSZ, while the other plot represents the scenario where methane is supplied from deeper sources via upward external fluxes (Bhatnagar et al., 2007).

We now compare our predictions with gas hydrate saturations inferred from proxy data or other simulation studies for four well characterized gas hydrate settings. We also show that incorporating mixed sources of methane can explain the difference in gas hydrate and free gas distribution between Ocean Drilling Program (ODP) Site 994 and Sites 995/997 at Blake Ridge. Finally, characteristics of systems with mixed sources of methane (both in situ biogenic and deeper sources), including conditions suitable for relatively high gas hydrate saturations, are explained through dimensionless groups.

6.2 Systems Dominated by Deep-Source Methane

The general features of the saturation contour plot for systems dominated by deep-methane sources are discussed in the previous chapter. Here we show the utility of

this contour map by applying it to Site 889 (Cascadia Margin), which is part of a gas hydrate system believed to be dominated by methane flux from depth (Hyndman and Davis, 1992; Westbrook et al., 1994; Davie and Buffett, 2003a).

6.2.1 The Cascadia Margin

The Cascadia Margin is an accretionary margin characterized by relatively low TOC content ($< 1\%$) and relatively high fluid flow rates (Westbrook et al., 1994; Tréhu et al., 2003). Research cruises, including ODP Legs 146 and Leg 204, have not only identified and quantified gas hydrate within sediments of this region, but have also revealed some surprising aspects concerning gas hydrate distribution. Layers of massive gas hydrate have been found at the southern summit of the Hydrate Ridge where methane actively vents from the seafloor (Tréhu et al., 2003; Haeckel et al., 2004; Torres et al., 2004). These layers are not expected from most numerical models for gas hydrate accumulation, which predict maximum gas hydrate saturations close to the base of the GHSZ (Xu and Ruppel, 1999; Davie and Buffett, 2001). Focused fluid flow through coarse-grained conduits (Tréhu et al., 2004; Milkov et al., 2005) and transport of methane in gas phase through the GHSZ (Haeckel et al., 2004; Torres et al., 2004) has been hypothesized to cause such heterogeneous distributions. The observations and explanations raise interesting issues regarding the presence and migration of free gas within the GHSZ. For example, they may necessitate slow kinetic rates for gas hydrate precipitation and gas dissolution in pore water (Haeckel et al., 2004; Torres et al., 2004) or salinity effects on thermodynamic stability caused by hydrate precipitation (Milkov, 2004;

Liu and Flemings, 2006, 2007). However, apart from specific sites near active seafloor venting, sites in the area appear to be characterized by gas hydrate saturations that increase with depth towards the BSR (Westbrook et al., 1994; Tréhu et al., 2004).

We examine data from ODP Site 889 (Leg 146) west of Vancouver Island (Westbrook et al., 1994) as an example of a gas hydrate system sourced by a deep methane flux. According to our model, the average gas hydrate saturation for this type of source can be constrained with the upward fluid velocity, sedimentation rate, methane diffusivity, porosity profile, and other seafloor parameters listed in Table 6.1. These dimensional variables can be combined into the dimensionless groups, Pe_1 and $\mathrm{Pe}_1 + \mathrm{Pe}_2$, which are the main parameters controlling the gas hydrate distribution at steady-state.

Davie and Buffett (2003a) indicated that an upward velocity of about 0.42 mm/yr ($v_{f,0}$, at the sediment interface) best fits the pore water chlorinity profile at Site 889. This value is similar to that ($\sim$1-2 mm/yr) believed to represent the region as a whole (Wang et al., 1993). We use a velocity of 1 mm/yr at the seafloor to get the net fluid flux ($U_f = v_{f,0}\phi_0$, Table 6.1), which characterizes the sum of the two Peclet numbers on the y-axis of the contour plot (Figure 6.1). The seafloor parameters at this site lead to a predicted GHSZ extending to 233 mbsf, which compares favorably with the BSR depth of 225 mbsf inferred from seismic data (Westbrook et al., 1994). Calculations from the transport parameters give values for $\mathrm{Pe}_1 + \mathrm{Pe}_2$ and Pe_1 of -5.1 and 0.061, respectively (Table 6.1). This locates the point corresponding to Site 889 at the contour close to $\mathrm{Pe}_1\langle S_h \rangle$ = 0.18% (Figure 6.1), and implies an

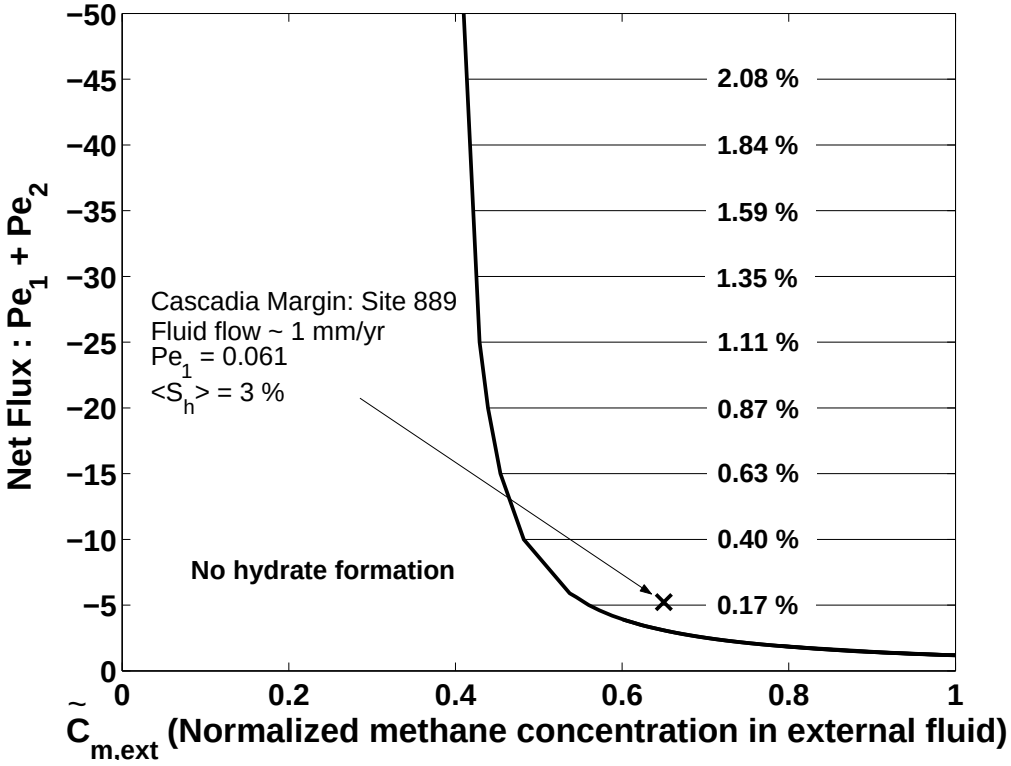

Figure 6.1: Contours of gas hydrate flux $\mathrm{Pe}_1\langle S_h\rangle$ plotted along with the curves separating the two regions of gas hydrate occurrence, for the case of non-zero sedimentation and $|\mathrm{Pe}_1| < |\mathrm{Pe}_2|$. Gas hydrate saturation can be calculated by dividing the contour values with . For example, if $\mathrm{Pe}_1 = 1$, these contours directly represent the average gas hydrate saturation in the pore space

average gas hydrate saturation of 3%. The gas hydrate profile was also generated (Figure 6.2), and shows gas hydrate saturation increasing toward 12% at the base of GHSZ.

Numerical results from Davie and Buffett (2003a) for parameters close to those listed in Table 6.1 indicate average hydrate saturation between 2 and 5%. As explained in their discussion, these modest gas hydrate contents at Site 889 are significantly lower than the 20-30% saturation above the BSR inferred from certain analyses of seismic velocity and log resistivity (Yuan et al., 1996; Hyndman et al.,

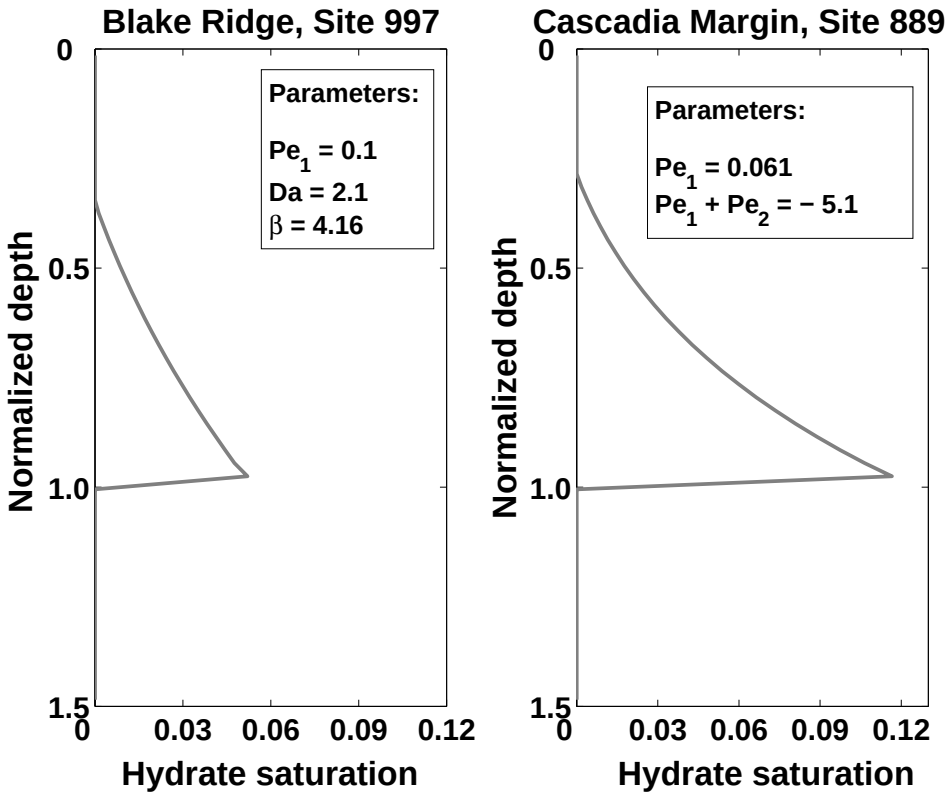

Figure 6.2: Steady state hydrate saturation profiles, obtained using the parameters listed in Table 6.1, at Blake Ridge, ODP Site 997 (left) and Cascadia Margin, ODP Site 889 (right).

1999), but are consistent with the $\sim$ 3% value obtained from core temperature measurements (Kastner et al., 1995).

6.3 Systems Dominated by in situ Methane Generation

We first describe general features of the average saturation contour plot obtained for in situ biogenic methane sources. In such systems, self-similarity occurs when we plot gas hydrate saturation contours as a function of Pe_1 and the net amount of organic carbon converted within the GHSZ (Figure 6.3). The net amount of

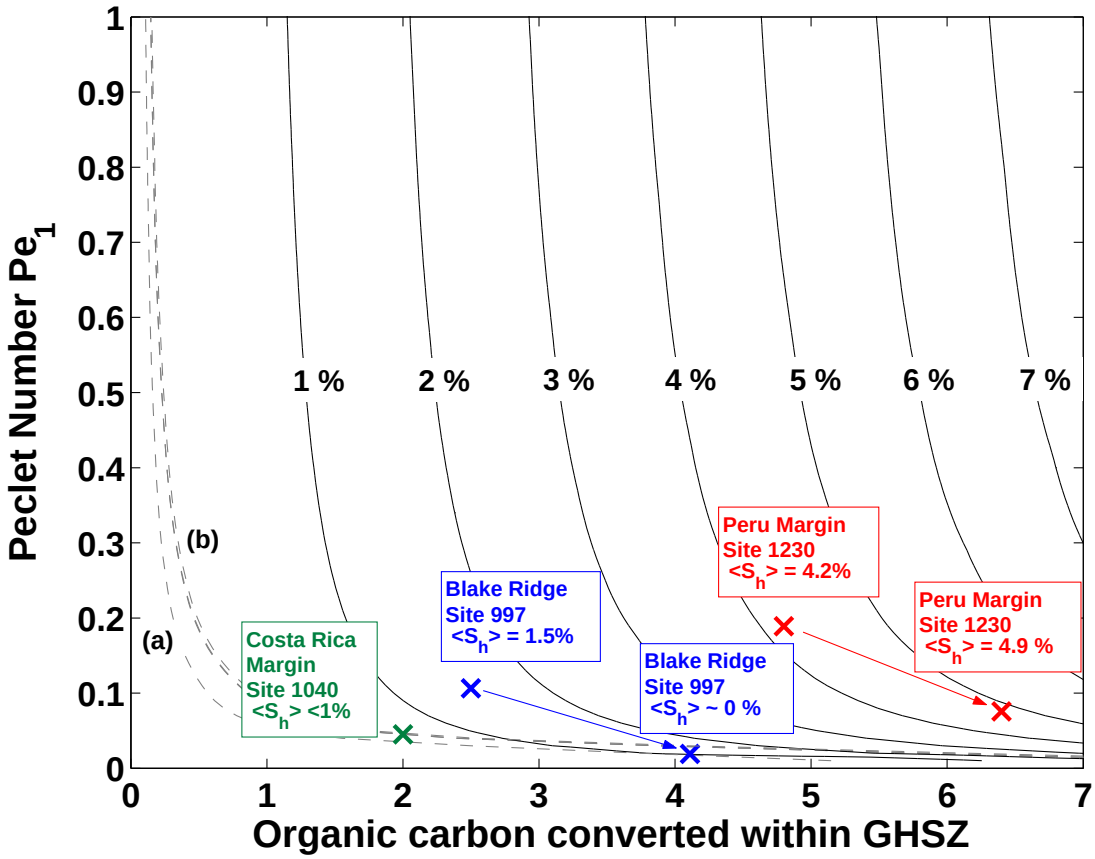

Figure 6.3: Gas hydrate saturation contours averaged over the entire GHSZ for systems where all methane is furnished through in situ biogenic reactions. Diffusive losses dominate at low values of Peclet number (Pe_1), implying that methane generation within the GHSZ has to increase to form any gas hydrate. The set of dashed curves, marked (a) and (b), represent the intermediate region of gas hydrate formation without free gas, with the region of no gas hydrate formation for x-axis values lesser than for curve (a) and gas hydrate with free gas immediately below for x-axis values greater than those for curve (b) (Bhatnagar et al., 2007). Average gas hydrate saturation at different gas hydrate settings can be obtained from this single contour map.

Table 6.1: Site-specific data, dimensionless groups and average gas hydrate saturation calculation for Cascadia Margin and Blake Ridge sites.

Site-specific Data	Cascadia Margin Site 889	Blake Ridge Site 997	Blake Ridge Site 997
Seafloor depth (m)	1311	2781	2781
Seafloor temperature ($^{\circ}\mathrm{C}$)	2.7	3.4	3.4
Geotherm ($^{\circ}\mathrm{C/m}$)	0.054	0.04	0.04
Depth of GHSZ (m)	233	458	458
Methane solubility at base of GHSZ ($c^{l}_{m,eqb}$)	—	2.7×10^{-3}	2.7×10^{-3}
Sedimentation rate $\dot{S}$ (cm/kyr)	25	22	4
CH_4 diffusivity D_m ($\mathrm{m^2/s}$)	10^{-9}	10^{-9}	10^{-9}
Methanogenesis rate λ ($\mathrm{s^{-1}}$)	—	10^{-14}	10^{-14}
Fluid flux due to sedimentation and compaction $U_{f,sed}$ (m/s)	2.64×10^{-13}	2.3×10^{-13}	4.2×10^{-14}
Net fluid flux $U_f = v_{f,0}\phi_0$ (m/s)	-2.2×10^{-11}	—	—
TOC α_0 (wt.%)	0	1.5	1.5
Dimensionless groups			
$\mathrm{Pe}_1 = \frac{U_{f,sed}L_t}{D_m}$	0.06	0.1	0.02
$\mathrm{Da} = \frac{\lambda L_t^2}{D_m}$	—	2.1	2.1
$\mathrm{Pe}_1 + \mathrm{Pe}_2 = \frac{U_f L_t}{D_m}$	-5.1	0.1	0.02
$\beta = \frac{(3/4)\alpha_0}{c^{l}_{m,eqb}}$	0	4.16	4.16
Organic carbon converted in GHSZ	0	2.5	4.1
$\langle S_h \rangle$ (% of pore space)	3.0	1.5	0

organic carbon converted within the GHSZ at steady state can be obtained from the analytical solution of the organic balance equation and is written as (Bhatnagar et al., 2007):

Net organic carbon converted within GHSZ

$$= \left(1 - \left[\eta + (1-\eta)\, e^{1}\right]^{-\frac{1}{(1+\gamma)\mathrm{Pe}_1/\mathrm{Da}}}\right)\beta \tag{6.1}$$

The set of dashed curves (Figure 6.3, (a) and (b)) separate the region of no gas hydrate formation on the left side of (a) from the region of gas hydrate formation with underlying free gas on the right side of (b). The narrow region enclosed by this set of curves bounds the region where gas hydrate forms without any free gas immediately below the GHSZ. This type of gas hydrate accumulation is discussed in more detail later. Diffusive losses of methane dominate at lower values of Pe_1, requiring methane generation within the GHSZ to increase to form gas hydrate (Figure 6.3). This can happen by either increasing the organic input to the sediment (β) or allowing faster conversion of organic carbon into methane (lower $\mathrm{Pe}_1/\mathrm{Da}$) (Bhatnagar et al., 2007). For the same amount of methane generated within the GHSZ, increasing Pe_1 causes the diffusive loss of methane to decrease, resulting in higher average gas hydrate saturation.

The utility of Figure 6.3 can be easily understood by realizing that this plot summarizes information from numerous simulations performed over the entire parameter space. Thus, data from different geologic sites can be transformed into dimensionless variables defined above and mapped onto this contour map, yielding

average gas hydrate saturation at that site without any new numerical simulations. Effects of perturbing the transport and seafloor parameters can also be directly studied from Figure 6.3. We later apply this general contour plot to three different gas hydrate settings dominated by in situ biogenic methane sources.

6.3.1 Gas hydrate formation without free gas below

Figure 6.3 shows that by gradually increasing β from a relatively low to high value, for a given Pe_1, causes the system to go from no hydrate to an intermediate region of hydrate with no free gas immediately below it and finally into the region of gas hydrate with free gas contact at the base of the GHSZ. The narrow regime of gas hydrate without free gas contact can be further divided into two subcategories. For given Pe_1 and Da, a relatively small value of β yields a steady state with an isolated gas hydrate layer within the GHSZ without any free gas below (Figure 6.4a). Increasing β causes an increase in the organic carbon input to the sediments and causes free gas to form below the GHSZ, but not immediately below this boundary (Figure 6.4b). Gas hydrate does not extend down to the base of the GHSZ in both these simulation cases.

Simulation results in which both gas hydrate and free gas contact each other at the base of the GHSZ (Davie and Buffett, 2001, 2003a; Bhatnagar et al., 2007) show that free gas saturation equals some non-zero value just below the GHSZ. This contrasts with the free gas saturation profile in Figure 6.4b, which starts to increase from zero saturation at some depth below the GHSZ, because it does not benefit from any excess methane input due to gas hydrate dissociation at the

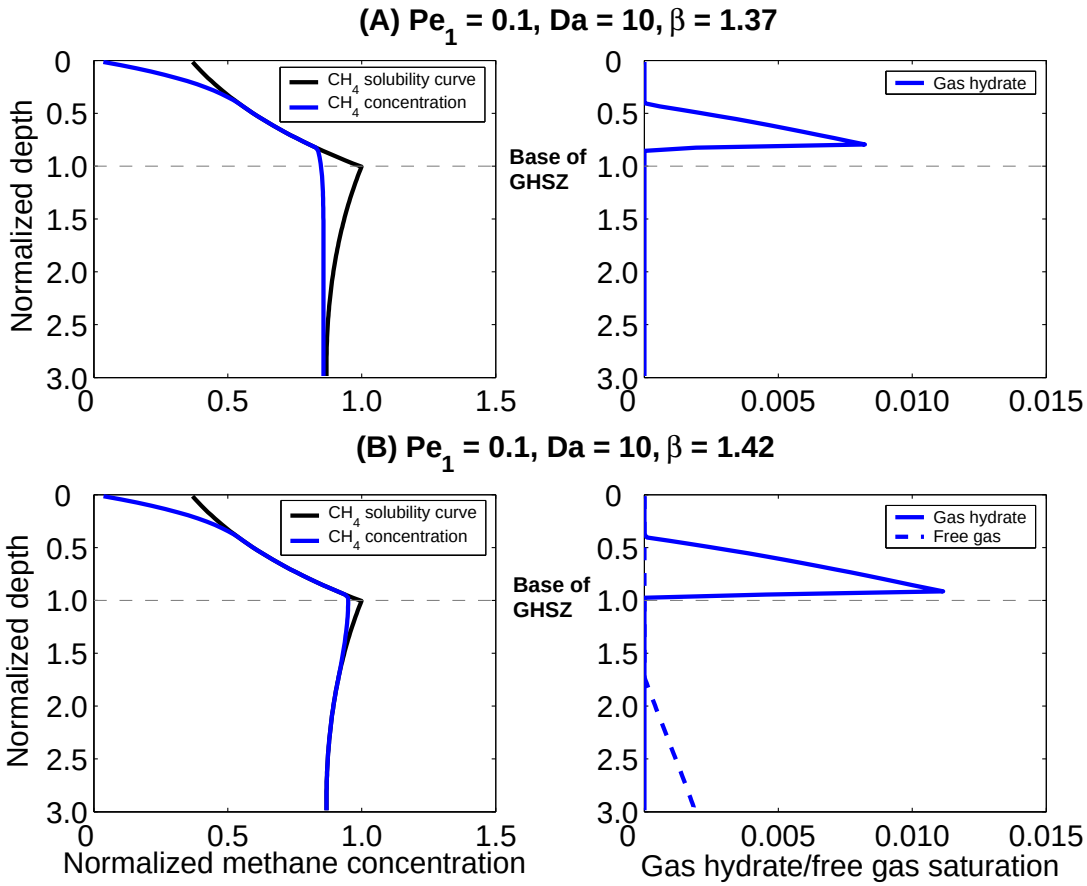

Figure 6.4: Different cases of gas hydrate formation without free gas immediately below the hydrate layer. (A) For given Pe_1 and Da, a relatively lower value of β implies lesser organic carbon input to the system, resulting in gas hydrate formation without any free gas below it. (B) Increasing β by a small amount raises organic carbon input such that free gas forms beneath the hydrate layer but does not contact it at the base of the GHSZ. The gas hydrate layer itself does not extend to the base of the GHSZ in both the cases. Further increase in β would bring the gas hydrate and free gas layers together at the base of the GHSZ.

base of the GHSZ. Thus, occurrence of a BSR for such cases is unlikely due to two reasons. First, there is no gas hydrate/free gas contact. Secondly, increasing β can bring together hydrate and free gas close to the base of the GHSZ, but because free gas saturation gradually increases from zero, the resulting impedance contrast might not be sufficient.

In general, average gas hydrate saturations for this special category of no free gas immediately beneath the GHSZ are low for $\mathrm{Pe}_1 >\sim 0.05$ (Figure 6.3). This can be inferred from the distance between the 1% contour and the dashed curve (a) in Figure 6.3, which represents the 0% contour as it marks the boundary where gas hydrate first forms. However, for $\mathrm{Pe}_1 <\sim 0.05$, the contours start to converge together such that average saturation within this narrow regime starts increasing to significant values. Hence, appreciable amounts of gas hydrate can form without free gas immediately below the GHSZ only for small values of Pe_1, which physically translates into geologic settings with low sedimentation rates. This relationship is used to model gas hydrate distribution at one of the Blake Ridge sites.

6.3.2 The Blake Ridge region

The Blake Ridge system is probably the most extensively studied marine gas hydrate province, with ODP Leg 164 providing detailed information about sediment properties, pore-water and gas composition, gas hydrate samples, well-log data and seismic profiles (Paull et al., 2000). This region is a passive margin setting characterized by low advection rates (Egeberg and Dickens, 1999) and modest organic content, with total organic carbon (TOC) between 0.5 - 1.5 wt.% (Site

997) (Paull et al., 2000). Linear sulfate gradients within the sulfate reduction zone (SRZ) of the Blake Ridge sediments indicate that the system is diffusion dominated (Borowski et al., 1996). Pore water Br^- and I^- profiles also suggest low advection rates (Egeberg and Dickens, 1999). Geochemical analysis of gas and other pore water constituents imply that the methane is of biogenic origin. These results indicate that the Blake Ridge system is dominated by in situ generated methane, which is also supported by the success of matching the chloride anomaly at Site 997 with that predicted from numerical models using in situ methane sources only (Davie and Buffett, 2001). Moreover, if upward migration of methane is assumed to be the only source, with flow rates obtained from pore-water bromide-iodide ratios (Egeberg and Dickens, 1999), no gas hydrate formation occurs at Site 997 (Davie and Buffett, 2003a). Hence, we model Site 997 as a gas hydrate setting where in situ generation is the only methane source.

Simulating gas hydrate accumulation due to this methane source requires specification of the Peclet number, Pe_1, the dimensionless organic carbon content at the seafloor, β, the Damkohler number, Da, and the seafloor parameters, i.e. porosity, seafloor depth, temperature and geothermal gradient. The definitions of these dimensionless groups in turn depend on parameters like sedimentation rate, TOC, rate of methanogenesis and methane diffusivity. These parameters, and subsequent calculation of dimensionless variables from these parameters, are given in Table 6.1 for Blake Ridge Site 997. The TOC at Site 997 is assumed to be 1.5 wt.% (Paull et al., 2000; Davie and Buffett, 2001). The fraction of labile TOC that is actually converted to methane is usually lesser than unity and a value of 50%

is commonly assumed (Henrichs and Reeburgh, 1987). However, to compare with simulation results of Davie and Buffett (2001), we assume available TOC to be 75% of the deposited value.

As mentioned before, an obvious advantage of representing gas hydrate saturation contours in the form shown in Figure 6.3 is the ability to track the dynamic evolution of gas hydrate systems over geologic time scales. This evolution can be studied by locating points corresponding to major changes in sedimentation rates and/or TOC content at the time of burial. Changes in seafloor parameters such as seafloor depth, bottom water temperature and geothermal gradient can also be incorporated through their effect on the depth of the GHSZ (L_t), which is an intrinsic parameter in the dimensionless groups. Plotting these points on the contour map and tracking their loci can then give information about how any given gas hydrate province has evolved in time. To illustrate this point, we plot two points (Figure 6.3) corresponding to different average sedimentation rates of 22 cm/kyr for the lower Pliocene and Miocene sequences and 4 cm/kyr for the entire Quaternary sediments at Site 997 (Paull et al., 1996; Davie and Buffett, 2001). The point corresponding to the earlier high sedimentation rate indicates average gas hydrate saturation of about 1.5%, while the relatively recent sedimentation rate moves the point out of the saturation contour region and into the regime of no gas hydrate formation (Figure 6.3). TOC contents for both sequences were assumed to be the same. Thus, the gas hydrate system at Blake Ridge is probably evolving from higher saturation towards a steady-state that is devoid of any gas hydrate. Moderate sedimentation rates in the past, along with modest TOC content, allowed

greater amounts of gas hydrate to accumulate, but this level of saturation cannot be sustained by the current influx of organic carbon. Hence, this gas hydrate system might be gradually losing more methane to diffusive losses than is being fed to it through methanogenesis.

Average gas hydrate saturation predicted from our contour plot using sedimentation rate of 22 cm/kyr ($\sim$1.5% of pore space) matches well with an average of 2% inferred from numerical simulations of Davie and Buffett (2001) for the same parameter set. It should be noted that the saturation predicted from the contour plot (Figure 6.3) is averaged over the entire GHSZ, while values presented in the literature usually report average gas hydrate saturation over the hydrate occurrence zone only. The gas hydrate saturation profile simulated for these parameters is shown in Figure 6.2 and indicates peak saturation of about 6% at the base of the GHSZ. This matches well with the results of Davie and Buffett (2001) that predict peak hydrate saturation of about 5%. Gas hydrate saturation averaged over the hydrate occurrence zone from our simulation (Figure 6.2) yields a saturation of about 2.4%. Different geophysical/geochemical techniques also constrain saturation within the the hydrate occurrence zone to be in the range 2-6% (Holbrook et al., 1996; Egeberg and Barth, 1999; Collett and Ladd, 2000; Lee, 2000). Hence, our simple one-dimensional model and the associated contour plot is able to give estimates consistent with other numerical studies and proxy data.

Heterogeneous gas hydrate/free gas distribution at Sites 994, 995 and 997

The point corresponding to Site 997, shown in Figure 6.3, lies in the region characterized by free gas immediately below the base of the GHSZ. However, this might not be representative of the entire Blake Ridge region. The actual distribution of gas hydrates and free gas at various sites might be quite different from each other qualitatively as well as quantitatively. This is evident from the patchy BSR and free gas distribution at Sites 994, 995 and 997. While gas hydrate and free gas extend as connected phases up to the base of the GHSZ at Site 997, free gas appears to be disconnected below the GHSZ at Site 995 and does not exist directly below the GHSZ at Site 994 (Holbrook et al., 1996; Paull et al., 2000). Relatively low fluid flux, compared to that at Sites 995 and 997, has been hypothesized to prevent gas hydrate and free gas from extending to the base of GHSZ at Site 994 (Xu and Ruppel, 1999). The model of Xu and Ruppel (1999), however, assumes no sedimentation or biogenic in situ generation of methane, i.e. all methane is supplied from deeper sources only. On the other hand, modest sedimentation rates and TOC contents across this region suggest that biogenic input of methane cannot be neglected. Hence, we now present a mixed-source mechanism (with continuous sedimentation) through which the absence of a BSR at Site 994 and occurrence of a BSR at the other two sites can be explained.

For all sites it is assumed that the biogenic input of methane, and the parameters that control this source, remain invariant. This can be justified by the similar sedimentation rates, TOC contents and seafloor parameters (i.e., seafloor depth,

temperature and geotherm). For simplicity, we also assume that the depth to the base of the GHSZ, L_t, is the same for all three sites. Hence, the dimensionless groups Pe_1, Da and β become equal for all sites as well.

We commented previously that gas hydrate without free gas immediately below can accumulate in substantial amounts through biogenic in situ sources at low Peclet numbers (Pe_1) only. Thus, if gas hydrate forms only through this methane input without free gas contact at Site 994, a relatively small Pe_1 will be required. The sedimentation rate used for Site 997 (Figure 6.3) varies between 22 cm/kyr and 4 cm/kyr, with the average rate between these limits. We choose an average sedimentation rate of 11 cm/kyr, which is in agreement with the value of 12.2 cm/kyr used by Egeberg and Dickens (1999) to model gas hydrate distribution at Site 997. Using this rate results in Pe_1 equal to 0.05. In calculating the normalized organic carbon input in Table 6.1, we assumed that only 75% of this TOC is available for methanogenesis, which was done to compare simulation results with those reported by Davie and Buffett (2001). This value of the actual fraction of available organic carbon is poorly constrained and, in general, lower than 75%, with values in the range 25-50% being more common (Henrichs and Reeburgh, 1987; Davie and Buffett, 2003a; Buffett and Archer, 2004). Consequently, we assume an intermediate value of 40%, which combined with a 1.5 wt.% TOC content yields a normalized organic carbon input of β = 2.2. The Damkohler number, Da, remains the same as calculated in Table 6.1.

This biogenic input remains constant for all three sites, but it is known that Sites 995 and 997 have free gas immediately below gas hydrate at the base of the GHSZ

(Holbrook et al., 1996). Hence, the only other methane source that can be invoked to bring the hydrate and free gas layers together at the base is an upward external fluid flux. This is also justified by previous modeling studies that show Site 997 to be characterized by low upward flux (Egeberg and Dickens, 1999; Hesse et al., 2000) and that the chloride anomaly at Site 997 can be matched well with a mixed methane source (Davie and Buffett, 2003a). Egeberg and Dickens (1999) used an upward flow rate of 0.2 mm/yr to fit pore water halide concentrations, thereby constraining the gas hydrate saturation at Site 997. Davie and Buffett (2003a) superimposed this flux with that due to sedimentation-compaction to arrive at a net upward velocity of 0.08 mm/yr at the seafloor. An external upward fluid flux is easily introduced in our model by specifying a negative value for Pe_2. The resulting net fluid flux through the system can be characterized by adding the two Peclet numbers, i.e., the net Peclet number for this mixed source system is $\mathrm{Pe}_1 + \mathrm{Pe}_2$. We use this seafloor velocity (0.08 mm/yr) as the net upward external flux through the system, which transforms into $\mathrm{Pe}_1 + \mathrm{Pe}_2 = -0.86$, resulting in $\mathrm{Pe}_2 = -0.81$.

Simulations are now performed for these two sets of parameters: one with biogenic in situ methane generation only (Figure 6.5a) and the other with a mixed source (Figure 6.5b). Compared to most saturation or concentration profiles in this thesis, Figure 6.5 shows a dimensional depth axis for comparison with field values. Figure 6.5a shows that at steady state and in the absence of any upward flux at Site 994, gas hydrate remains isolated within the GHSZ without any free gas contact directly below the hydrate. Free gas does form in the system starting at about 550 mbsf, which is in agreement with the depth inferred from vertical seismic pro-

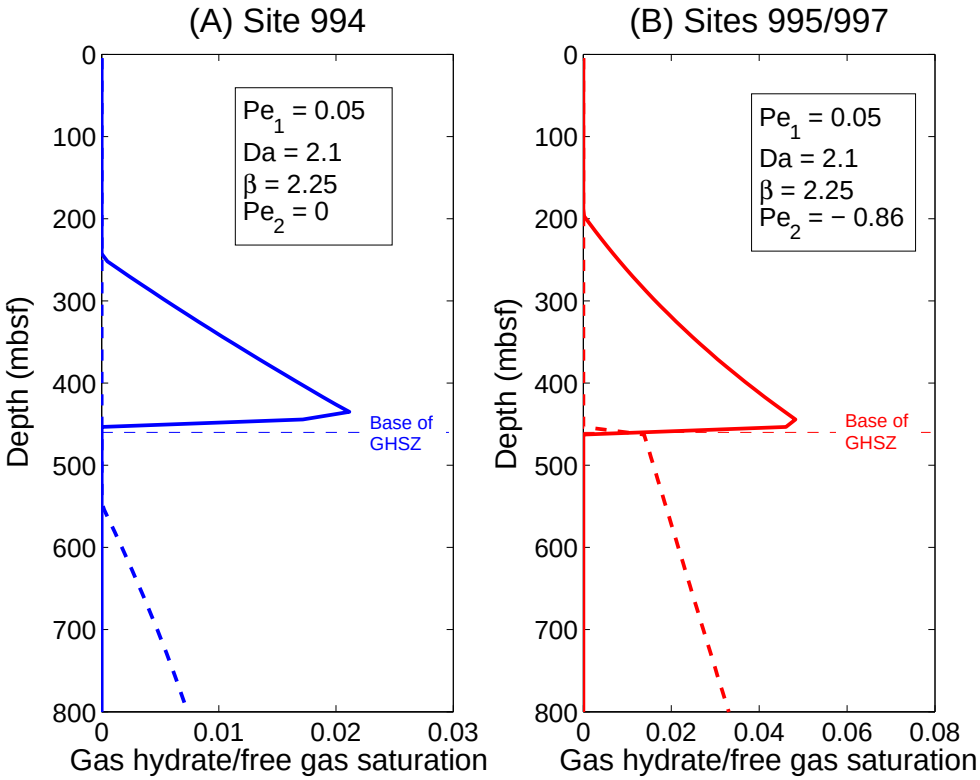

Figure 6.5: Steady state heterogeneous gas hydrate (solid curves) and free gas (thick dashed curves) distribution at Sites 994, 995 and 997 (Blake Ridge). The biogenic parameters remain constant for both cases. $\mathrm{Pe}_1 = 0.05$ and $\beta = 2.25$ listed in the insets correspond to an average sedimentation rate of 11 cm/kyr and TOC content of 1.5 % (with 40 % available organic carbon), respectively. Other seafloor parameters and constants are the same as those listed in Table 6.1 for Blake Ridge Site 997. (A) Site 994, simulated only with a biogenic in situ methane input, shows an isolated gas hydrate layer that does not extend to the base of the GHSZ. Free gas starts at 550 mbsf, leaving a 90 m zone beneath the GHSZ devoid of any free gas, thus explaining the absence of any BSR at this site. (B) Using the same biogenic methane input as in case (A), but with a low upward flux recycling methane back into the GHSZ, gas hydrate as well as free gas extend to the base of the GHSZ at Sites 995 and 997, resulting in BSRs at both these locations.

filing (VSP) data (Holbrook et al., 1996). Gas hydrate saturation averaged over the GHSZ at Site 994 is 0.5%, averaged over the hydrate occurrence zone is 1.2% and the peak saturation close to the base of the GHSZ is 2.1%. For Sites 995 and 997, we use identical upward fluid flux in addition to in situ methane generation, which gives the same saturation profiles for both sites. Figure 6.5b indicates a steady-state where gas hydrate is in contact with free gas at the base of the GHSZ, with average saturation over the GHSZ, over the hydrate occurrence zone and peak saturations of 1.3%, 2.3%, and 5%, respectively.

Site 995 has smaller amounts of gas hydrate compared to Site 997 (Paull et al., 2000), which can be simulated by lowering the net upward fluid flux at this site. This would lower the average gas hydrate saturation, but free gas still forms immediately beneath the hydrate layer. However, due to lack of fluid flow rate data at Site 995, we approximate it by the same flux as that present at Site 997. Free gas beneath the GHSZ occurs as a disconnected phase at Site 995, which cannot be simulated using our simple one-dimensional model. Such features are probably governed by lateral migration of fluids and lithologic heterogeneities, which would require modeling in at least two spatial dimensions. Although our model cannot resolve all these complex features or finer-scale features of hydrate distribution, it gives good average estimates of average gas hydrate saturation at these three sites in the Blake Ridge region.

6.3.3 The Peru Margin

The Peruvian continental margin has been the subject of two previous ODP Legs. While the primary objective of ODP Leg 112 was to study the tectonic evolution of the margin, the more recent Leg 201 was dedicated towards studying microbial life deep beneath the seafloor. Gas hydrates were recovered at two sites cored during Leg 112 (Site 685 and 688), in addition to geochemical evidence for hydrates and BSR occurrence at most of the drilled sites (Kvenvolden and Kastner, 1990). Chloride excursions near the base of the holes indicate hydrate saturation of 10%, 9%, 3% and 9% at Sites 682, 683, 685, and 688, respectively (Kvenvolden and Kastner, 1990). Molecular composition of hydrocarbon gases and the carbon isotopic compositions of methane and carbon dioxide indicate that microbial mediated processes are primarily responsible for methane in the hydrates (Suess and von Heune, 1988; Kvenvolden and Kastner, 1990). An interesting feature of the Peruvian continental margin sediments is the consistently high organic carbon contents at all sites, reaching fractions as high as 8% in the Pliocene to Quaternary section (Suess and von Heune, 1988). For example, TOC content at Site 679 ranges between 1.5-7.8% (averaging $\sim$ 4%) in the Quaternary section and between 1.5-6.5% (averaging $\sim$ 4.7%) in the early Pliocene interval (ten Haven et al., 1990). These observations, along with the high sedimentation rates, clearly indicate a high carbon influx into the system. Additionally, this large carbon input appears to be relatively recent, which implies that this hydrate system might not have achieved steady-state.

Table 6.2: Site-specific data, dimensionless groups and average gas hydrate saturation calculation for Costa Rica Margin and Peru Margin sites.

Site-specific Data	Costa Rica Margin Site 1040	Peru Margin Site 1230	Peru Margin Site 1230
Seafloor depth (m)	4188	5086	5086
Seafloor temperature ($^{\circ}\mathrm{C}$)	2.0	1.7	1.7
Geotherm ($^{\circ}\mathrm{C}/\mathrm{m}$)	0.007	0.034	0.034
Depth of GHSZ (m)	370	715	715
Methane solubility at base of GHSZ ($c^{l}_{m,eqb}$)	1×10^{-3}	3.3×10^{-3}	3.3×10^{-3}
Sedimentation rate $\dot{S}$ (cm/kyr)	10	25	10
CH_4 diffusivity D_m (m^2/s)	10^{-9}	10^{-9}	10^{-9}
Methanogenesis rate λ (s^{-1})	10^{-14}	10^{-14}	10^{-14}
Fluid flux due to sedimentation and compaction $U_{f,sed}$ (m/s)	1.1×10^{-13}	2.6×10^{-13}	1.1×10^{-13}
TOC α_0 (wt.%)	1.0	3.0	3.0
Dimensionless groups			
$\mathrm{Pe}_1 = \frac{U_{f,sed}L_t}{D_m}$	0.04	0.19	0.08
$\mathrm{Da} = \frac{\lambda L_t^2}{D_m}$	1.4	5.1	5.1
$\beta = \frac{(3/4)\alpha_0}{c^{l}_{m,eqb}}$	2.5	6.8	6.8
Organic carbon converted in GHSZ	2.0	4.8	6.4
$\langle S_h \rangle$ (% of pore space)	$<$1.0	4.2	4.9

During Leg 201, Site 1230 was drilled through hydrate bearing sediments on the lower slope of the Peru Trench to study how microbial activities in hydrate sequences differ from sediments that lack hydrate. This site lies close to Site 685 of Leg 112 and is also characterized by modest sedimentation rates (10-25 cm/k.y.) and TOC rich sediments (2-4%) (D'Hondt et al., 2003). Pore water analyses at Site 1230 indicate high microbial activity through elevated DIC, alkalinity and ammonium concentrations (D'Hondt et al., 2003). Hence, we model Site 1230 as a geologic setting dominated by biogenic in situ methane generation. Site-specific parameters and calculation of dimensionless groups is shown in Table 6.2. We use two different sedimentation rates to model Site 1230 and assume an average TOC content of 3 wt.%, with 75% of this organic carbon being available for methanogenesis (Table 6.2).

We explained the use of our contour plot in tracing the geologic history of any gas hydrate province in the previous section (Blake Ridge). As another example of this feature, we plot two points (Figure 6.3) corresponding to different average sedimentation rates of 25 cm/k.y. for the Miocene sequence and 10 cm/k.y. for the Pleistocene sequence at Site 1230 (D'Hondt et al., 2003). The corresponding Pe_1 are 0.19 and 0.08, respectively. With the same TOC for both sedimentation rates, the net amount of methane generated within the GHSZ is 4.2 and 4.9 normalized units, respectively (Table 6.2). On plotting these points on the contour plot (Figure 6.3) we note that the point corresponding to the relatively recent Pleistocene sedimentation rate indicates average gas hydrate saturation of about 4.9%, while the Miocene sedimentation rate yields an average saturation close to 4.2%. Thus,

the gas hydrate system at Peru Margin is probably evolving from a lower average saturation towards a higher average saturation.

This feature is non-intuitive in the sense that lower sedimentation rate would generally imply a lower organic carbon influx to the system, but in this case yields a higher gas hydrate saturation at steady-state. Such behavior can be explained by realizing that decreasing sedimentation rate also decreases the sediment velocity through the GHSZ, thereby allowing more time for the organic carbon to fully convert to methane. If the reaction rate is kept constant, decreasing sedimentation rate beyond some critical value leads to higher average gas hydrate saturation (Bhatnagar et al., 2007).

The analysis presented above assumes that the gas hydrate system has achieved steady state after applying perturbations to the sedimentation rate. However, the high TOC input to the sediments in the Peru Margin appears to be relatively recent, implying that this system might not have achieved steady state. Hence, the average gas hydrate saturation predicted at the recent sedimentation rates might be higher than that inferred from log data at Site 1230. Interstitial water chloride excursions at 80 mbsf and 150 mbsf at Site 1230 coincide with the two intervals from which solid hydrate samples were recovered. These chloride anomalies suggest gas hydrate saturation of about 20% in the pore space (D'Hondt et al., 2003).

6.3.4 The Costa Rica Margin

ODP Leg 170 was dedicated towards studying heat, mass and fluid fluxes in the accretionary complex formed by the subduction of the Cocos plate beneath

the Caribbean plate. Upper plate sediments drilled at Site 1040 indicate a shallow sulfate depleted zone, methane saturated pore waters beneath this SRZ and small amounts of disseminated gas hydrate down to the décollement (Kimura et al., 1997). In contrast, the underthrust sediments are rich in sulfate, have low methane content and exhibit a second sulfate reduction zone beneath the décollement (Kimura et al., 1997). TOC contents in the upper plate sediments at Site 1040 vary slightly, with a mean value of about 1 wt.% (Kimura et al., 1997; Hensen and Wallman, 2005). A large ammonia peak observed at about 150 mbsf indicates high rates of organic decay and in situ methane formation. These observations reflect the importance of methane generation within the upper plate sediments from organic carbon decay and consequently we model the Costa Rica margin sediments as an in situ methane source setting. We acknowledge that due to the given geologic setting, lateral and cross-décollement fluid flow can occur due to compaction of the incoming sediments. Hensen and Wallman (2005) modeled possible effects of such fluid fluxes along with in situ methane generation on the amount of gas hydrate. Application of contour plot (Figure 6.3) to Site 1040 can not include these mixed sources, but will help constrain the amount of gas hydrates accumulating due to in situ methane sources only.

An interesting feature of Site 1040 is the anomalously low geothermal gradient, averaging 7.2 °C/km, which leads to the GHSZ extending over the entire sediment column (Kimura et al., 1997). This leads to the absence of any free gas zone beneath the GHSZ within considerable sediment depth, which might explain the absence of any BSRs on the seismic sections obtained in the Leg 170 study

area. Our model, however, requires specification of the GHSZ depth, L_t, to calculate various dimensionless groups (Table 6.2). Consequently, we set L_t to be equal to the décollement depth ($\sim$ 370 mbsf), which can be justified by low pore water methane contents and absence of other gas hydrate proxies beneath the décollement (Kimura et al., 1997). Thus, we assume $L_t = 370$ mbsf for the calculations and an average sedimentation rate of 10 cm/kyr (Hensen and Wallman, 2005). This leads to $\mathrm{Pe}_1 = 0.04$, $\mathrm{Da} = 1.4$ and normalized TOC input of $\beta = 2.5$ (Table 6.2). In this case the amount of available organic carbon within the TOC is assumed to be 25% for comparison with the results of Hensen and Wallman (2005) for a similar parameter set. On calculating the net amount of methane generated within the GHSZ, the point corresponding to the Site 1040 parameters is plotted in Figure 6.3 at an average gas hydrate saturation of about 0.2%.

Hensen and Wallman (2005) simulated various scenarios to predict gas hydrate saturation at Site 1040, one of them being the case where all methane derives from in situ organic decay. This scenario yields average gas hydrate saturation of 0.8% over the hydrate occurrence zone using transport parameters similar to those stated above. Gas hydrate saturation averaged over the entire GHSZ is always less than that averaged over the occurrence zone, and can be a factor of two or three smaller than the latter value. This indicates an average value over the occurrence zone of about 0.4-0.6% from our method, which is in agreement with the value predicted by Hensen and Wallman (2005). It is also worth mentioning that Site 1040 in Figure 6.3 lies within the region of gas hydrate formation without free gas contact at the base of the GHSZ, which indicates that the gas hydrate

layer does not extend down to the décollement. Interestingly, some of the scenarios simulated by Hensen and Wallman (2005) that included upward fluid flow also indicated this feature. However, absence of free gas beneath the décollement at Site 1040, as predicted by its location in the contour plot, should not be understood as a direct result of our model. In other words, absence of free gas is due to the GHSZ extending all the way to the basement and not due to insufficient supply of methane.

6.4 Conditions Causing Increase in Gas Hydrate Saturation

The contour plot (Figure 6.3) summarizes qualitative and quantitative information about gas hydrate saturations in marine sediments under a host of different seafloor and transport conditions. In addition, it also helps in formulating some general predictions about conditions where gas hydrate might accumulate in large amounts. We first discuss such conditions for hydrate settings with only deeper methane sources (due to their simplicity) and then generalize them for systems with in situ biogenic or mixed methane sources.

6.4.1 Conditions for deeper methane sources

For gas hydrate formation from deeper sources, the analysis is relatively straightforward. Higher net fluid fluxes ($\mathrm{Pe}_1 + \mathrm{Pe}_2$) will give higher gas hydrate saturations, while higher sedimentation rates characterized by Pe_1 will result in lower average saturation. Gas hydrate saturation is thus proportional to the ratio of these two

groups, that is $(\mathrm{Pe}_1 + \mathrm{Pe}_2)/\mathrm{Pe}_1$. Taking this ratio cancels the GHSZ thickness L_t and methane diffusivity from the expressions, so that average saturation becomes a function of the external flux and sedimentation rate only. The thickness of the gas hydrate layer within the GHSZ, however, is only a function of the net flux.

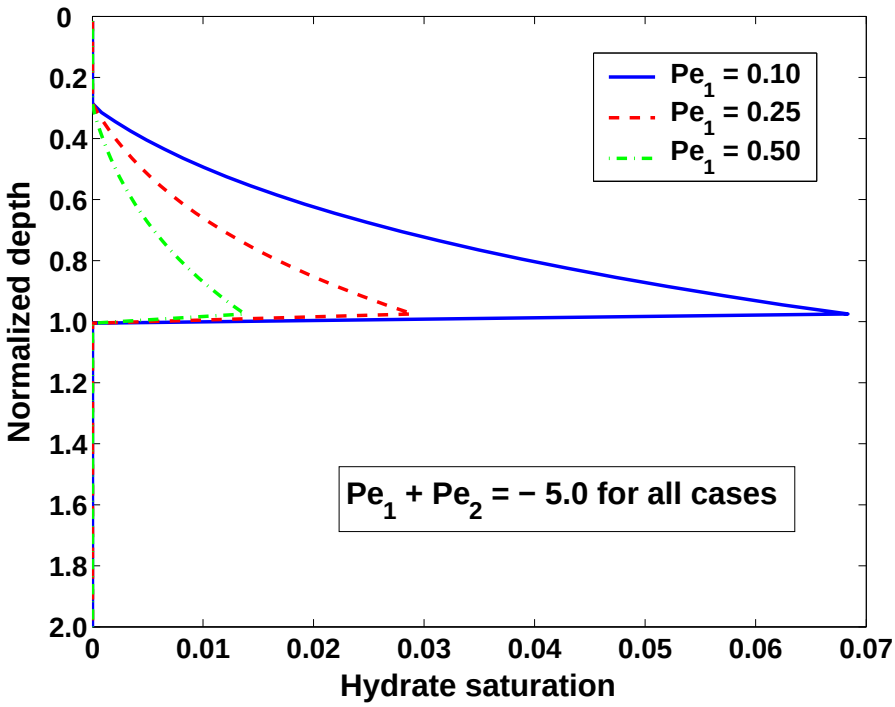

Figure 6.6: Effect of burial rate, as characterized through the Peclet number Pe_1, on steady state gas hydrate saturation profiles from deeper sources of methane. The three simulations represent different Pe_1 for the same net fluid flux $\mathrm{Pe}_1 + \mathrm{Pe}_2$. Increasing Pe_1 results in higher sediment velocities, shorter residence times within the GHSZ and lower gas hydrate saturation. Depth to the top of the gas hydrate layer depends on the net fluid flux $(\mathrm{Pe}_1 + \mathrm{Pe}_2)$, which being constant for all three simulations, fixes the top of hydrate layer to the same depth.

Figure 6.6 shows the variation of gas hydrate thickness and saturation as a function of three different Pe_1, keeping the net fluid flux constant. It can be seen that increasing Pe_1 decreases the saturation within the fixed thickness of about two-thirds of the GHSZ, but does not changes the vertical extent of hydrate occurrence.

The thickness of the gas hydrate layer only depends on the net fluid flux, $\mathrm{Pe}_1 + \mathrm{Pe}_2$, and once this finite zone of hydrate occurrence is fixed by specifying the sum of the Peclet numbers, hydrate saturation at any point within this zone depends on how long this point resides within the GHSZ. The sedimentation rate governs this residence time and, hence, controls the final average saturation. To summarize, for geologic settings with only deeper methane sources, higher gas hydrate saturations at steady state will be possible in systems characterized by high regional fluid fluxes and low sedimentation rates.

6.4.2 Conditions for biogenic in situ methane sources

Predicting general conditions, like those formulated in the previous section, for biogenic in situ sources is not trivial. The effect of the normalized organic content β is simple; increasing it always leads to more organic input and methane generation resulting in higher average gas hydrate saturations as well as thickness of the gas hydrate layer. Increasing the Damkohler number also causes more methane generation within the GHSZ and yields higher saturations. The role of the sedimentation rate, however, is not monotonous because of competing effects. As seen through the two examples of Blake Ridge and Peru Margin, a decrease in sedimentation rates of recent sediments compared to older sequences results in opposite average gas hydrate saturation trends. This happens because Pe_1 is present in both the x-axis and y-axis terms of the contour plot (Figure 6.3), thereby affecting the saturation in different ways. At lower Pe_1, when diffusive losses of methane dominate the system, an increase in sedimentation rate results in more

organic content influx. Average hydrate saturation consequently increases. However, at higher Pe_1 diffusion is no longer a constraint and instead of being controlled by Pe_1 alone, the system now depends on the ratio $\mathrm{Pe}_1/\mathrm{Da}$. This ratio controls the amount of methane generated from in situ sources within the GHSZ. Increase in sedimentation rate now causes shorter residence times for the organic carbon and hydrate phases in the GHSZ, resulting in lower average saturations. Hence, there is no unique answer to gas hydrate saturation behavior in response to changes in sedimentation rate. Based on whether the system is diffusion or advection dominated, hydrate saturation can decrease or increase on lowering the sedimentation rates, respectively.

6.4.3 Conditions for mixed methane sources

A similar argument can be formulated for gas hydrate systems with mixed sources of methane, that is, both in situ biogenic as well as deeper sources. Methane from an external deep source will only come into effect when $|\mathrm{Pe}_2| > |\mathrm{Pe}_1|$, otherwise the net fluid flow will be downwards from the seafloor and the deeper methane will not be advectively transported into the GHSZ. The net behavior of this mixed system will have common elements of each individual system. We first study the effect of the biogenic input parameters (Pe_1, Da, β) and then discuss the role of the external fluid flux (Pe_2).

Similar to the system where biogenic in situ methane is the only source, a mixed source system will have higher gas hydrate saturations for larger values of Da and β. The role of Pe_1, as mentioned before, is not so straightforward. Figure 6.7 shows

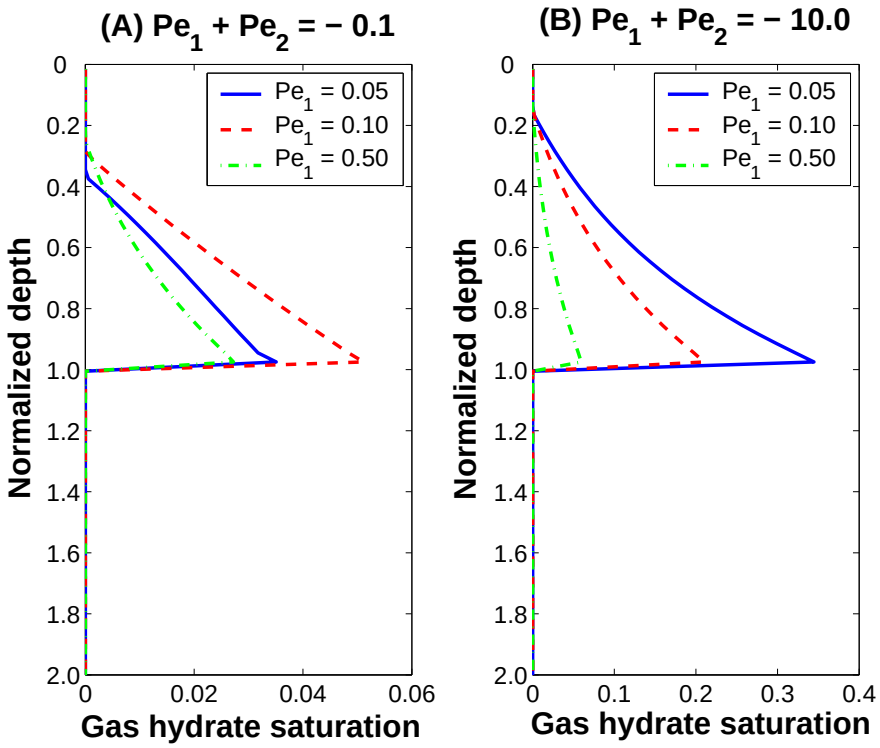

Figure 6.7: Variable effects of Pe_1 on systems with mixed sources of methane. $\mathrm{Da} = 5$ and $\beta = 3$ for all simulations. (A) A diffusive mixed source system ($\mathrm{Pe}_1 + \mathrm{Pe}_2 < 1$) shows that increasing Pe_1 initially causes an increase in gas hydrate saturation due to higher organic carbon flux into the sediments. Further, increase in Pe_1 results in a drop in hydrate saturation because sediment velocity become high enough to cause large amounts of carbon pass through the GHSZ unreacted. (B) For an advective mixed source system ($\mathrm{Pe}_1 + \mathrm{Pe}_2 > 1$) increasing Pe_1 results in a monotonous decrease in gas hydrate saturation due to shorter residence times of the hydrate within the GHSZ.

the opposite effect of Pe_1 on gas hydrate saturation for two cases: diffusion- and advection-dominated systems. For example, when the net fluid flux is upward and small in magnitude, so that diffusion dominates ($\mathrm{Pe}_1 + \mathrm{Pe}_2 < 1$), we observe that increase in sedimentation rates increases the gas hydrate saturation as we go from $\mathrm{Pe}_1 = 0.05$ to $\mathrm{Pe}_1 = 0.1$ (Figure 6.7A). This happens because methane input to the system from below the GHSZ is small at lower values of combined Peclet numbers

and any increase in Pe_1 results in more organic input to the sediments, causing higher hydrate saturation. Further increase in Pe_1 causes the sediments to move faster through the GHSZ causing lesser generation of methane within the stability zone, causing a decrease in hydrate saturation. Hence, for diffusion-dominated systems with mixed sources, on increasing Pe_1, hydrate saturation first increases, reaches a maximum and eventually decreases in value.

At higher net Peclet numbers, fluid advection dominates the system and the methane input is also dominated by this external source. An increase in sedimentation rate for this case results in smaller average gas hydrate saturation, because now the main effect of higher Pe_1 is to move the sediments faster through the GHSZ (Figure 6.7B). This results in shorter residence times of the gas hydrate layer, consequently lowering the average saturation.

Finally, the effect of varying Pe_2, with constant Pe_1, Da and β, is shown in Figure 6.8. The biogenic in situ generation of methane is fixed in this mixed source system and only the upward flux of methane is changed. Pe_2 for the three simulations in Figure 6.8 was varied such that diffusion as well as advection dominated systems are represented. It can be seen that increasing Pe_2 leads to an increase in gas hydrate saturation and makes the top of the gas hydrate layer shallower due to greater recycling of methane back into the GHSZ. To summarize, for mixed source systems, increasing Da, β and Pe_2 always leads to higher gas hydrate saturations. Effect of Pe_1, however, depends on whether the hydrate system is advection- or diffusion-dominated.

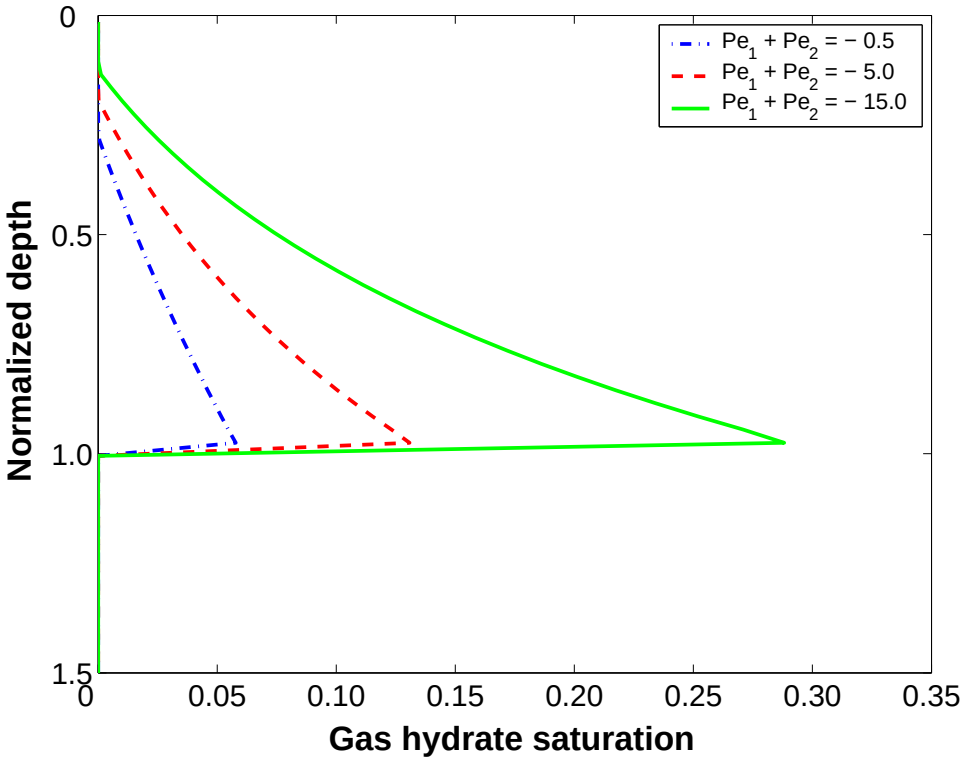

Figure 6.8: Effect of variable upward fluid flux Pe_2 on gas hydrate saturation with constant biogenic in situ methane generation. Pe_1, Da and β were set to 0.1, 5.0 and 3.0,respectively, for all three cases. Keeping biogenic input constant and increasing the magnitude of net methane flux $\mathrm{Pe}_1 + \mathrm{Pe}_2$ (by increasing Pe_2) causes higher steady state gas hydrate saturations as well as shallower depths to the top of the hydrate layer.

6.5 Conclusions

We have developed generalized average gas hydrate saturation contour plots that summarize the saturation dependence on various parameters by scaling dimensionless groups from our numerical model. We used one of these plots, which assumes biogenic in situ generation as the only methane source, to model gas hydrate provinces like Blake Ridge, Peru Margin and Costa Rica Margin. Application of this contour plot to these three distinct settings shows good match between

predicted saturations and those inferred from proxy methods or other numerical simulations. The saturation plot also serves as a simple tool to study the temporal evolution of any gas hydrate system over geologic time-scales. This is achieved by tracking the system's path across the contours in response to the applied perturbation in sedimentation rate and/or TOC content. Based on burial histories of sediment sequences at the Blake Ridge and Peru Margin, it is shown that the former system might be a depleting methane reservoir, whereas the latter might be accumulating more methane to attain higher gas hydrate saturations. Non-intuitive features, such as gas hydrate without free gas contact at steady state and higher gas hydrate saturations at lower sedimentation rates, can also be explained by our contour plot on the basis of different values of dimensionless groups.

We also show that gas hydrate systems without free gas immediately below the hydrate layer can exist in two distinct scenarios. At relatively lower TOC contents, gas hydrate forms but remains isolated within the GHSZ, with no free gas formation below. On increasing the TOC content, simulations show that free gas does form beneath the base of the GHSZ, but remains disconnected from the bottom of the hydrate layer. Further increase in TOC input causes both the hydrate and free gas layers to approach the base of the GHSZ. The general contour plot shows that average gas hydrate saturation within this special regime can achieve significant amounts only at relatively low Pe_1, or low sedimentation rates. These features are collectively used to model presence of hydrate and free gas, but without a BSR at Site 994 (Blake Ridge) using an in situ methane source only. Contact between gas hydrate and free gas at neighboring Sites 995/997 is then explained by using the

same biogenic input, but supplemented by a small upward flux.

General conditions for high gas hydrate saturations are predicted for systems dominated by either of the two sources of methane or a mixture of both. For hydrate systems dominated by deeper sources of methane, high saturations are achieved at high fluid flux and low sedimentation rates, with the thickness of the hydrate layer only depending on the net fluid flux. In situ methanogenesis dominated settings can be divided into diffusive and advective systems, with increase in sedimentation rates causing higher hydrate saturations in the former regime. This behavior is reversed for advection-dominated systems. Thus, apart from giving approximate hydrate saturations for a wide variety of geologic settings, our model also provides physical insight into the processes governing different hydrate systems. Although detailed hydrate saturation profiles cannot be obtained from our contour plot, it gives good estimates averaged over the regional scale without the need of any further numerical simulations.

Chapter 7

Sulfate-Methane Transition as Proxy for Gas Hydrate Saturation (Numerical Model)

7.1 Introduction

Based on the supply of methane, marine gas hydrate systems can be distinguished into two end-members: in situ systems where microbes generate methane within the GHSZ (Claypool and Kvenvolden, 1983); and deep-source systems where rising fluids bring methane from depth (Hyndman and Davis, 1992). However, quantifying gas hydrate abundance in either of the two systems remains a challenge, especially without dedicated drilling. In this chapter, we develop a model to predict gas hydrate saturation in deep-source systems using sulfate-methane transition (SMT) depth below the seafloor as the proxy.

For both gas hydrate systems, SMT denotes a relatively thin zone near the seafloor where pore water sulfate and methane are depleted to zero (Figure 7.1). This co-consumption occurs due to the microbially mediated anaerobic oxidation of methane reaction (AOM: $\mathrm{CH_4 + SO_4^{2-} \rightarrow HCO_3^- + HS^- + H_2O}$) (Borowski et al., 1999). Although microbes can also consume sulfate using solid organic carbon (Berner, 1980), AOM can dominate overall sulfate depletion in sediment sequences with gas hydrates and modest methane fluxes (Borowski et al., 1996; Luff and Wallman,

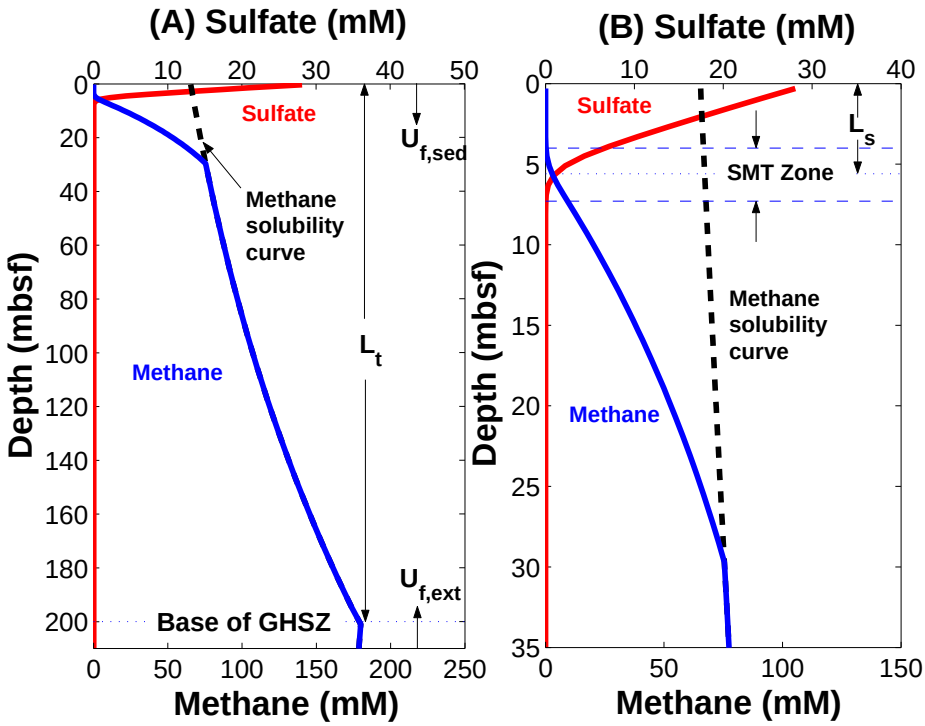

Figure 7.1: (A) Schematic representation of a gas hydrate system showing pore water sulfate and methane concentrations, which go to zero at some shallow depth because of anaerobic oxidation of methane (AOM). Also shown are methane solubility in water, the two fluid fluxes ($U_{f,sed}$ and $U_{f,ext}$), and depth to the base of the gas hydrate stability zone (L_t). (B) Close-up of the sulfate-methane transition (SMT) showing overlap of sulfate and methane profiles, and its depth below the seafloor (L_s).

2003; Snyder et al., 2007). Further, since we focus only on deep-source systems (i.e., sites with low organic carbon input), AOM becomes the only sulfate sink. The sulfate profile and SMT depth in such systems should depend on methane flux from below because of the simple 1:1 AOM reaction (Borowski et al., 1996). Additionally, the vertical extent and abundance of gas hydrate is a function of upward methane flux (Davie and Buffett, 2003a; Luff and Wallman, 2003). Thus, SMT depth (L_s, Figure 7.1) should relate to gas hydrate abundance, with relatively shallow SMTs

indicating elevated methane flux and high gas hydrate content (Borowski et al., 1996, 1999; Davie and Buffett, 2003b; Luff and Wallman, 2003; Coffin et al., 2007).

We previously developed a one-dimensional numerical model that explains the relationship between methane flux and gas hydrate distribution (Bhatnagar et al., 2007). Here, we expand that model by incorporating a SMT for deep source systems (Figure 7.1). We show that, at steady-state conditions, the depth of the SMT relates to net fluid flux in the system and to average gas hydrate saturation (AGHS, expressed as volume fraction of pore space) within the GHSZ. While previous studies have used sulfate profiles to constrain gas hydrate saturations at individual locations (Davie and Buffett, 2003b; Luff and Wallman, 2003), our model generalizes the relationship between SMT depth and AGHS at any gas hydrate setting dominated by methane flux from depth. This enables a first order estimation of AGHS from pore water sulfate profiles.

7.2 Mathematical Model for Gas Hydrate Accumulation and AOM

Gas hydrate accumulation in marine sediment can be simulated using a numerical model that includes phase equilibrium, sedimentation, diffusion, compaction-driven fluid flow, and external fluid flow (Bhatnagar et al., 2007). Figure 7.1 shows the important system parameters governing these processes, along with the two key depths in our model: L_t denoting the dimensional depth of the GHSZ, and L_s representing the dimensional SMT depth below the seafloor. Following Bhatnagar et al. (2007), the three-phase methane mass balance (liquid, gas hydrate and free

gas) can be written to include the AOM reaction in dimensionless form as:

$$\frac{\partial}{\partial \tilde{t}}\left[\frac{1+\gamma\tilde{\phi}}{\gamma}\left(S_w\tilde{c}_m^w + S_h\tilde{c}_m^h\tilde{\rho}_h + S_g\tilde{c}_m^g\tilde{\rho}_g\right)\right]$$
$$+\frac{1+\gamma}{\gamma}\frac{\partial}{\partial \tilde{z}}\left[\left(\mathrm{Pe}_1+|\mathrm{Pe}_2|\right)\tilde{U}_f\tilde{c}_m^w + \mathrm{Pe}_1\tilde{U}_s\frac{1+\gamma\tilde{\phi}}{\gamma\left(1-\tilde{\phi}\right)}(S_h\tilde{c}_m^h\tilde{\rho}_h + S_g\tilde{c}_m^g\tilde{\rho}_g)\right]$$
$$= \frac{\partial}{\partial \tilde{z}}\left[\frac{1+\gamma\tilde{\phi}}{\gamma}S_w\frac{\partial \tilde{c}_m^w}{\partial \tilde{z}}\right] - \mathrm{Da}_{\mathrm{AOM}}\frac{M_{CH_4}c_{s,0}^w}{M_{SO_4}c_{m,eqb}^w}\left(\frac{1+\gamma\tilde{\phi}}{\gamma}S_w\right)\tilde{c}_s^w\tilde{c}_m^w \qquad (7.1)$$

where S_i represents saturation of phase i in pore space, $\tilde{\rho}_i$ is the density of phase i scaled by water density, M_i is molecular weight, and subscripts or superscripts w, h and g denote liquid water, hydrate and free gas phases, respectively. The vertical depth in our model is scaled by the depth of GHSZ ($\tilde{z} = z/L_t$). Consequently, the SMT depth is also shown later in the results as a scaled depth $\tilde{L}_s = L_s/L_t$. Time is made dimensionless by a combination of L_t and methane diffusivity D_m ($\tilde{t} = t/(L_t^2/D_m)$).

Methane mass fraction in phase i (c_m^i) is scaled by methane solubility in the liquid phase at the base of GHSZ ($c_{m,eqb}^w$), while sulfate mass fraction in pore water (c_s^w) is scaled by the seawater value ($c_{s,0}^w$), to get the corresponding normalized variables:

$$\tilde{c}_m^i = \frac{c_m^i}{c_{m,eqb}^w} \quad \text{for} \quad i \in \{w,h,g\} \quad , \quad \tilde{c}_s^w = \frac{c_s^w}{c_{s,0}^w} \qquad (7.2)$$

The reduced porosity parameters, $\tilde{\phi}$ and γ, and normalized sediment flux, $\tilde{U}_s$, are defined as:

$$\tilde{\phi} = \frac{\phi - \phi_\infty}{1 - \phi_\infty} \quad , \quad \gamma = \frac{1 - \phi_\infty}{\phi_\infty} \quad , \quad \tilde{U}_s = \frac{U_s}{U_{f,sed}} \tag{7.3}$$

where ϕ is sediment porosity, ϕ_∞ is the minimum porosity at great depth, and $U_{f,sed}$ is the fluid flux resulting from sedimentation and compaction. Porosity loss can be related to depth using a constitutive relationship between porosity and effective stress assuming hydrostatic pressure (Bhatnagar et al., 2007):

$$\tilde{\phi} = \frac{\eta}{\eta + (1 - \eta)\, e^{\tilde{z}}} \quad , \quad \eta = \frac{\phi_0 - \phi_\infty}{1 - \phi_\infty} \tag{7.4}$$

where η and ϕ_0 are the reduced and actual porosities at the seafloor, respectively. The fluid flux ($U_{f,sed}$) can be related to the seafloor sedimentation rate ($\dot{S}$) and porosities as follows (Davie and Buffett, 2003b):

$$U_{f,sed} = \frac{1 - \phi_0}{1 - \phi_\infty} \dot{S} \phi_\infty \tag{7.5}$$

The two Peclet numbers (Pe_1, Pe_2) and the Damkohler number ($\mathrm{Da}_{\mathrm{AOM}}$) are defined as:

$$\mathrm{Pe}_1 = \frac{U_{f,sed} L_t}{D_m} \ , \ \mathrm{Pe}_2 = \frac{U_{f,ext} L_t}{D_m} \ , \ \mathrm{Da}_{\mathrm{AOM}} = \frac{\rho_w c^w_{m,eqb}}{M_{CH_4}} \frac{\lambda L_t^2}{D_m} \tag{7.6}$$

where $U_{f,ext}$ is the fluid flux due to external sources and λ is the second order rate constant for AOM. Importantly, the first Peclet number (Pe_1) characterizes the ratio of sedimentation driven fluid flux to methane diffusion, while the second Peclet number (Pe_2) represents the ratio of external fluid flux to methane diffusion; the

Damkohler number compares AOM rate to methane diffusion. Finally, we complete the system by formulating the dimensionless sulfate mass balance:

$$\frac{\partial}{\partial \tilde{t}}\left[\frac{1+\gamma\tilde{\phi}}{\gamma}S_w\tilde{c}_s^w\right]+\frac{1+\gamma}{\gamma}\left(\mathrm{Pe}_1+|\mathrm{Pe}_2|\right)\frac{\partial}{\partial \tilde{z}}\left[\tilde{U}_f\tilde{c}_s^w\right]= \\ \frac{\partial}{\partial \tilde{z}}\left[\frac{1+\gamma\tilde{\phi}}{\gamma}S_w\frac{D_s}{D_m}\frac{\partial \tilde{c}_s^w}{\partial \tilde{z}}\right]-\mathrm{Da}_{\mathrm{AOM}}\left(\frac{1+\gamma\tilde{\phi}}{\gamma}S_w\right)\tilde{c}_s^w\tilde{c}_m^w \tag{7.7}$$

where D_s denotes sulfate diffusivity. The following initial and boundary conditions are used for the two mass balances:

$$I.C.: \quad \tilde{c}_s^w(\tilde{z},0)=\tilde{c}_m^w(\tilde{z},0)=0 \tag{7.8}$$

$$B.C.(1): \quad \tilde{c}_s^w(0,t)=1 \quad , \quad \tilde{c}_m^w(0,t)=0 \tag{7.9}$$

$$B.C.(2): \quad \frac{\partial \tilde{c}_s^w}{\partial \tilde{z}}(D,t)=0 \quad , \quad \tilde{c}_m^w(D,t)=\tilde{c}_{m,ext}^w=\frac{c_{m,ext}^w}{c_{m,eqb}^w} \tag{7.10}$$

where $c_{m,ext}^w$ is the methane concentration in the external flux and D denotes the bottom of the model domain.

7.3 Results

Equations (7.1) and (7.7) are solved numerically to obtain steady-state profiles for methane, gas hydrate saturation, and pore-water sulfate. For results shown later, we assume seafloor temperature of 3°C, a geotherm of 0.04°C/m, and pore water salinity representative of standard seawater. Scalings outlined previously make

results relatively insensitive to changes in seafloor temperature and the geotherm (Bhatnagar et al., 2007). The AGHS, however, is more sensitive to seafloor depth. Thus, simulations illustrating the effects of different transport parameters (Figures 7.2 and 7.3) use a seafloor depth of 1000 m, whereas the general relationship between AGHS and SMT depth (Figure 7.4) summarizes results for multiple seafloor depths. Porosity at seafloor (ϕ_0) and at depth (ϕ_∞) are assumed to be 0.7 and 0.1, respectively. Diffusivities D_s and D_m are taken to be 0.56×10^{-9} and 0.87×10^{-9} m^2/s, respectively (Iversen and Jørgensen, 1993), c_m^h is set to 0.134, seawater sulfate concentration equals 28 mM, and ρ_h and ρ_f are assumed to be 930 and 1030 kg/m^3, respectively. At steady state, the external methane concentration ($\tilde{c}^w_{m,ext}$) is not significant, provided it exceeds some minimum threshold required to form hydrate (Bhatnagar et al., 2007). Consequently, we assume in all simulations here that $\tilde{c}^w_{m,ext}$ equals unity.

We first study the effect of $\mathrm{Da_{AOM}}$ on steady-state profiles. For fixed $\mathrm{Pe_1}$ and $\mathrm{Pe_2}$, decreasing $\mathrm{Da_{AOM}}$ results in a relatively thick SMT zone (Figure 7.2a). Higher $\mathrm{Da_{AOM}}$ implies faster consumption of methane and sulfate compared to diffusion, causing a relatively sharp SMT. The SMT is usually less than a few meters at most gas hydrate settings (Borowski et al., 1999; Riedel et al., 2006), so we use a large value of $\mathrm{Da_{AOM}}$ (10^8) in further simulations.

Concentration profiles simulated for three different sets of $\mathrm{Pe_1}$ and $\mathrm{Pe_2}$, but with the sum $\mathrm{Pe_1} + \mathrm{Pe_2}$ held constant at -10, are shown in Figure 7.2b. Overlap of these profiles demonstrates that neither $\mathrm{Pe_1}$ nor $\mathrm{Pe_2}$ individually controls the system, but that their sum determines the concentrations and the scaled SMT depth, $\tilde{L}_s$. This

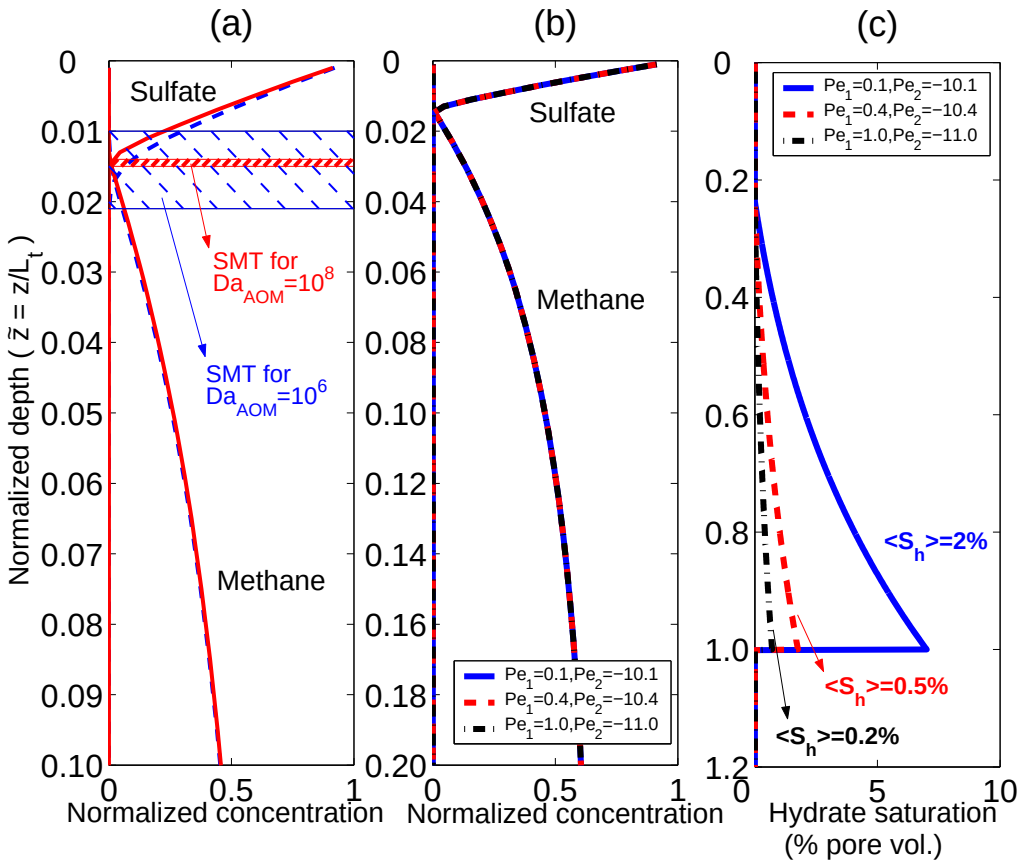

Figure 7.2: Effect of Damkohler number ($\mathrm{Da_{AOM}}$) and Peclet numbers ($\mathrm{Pe_1}$, $\mathrm{Pe_2}$) on steady state profiles. $\mathrm{Pe_1} + \mathrm{Pe_2} = -10$ for all simulations (Note different y-axis scale for each plot). (a) Sulfate and methane profiles for $\mathrm{Da_{AOM}} = 10^8$ (solid curves) and $\mathrm{Da_{AOM}} = 10^6$ (dashed curves). The hatched regions compare the thickness of the SMT zone for the two cases. (b) Simulations for different sets of $\mathrm{Pe_1}$ and $\mathrm{Pe_2}$, but with $\mathrm{Pe_1} + \mathrm{Pe_2} = -10$. Overlap of methane and sulfate profiles shows that the sum $\mathrm{Pe_1} + \mathrm{Pe_2}$ controls the concentrations. (c) Gas hydrate saturation profiles do not depend only on $\mathrm{Pe_1} + \mathrm{Pe_2}$, because different $\mathrm{Pe_1}$ causes distinct residence times of gas hydrate within the GHSZ.

sum, $\mathrm{Pe}_1 + \mathrm{Pe}_2$, represents the net fluid flux through the system. Hydrate saturation profiles, however, depend on more than the sum of the Peclet numbers (Figure 7.2c). The AGHS, denoted $\langle S_h \rangle$, for each of the three cases, is about 0.2%, 0.5% and 2%, with the highest value corresponding to the smallest Pe_1 (0.1) and largest Pe_2 (-10.1). Small Pe_1 and large Pe_2 correspond to low sedimentation rate and high methane flux, respectively. High external flux and low sedimentation rate result in higher methane input to the system and longer residence time for gas hydrate within the GHSZ, causing higher AGHS. However, for all three cases, the product $\mathrm{Pe}_1\langle S_h \rangle$ is the same. Thus, Figure 7.2c demonstrates that this product ($\mathrm{Pe}_1\langle S_h \rangle$), which characterizes the flux of gas hydrate through the GHSZ, is only a function of the net fluid flux, $\mathrm{Pe}_1 + \mathrm{Pe}_2$ (Bhatnagar et al., 2007).

Increasing net methane flux from depth (i.e., raising the magnitude of $\mathrm{Pe}_1 + \mathrm{Pe}_2$) results in a shallow scaled SMT depth (Figure 7.3a), as proposed by Borowski et al. (1996, 1999). Increasing Pe_2, with Pe_1 held constant, increases gas hydrate saturation (Figure 7.3b) due to higher methane input to the system. Consequently, the product $\mathrm{Pe}_1\langle S_h \rangle$ also increases. Hence, the scaled depth to the SMT, $\tilde{L}_s$, and the product $\mathrm{Pe}_1\langle S_h \rangle$ both depend on the sum $\mathrm{Pe}_1 + \mathrm{Pe}_2$. As a consequence, scaled SMT depth and $\mathrm{Pe}_1\langle S_h \rangle$ become correlated (Figure 7.4). Thus, AGHS can be estimated using Figure 7.4 if $\tilde{L}_s$ and Pe_1 are known from site data.

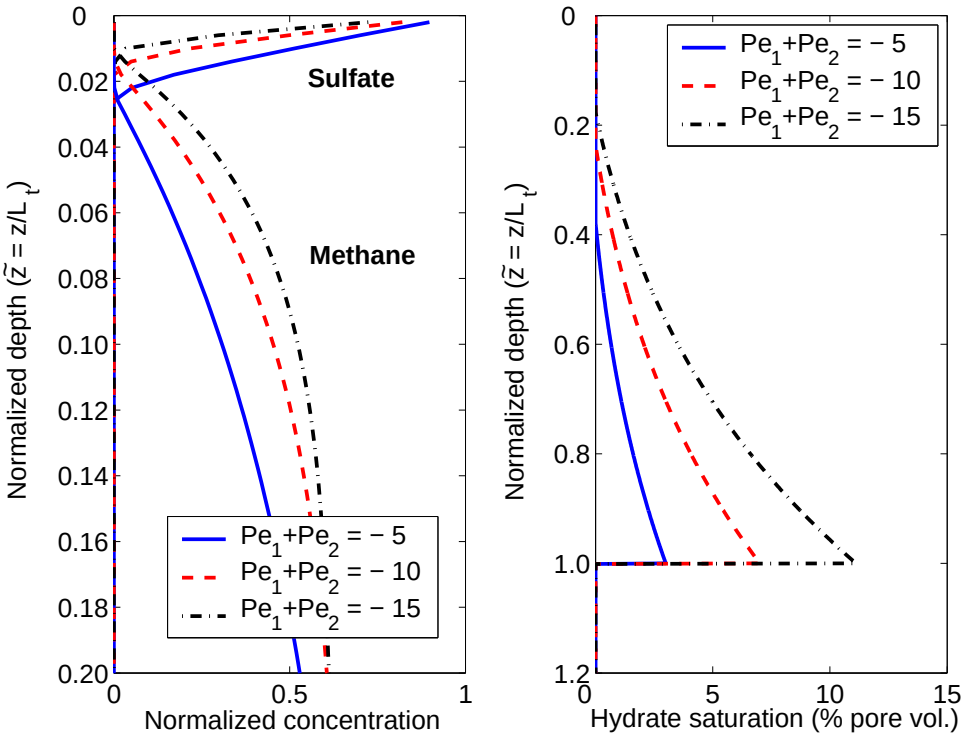

Figure 7.3: Effect of net fluid flux ($\mathrm{Pe}_1 + \mathrm{Pe}_2$) on steady-state concentrations. Pe_1 equals 0.1 for all simulations. (a) High $\mathrm{Pe}_1 + \mathrm{Pe}_2$ defines higher net methane fluxes, resulting in shallower SMT zones. (b) Gas hydrate saturation at steady state increases as $\mathrm{Pe}_1 + \mathrm{Pe}_2$ increases.

7.4 Application to Marine Sites

Sites drilled by Ocean Drilling Program (ODP) Leg 146 and Integrated Ocean Drilling Program Expedition (IODP) 311 penetrate gas hydrate systems along Cascadia Margin (Westbrook et al., 1994; Riedel et al., 2006). The low organic carbon content of sediment and pervasive upward fluid migration at these sites suggests that gas hydrate in the region is controlled by methane supplied from depth (Riedel et al., 2006). The procedure to calculate AGHS, $\langle S_h \rangle$, from site-specific data is now summarized:

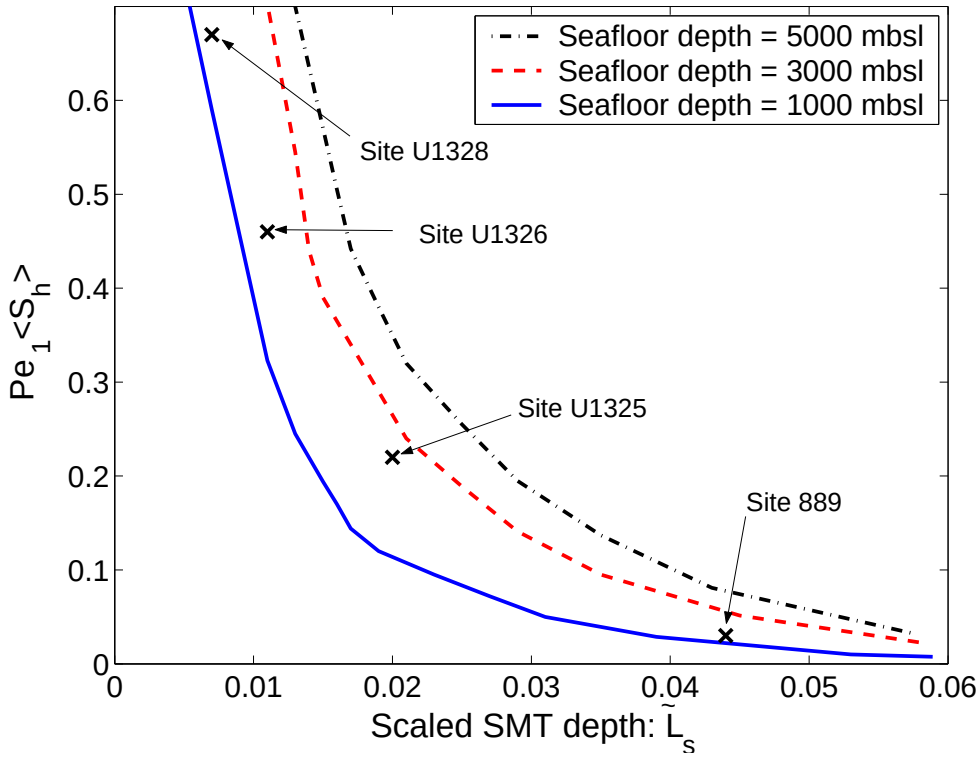

Figure 7.4: Relationship between $\mathrm{Pe_1}\langle \mathrm{S_h} \rangle$ and scaled SMT depth ($\tilde{L}_s = L_s/L_t$) for several seafloor depths. Points corresponding to different Cascadia Margin sites are plotted to show how AGHS can be estimated from $\tilde{L}_s$ using this plot (Table 7.1).

- Use sedimentation rate ($\dot{S}$) to calculate $\mathrm{Pe_1}$ from equations (7.5) and (7.6);
- Calculate the normalized SMT depth $\tilde{L}_s$ using the dimensional depths L_s and L_t;
- For given seafloor depth and $\tilde{L}_s$, obtain average hydrate flux $\mathrm{Pe_1}\langle S_h \rangle$ from Figure 7.4;
- Divide this average hydrate flux by $\mathrm{Pe_1}$ to yield $\langle S_h \rangle$.

These calculations and comparison with estimated AGHS are shown in Table 7.1.

Table 7.1: Site-specific parameters for Cascadia Margin sites

Site	$\dot{S}$ (cm/k.y.)	Pe_1	D_0 (m)	L_s/L_t $=\tilde{L}_s$	$\mathrm{Pe}_1\langle S_h\rangle$	$\langle S_h\rangle$ (calc.)	$\langle S_h\rangle$ (Res.)	$\langle S_h\rangle$ (Cl^-)
889	25	0.07	1311	10/225 =0.044	0.03	0.4%	—	$<$1%
U1325	38.3	0.11	2195	4.5/230 =0.02	0.22	2%	3.7%	5.3%
U1326	38.3	0.11	1828	2.5/230 =0.011	0.46	4.2%	6.7%	5.5%
U1329	34.3	0.09	1267	1.5/219 =0.007	0.67	7.4%	12.6%	—

Site 889 (ODP Leg 146) has been previously modeled as a gas hydrate system dominated by deeper methane sources, with the pore water chloride profile indicating a peak hydrate saturation between 1.5-2% near the base of GHSZ, and AGHS $<$1% within the GHSZ (Davie and Buffett, 2003a). Although several fundamental problems confront such estimates (Egeberg and Dickens, 1999), this result agrees fairly well with our calculated AGHS of 0.4% across the GHSZ, using the SMT as a proxy (Table 7.1).

For the IODP Expedition 311 sites, we compute gas hydrate saturation profiles and AGHS using LWD resistivity log data and Archie parameters given in Riedel et al. (2006) (Table 7.1). Overall, hydrate saturations derived using resistivity logs and those simulated using our model match well, although simulations consistently

have lower AGHS than the log predictions at all four IODP sites. A possible explanation for this deviation is that interpretations of resistivity logs depend on knowledge of formation water resistivity and three empirical constants (Archie, 1942), which are hard to constrain in clay-rich sediments. Additionally, our model-based predictions have gas hydrate first occurring well below the seafloor (Figures 7.2 and 7.3), compared to log-based results that often predict gas hydrate immediately below the seafloor. Apart from the small deviations between model and log predictions, and more importantly, our model captures the variation in average saturations across this transect correctly.

7.5 Conclusions

We show that scaled depth to the SMT can be used to estimate AGHS for deep source gas hydrate systems. Simulation results demonstrate that the net fluid flux uniquely determines the scaled depth to SMT ($\tilde{L}_s$) as well as the average gas hydrate flux ($\mathrm{Pe}_1\langle S_h\rangle$) through the GHSZ. Results also show that shallow scaled SMT depths and low Peclet number (Pe_1) lead to higher hydrate saturations. Application of this method to sites along Cascadia Margin reveals a good match with observed hydrate saturations and accurately predicts lateral variability in gas hydrate saturation.

Chapter 8

Analytical Theory for Sulfate-Methane Transition as Proxy for Gas Hydrate Saturation

8.1 Introduction

Quantitative estimation of the amount of gas hydrate in marine sediment impacts several important areas of research, such as evaluation of hydrates as a potential energy resource (Collett, 2002; Buffett and Archer, 2004; Milkov, 2004), a natural geohazard (Sultan et al., 2004), a component of the global carbon cycle (Dickens, 2003) or an agent of climate change (Dickens et al., 1995; Kennett et al., 2003). Consequently, several geophysical/geochemical techniques have been developed that make use of some anomaly associated with presence of gas hydrates in the sediment (Paull et al., 2000; Hesse, 2003; Tréhu et al., 2004). Pore water anomalies, in particular, have been used in conjunction with coupled transport models to better constrain gas hydrate saturations at different geologic locations. These often include dissolved halides (usually chloride), ammonium and sulfate (Egeberg and Barth, 1999; Ussler and Paull, 2001; Davie and Buffett, 2003a,b; Haeckel et al., 2004; Torres et al., 2004; Hensen and Wallman, 2005; Wallman et al., 2006). Although chloride anomalies seem to be the most widely used proxy in numerical models, predicting gas hydrate saturation requires accurate specification of a base-

line profile (Egeberg and Dickens, 1999). Different choices of this baseline chloride profile will lead to different gas hydrate saturations (Ussler and Paull, 2001). Further, gas hydrate dissociation at the base of the GHSZ causes localized freshening of the pore water, which when brought back into the GHSZ by upward fluxes, can result in a decrease in the chloride anomaly (Ussler and Paull, 2001; Hesse, 2003). Finally, in geologic settings where only shallow piston cores have been collected, gas hydrate saturation cannot be predicted for the depth interval below the cored section.

We develop a simple one-dimensional analytical model that utilizes pore water sulfate profile as the main proxy for gas hydrate saturation. This is motivated by the fact that most of the geologic settings where gas hydrate has been recovered, or inferred to be present, exhibit a relatively shallow sulfate reduction zone (SRZ), along with a sharp sulfate-methane transition (SMT)(Borowski et al., 1999; Tréhu et al., 2004; Riedel et al., 2006). The advantage of this approach is that interpretation of the pore-water sulfate profile does not depend on specification of any baseline curves. Moreover, our analysis differs from the traditional approach that involves simulating gas hydrate distribution using numerical models and then matching them with observed sulfate profiles at a given site (Davie and Buffett, 2003b; Luff and Wallman, 2003; Hensen and Wallman, 2005). We follow the inverse route and predict gas hydrate saturation directly from the sulfate profile.

We have previously developed a numerical model that incorporates a dynamic SMT in gas hydrate simulations (Bhatnagar et al., 2008). It was shown that the net upward fluid flux in the system controls the pore water methane and sulfate

concentration profiles, and thus the depth to the SMT, as well as the average gas hydrate flux through the GHSZ. We simulated several different parameter sets to generalize this relationship, but the simulation methodology suffers from a few disadvantages. First, the entire gas hydrate saturation profile cannot be constructed from the general relationship between SMT depth and gas hydrate flux. New simulations have to be performed to get the saturation profile, which can get computationally expensive in order to resolve the thin SRZ. Second, the relation between gas hydrate flux and SMT depth was generalized in our numerical study for certain parameter values (for example, constant porosity parameters, constant seafloor temperature and depths, geotherm) (Bhatnagar et al., 2008). By deriving analytical expressions, exact solutions can be obtained for the site-specific parameters without performing any simulations.

8.2 Sulfate depletion in marine sediment

Pore-water sulfate depletion in marine sediments is believed to occur through two main reactions. In the absence of methane in the system, sulfate gets reduced through bacterial communities utilizing organic carbon as the substrate (Berner, 1980; Boudreau and Westrich, 1984). The other important sink of sulfate in these systems is the anaerobic oxidation of methane (AOM), which uses dissolved methane for sulfate reduction through the following reaction (Borowski et al., 1996):

$$\mathrm{CH_4 + SO_4^{2-} \quad \longrightarrow \quad HCO_3^- + HS^- + H_2O} \tag{8.1}$$

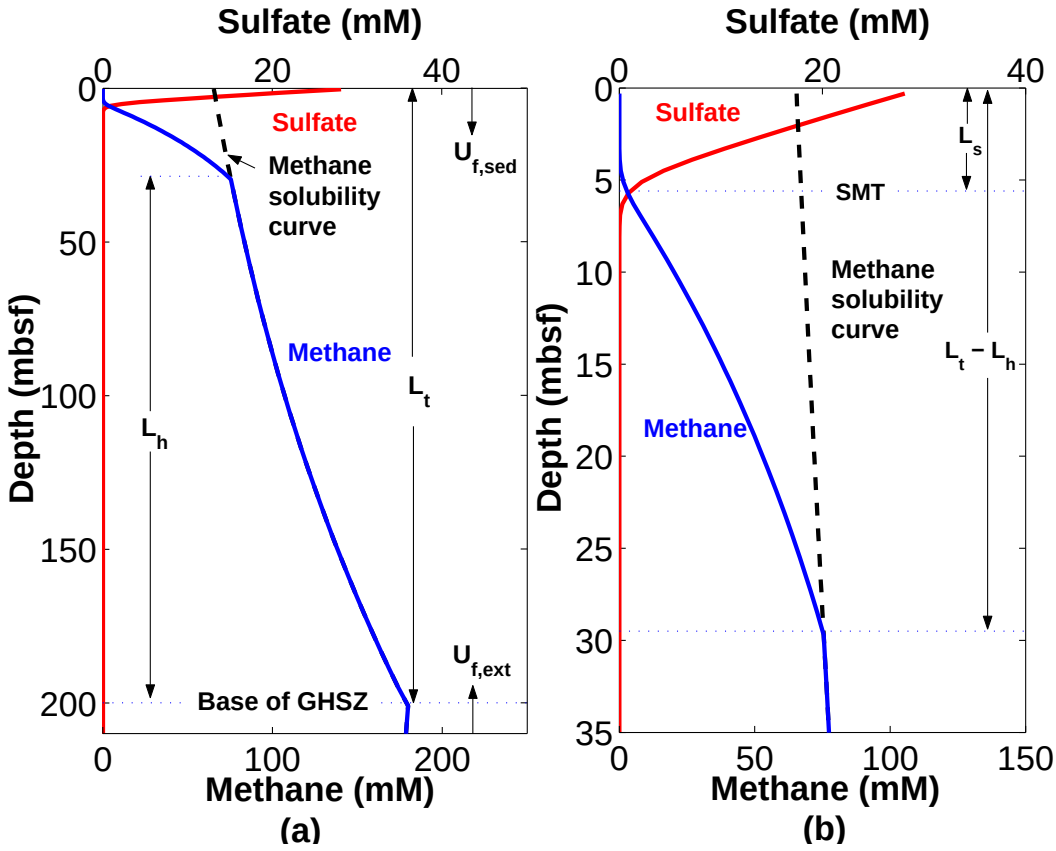

Figure 8.1: (A) Schematic representation of a gas hydrate system showing pore water sulfate and methane concentrations, which go to zero at some shallow depth because of anaerobic oxidation of methane (AOM). Also shown are methane solubility in water, the two fluid fluxes ($U_{f,sed}$ and $U_{f,ext}$), and depth to the base of the gas hydrate stability zone (L_t). (B) Close-up of the sulfate-methane transition (SMT) showing overlap of sulfate and methane profiles, its depth below the seafloor (L_s), and the depth to the top of the gas hydrate layer (L_h).

The presence of gas hydrates in shallow sediments implies a significant methane flux towards the seafloor, which can make this second route for sulfate depletion significant (Borowski et al., 1996; Niewöhner et al., 1998; Davie and Buffett, 2003b; Luff and Wallman, 2003).

Modeling results of Davie and Buffett (2003b) applied to Site 997 of the Blake Ridge region suggest that sulfate depletion is mainly governed by the AOM reaction in the presence of deeper dissolved methane. Recently, Snyder et al. (2007) showed that upward flux of methane approximately balances downward sulfate flux, in accordance with the 1:1 ratio suggested by the AOM reaction, across three sites along Umitaka Spur, Japan Sea. Dominance of the AOM reaction over the organic carbon pathway in depleting sulfate is also suggested by the linearity and factor of 16 variation of sulfate gradients in the Carolina Rise-Blake Ridge region, which cannot be described by the variability of sedimentation rates and TOC content at these sites (Borowski et al., 1996, 1999). The Blake Ridge is characterized by modest TOC content ($\sim$1.5 %, (Paull et al., 2000)). Hence, if sulfate depletion through sedimentary organic carbon is inconsequential in determining the sulfate profile at these sites, we can safely assume the AOM reaction to be the only sulfate sink in our model. This is possible because, as mentioned before, we focus on hydrate settings with low TOC where all methane is supplied by deeper sources only.

8.3 Mathematical Model

In this section we first derive a relationship between sulfate flux and depth of the SMT zone using a steady-state sulfate mass balance. This also enables calculation of the sulfate concentration profile as a function of vertical depth below the seafloor. We then use the equality of molar fluxes of sulfate and methane at the SMT to express the results in terms of the methane flux from depth. This is followed by writing a two-phase methane balance for the system, which links the thickness of the gas hydrate layer and gas hydrate saturation to the methane flux. Finally, by eliminating methane flux between the sulfate and methane mass balances, we show how the SMT depth is related to thickness of the gas hydrate layer and its saturation. All equations are converted to dimensionless form to help reduce the number of free parameters.

The methane flux input to the system from depth would depend on the net fluid flux as well as the methane concentration in the rising pore waters. In this formulation we assume that at steady state the gas hydrate layer extends to the base of GHSZ (due to continuous sedimentation, (Bhatnagar et al., 2007)), and methane concentration in the pore fluid at this depth is set equal to the peak solubility value at the point of three-phase equilibrium.

8.3.1 Sulfate Mass Balance

We start with the sulfate mass balance applied between the seafloor and the SMT. Following assumptions are made while formulating this mass balance:

1. No depletion of sulfate within the SRZ occurs due to reduction by organic carbon;

2. Both methane and sulfate react at the SMT fast enough such that their concentrations go to zero at a single depth.

Geochemical data at most gas hydrate settings suggests that a finite region of sulfate-methane overlap exists, instead of a sharp interface. However, as explained later, we normalize the vertical depth in our model by the depth to the base of the GHSZ. This causes the finite region of sulfate-methane overlap, which is usually a few meters thick, to become thin in the dimensionless form and approach a relatively sharp interface.

We start with the steady-state sulfate mass balance, which is written as:

$$\frac{d}{dz}\left[U_{f,tot}\rho_f c_s^l - \phi\rho_f D_s \frac{dc_s^l}{dz}\right] = 0, \quad 0 < z < L_s \tag{8.2}$$

where $U_{f,tot}$ is the net fluid flux, ρ_f is pore water density, c_s^l is the mass fraction of sulfate in pore water, ϕ denotes porosity, D_s is sulfate diffusivity and L_s is the depth to the SMT (Figure 8.1). The vertical depth z is set to zero at the seafloor and is positive downwards. The mass balance (8.2) implies that the mass flux of sulfate, F_{SO_4}, remains constant within the SRZ, and can be rewritten as:

$$U_{f,tot}\rho_f c_s^l - \phi\rho_f D_s \frac{dc_s^l}{dz} = F_{SO_4}, \quad 0 < z < L_s \tag{8.3}$$

This equation is now expressed in dimensionless form. The vertical depth scale is normalized by L_t, the depth to the base of the GHSZ ($\tilde{z} = z/L_t, \tilde{L}_s = L_s/L_t$), while sulfate concentration is scaled by its seawater value, $c^0_{SO_4}$, to rewrite the mass balance in terms of the normalized concentration ($\tilde{c}^l_s = c^l_s/c^0_{SO_4}$). The total fluid flux is written as the sum of its two components: $U_{f,sed}$ due to sedimentation-compaction and $U_{f,ext}$ due to upward external sources (Appendix A1). This enables us to define two separate Peclet numbers that compare each fluid flux to methane diffusion, as follows:

$$\mathrm{Pe}_1 = \frac{U_{f,sed} L_t}{D_m} \ , \ \mathrm{Pe}_2 = \frac{U_{f,ext} L_t}{D_m} \tag{8.4}$$

The dimensionless sulfate balance (8.3) can now be rewritten as:

$$\left(\frac{1+\gamma}{\gamma}\right)(\mathrm{Pe}_1 + \mathrm{Pe}_2)\,\tilde{c}^l_s - \left(\frac{1+\gamma\tilde{\phi}}{\gamma}\right)\frac{D_s}{D_m}\frac{d\tilde{c}^l_s}{d\tilde{z}} = \left(\frac{1}{1-\phi_\infty}\right)\frac{F_{SO_4}}{\rho_f c^0_{SO_4}}\frac{L_t}{D_m} \quad , \quad 0 < \tilde{z} < \tilde{L}_s \tag{8.5}$$

where $\tilde{\phi}$ is the reduced porosity, γ is $\frac{1-\phi_\infty}{\phi_\infty}$, and ϕ_∞ is the minimum porosity achieved at great depth. The porosity model, assuming hydrostatic pore pressure and equilibrium compaction, and details of non-dimensionalization are given in Appendix A1. To simplify the notation, let us define the following groups:

$$\left(\frac{1+\gamma}{\gamma}\right)(\mathrm{Pe}_1 + \mathrm{Pe}_2) = Q \tag{8.6}$$

$$\left(\frac{1}{1-\phi_\infty}\right)\frac{F_{SO_4}}{\rho_f c^0_{SO_4}}\frac{L_t}{D_m} = f_{SO_4} \tag{8.7}$$

Using these definitions equation, (8.5) can be written as:

$$Q\tilde{c}^l_s - \left(\frac{1+\gamma\tilde{\phi}}{\gamma}\right)\tilde{D}_s\frac{d\tilde{c}^l_s}{d\tilde{z}} = f_{SO_4} \tag{8.8}$$

where $\tilde{D}_s$ is the ratio of sulfate to methane diffusivity. Two boundary conditions are used to get an analytical relationship between sulfate flux and the SMT depth. The first one is applied at the seafloor where the normalized sulfate concentration is equal to unity, while the second is applied at the base of the SRZ, where both methane and sulfate concentration go to zero:

$$\text{B.C.}(1) : \tilde{c}^l_s = 1 \text{ at } \tilde{z} = 0 \tag{8.9}$$

$$\text{B.C.}(2) : \tilde{c}^l_s = 0 \text{ at } \tilde{z} = \tilde{L}_s \tag{8.10}$$

Equation (8.8) can be rearranged using the above B.C.s as:

$$\int_{\tilde{L}_s}^{0}\left(\frac{\gamma}{1+\gamma\tilde{\phi}}\right)d\tilde{z} = \int_0^1\left(\frac{\tilde{D}_s}{Q\tilde{c}^l_s - f_{SO_4}}\right)d\tilde{c}^l_s \tag{8.11}$$

Integrating equation (8.11) yields the following:

$$g(\tilde{z})|_{\tilde{z}=0} - g(\tilde{z})|_{\tilde{z}=\tilde{L}_s} = \frac{\tilde{D}_s}{Q}\ln\left(1-\frac{Q}{f_{SO_4}}\right) \tag{8.12}$$

where $g(\tilde{z})$ represents the integral of the porosity term on the left hand side of equation (8.11), and is written as:

$$g(\tilde{z}) = \frac{\gamma\tilde{z} + \gamma^2 \ln\left(\eta(1+\gamma) + (1-\eta)e^{\tilde{z}}\right)}{1+\gamma} \tag{8.13}$$

The above relation is a non-linear function of the scaled depth $\tilde{z}$. However, for the case of no compaction, $g(\tilde{z})$ can be expressed as a simple linear function of $\tilde{z}$. This can be obtained by setting η to zero, which gives:

$$g(\tilde{z}) = \gamma\tilde{z} \tag{8.14}$$

The function $g(\tilde{z})$ is plotted in Figure 8.2 for different values of the reduced porosity parameters. From here on, we denote function evaluations at a particular depth $\tilde{z}$ simply as $g[\tilde{z}]$, so that $g(\tilde{z})|_{\tilde{z}=0}$ and $g(\tilde{z})|_{\tilde{z}=\tilde{L}_s}$ are written as $g[0]$ and $g[\tilde{L}_s]$, respectively. Rearranging equation (8.12), the following relation is obtained between sulfate flux and SMT depth:

$$f_{SO_4} = \frac{Q}{1 - \exp\left(\frac{Q}{\tilde{D}_s}\left[g[0] - g[\tilde{L}_s]\right]\right)} \tag{8.15}$$

To obtain the steady-state sulfate concentration profile, equation (8.8) is integrated from $[\tilde{z}, \tilde{L}_s]$, which yields a relation similar to equation (8.12), and is written as:

$$g[\tilde{z}] - g[\tilde{L}_s] = \frac{\tilde{D}_s}{Q} \ln\left(1 - \frac{Q\tilde{c}_s^l(\tilde{z})}{f_{SO_4}}\right) \tag{8.16}$$

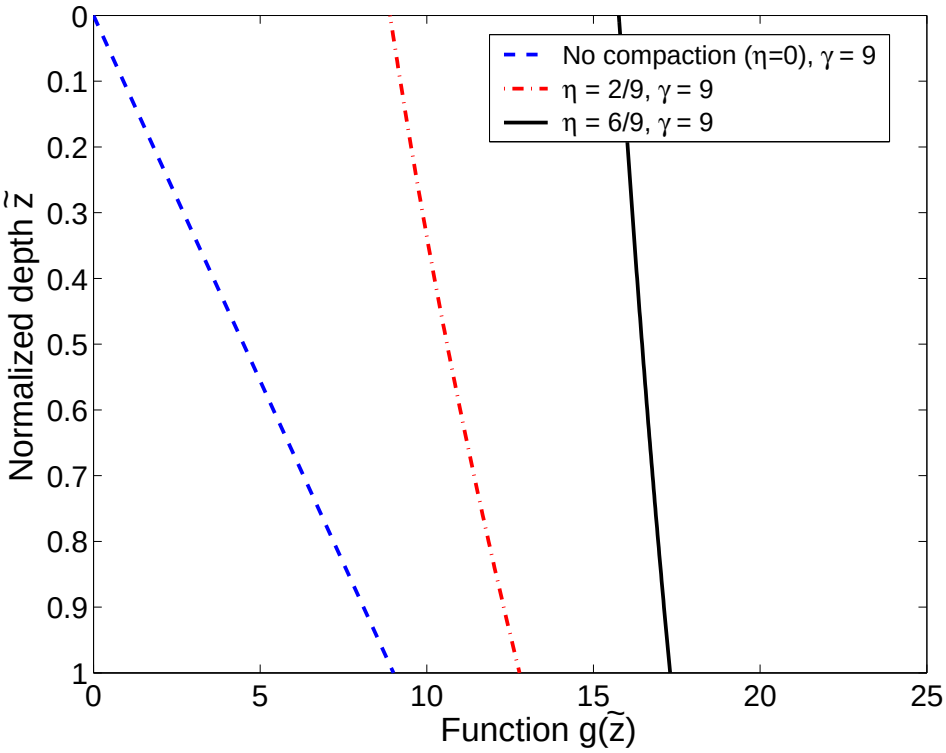

Figure 8.2: The function $g(\tilde{z})$, equation(8.13), plotted for three different porosity parameters. The dashed line represents the case of zero compaction $\eta = 0$, the dash-dot curve represents the case $\eta = 2/9$ (or $\phi_0 = 0.3$), while the solid curve denotes the case $\eta = 6/9$ (or $\phi_0 = 0.7$). The parameter $\gamma = 9$ (or $\phi_\infty = 0.1$) for all cases.

Rearranging the above yields:

$$\frac{Q\tilde{c}_s^l(\tilde{z})}{f_{SO_4}} = 1 - \exp\left(\frac{Q}{\tilde{D}_s}\left(g[\tilde{z}] - g[\tilde{L}_s]\right)\right) \quad , \quad 0 < \tilde{z} < \tilde{L}_s \tag{8.17}$$

Finally, substituting the expression for f_{SO_4} (equation (8.15)) into the above equation gives the sulfate concentration profile at steady-state:

$$\tilde{c}_s(\tilde{z}) = \frac{1 - \exp\left[\frac{Q}{\tilde{D}_s}\left(g[\tilde{z}] - g[\tilde{L}_s]\right)\right]}{1 - \exp\left[\frac{Q}{\tilde{D}_s}\left(g[0] - g[\tilde{L}_s]\right)\right]} \quad , \quad 0 < \tilde{z} < \tilde{L}_s \tag{8.18}$$

This steady-state sulfate concentration profile is a function of the scaled SMT depth, $\tilde{L}_s$, and the net fluid flux, Q. We later show that $\tilde{L}_s$ depends uniquely on Q, which helps us to obtain the sulfate concentration profile by just specifying $\tilde{L}_s$ at a given hydrate site. Thus, sulfate concentration profiles from equation (8.18) for different values of SMT depth ($\tilde{L}_s$) are shown later in the Results section.

8.3.2 Relation between sulfate and methane flux

We now rewrite equation (8.15) in terms of the methane flux from depth. At the base of the SRZ, the magnitude of the molar fluxes of methane and sulfate are equal due to the 1:1 stoichiometry of the AOM reaction. Thus, the sulfate mass flux (F_{SO_4}) can be written in terms of the methane mass flux (F_{CH_4}) from below as follows:

$$F_{SO_4} = -\frac{M_{SO_4}}{M_{CH_4}} F_{CH_4} \quad \text{at} \quad \tilde{z} = \tilde{L}_s \tag{8.19}$$

where M_i denotes molecular weight. Substituting equation (8.19) into equation (8.7) yields:

$$f_{SO_4} = -\left(\frac{1}{1-\phi_\infty}\right) \frac{1}{\rho_f c^0_{SO_4}} \frac{M_{SO_4}}{M_{CH_4}} \frac{L_t}{D_m} F_{CH_4} \tag{8.20}$$

To simplify the notation, we define the following relationship:

$$f_{CH_4} = \left(\frac{1}{1-\phi_\infty}\right)\frac{F_{CH_4}}{\rho_f c^l_{m,eqb}}\frac{L_t}{D_m} \tag{8.21}$$

where $c^l_{m,eqb}$ is the methane solubility at the base of GHSZ. Using this notation, equation (8.20) is used to express the dimensionless methane flux in terms of the dimensionless sulfate flux:

$$f_{CH_4} = -f_{SO_4}/m \quad , \quad \text{where} \quad m = \frac{M_{SO_4}}{M_{CH_4}}\frac{c^l_{m,eqb}}{c^0_{SO_4}} \tag{8.22}$$

To summarize, in this section we obtained an expression between the scaled SMT depth ($\tilde{L}_s$) and methane flux (f_{CH_4}), which is rewritten below using equations (8.15) and (8.22):

$$f_{CH_4} = -f_{SO_4}/m = \frac{Q/m}{1-\exp\left[\frac{Q}{\tilde{D}_s}\left(g[0]-g[\tilde{L}_s]\right)\right]} \tag{8.23}$$

8.3.3 Methane mass balance

We now perform mass balances on methane and water and apply them to two distinct spatial domains. The first domain extends from the SMT to the top of the gas hydrate layer, whereas the second domain extends from the top of the gas hydrate layer to the base of the GHSZ (Figure 8.1). These two mass balances, coupled with the sulfate balance in the previous section, are used to solve the unknowns using SMT depth as an input.

Following is the two-phase (aqueous and hydrate), steady-state, methane mass

balance, valid from the SMT depth to the base of the GHSZ:

$$\frac{\partial}{\partial z}\left[U_f c_m^l \rho_f + \frac{U_s}{1-\phi}\phi S_h c_m^h \rho_h - \phi(1-S_h)\rho_f D_m \frac{\partial c_m^l}{\partial z}\right] = 0 \quad , \quad L_s < z < L_t \tag{8.24}$$

where U_s denotes sediment flux, S_h denotes gas hydrate saturation (volume fraction of pore space), and c_m^h is the methane mass fraction in the hydrate phase (a constant, $c_m^h = 0.134$ for structure I hydrate (Sloan and Koh, 2007). This methane flux invariance can be restated as:

$$U_f c_m^l \rho_f + \frac{U_s}{1-\phi}\phi S_h c_m^h \rho_h - \phi(1-S_h)\rho_f D_m \frac{\partial c_m^l}{\partial z} = F_{CH_4} \quad , \quad L_s < z < L_t \tag{8.25}$$

where F_{CH_4}, defined before, is the methane mass flux. To non-dimensionalize the above equation, we scale sediment flux by $U_{f,sed}$, methane mass fractions by methane solubility at the base of the GHSZ ($c_{m,eqb}^l$) and gas hydrate density by the pore water density, as follows:

$$\tilde{U}_s = \frac{U_s}{U_{f,sed}} \ , \ \tilde{c}_m^l = \frac{c_m^l}{c_{m,eqb}^l} \ , \ \tilde{c}_m^h = \frac{c_m^h}{c_{m,eqb}^l} \ , \ \tilde{\rho}_h = \frac{\rho_h}{\rho_f} \tag{8.26}$$

Using the water mass balance, the methane mass balance is written in the follow-

ing dimensionless form (see Appendix A2):

$$Q\tilde{c}_m^l + \frac{\mathrm{Pe}_1\tilde{U}_s}{1-\tilde{\phi}}\left(\frac{1+\gamma}{\gamma}\right)\left(\frac{1+\gamma\tilde{\phi}}{\gamma}\right)S_h\tilde{\rho}_h\left(\tilde{c}_m^h - c_w^h\tilde{c}_m^l\right) - \left(\frac{1+\gamma\tilde{\phi}}{\gamma}\right)(1-S_h)\frac{\partial\tilde{c}_m^l}{\partial\tilde{z}} = f_{CH_4}, \quad \tilde{L}_s < \tilde{z} < 1 \tag{8.27}$$

where the terms Q and f_{CH_4} have been defined previously (equations (8.6) and (8.21)).

Region 1: From SMT to top of hydrate layer

The methane mass balance (8.27) is first applied to the region extending from the SMT to the top of the hydrate layer. Let the thickness of the gas hydrate layer be L_h, which implies that depth from the seafloor to the top of the gas hydrate layer is $L_t - L_h$. In normalized form, the thickness of the gas hydrate layer becomes $\tilde{L}_h = L_h/L_t$, while depth to the top of hydrate is $(1-\tilde{L}_h)$. This region ($z < 1-\tilde{L}_h$) does not contain any hydrate, so that equation (8.27) can be simplified by setting $S_h = 0$:

$$Q\tilde{c}_m^l - \left(\frac{1+\gamma\tilde{\phi}}{\gamma}\right)\frac{\partial\tilde{c}_m^l}{\partial\tilde{z}} = f_{CH_4}\ , \ \tilde{L}_s < \tilde{z} < 1-\tilde{L}_h \tag{8.28}$$

Methane concentration in this region ($\tilde{L}_s < \tilde{z} < 1-\tilde{L}_h$) is bounded by zero at the depth of SMT ($\tilde{L}_s$) and by the methane solubility curve at the top of the gas hydrate

layer. Hence, the two boundary conditions for this equation are:

$$\text{B.C.}(1) : \tilde{c}_m^l = 0 \quad \text{at} \quad \tilde{z} = \tilde{L}_s \tag{8.29}$$

$$\text{B.C.}(2) : \tilde{c}_m^l = \tilde{c}_{m,sol}(\tilde{z})|_{\tilde{z}=1-\tilde{L}_h} \quad \text{at} \quad \tilde{z} = 1 - \tilde{L}_h \tag{8.30}$$

where $\tilde{c}_{m,sol}(\tilde{z}) = c_{m,sol}(\tilde{z})/c^l_{m,eqb}$ is the normalized methane solubility curve within the GHSZ (i.e., methane mass fraction in pore water in equilibrium with gas hydrate) as a function of the scaled depth $\tilde{z}$. Similar to the function $g[\tilde{z}]$, we denote function evaluations of the solubility curve as $\tilde{c}_{m,sol}[\tilde{z}]$, so that $\tilde{c}_{m,sol}(\tilde{z})|_{\tilde{z}=1-\tilde{L}_h}$ is simply denoted as $\tilde{c}_{m,sol}[1-\tilde{L}_h]$. Analogous to the solution of the sulfate balance, equation (8.28) can be integrated with the above boundary conditions as:

$$\int_{\tilde{L}_s}^{1-\tilde{L}_h} \left(\frac{\gamma}{1+\gamma\tilde{\phi}}\right) d\tilde{z} = \int_0^{\tilde{c}_{m,sol}[1-\tilde{L}_h]} \left(\frac{1}{Q\tilde{c}_m^l - f_{CH_4}}\right) d\tilde{c}_m^l \tag{8.31}$$

Using the function $g[\tilde{z}]$ defined in equation (8.13), the above equation is written as:

$$g[1-\tilde{L}_h] - g[\tilde{L}_s] = \frac{1}{Q} \ln\left(1 - \frac{Q\tilde{c}_{m,sol}[1-\tilde{L}_h]}{f_{CH_4}}\right) \tag{8.32}$$

which can be rearranged to yield the methane flux in terms of the two scaled depths ($\tilde{L}_s$ and $\tilde{L}_h$):

$$f_{CH_4} = \frac{Q\tilde{c}_{m,sol}[1-\tilde{L}_h]}{1 - \exp\left[Q\left(g[1-\tilde{L}_h] - g[\tilde{L}_s]\right)\right]} \tag{8.33}$$

The solution to the methane concentration profile in this region is obtained in a manner similar to the sulfate concentration profile discussed in section 8.3.1. The

steady-state methane concentration profile is:

$$\tilde{c}_m(\tilde{z}) = \tilde{c}_{m,sol}[1-\tilde{L}_h]\frac{1-\exp\left[Q\left(g[\tilde{z}]-g[\tilde{L}_s]\right)\right]}{1-\exp\left[Q\left(g[1-\tilde{L}_h]-g[\tilde{L}_s]\right)\right]} \;,\; \tilde{L}_s < \tilde{z} < 1-\tilde{L}_h \quad (8.34)$$

Region 2: From the top of hydrate layer to the base of GHSZ

The general methane mass balance equation (8.27) is now applied to the region extending from the top of hydrate layer to the base of the GHSZ. In this region, the pore-water methane concentration is constrained by the solubility curve, which was defined previously as $\tilde{c}_{m,sol}[\tilde{z}]$. Thus, instead of pore-water methane concentration, gas hydrate saturation (S_h) becomes the primary dependent variable. Substituting $\tilde{c}_{m,sol}[\tilde{z}]$ for the pore-water concentration $\tilde{c}^l_m(\tilde{z})$ into equation (8.27), we get the following expression in terms of gas hydrate saturation as the main variable:

$$\begin{aligned} Q\tilde{c}_{m,sol}[\tilde{z}] + \frac{\mathrm{Pe}_1\tilde{U}_s}{1-\tilde{\phi}}\left(\frac{1+\gamma}{\gamma}\right)\left(\frac{1+\gamma\tilde{\phi}}{\gamma}\right) \\ S_h\tilde{\rho}_h\left(\tilde{c}^h_m - c^h_w\tilde{c}_{m,sol}[\tilde{z}]\right) - \left(\frac{1+\gamma\tilde{\phi}}{\gamma}\right)(1-S_h)\tilde{c}'_{m,sol}[\tilde{z}] \\ = f_{CH_4} \quad , \quad 1-\tilde{L}_h < \tilde{z} < 1 \end{aligned} \quad (8.35)$$

where $\tilde{c}'_{m,sol}[\tilde{z}]$ denotes the derivative of the solubility curve at any given depth $\tilde{z}$.

Several previous simulation studies have shown that gas hydrate saturation monotonously increases from zero at the top of the gas hydrate layer to a maximum value at the base of the GHSZ (Davie and Buffett, 2001, 2003a; Bhatnagar et al.,

2007, 2008). We use this observation to impose the constraint that gas hydrate saturation goes to zero as the top of the hydrate layer is approached. This condition can be written mathematically as:

$$S_h \to 0 \quad \text{as} \quad \tilde{z} \to (1 - \tilde{L}_h)^+ \tag{8.36}$$

Substituting the above condition into equation (8.35) gives:

$$Q\tilde{c}_{m,sol}[\tilde{z}] - \left(\frac{1+\gamma\tilde{\phi}}{\gamma}\right)\tilde{c}'_{m,sol}[\tilde{z}] = f_{CH_4}\ ,\ \tilde{z} \to (1 - \tilde{L}_h)^+ \tag{8.37}$$

We now have three equations (8.23, 8.33, 8.37) in terms of four unknowns ($\tilde{L}_s$, f_{CH_4}, Q, and $\tilde{L}_h$). Hence, by using scaled SMT depth ($\tilde{L}_s$) as an input from site data, the other three unknowns can be calculated. The next section illustrates this procedure, whereas the complete steps to perform the overall calculation are summarized in the Results section.

8.3.4 Coupled equations for $\tilde{L}_s$ and $\tilde{L}_h$

In this section, we obtain two non-linear coupled equations in terms of the three variables $\tilde{L}_s$, $\tilde{L}_h$, and Q. This is achieved by eliminating f_{CH_4} from the three mass balance equations (8.23, 8.33, 8.37). First, we eliminate f_{CH_4} between equations (8.23) and (8.33), which amounts to equating the sulfate flux to the methane flux from depth at the SMT:

$$\frac{-Q/m}{1-\exp\left[\frac{Q}{\tilde{D}_s}\left(g[0]-g[\tilde{L}_s]\right)\right]}=\frac{Q\tilde{c}_{m,sol}[1-\tilde{L}_h]}{1-\exp\left[Q\left(g[1-\tilde{L}_h]-g[\tilde{L}_s]\right)\right]} \tag{8.38}$$

Second, we equate methane flux in the region containing dissolved methane to the methane flux in the region containing gas hydrate. This helps to eliminate f_{CH_4} between equations (8.33) and (8.37), yielding:

$$\frac{Q\tilde{c}_{m,sol}[1-\tilde{L}_h]}{1-\exp\left[Q\left(g[1-\tilde{L}_h]-g[\tilde{L}_s]\right)\right]}=Q\tilde{c}_{m,sol}[1-\tilde{L}_h]-\left(\frac{1+\gamma\tilde{\phi}}{\gamma}\right)\tilde{c}'_{m,sol}[1-\tilde{L}_h] \tag{8.39}$$

Thus, once $\tilde{L}_s$ is known for a particular site, equations (8.38) and (8.39) can be solved iteratively (e.g., using a Newton-Raphson and/or bisection algorithm) to get the scaled thickness $\tilde{L}_h$ and modified sum of Peclet numbers (Q). Apart from $\tilde{L}_s$, the site-specific parameters needed to completely specify the system include the minimum and maximum reduced porosities (γ and η, Appendix A1), diffusivity ratio ($\tilde{D}_s$), parameter m (eq. (8.22)), and the methane solubility curve within the GHSZ ($\tilde{c}_{m,sol}[\tilde{z}]$).

It should be noted that the Peclet numbers occur in equations (8.38) and (8.39) as the modified sum, Q, rather than Pe_1 or Pe_2. This implies that we do not need to know their individual values to calculate the steady-state concentration profiles or $\tilde{L}_h$. However, to compute the gas hydrate saturation profile, Pe_1 needs to be specified, which is discussed next.

8.3.5 Gas hydrate saturation profile

A major advantage of our formulation is that it gives an analytical expression for the steady-state gas hydrate saturation profile below the top of the hydrate layer through equation (8.35). This equation can be rewritten as:

$$\frac{\mathrm{Pe}_1 \tilde{U}_s}{1-\tilde{\phi}} \left(\frac{1+\gamma}{\gamma}\right) \left(\frac{1+\gamma\tilde{\phi}}{\gamma}\right) S_h \tilde{\rho}_h \left(\tilde{c}_m^h - c_w^h \tilde{c}_{m,sol}[\tilde{z}]\right) - \left(\frac{1+\gamma\tilde{\phi}}{\gamma}\right)(1-S_h)\tilde{c}'_{m,sol}[\tilde{z}] = f_{CH_4} - Q\tilde{c}_{m,sol}[\tilde{z}] \quad , \quad 1-\tilde{L}_h < \tilde{z} < 1 \tag{8.40}$$

On rearranging, the gas hydrate saturation profile is written as a function of the scaled depth $\tilde{z}$, as follows:

$$S_h = \frac{\left(\frac{f_{CH_4} - Q\tilde{c}_{m,sol}[\tilde{z}]}{\left(\frac{1+\gamma\tilde{\phi}}{\gamma}\right)}\right) + \tilde{c}'_{m,sol}[\tilde{z}]}{\left[\frac{\mathrm{Pe}_1\tilde{U}_s}{1-\tilde{\phi}} \frac{1+\gamma}{\gamma} \tilde{\rho}_h \left(\tilde{c}_m^h - c_w^h \tilde{c}_{m,sol}\left[\tilde{z}\right]\right) + \tilde{c}'_{m,sol}[\tilde{z}]\right]}, \quad 1-\tilde{L}_h < \tilde{z} < 1 \tag{8.41}$$

As mentioned in the previous section, specifying $\tilde{L}_s$ allows calculation of $\tilde{L}_h$ and Q through solution of the coupled equations (8.38) and (8.39). Substituting these variables into any of the methane flux expressions (for example, equation (8.33)) yields the methane flux f_{CH_4}. Using these values of $\tilde{L}_h$, Q, f_{CH_4}, and other system parameters, equation (8.41) gives the complete gas hydrate saturation profile within the GHSZ.

8.3.6 Relating gas hydrate flux to scaled SMT depth

We have shown through numerical simulations that the steady state gas hydrate flux through the GHSZ is related to the scaled SMT depth, through their dependence on the net fluid flux in the system (Bhatnagar et al., 2007). The average gas hydrate flux was defined as the product of the Peclet number , Pe_1, and gas hydrate saturation averaged over the entire GHSZ, $\langle S_h \rangle$. This relationship helps in the estimation of $\langle S_h \rangle$ from $\tilde{L}_s$ (Bhatnagar et al., 2007). We now show that this dependence can also be derived from our analytical formulation.

The first term in the denominator of equation (8.41) contains the expression $\left(\tilde{c}_m^h - c_w^h \tilde{c}_{m,sol}[\tilde{z}]\right)$, where $\tilde{c}_m^h$ was defined as $\tilde{c}_m^h = c_m^h / c_{m,eqb}^l$, which for most marine systems is of the order of $\tilde{c}_m^h = 0.134/10^{-3} \approx 10^2$. The other two terms $c_w^h \tilde{c}_{m,sol}\,[\tilde{z}]$ and $\tilde{c}'_{m,sol}[\tilde{z}]$ are usually less than unity. This implies that $\tilde{c}_m^h$ will be about two orders in magnitude greater than the other terms in the denominator and this approximation helps us to simplify equation (8.41) as follows:

$$S_h \approx \frac{\left(\frac{f_{CH_4} - Q\tilde{c}_{m,sol}[\tilde{z}]}{\left(\frac{1+\gamma\tilde{\phi}}{\gamma}\right)}\right) + \tilde{c}'_{m,sol}[\tilde{z}]}{\frac{\mathrm{Pe}_1 \tilde{U}_s}{1-\tilde{\phi}} \left(\frac{1+\gamma}{\gamma}\right) \tilde{\rho}_h \tilde{c}_m^h}\,,\ 1 - \tilde{L}_h < \tilde{z} < 1 \tag{8.42}$$

Finally, the above equation can be written in terms of the product $\mathrm{Pe}_1 S_h$:

$$\mathrm{Pe}_1 S_h \approx \frac{\left(\frac{f_{CH_4} - Q\tilde{c}_{m,sol}[\tilde{z}]}{\left(\frac{1+\gamma\tilde{\phi}}{\gamma}\right)}\right) + \tilde{c}'_{m,sol}[\tilde{z}]}{\frac{\tilde{U}_s}{1-\tilde{\phi}} \left(\frac{1+\gamma}{\gamma}\right) \tilde{\rho}_h \tilde{c}_m^h}\,,\ 1 - \tilde{L}_h < \tilde{z} < 1 \tag{8.43}$$

Equation (8.43) can be integrated over depth to give the term $\mathrm{Pe}_1 \langle S_h \rangle$ as a function

of the system parameters:

$$\mathrm{Pe}_1\langle S_h\rangle \approx \int_{1-\tilde{L}_h}^{1} \frac{\left(\frac{f_{CH_4}-Q\tilde{c}_{m,sol}[\tilde{z}]}{\left(\frac{1+\gamma\tilde{\phi}}{\gamma}\right)}\right)+\tilde{c}'_{m,sol}[\tilde{z}]}{\frac{\tilde{U}_s}{1-\tilde{\phi}}\left(\frac{1+\gamma}{\gamma}\right)\tilde{\rho}_h\tilde{c}^h_m} d\tilde{z} \tag{8.44}$$

8.3.7 Maximum SMT depth for a given system

One of the assumptions in the previous analysis is that gas hydrate exists within the GHSZ, and at steady-state extends to the base of the GHSZ. However, if the upward methane flux is low, pore-water methane concentration might not exceed the local solubility and will result in no hydrate formation. This situation is depicted schematically in Figure 8.3, which compares methane and sulfate concentration profiles for two distinct methane fluxes. For relatively low fluxes (dashed set of curves), methane concentration does not exceed the local solubility anywhere within the GHSZ, causing no hydrate formation. A finite SMT still exists for this case. Progressively increasing the methane flux from depth will cause methane concentration to approach the solubility curve and for a certain value of this flux, the methane concentration becomes equal to the solubility curve at some depth within the GHSZ. This case, depicted by the solid set of curves, corresponds to the minimum methane flux required for gas hydrates to form. Any methane flux greater than this minimum will have a SMT as well as finite gas hydrate saturation within the GHSZ.

Hence, gas hydrate systems sourced by deeper methane are characterized by a minimum flux required to form hydrates, with the actual value being dependent on

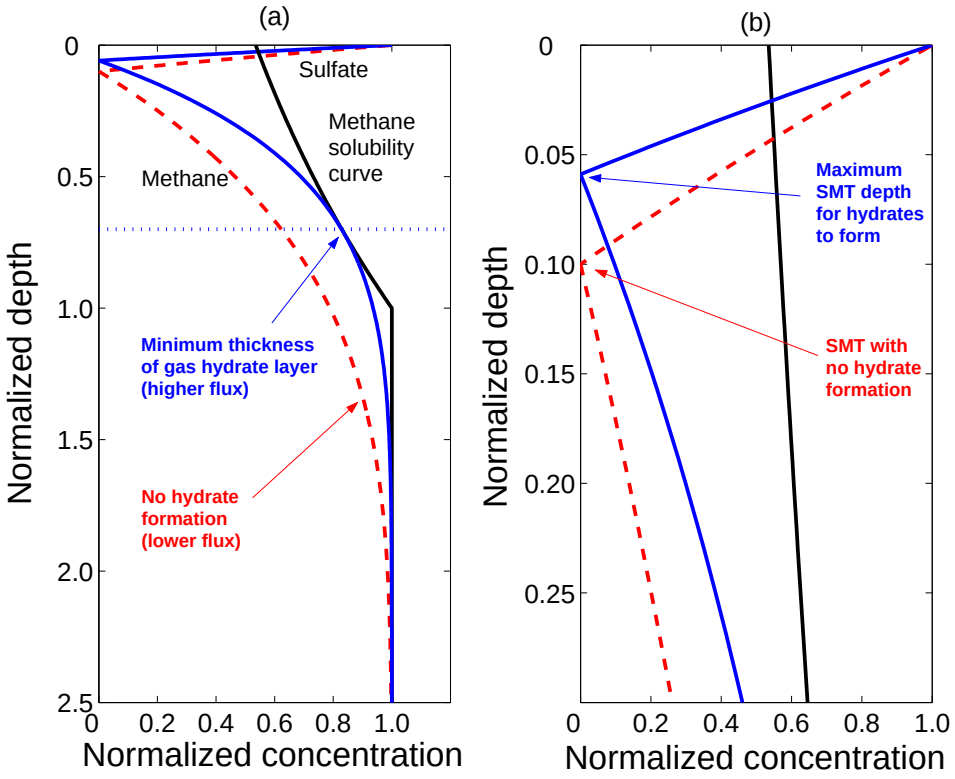

Figure 8.3: (a) Schematic representation of a gas hydrate system showing effect of upward fluid fluxes on pore water sulfate and methane concentration profiles. The solid curves represent the minimum flux case for which the methane concentration just exceeds the local solubility curve, causing hydrates to form. Any fluid flux lower than this minimum value (dashed curves) will not be able to exceed the solubility curve or form any gas hydrate, though a relatively deeper SMT will still exist. (b) Close-up of the same plot showing the maximum allowed SMT depth (solid curves) for a given gas hydrate system. The deeper SMT depth (dashed curves) exceeds the maximum allowed value, implying no gas hydrate formation for this case.

the solubility curve and the methane concentration in the rising fluids. This feature indirectly imposes a maximum limit on the SMT depth (for hydrates to precipitate) as well as a minimum thickness of the gas hydrate layer, $\tilde{L}_{h,min}$. We now derive expressions for these limits.

Gas hydrates start to precipitate when the methane concentration curve just becomes equal to the solubility curve, which can be mathematically imposed by requiring the two curves to become tangential to each other. Let this tangency occur at depth $\tilde{z} = 1 - \tilde{L}_{h,min}$, which marks the minimum thickness of the gas hydrate layer. The following two conditions can then be imposed:

$$\tilde{c}^{l}_{m}(\tilde{z})|_{\tilde{z}=1-\tilde{L}_{h,min}} = \tilde{c}_{m,sol}(\tilde{z})|_{\tilde{z}=1-\tilde{L}_{h,min}} \tag{8.45}$$

$$\frac{d\tilde{c}^{l}_{m}(\tilde{z})}{d\tilde{z}}|_{\tilde{z}=1-\tilde{L}_{h,min}} = \frac{d\tilde{c}_{m,sol}(\tilde{z})}{d\tilde{z}}|_{\tilde{z}=1-\tilde{L}_{h,min}} \tag{8.46}$$

Using expressions for concentration profiles and fluxes derived earlier, the above conditions can be recast into the following set of non-linear equations (see Appendix A3 for derivation):

$$1 - \exp\left[\tilde{D}_s \ln\left(\frac{1+m\tilde{c}_{m,ext}}{m\tilde{c}_{m,ext}}\right)\frac{g[1-\tilde{L}_{h,min}] - g[\tilde{L}_{s,max}]}{g[0] - g[\tilde{L}_{s,max}]}\right] - \frac{\tilde{c}_{m,sol}[1-\tilde{L}_{h,min}]}{\tilde{c}_{m,ext}} = 0 \tag{8.47}$$

and

$$\left[\frac{\tilde{D}_s \ln\left(\frac{1+m\tilde{c}_{m,ext}}{m\tilde{c}_{m,ext}}\right) g^{'}[1-\tilde{L}_{h,min}]}{g[0]-g[\tilde{L}_{s,max}]}\right] \exp\left[\tilde{D}_s \ln\left(\frac{1+m\tilde{c}_{m,ext}}{m\tilde{c}_{m,ext}}\right)\right.$$
$$\left.\frac{g[1-\tilde{L}_{h,min}]-g[\tilde{L}_{s,max}]}{g[0]-g[\tilde{L}_{s,max}]}\right] + \frac{\tilde{c}^{'}_{m,sol}[1-\tilde{L}_{h,min}]}{\tilde{c}_{m,ext}} = 0 \tag{8.48}$$

where $g^{'}$ represents the derivative of the function $g[\tilde{z}]$, the depth $\tilde{L}_{s,max}$ corresponds to the maximum SMT depth at tangency, and $\tilde{c}_{m,ext}$ is the normalized methane concentration in the external fluid.

The above set of equations contain two unknowns, $\tilde{L}_{h,min}$ and $\tilde{L}_{s,max}$, in terms of the two system parameters, $\tilde{c}_{m,sol}[\tilde{z}]$ and $\tilde{c}_{m,ext}$. For simplicity, we henceforth assume that pore water from depth is saturated with methane so that $\tilde{c}_{m,ext} = 1$. Thus, any given gas hydrate setting, characterized by its unique solubility curve through local seafloor depth, temperature and geotherm conditions, will have a unique maximum $\tilde{L}_s$ $(= \tilde{L}_{s,max})$ and minimum $\tilde{L}_h$ $(= \tilde{L}_{h,min})$ required for gas hydrate to be present. Hence, before actual calculations for gas hydrate saturation are performed, the observed SMT depth should be checked against the maximum allowed value to see whether hydrates exist or not. Values of $\tilde{L}_{s,max}$ and $\tilde{L}_{h,min}$ for our test cases are presented in section (8.4.2).

8.4 Results

We first summarize the overall calculation procedure to obtain the results:

1. Given the local solubility curve $\tilde{c}_{m,sol}[\tilde{z}]$ and other site-specific parameters

(m, $\tilde{D}_s$, γ and η), solve equations (8.47) and (8.48) to obtain the maximum allowed SMT depth $\tilde{L}_{s,max}$. If the observed scaled SMT depth, $\tilde{L}_s$, for this site exceeds $\tilde{L}_{s,max}$, gas hydrate will not form.

2. If $\tilde{L}_s < \tilde{L}_{s,max}$, solve coupled equations (8.38) and (8.39) to obtain the modified fluid flux, Q, and thickness of gas hydrate layer, $\tilde{L}_h$.

3. Using these values, calculate methane flux, f_{CH_4}, from any of the the three expressions, (8.23), (8.33) or (8.37).

4. Substitute into equations (8.18) and (8.34) to get the sulfate and methane concentration profiles, respectively.

5. By specifying the parameters $\tilde{\rho}_h$, Pe_1, $\tilde{c}_m^h$ and c_w^h, equation (8.41) gives the gas hydrate saturation profile $S_h(\tilde{z})$ within the GHSZ.

8.4.1 Normalized methane solubility curve

An important parameter in our formulation is the methane solubility curve within the GHSZ. It can be calculated for any geologic setting either through rigorous thermodynamic modeling (Handa, 1990; Bhatnagar et al., 2007) or empirical relationships (Davie et al., 2004; Tishchenko et al., 2005). A simple exponential type dependence of this solubility on depth has been proposed by Davie et al. (2004). For sake of demonstration and simplicity, we also approximate the solubility curve $\tilde{c}_{m,sol}[\tilde{z}]$ by an exponential function, although more accurate approximations can be used if needed. We start with this simple two-parameter solubility function:

$$\tilde{c}_{m,sol}[\tilde{z}] = r_1 e^{r_2 \tilde{z}} \tag{8.49}$$

where r_1 and r_2 are fitting constants. As mentioned before, this solubility curve is scaled by methane solubility at the base of the GHSZ, so that its normalized value is equal to unity at $\tilde{z} = 1$. This constraint yields the following relationship between r_1 and r_2:

$$r_1 e^{r_2} = 1 \quad \Rightarrow \quad r_1 = e^{-r_2} \tag{8.50}$$

which allows us to reduce equation (8.49) to a single parameter equation:

$$\tilde{c}_{m,sol}[\tilde{z}] = e^{-r_2(1-\tilde{z})} \tag{8.51}$$

This simple equation, with a single fitting parameter r_2, yields very good fits to solubility curves (Figure 8.4) obtained through rigorous thermodynamic models (Bhatnagar et al., 2007), for two different seafloor depths, seawater salinity, seafloor temperature of 3°C, and a geotherm of 0.04°C/m.

8.4.2 Effect of $\tilde{L}_s$ on the gas hydrate system

We now explain the system in terms of the input parameter, $\tilde{L}_s$. The following constant parameter values are assumed for all results shown later: $\eta = 6/9, \gamma = 9$ (which correspond to $\phi_0 = 0.7, \phi_\infty = 0.1$), $c_m^h = 0.134$, $\tilde{\rho}_h = 0.9$, $M_{CH_4} = 16$ g/mol, $M_{SO_4} = 96$ g/mol, seawater sulfate concentration equals 28 mM, and $\tilde{D}_s = 0.64$

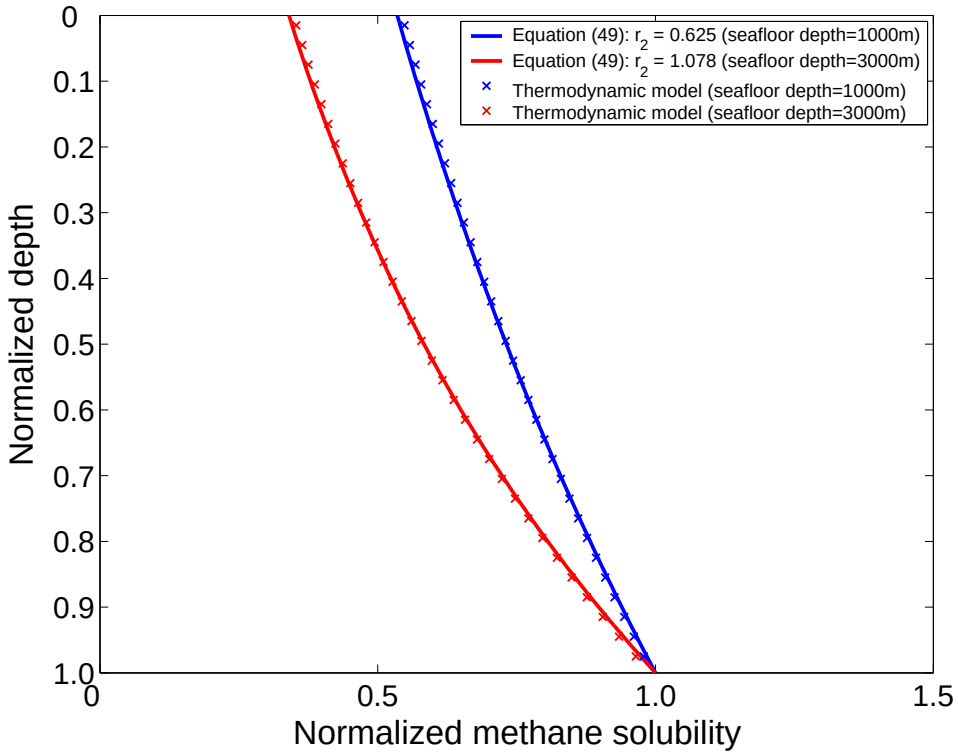

Figure 8.4: Comparison of normalized methane solubility curves, $\tilde{c}_{m,sol}[\tilde{z}]$, computed from rigorous thermodynamic models versus those fitted with equation (8.51). Two different seafloor depths are considered, with the corresponding fitting parameters, r_2, listed in the inset. A geotherm of 0.04°C/m, seafloor temperature of 3°C, and seawater salinity were used for the solubility curves.

(Iversen and Jørgensen, 1993).

Figure 8.5 shows the steady-state sulfate concentration profiles, obtained through equation (8.18), for three different scaled SMT depths. The sum $\mathrm{Pe}_1 + \mathrm{Pe}_2$ corresponding to each scaled SMT depth is also shown. Figure 8.6 shows plots of the steady-state sulfate as well as the methane concentration profiles as a function of normalized depth below the seafloor for the same scaled SMT depths as shown in Figure 8.5. The solubility curve corresponding to seafloor depth of 1000 mbsl ($r_2 = 0.625$) is used for the results in Figures 8.5 and 8.6. Due to co-consumption

of sulfate and methane at the SMT, shorter $\tilde{L}_s$ indicates higher methane flux from below, thereby leading to a shallower top of the gas hydrate layer (Figure 8.6).

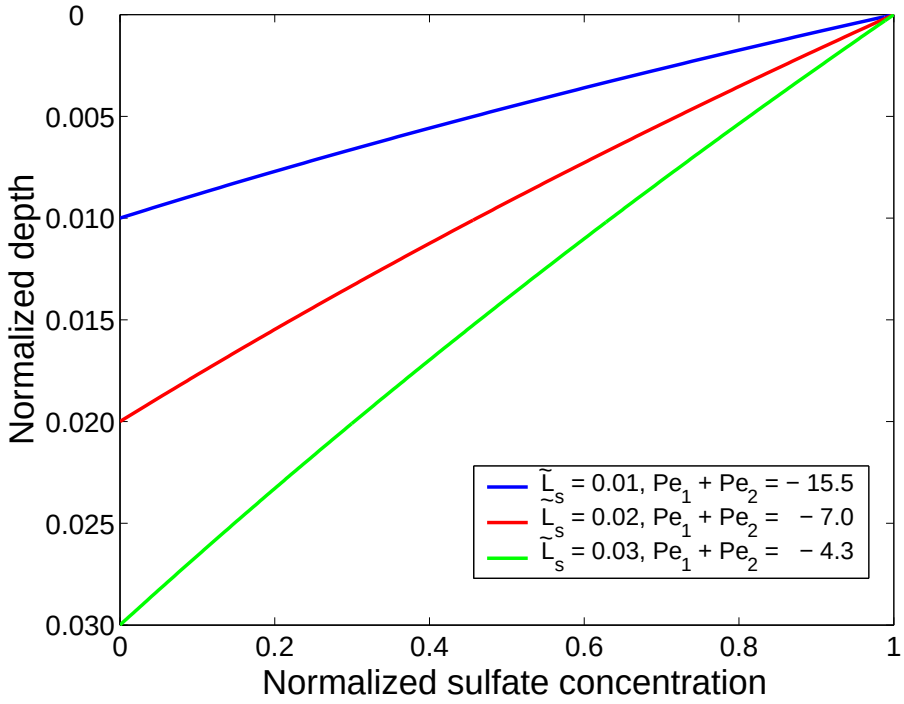

Figure 8.5: Normalized sulfate concentration profiles, obtained through equation (8.18), for three distinct SMT depths . Sulfate concentration is scaled by its seawater value that makes it equal to unity at the seafloor. Shallower SMT depths indicate higher net methane fluxes from depth. The methane solubility curve corresponds to seafloor depth of 1000m, seafloor temperature of 3°C, and geotherm of 0.04°C/m. Other parameters include: $\eta = 6/9$, $\gamma = 9$ and $\tilde{D}_s = 0.64$.

Gas hydrate saturation profiles as a function of scaled SMT depths show higher saturations within the GHSZ with decreasing $\tilde{L}_s$, again due to net increase in methane flux (Figure 8.7). Increase in the thickness of the hydrate layer with decreasing $\tilde{L}_s$ is also evident from the saturation profiles. We further compare steady-state gas hydrate saturation profiles obtained from simulation results (crosses) of Bhatnagar et al. (2008), which reveal good agreement between the theory devel-

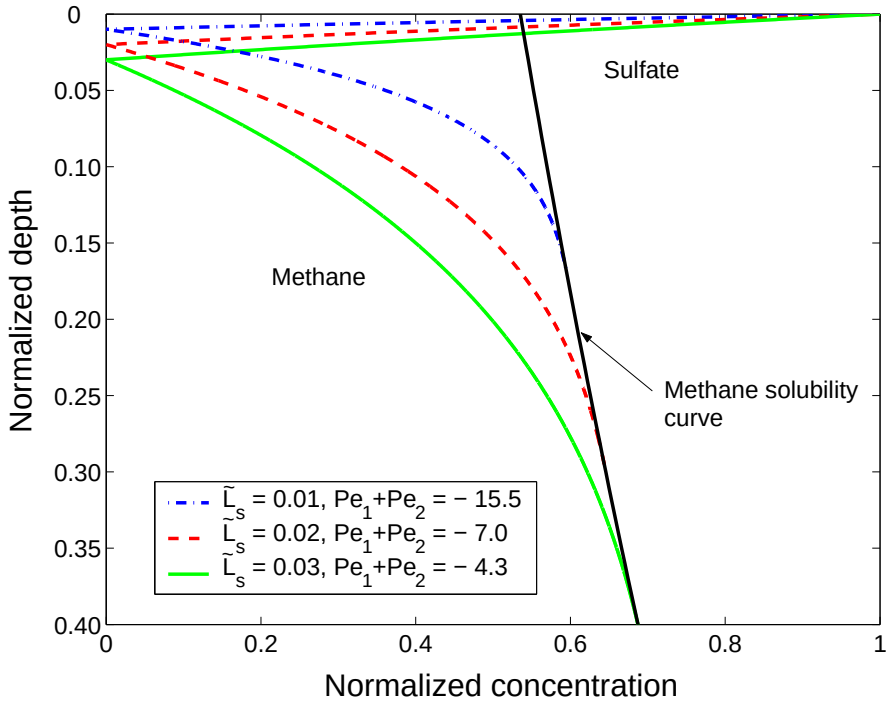

Figure 8.6: Effect of different SMT depths on steady-state pore water concentration profiles. The methane solubility curve corresponds to seafloor depth of 1000m, seafloor temperature of 3°C, and geotherm of 0.04°C/m. Specifying the scaled SMT depth, $\tilde{L}_s$, uniquely constrains the sulfate and methane concentration profiles, as well as the top of the gas hydrate layer (intersection of the methane concentration profile with the solubility curve). Lower values of $\tilde{L}_s$ imply faster depletion of sulfate due to higher methane flux from below, causing shallower occurrence of the top of the gas hydrate layer.

oped in this paper and the numerical formulation. The profiles in Figures 8.6 and 8.7 clearly highlight that each distinct value of $\tilde{L}_s$ results in a unique profile for dissolved sulfate, methane and gas hydrate saturation.

We previously related the gas hydrate flux ($\mathrm{Pe}_1\langle S_h\rangle$) to $\tilde{L}_s$ through equation (8.44). This relationship is depicted in Figure 8.8 for two different seafloor depths of 1000 mbsl and 3000 mbsl (same solubility curves as in Figure 8.4). Both curves show that a decrease in $\tilde{L}_s$ leads to higher values of $\mathrm{Pe}_1\langle S_h\rangle$ due to higher net

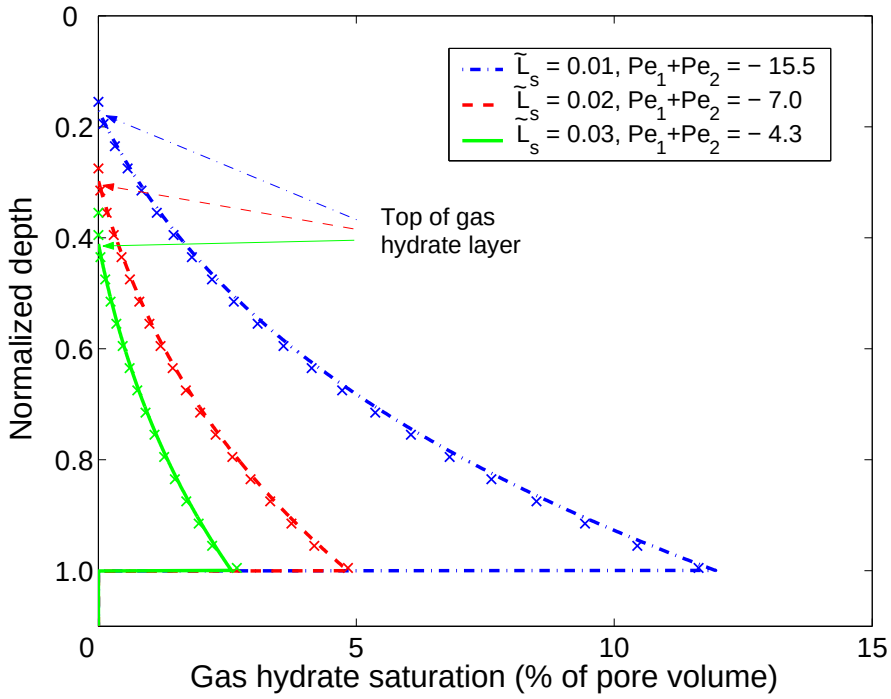

Figure 8.7: Effect of variable SMT depths (same as in Figure 8.6) on steady-state gas hydrate saturation profiles. Shallower SMT depths, indicating higher net methane flux from depth, result in higher gas hydrate saturations within the GHSZ. Calculation of gas hydrate saturation profile requires specification of Pe_1, which was set equal to 0.1 for all three cases. Numerical simulation results (crosses) from the model of Bhatnagar et al. (2008) match well with the analytical saturation profiles (curves). Methane solubility curve used is the same as in Figure 8.6.

methane input to the system. Both set of curves also truncate at a maximum scaled SMT depth ($\tilde{L}_{s,max}$), beyond which the methane flux is too low to form any gas hydrate. $\tilde{L}_{s,max}$ for the solubility curves corresponding to seafloor depths of 1000 mbsl and 3000 mbsl are equal to 0.059 and 0.058, respectively. Again, results from our analytical model match well with simulations performed for the same set of parameters by Bhatnagar et al. (2008).

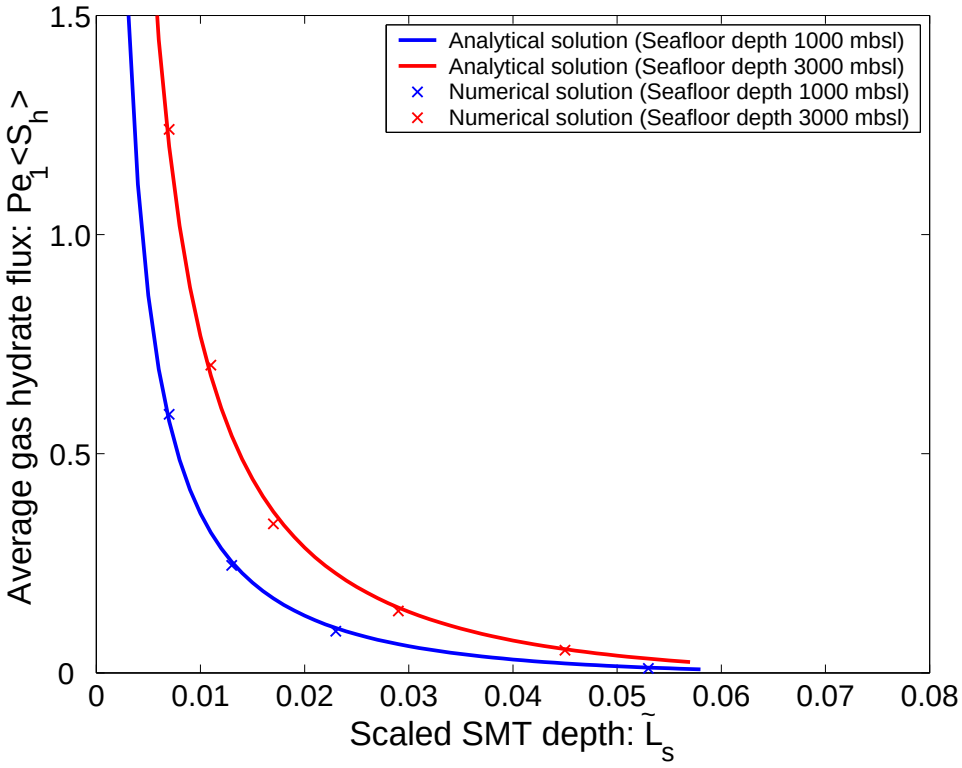

Figure 8.8: Relationship between average gas hydrate flux ($\mathrm{Pe}_1\langle S_h\rangle$) and scaled SMT depth ($\tilde{L}_s$) for different seafloor depths. Curves representing analytical solutions are also compared with steady state numerical simulations of Bhatnagar et al. (2008). Shallow SMT depths indicate higher methane flux from deeper sources causing higher average gas hydrate flux (and saturations) through the GHSZ.

8.4.3 Ratio of top of gas hydrate layer to SMT depth

Several gas hydrate settings show correlation between the SMT depth and the depth to the shallowest occurrence of gas hydrate (e.g., Borowski et al., 1999), with some sites suggesting gas hydrate first occurring at a depth 10 times the SMT depth (e.g., Paull et al., 2005). Our model allows the estimation of this ratio $[(L_t - L_h)/L_s]$, or $[(1 - \tilde{L}_h)/\tilde{L}_s]$ in scaled form, as a function of the system parameters. Figure 8.9 shows this ratio as a function of $\tilde{L}_s$ for the two solubility curves shown in Figure 8.4. Overall, the ratio increases with decreasing $\tilde{L}_s$, though the

variation with scaled SMT depth is more gradual at relatively large values of $\tilde{L}_s$. However, this ratio increases rapidly with decreasing $\tilde{L}_s$ at relatively small values of $\tilde{L}_s$, implying that with increasing methane flux from below, the SMT migrates upwards faster than the increase in thickness of the gas hydrate layer (L_h). Except at gas vents or sites neighboring rapid fluid flow conduits, the scaled SMT depth at most gas hydrate settings is usually greater than about 0.01, which indicates that the top of the gas hydrate layer occurring at about $10-12$ times the SMT depth might be a reasonable approximation.

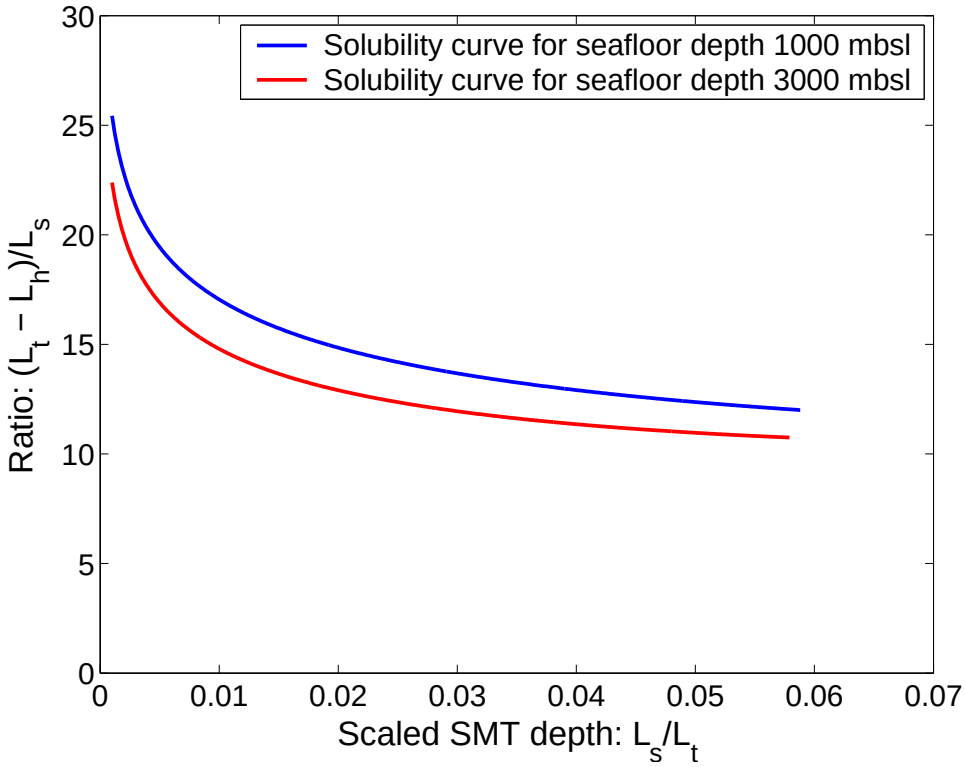

Figure 8.9: Relationship between the ratio of depth to the first occurrence of gas hydrate to the SMT depth as a function of the scaled SMT depth for two different solubility curves (Figure 8.4). This ratio is close to $10-12$ for relatively large SMT depths but significantly departs from this suggested range for shallower SMT depths. Similar to Figure 8.8, both curves truncate at the maximum allowed SMT depth for each case.

8.5 Application to Cascadia Margin sites

The Cascadia Margin is an accretionary margin characterized by pervasive upward fluid flow and localized areas of gas venting (Tréhu et al., 2004; Riedel et al., 2006). Results from Ocean Drilling Program Leg 204 and Integrated Ocean Drilling Program Expedition 311 have given great insight into the complex and heterogeneous gas hydrate distribution at several sites drilled along this margin (Tréhu et al., 2003, 2004; Riedel et al., 2006). Sites in this region are characterized by relatively high fluid fluxes and low average total organic carbon (TOC) content (Westbrook et al., 1994; Riedel et al., 2006), implying that fluids from depth form the dominant methane source. This makes sites along Cascadia Margin a good location to test our model. We use SMT depths and other data for four Cascadia Margin sites (Table 8.1) to predict gas hydrate saturations, average saturation and depth to the first occurrence of gas hydrate below the seafloor (Table 8.2). These sites include Site 889, drilled as part of ODP Leg 146, and Sites U1325, U1326 and U1329 that were drilled along a transect during IODP Expedition 311.

Table 8.1 lists the site number, sedimentation rate ($\dot{S}$), seafloor temperature (T), geothermal gradient (G), seafloor depth (D_0), dimensional SMT depth (L_s), dimensional BSR depth (L_t), methane solubility in water at the base of the GHSZ ($c^l_{m,eqb}$), constant m (equation (8.22)), and the fitting constant to the solubility curve r_2 (equation (8.51)) for all four sites. For each site, the methane solubility curve is generated for the corresponding seafloor conditions using the rigorous thermodynamic model of Bhatnagar et al. (2007). These calculations also give $c^l_{m,eqb}$ for

Table 8.1: Site-specific parameters for Cascadia Margin sites

Site	$\dot{S}$ (cm/k.y.)	T_0 (^{o}C)	G (^{o}C/m)	D_0 (m)	L_s (m)	L_t (m)	$c^l_{m,eqb}$	m	r_2
889	25	3	0.054	1311	10	225	2.1×10^{-3}	4.4	0.73
U1325	38.3	3	0.06	2195	5	230	2.5×10^{-3}	5.2	0.93
U1326	38.3	3	0.06	1828	2.5	230	2.3×10^{-3}	4.8	0.86
U1329	9.2	3.3	0.072	946	9.4	126	1.8×10^{-3}	3.8	0.52

each site, from which the constant m can be computed. The generated solubility curve is then fit to equation (8.51) to give the fitting constant r_2.

Table 8.2 illustrates the calculation procedure summarized before. We briefly explain how various columns in Table 8.2 are sequentially obtained from site-specific data. Using the sedimentation rate and porosity, the first Peclet number (Pe_1) is computed for each site. Ratio of the dimensional depths L_s and L_t give the scaled SMT depth $\tilde{L}_s$. Using this value, and other site-specific parameters, the maximum SMT depth for hydrates to form ($\tilde{L}_{s,max}$) is computed. Solution of equations (8.38) and (8.39) gives methane flux and thickness of the gas hydrate layer from which the scaled depth to the first occurrence of gas hydrate ($1-\tilde{L}_h$) is calculated. Multiplying this by L_t yields the dimensional depth to the first occurrence of hydrate ($L_t - L_h$). Using Pe_1 characteristic of each site, we next compute the gas hydrate saturation profile (equation (8.41)). Averages of this gas hydrate saturation

Table 8.2: Results for Cascadia Margin sites

Site	Pe_1	$\tilde{L}_s$	$\tilde{L}_{s,max}$	$L_t - L_h$ (m)	$\langle S_h \rangle_{GHSZ}$ (calc.)	$\langle S_h \rangle_{GHSZ}$ (res. log)	$\langle S_h \rangle_{GHSZ}$ (Cl^-)
889	0.068	0.04	0.058	113	0.6%	-	$<$1 %
U1325	0.11	0.02	0.059	62	2.3%	3.7%	5.3%
U1326	0.11	0.01	0.060	36	5.5%	6.7%	5.5%
U1329	0.014	0.075	0.057	-	0%	2%	0.1%

profile over the entire GHSZ as well as the gas hydrate occurrence zone (GHOZ) are also computed. Finally, average gas hydrate saturations at these sites from other proxy data (resistivity log and chloride) are listed. Figure 8.10 shows the gas hydrate saturation profiles at three of these sites. Site U1329 is not shown on this plot as our model predicts zero gas hydrate at this location.

Site 889 (ODP Leg 146) has been previously modeled as a gas hydrate system dominated by deeper methane sources (Davie and Buffett, 2003a; Bhatnagar et al., 2007). Davie and Buffett (2003a) fit the pore water chloride profile at Site 889 using a coupled numerical model with methane supply from depth. Their results indicate peak hydrate saturation close to 2% at the base of GHSZ and average saturation $<$1% within the GHSZ (Davie and Buffett, 2003a). This result agrees favorably with our simulation that shows peak saturation of about 2.7% at the base of GHSZ (Figure 8.10) and average saturation of 0.6% across the entire GHSZ (Table 8.2).

Hyndman et al. (1999) calculated gas hydrate saturation between 25-30% of pore space in the 100 m interval above the base of GHSZ at Site 889 using resistivity log data. However, subsequent calculations using a different set of Archie parameters have revised this estimate to 5-10% in that 100 m interval (Collett, 2000). Further, Ussler and Paull (2001) show that a smoothly decreasing chlorinity profile at Site 889 yields gas hydrate saturation of 2-5% within discrete layers. Temperature measurements of cores also indicate hydrate saturation of about 3% at Site 889 (Kastner et al., 1995). Although several parameter uncertainties confront such geochemical and geophysical estimates (Egeberg and Dickens, 1999; Riedel et al., 2006), average saturation predicted using our SMT based model concurs with the lower estimates at Site 889.

For the IODP Expedition 311 sites, drilled along the northern Cascadia Margin, we compare our predictions with average saturations computed from chloride anomalies and resistivity log data (Table 8.2). Average saturation is calculated from chloride data by assuming a background in situ chloride profile and attributing the relative pore water freshening to gas hydrate dissociation (e.g., (Egeberg and Dickens, 1999)). Average saturation is obtained from resistivity data using the Archie equation and parameters given in Riedel et al. (2006). Average saturation over the GHSZ at Site U1325 is estimated from resistivity data and chloride anomalies to be 3.7% and 5.3%, respectively. Corresponding estimates from resistivity and chlorinity for Site U1326 are 6.7% and 5.5%, respectively. These values compare favorably with 3.1% and 6.6% average saturation from our SMT based model at Sites U1325 and U1326, respectively (Table 8.2).

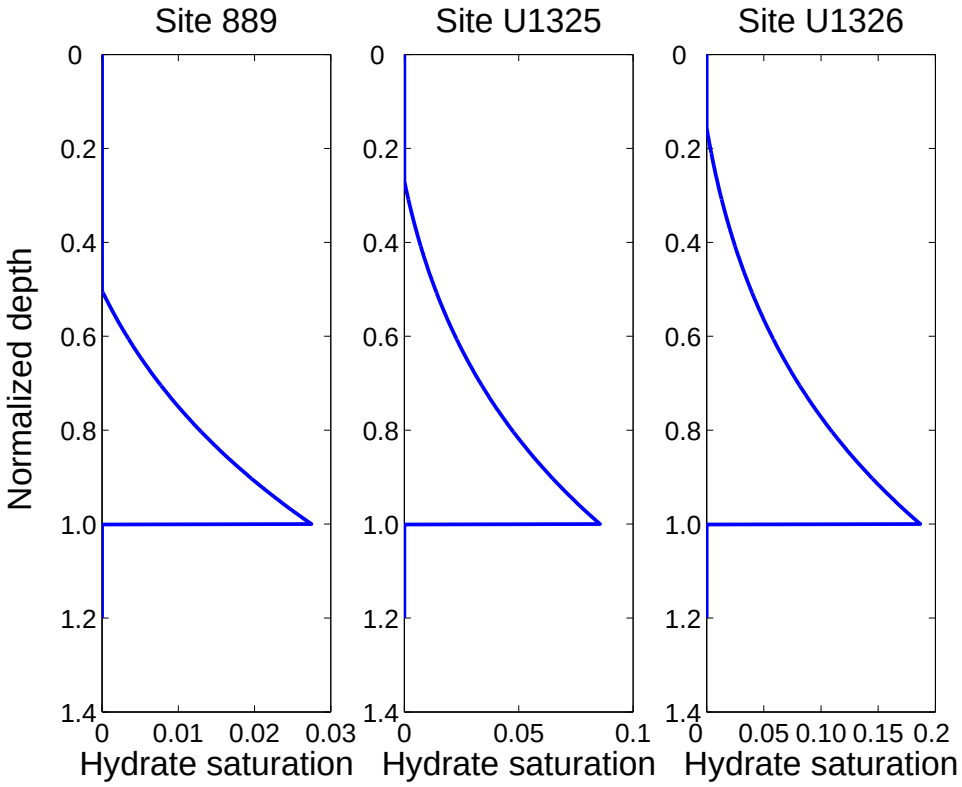

Figure 8.10: Steady-state gas hydrate saturation profiles computed from scaled SMT depths at Cascadia Margin Sites 889, U1325 and U1326. Scaled SMT depth is highest for Site 889 and lowest for Site U1326, implying higher methane flux and greater gas hydrate saturation at Site U1326 and relatively low methane flux and hydrate saturation at Site 889.

At Site U1329, our model predicts that the SMT is greater than the maximum allowed, implying that methane flux is too low at this site to precipitate any gas hydrate. Although resistivity data suggests a small amount of gas hydrate within the GHSZ, our prediction is supported by the very low saturation predicted from chlorinity data. Site U1329 is supposed to mark the eastern limit of gas hydrate occurrence along this transect and has a very faint BSR (Riedel et al., 2006). Further, no gas hydrate was recovered from cores at this site. These features indicate that, in general, Site U1329 has no hydrate or very little hydrate within some local-

ized layers.

In general, we get good first order agreement between average saturations derived using resistivity logs/chloride anomalies and those predicted using our model, although our model consistently predicts lower average saturation at all four sites along Cascadia Margin. For estimates from resistivity logs, a possible explanation for the deviation is that interpretations of resistivity logs depend on knowledge of formation water resistivity and three empirical constants, which are hard to constrain in clay-rich sediments. As mentioned before, early estimates of hydrate saturation at Site 889 from resistivity data have since then been revised to much lower values using new Archie parameters (Riedel et al., 2006). Moreover, most studies employing transport models (e.g., (Xu and Ruppel, 1999; Davie and Buffett, 2003a; Bhatnagar et al., 2007)) predict gas hydrate to first occur well below the seafloor. In contrast, log-based results often predict gas hydrate starting immediately below the seafloor. This will cause saturations from transport models to be lower than those predicted using resistivity log data. Similarly, estimation of hydrate saturation from chloride data is quite sensitive to the choice of baseline curves. Apart from the small deviations between model and chloride/resistivity log predictions, our model gives a good average estimate of gas hydrate saturation. Further, it captures the variation in average saturation across the IODP Expedition 311 transect correctly and likely provides a lower bound on average saturation at Site 889.

8.6 Caveats

The analytical formulation outlined in previous sections provides a simple tool to infer steady-state gas hydrate saturation at sites dominated by deep methane sources. Compared to full numerical simulations, this method gives a quick and accurate first-order estimate of gas hydrate saturation. However, some caveats exist that should be noted before applying to it new settings.

- The above analysis only applies to gas hydrate systems where methane from depth is the only source. Gas hydrate settings with significant organic carbon input can deplete pore water sulfate by bacteria that utilize organic carbon instead of methane (Berner, 1980). Thus, if some of the pore water sulfate is depleted through this alternate pathway, the resulting SMT will become shallower than the SMT due to methane flux alone. In such cases, our method will yield gas hydrate saturations higher than the actual saturation.

- Methane is the only hydrate forming gas in our model. In some regions (e.g., Gulf of Mexico), upward fluid flux might contain higher alkanes that can also consume sulfate (Joye et al., 2004), making the 1:1 sulfate-methane flux relationship invalid. Such sites might be more appropriately characterized by a sulfate-hydrocarbon transition (Castellini et al., 2006) instead of a SMT.

- The equations developed here apply only to one-dimensional systems. Thus, sites dominated by focused fluid flow, possibly along high permeability conduits, will probably show greater deviations between gas hydrate saturation

estimated from our model and that inferred from other proxy data (e.g., resistivity). Further, different geophysical and geochemical proxies often predict gas hydrate distributed heterogeneously within the GHSZ that is possibly controlled by the local lithology. Our simple formulation does not include such small-scale heterogeneities, but gives a good first-order estimate in the average sense.

- Our model does not account for free gas existence or migration within the GHSZ. Several sites associated with free gas venting have been drilled along Cascadia Margin (e.g., Sites 1249 and 1250, ODP Leg 204). These sites show massive layers of hydrate close to the seafloor. Due to relatively high methane flux, such sites might not have any detectable pore water sulfate (Tréhu et al., 2003). Further, gas hydrate saturation at such sites decreases with depth below the seafloor (Haeckel et al., 2004; Liu and Flemings, 2006), as opposed to other numerical models that predict monotonous increase of gas hydrate saturation with depth below the seafloor (Xu and Ruppel, 1999; Davie and Buffett, 2001; Bhatnagar et al., 2007, 2008). Predictions from our analytical model agree with this latter category of models. Consequently, the formulation developed here will not predict massive gas hydrate layers close to the seafloor at gas vent sites.

8.7 Conclusions

We have developed analytical expressions to estimate steady-state gas hydrate saturation from scaled depth of the sulfate-methane transition (SMT) for gas hydrate systems dominated by deep-methane sources. This scaled SMT depth is the ratio of the dimensional depth of the SMT below the seafloor to the depth of the gas hydrate stability zone (GHSZ) below the seafloor. Using simple one-dimensional mass balances for sulfate and methane, we show that net methane flux in such deep-source systems uniquely determines the scaled SMT depth, the thickness of the gas hydrate layer and steady-state gas hydrate saturation within the GHSZ. This dependence allows estimation of the vertical extent of gas hydrate and its saturation through knowledge of SMT depth at a given site. Steady-state results show that as the SMT becomes shallower, methane flux and, consequently, gas hydrate saturation increases.

Our formulation also gives an estimate of the maximum scaled SMT depth and minimum gas hydrate thickness (or, equivalently, minimum methane flux) for gas hydrates to be present at any given setting. Any scaled SMT depth greater than this maximum implies that methane flux is lower than the minimum required to form hydrate. The one-to-one relationship between SMT depth and thickness of the gas hydrate layer allows us to obtain the ratio of the first occurrence of gas hydrate below the seafloor to the SMT depth. We show that this ratio can be about 10-12 for sites characterized by low to moderate methane fluxes. However, relatively higher methane fluxes will cause this ratio to increase towards much higher values.

Average saturations over the GHSZ at four Cascadia Margin locations, calculated from our method, are 0.6%, 2.3%, 5.5% and 0% for Sites 889, U1325, U1326 and U1329, respectively. These values compare favorably with averages computed from resistivity log and chlorinity data for all sites. Hence, our analytical formulation provides a simple and fast technique to constrain gas hydrate saturation in deep-source gas hydrate systems

Chapter 9

Overpressure Development in Gas Hydrate Systems

9.1 Introduction

Marine gas hydrate systems are often characterized by overpressure, i.e. pore water pressures higher than hydrostatic. This is particularly evident at settings dominated by low permeability silts/clays, e.g. Blake Ridge (Paull et al., 2000; Flemings et al., 2003). Over geologic time-scales, continuous sedimentation causes increase in the overburden stress, resulting in consolidation of sediments (Gibson, 1958). Overpressure can develop in such systems if pore water cannot be expelled from the pore space fast enough and, instead, starts to support some of the overburden stress. Since permeability controls this rate of pore water expulsion, sediments with low permeability can develop overpressure (Wangen, 1992; Dugan and Flemings, 2000). Alternatively, overpressure can also develop in sediments with relatively high permeability if the sedimentation rate is fast, i.e. increase in overburden is faster than rate of pore water expulsion (Wangen, 1992).

Overpressure becomes an important issue in gas hydrate dynamics because of its obvious effect on fluid flow (Dugan and Flemings, 2000; Flemings et al., 2003; Gering, 2003). However, overpressure also impacts the behavior of such systems in less intuitive ways. For example, the thickness of the free gas layer below the

base of the gas hydrate stability zone (GHSZ) depends on the magnitude of overpressure. The free gas saturation profile associated with marine gas hydrate systems is often obtained in earlier numerical models by assuming it to be an immobile phase (Davie and Buffett, 2001, 2003a; Bhatnagar et al., 2007). However, when free gas saturation exceeds its critical saturation, it no longer moves as a trapped phase within the sediment matrix. Instead, free gas forms a connected column that is sealed by the high capillary entry pressure at the base of the GHSZ due to gas hydrate (Liu and Flemings, 2007). The pressure within this connected gas column increases towards the base of the GHSZ, whereas the length of this gas column is regulated by the difference between pore water pressure and lithostatic stress. Once gas pressures reach this lithostatic limit at the base of the GHSZ, the vertical gas effective stress becomes zero. Figure 9.1 illustrates this mechanism schematically. For hydrostatically-pressured systems, Figure 9.1a, pore water pressure is relatively low, thereby allowing a large gas column to form before maximum gas pressure at the top of the connected column equals the lithostatic stress (overburden). When gas pressure exceeds the lithostatic limit, fractures can dilate, allowing free gas migration into the GHSZ (Flemings et al., 2003; Hornbach et al., 2003; Tréhu et al., 2004). Sediments might, however, fail at much lower gas pressures due to shear failure (Finkbeiner et al., 2001; Hornbach et al., 2003). Compared to this scenario, Figure 9.1b shows a case where pore pressure gradient deviates significantly from the hydrostatic gradient. This results in higher pore water pressure beneath the GHSZ, thereby reducing the maximum thickness of the free gas column. Thus, the thickness of the connected free gas layer is regulated by the

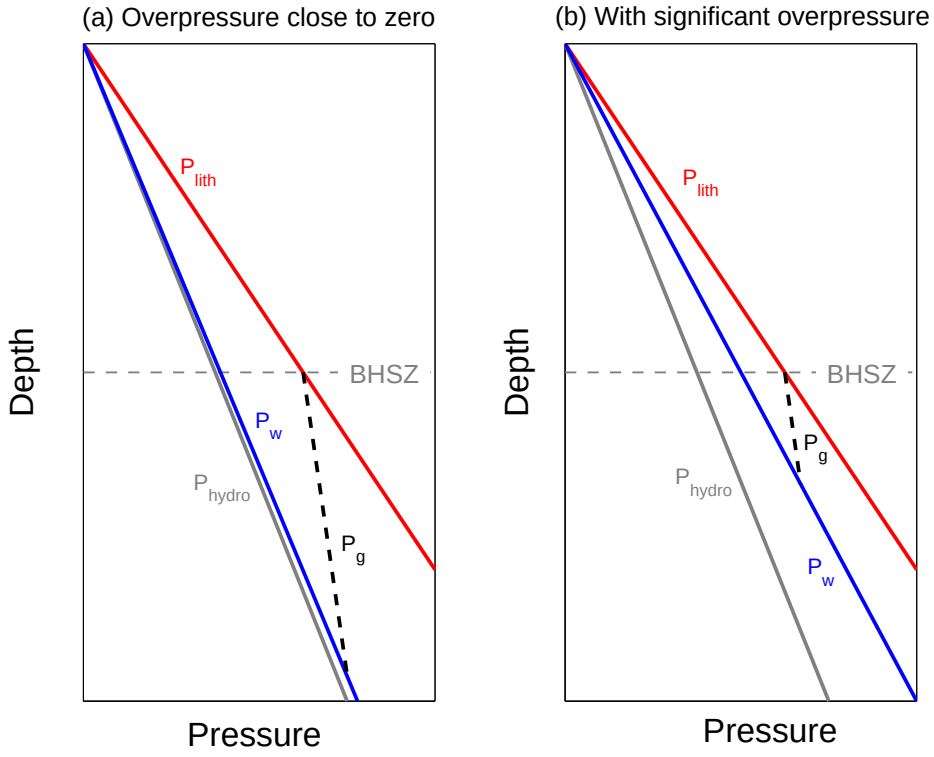

Figure 9.1: Schematic illustration of effect of overpressure on maximum thickness of the connected free gas column beneath a gas hydrate layer. P_{lith}, P_{hydro}, P_w and P_g denote lithostatic stress, hydrostatic pressure, water pressure and gas pressure, respectively . Free gas only exists below the GHSZ and its pressure follows the gas-static profile above the free water level. The length of the free gas column is maximum when gas pressure just below the base of the GHSZ equals the lithostatic stress. (a) When overpressure is close to zero, i.e. pore pressure gradient is almost hydrostatic, a relatively deep gas column can be formed. (b) When significant overpressure exists, the length of the connected free gas column can be substantially reduced.

pore water pressure, making overpressure an important parameter in gas hydrate dynamics.

A less intuitive, yet significant, aspect of overpressure is its effect on sediment and gas hydrate velocity through the GHSZ. At hydrostatic pore pressures, sediments achieve maximum compaction due to high effective stresses acting on them. Overpressure reduces this effective stress, resulting in higher sediment porosities, which leads to faster sediment velocities through the GHSZ. This curtails the amount of organic carbon converted within the GHSZ as well as the residence time of gas hydrate in this zone, resulting in lower gas hydrate and free gas saturations.

Increase in pore pressure also changes the thermodynamic stability regime and extends the base of the GHSZ to greater depths below the seafloor. This will possibly lead to deeper gas hydrate occurrences below the seafloor. This might also lead to greater deviation between the thermodynamically predicted depth of GHSZ, assuming hydrostatic pressure, and that obtained from a seismic BSR. However, we show through numerical simulations that this increase in depth of the GHSZ due to overpressure is relatively small, even when pore pressures become close to lithostatic limits. Thus, BSR depths in agreement with thermodynamically predicted depths of GHSZ may not be reliable indicators of in situ pore pressures in a gas hydrate system.

9.2 Non-hydrostatic compaction in gas hydrate systems

We now develop a one-dimensional numerical model to simulate overpressure generation in marine gas hydrate systems and study the parameters governing this process. Since pore pressure is no longer constrained to be hydrostatic, we make use of Darcy's law to model fluid flow relative to the compacting sediment. As mentioned before, free gas becomes mobile only when its saturation exceeds some critical value, which can be about 5-10% gas saturation. We focus on the effects of overpressure arising from sedimentation-compaction and sediment permeability in this chapter and consequently assume a relatively higher value of critical gas saturation of 10%. This ensures that free gas will remain immobile within the sediment matrix. Mobile free gas will be modeled in the next chapter.

We start with the mass balances for different system components.

9.2.1 Mass balances

The water, methane, sediment and organic mass balances are written as:

Water Balance

$$\frac{\partial}{\partial t}\left[\phi S_w c_w^l \rho_w + \phi S_h c_w^h \rho_h\right] + \frac{\partial}{\partial z}\left[\phi S_w c_w^l \rho_w v_w + \phi S_h c_w^h \rho_h v_s\right] = 0 \qquad (9.1)$$

Methane Balance

$$\frac{\partial}{\partial t}\left[\phi S_w c_m^l \rho_w + \phi S_h c_m^h \rho_h + \phi S_g c_m^g \rho_g\right] +$$

$$\frac{\partial}{\partial z}\left[\phi S_w c_m^l \rho_w v_w + \phi S_h c_m^h \rho_h v_s + \phi S_g c_m^g \rho_g v_g\right] = \frac{\partial}{\partial z}\left[\phi S_w D_m \rho_w \frac{\partial c_m^l}{\partial z}\right] + \frac{M_{CH_4}}{M_{org}} \rho_s \lambda (1-\phi)\,\alpha \tag{9.2}$$

Sediment Balance

$$\frac{\partial}{\partial t}\left[(1-\phi)\,\rho_s\right] + \frac{\partial}{\partial z}\left[(1-\phi)\,\rho_s v_s\right] = 0 \tag{9.3}$$

Organic Balance

$$\frac{\partial}{\partial t}\left[(1-\phi)\,\rho_s \alpha\right] + \frac{\partial}{\partial z}\left[(1-\phi)\,\rho_s v_s \alpha\right] = -\rho_s \lambda (1-\phi)\,\alpha \tag{9.4}$$

where c_i^j represents mass fraction of component i in phase j, S_j represents phase saturation, v_j denotes velocity of phase j, ρ_j denotes phase density, λ is the methanogenesis reaction rate constant, and α is organic carbon content in sediments.

9.2.2 Constitutive relationships

We now list the constitutive relationships used in this formulation.

- Darcy's law for water flux in a compacting medium (Bear, 1988)

$$S_w \phi (v_w - v_s) = -\frac{k k_{rw}}{\mu_w}\left(\frac{\partial p_w}{\partial z} - \rho_w g\right) \tag{9.5}$$

where v_w and v_s represent water and sediment velocities, respectively, k is the

absolute permeability of the sediment, and k_{rw} denotes relative permeability of water.

• Absolute permeability of sediment is modeled as a power law function of porosity (Smith, 1971)

$$k = k_0 \left(\frac{\phi}{\phi_0} \right)^8 \tag{9.6}$$

where k_0 and ϕ_0 are the initial sediment permeability and porosity at time of deposition.

• Water relative permeability model in the presence of gas hydrate is (with pore-filling structure) (Kleinberg et al., 2003)

$$k_{rw} = 1 - S_h^2 + \frac{2(1 - S_h)^2}{\ln(S_h)} \tag{9.7}$$

• Water relative permeability model in the presence of free gas is (Bear, 1988):

$$k_{rw} = k_{rw}^0 (S_w^*)^4, \quad \text{where} \quad S_w^* = \frac{S_w - S_{wr}}{1 - S_{wr}} \tag{9.8}$$

• Porosity-effective stress relationship is defined as (Rubey and Hubbert, 1959):

$$\phi = \phi_\infty + (\phi_0 - \phi_\infty) e^{-\frac{\sigma_v - p_w}{\sigma_\phi}} \tag{9.9}$$

• Lithostatic stress gradient as a function of densities and porosity is:

$$\frac{\partial \sigma_v}{\partial z} = \left[(1 - \phi)\rho_s + \phi \rho_w \right] g \tag{9.10}$$

9.2.3 Normalized variables and dimensionless groups

The above equations are now written in dimensionless form. Reduced porosities are defined as follows:

$$\tilde{\phi} = \frac{\phi - \phi_\infty}{1 - \phi_\infty} \quad , \quad \eta = \frac{\phi_0 - \phi_\infty}{1 - \phi_\infty} \quad , \quad \gamma = \frac{1 - \phi_\infty}{\phi_\infty} \tag{9.11}$$

The dimensionless Peclet number and Damkohler number are defined as before:

$$\mathrm{Pe}_1 = \frac{U_{f,sed} L_t}{D_m} \quad , \quad \mathrm{Da} = \frac{\lambda L_t^2}{D_m} \tag{9.12}$$

A new dimensionless group corresponding to the ratio of absolute permeability and sedimentation rate, thus quantifying the effects of sedimentation and compaction, is also defined as:

$$N_{sc} = \frac{k_0 \rho_w g}{\mu_w \dot{S}} \tag{9.13}$$

Larger values of N_{sc} correspond to higher absolute permeability and/or low sedimentation rate, implying hydrostatic pressures. Conversely, low N_{sc} values imply low sediment permeability and/or high sedimentation rate, thereby causing pore pressures higher than hydrostatic. Dimensionless groups similar to N_{sc} have been defined in earlier one-dimensional compaction models (Yang and Fowler, 1998; Gutierrez and Wangen, 2005).

The ratio of compaction depth to base of GHSZ is defined by the dimensionless

group $N_{t\phi}$:

$$N_{t\phi} = \frac{L_\phi}{L_t} = \frac{\sigma_\phi/(\rho_w g)}{L_t} \tag{9.14}$$

The normalized methane concentrations are defined as:

$$\tilde{c}_m^l = \frac{c_m^l}{c_{m,eqb}^l} \quad , \quad \tilde{c}_m^h = \frac{c_m^h}{c_{m,eqb}^l} \quad , \quad \tilde{c}_m^g = \frac{c_m^g}{c_{m,eqb}^l} \tag{9.15}$$

Lithostatic stress (σ_v), water pressure and gas pressure are normalized by hydrostatic water pressure at the base of the GHSZ:

$$\tilde{\sigma}_v = \frac{\sigma_v}{\rho_w g L_t} \quad , \quad \tilde{p}_w = \frac{p_w}{\rho_w g L_t} \quad , \quad \tilde{p}_g = \frac{p_g}{\rho_w g L_t} \tag{9.16}$$

The dimensionless depth and time are defined as:

$$\tilde{z} = \frac{z}{L_t} \quad , \quad \tilde{t} = \frac{t}{L_t^2/D_m} \tag{9.17}$$

All phase densities are normalized by water density as:

$$\tilde{\rho}_h = \frac{\rho_h}{\rho_w} \quad , \quad \tilde{\rho}_g = \frac{\rho_g}{\rho_w} \quad , \quad \tilde{\rho}_s = \frac{\rho_s}{\rho_w} \tag{9.18}$$

The sediment velocity v_s is normalized by the sedimentation rate at the seafloor $\dot{S}$:

$$\tilde{v}_s = \frac{v_s}{\dot{S}} \tag{9.19}$$

Finally, organic carbon content and initial TOC are scaled as:

$$\tilde{\alpha} = \frac{\alpha}{\alpha_0} \quad , \quad \beta = \frac{\alpha_0}{c^l_{m,eqb}} \tag{9.20}$$

9.2.4 Dimensionless mass balances

The above scaling schemes lead to the following dimensionless form of the four mass balances, initial and boundary conditions.

Water Balance:

$$\begin{aligned} &\frac{\partial}{\partial \tilde{t}}\left[\frac{1+\gamma\tilde{\phi}}{\gamma}\left((1-S_h-S_g)(1-c^l_{m,eqb}\tilde{c}^l_m)+S_h c^h_w \tilde{\rho}_h\right)\right]+ \\ &\mathrm{Pe}_1\left(\frac{1+\gamma}{1-\eta}\right)\frac{\partial}{\partial \tilde{z}}\Big[\frac{1+\gamma\tilde{\phi}}{\gamma}(1-S_h-S_g)(1-c^l_{m,eqb}\tilde{c}^l_m)\tilde{v}_s - \\ N_{sc}\frac{1+\gamma}{\gamma}&\left(\frac{1+\gamma\tilde{\phi}}{1+\gamma\eta}\right)^8(1-c^l_{m,eqb}\tilde{c}^l_m)k_{rw}\left(\frac{\partial \tilde{p}_w}{\partial \tilde{z}}-1\right)+\frac{1+\gamma\tilde{\phi}}{\gamma}S_h c^h_w\tilde{\rho}_h\tilde{v}_s\Big]=0 \end{aligned} \tag{9.21}$$

$$\text{I.C.} : \tilde{p}_w(\tilde{z},0) = \frac{\rho_w g D_0 + \rho_w g z}{\rho_w g L_t} = \frac{D_0}{L_t} + \tilde{z} \tag{9.22}$$

$$\text{B.C.}(1) : \tilde{p}_w(0,\tilde{t}) = \frac{D_0}{L_t} \tag{9.23}$$

$$\text{B.C.}(2) : \frac{\partial \tilde{p}_w}{\partial \tilde{z}}(D,\tilde{t}) = 1 \quad , \quad (\text{Hydrostatic gradient}) \tag{9.24}$$

where D_0 is seafloor depth and D is bottom of the domain.

Methane balance:

$$\frac{\partial}{\partial \tilde{t}}\left[\frac{1+\gamma\tilde{\phi}}{\gamma}\left((1-S_h-S_g)\tilde{c}^l_m+S_h\tilde{c}^h_m\tilde{\rho}_h+S_g\tilde{c}^g_m\tilde{\rho}_g\right)\right]+$$

$$\mathrm{Pe}_1\left(\frac{1+\gamma}{1-\eta}\right)\frac{\partial}{\partial\tilde{z}}\left[\frac{1+\gamma\tilde{\phi}}{\gamma}(1-S_h-S_g)\tilde{c}_m^l\tilde{v}_s+\right.$$
$$\left(\frac{1+\gamma\tilde{\phi}}{\gamma}\right)S_h\tilde{c}_m^h\tilde{\rho}_h\tilde{v}_s-N_{sc}\frac{1+\gamma}{\gamma}\left(\frac{1+\gamma\tilde{\phi}}{1+\gamma\eta}\right)^8 k_{rw}\tilde{c}_m^l\left(\frac{\partial\tilde{p}_w}{\partial\tilde{z}}-1\right)+$$
$$\left.\left(\frac{1+\gamma\tilde{\phi}}{\gamma}\right)S_g\tilde{c}_m^g\tilde{\rho}_g\tilde{v}_s-N_{sc}\frac{1+\gamma}{\gamma}\left(\frac{1+\gamma\tilde{\phi}}{1+\gamma\eta}\right)^8 k_{rg}\tilde{\rho}_g\tilde{c}_m^g\left(\frac{\mu_w}{\mu_g}\right)\left(\frac{\partial\tilde{p}_g}{\partial\tilde{z}}-\tilde{\rho}_g\right)\right]=$$
$$\frac{\partial}{\partial\tilde{z}}\left[\frac{1+\gamma\tilde{\phi}}{\gamma}(1-S_h-S_g)\frac{\partial\tilde{c}_m^l}{\partial\tilde{z}}\right]+\frac{M_{CH_4}}{M_{org}}\tilde{\rho}_s\mathrm{Da}(1-\tilde{\phi})\tilde{\alpha}\beta \quad (9.25)$$

$$\text{I.C.}:\tilde{c}_m^l(\tilde{z},0)=0 \quad (9.26)$$

$$\text{B.C.}(1):\tilde{c}_m^l(0,\tilde{t})=0 \quad (9.27)$$

$$\text{B.C.}(2):\frac{\partial\tilde{c}_m^l}{\partial\tilde{z}}(D,\tilde{t})=0 \quad (9.28)$$

Sediment balance:

$$\frac{\partial}{\partial\tilde{t}}\left[1-\tilde{\phi}\right]+\mathrm{Pe}_1\left(\frac{1+\gamma}{1-\eta}\right)\frac{\partial}{\partial\tilde{z}}\left[(1-\tilde{\phi})\tilde{v}_s\right]=0 \quad (9.29)$$

$$\text{I.C.}:\tilde{v}_s(\tilde{z},0)=\frac{1-\eta}{1-\tilde{\phi}}\text{, (for hydrostatic compaction)} \quad (9.30)$$

$$\text{B.C.}(1):\tilde{v}_s(0,\tilde{t})=1 \quad (9.31)$$

Organic balance:

$$\frac{\partial}{\partial\tilde{t}}\left[\left(1-\tilde{\phi}\right)\tilde{\alpha}\right]+\mathrm{Pe}_1\left(\frac{1+\gamma}{1-\eta}\right)\frac{\partial}{\partial\tilde{z}}\left[(1-\tilde{\phi})\tilde{v}_s\tilde{\alpha}\right]$$
$$=-\mathrm{Da}\left(1-\tilde{\phi}\right)\tilde{\alpha} \quad (9.32)$$

$$\text{I.C.}:\tilde{\alpha}(\tilde{z},0)=0 \quad (9.33)$$

$$\text{B.C.}(1) : \tilde{\alpha}(0, \tilde{t}) = 1 \tag{9.34}$$

9.2.5 Porosity relationship and initial profiles

Reduced porosity $\tilde{\phi}$ is related to the dimensionless lithostatic stress ($\tilde{\sigma}$) and dimensionless pore water pressure ($\tilde{p}_w$):

$$\tilde{\phi} = \eta \exp\left[-\frac{\tilde{\sigma}_v - \tilde{p}_w}{N_{t\phi}}\right] \tag{9.35}$$

At hydrostatic pressure, the porosity profile can be computed as an analytical expression to serve as an initial condition:

$$\tilde{\phi} = \frac{\eta}{\eta + (1-\eta)\exp\left(\frac{\gamma\tilde{z}(\tilde{\rho}_s - 1)}{N_{t\phi}(1+\gamma)}\right)} \tag{9.36}$$

Similarly, the dimensionless lithostatic stress gradient can be written at hydrostatic pore pressures as follows:

$$\frac{\partial\tilde{\sigma}_v}{\partial\tilde{z}} = \frac{1}{1+\gamma}\left[\tilde{\rho}_s\gamma\left(1-\tilde{\phi}\right) + \left(1+\gamma\tilde{\phi}\right)\right] \tag{9.37}$$

9.2.6 Numerical solution

The coupled equations (9.21), (9.25), (9.29) and (9.32) are solved numerically using a fully implicit formulation, with the primary variables being $\tilde{p}_w$, $\tilde{v}_s$, $\tilde{\alpha}$ and one of the following three ($\tilde{c}_m^l$,S_h, S_g). Choice between these last three primary variables is made according to the local thermodynamic conditions at any gridblock

at any given timestep. All four mass balances are cast in residual form and the Newton-Raphson method is used to iterate on them to converge to the solution.

9.3 Results

To study the effect of overpressure on gas hydrate and free gas saturation, we simulate cases with different values of the sedimentation-compaction parameter N_{sc}. Apart from the parameter N_{sc}, other primary simulation parameters include the Peclet number, the Damkohler number, the normalized organic carbon input and the reduced porosity parameters. Values of these parameters used in all simulations shown in this chapter are: $\mathrm{Pe}_1 = 0.1$, $\mathrm{Da} = 10$, $\beta = 3$, $N_{t\phi} = 1$, $\eta = 6/9$, and $\gamma = 9$. Seafloor parameters are chosen to be similar to the Blake Ridge region (Paull et al., 2000), with seafloor temperature of 3°C, seafloor depth of 2700 m, and geotherm of 0.04°C/m. We keep these parameters constant in simulations shown later and only vary N_{sc} from higher to progressively lower values.

Figure 9.2 shows steady-state pore pressure profiles versus depth below the seafloor for four different values of N_{sc}. Hydrostatic pressure profile and lithostatic stress profiles are also plotted for each case as minimum and maximum bounds to the pore pressure, respectively. Importantly, simulations show that relatively higher values of N_{sc} ($\sim 10^4$) lead to almost hydrostatic pore pressures, whereas relatively lower N_{sc} (of order unity) lead to pore pressures that are close to the lithostatic limit (Figure 9.2). This occurs because relatively low N_{sc} values imply lower sediment permeability and/or fast sedimentation rate. Either of these conditions can reduce

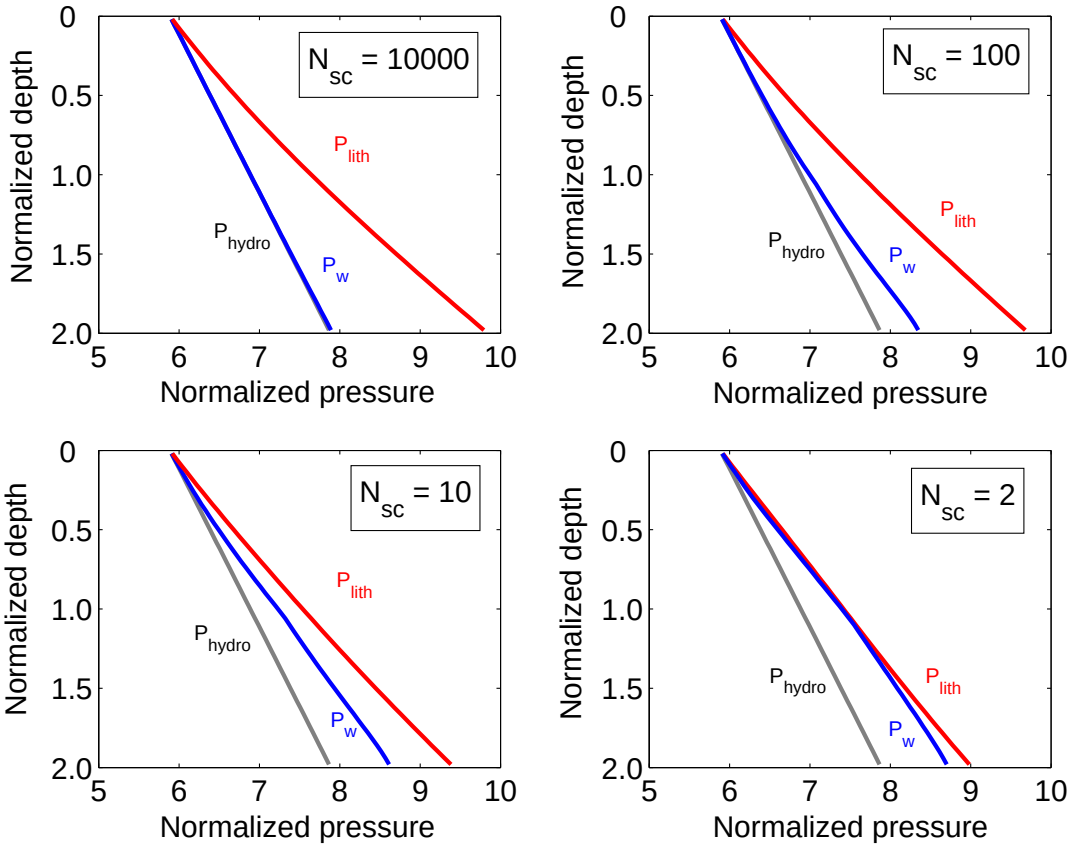

Figure 9.2: Effect of the sedimentation-compaction parameter N_{sc} on steady state pore pressure profiles. Lower values of N_{sc} imply higher sedimentation rates and/or lower permeabilities resulting in pore pressures higher than hydrostatic. Each pore pressure curve is bounded by the hydrostatic pressure profile as the lower limit and the lithostatic stress profile as the upper limit. At relatively higher values of N_{sc} pore pressure is almost hydrostatic, whereas relatively lower values of N_{sc} lead to almost lithostatic pore pressures.

the rate of expulsion of pore water in response to increasing overburden, leading to pore pressures higher than hydrostatic values. Conversely, relatively higher values of N_{sc} imply high sediment permeability and/or low sedimentation rate. This maintains equilibrium compaction and pore pressures that remain close to hydrostatic values.

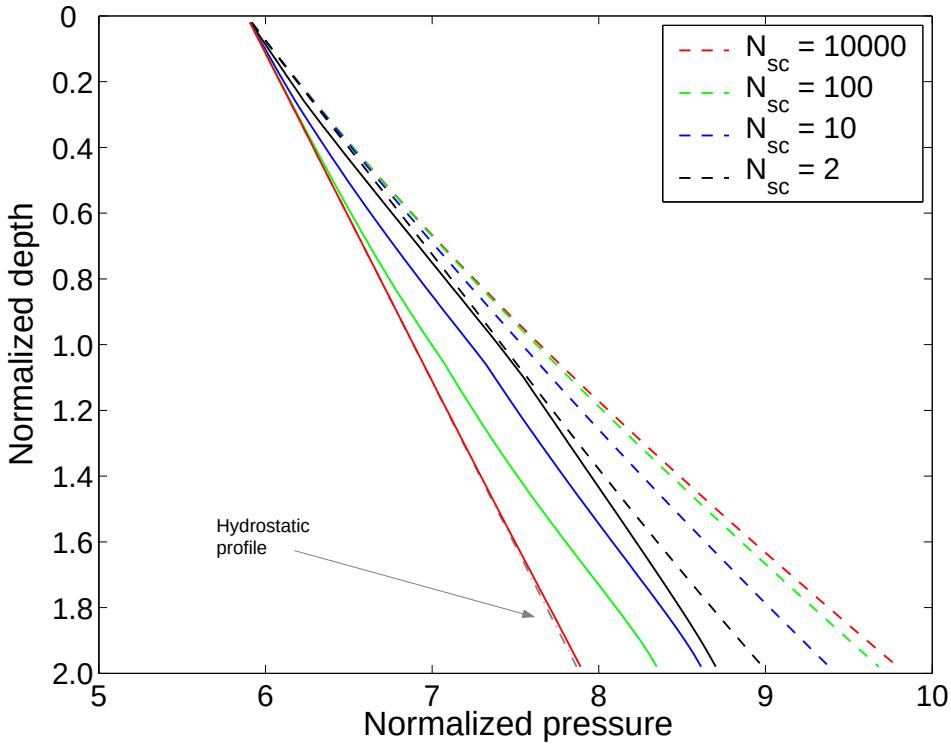

Figure 9.3: Pressure profiles shown in Figure 9.2 plotted together for all four cases. Lithostatic stress profiles (dashed curves) and the corresponding pore pressure profiles (solid curves) for the same value of N_{sc} are color-coded together.

Figure 9.2 also reveals that the lithostatic stress reduces as pore pressures increase. To illustrate this more clearly, we plot pore pressure and lithostatic stress profiles corresponding to the four cases together in Figure 9.3. Dashed set of curves in Figure 9.3 correspond to the lithostatic stress profiles, while solid curves

denote pore pressure profiles. It can be seen from Figure 9.3 that pore pressure and lithostatic profiles remain separated from each other at large N_{sc}. However, on lowering N_{sc}, both pore pressure and lithostatic curves approach each other. Decrease in lithostatic stress on reducing N_{sc} occurs because increased porosities, resulting from lower effective stresses acting on the sediments, cause lower bulk densities of the sediment. Since the lithostatic stress gradient is a function of sediment bulk density, overpressure and higher porosities lead to lower lithostatic stress (Figure 9.3). Steady-state reduced porosity profiles for the four cases are plotted in Figure 9.4. As expected, higher pore pressures at low N_{sc} lead to lower effective stresses and higher porosities.

As mentioned before, increase in pore pressure influences the thermodynamic stability of gas hydrates. Specifically, increase in pore pressure extends the depth to the base of the GHSZ deeper into the sediments. This change is shown through the methane solubility curves in Figure 9.5 for the same set of N_{sc} values simulated in the previous figures. We start with the case N_{sc}=10000, which corresponds to near-hydrostatic pore pressures. According to the scaling scheme defined previously, the solubility curve for this case has a peak methane solubility equal to unity at unit normalized depth. As pore pressure increases, i.e. N_{sc} decreases, we observe that the peak values of the solubility curves shift to higher values, with the peak itself occurring at slightly deeper depths. This demonstrates that the base of GHSZ is a dynamic boundary that moves in response to the pore pressure. However, even when pore pressures are close to lithostatic, the downward shift in the base of the GHSZ is very small in the normalized form. When this normalized

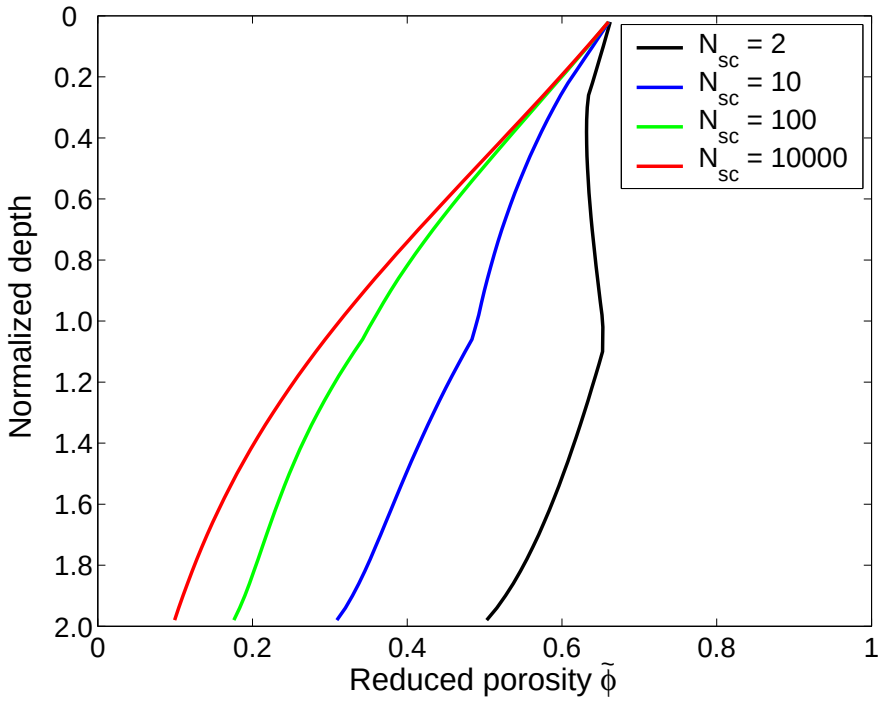

Figure 9.4: Effect of the parameter N_{sc} on steady-state reduced porosity profiles. At relatively high values of N_{sc}, pore pressure remains close to hydrostatic, causing equilibrium compaction and maximum porosity loss. As N_{sc} is reduced, pore pressure increases from hydrostatic values, resulting in lower effective stresses, lesser compaction and significantly higher porosities.

depth scale is converted back to the physical scale by multiplying with L_t, the depth to the base of GHSZ, this increase in the thickness of the GHSZ becomes larger, but is still relatively small. For example, for the case corresponding to almost lithostatic pore pressure, the downward shift in the base of the GHSZ is about 20 m, which, for Blake Ridge type seafloor conditions, is only about 0.7% of the water depth.

The effect of N_{sc} on steady-state gas hydrate and free gas saturation profiles is shown in Figure 9.6. Maximum gas hydrate and free gas saturations occur at the highest values of N_{sc} that corresponds to hydrostatic pore pressures. Progressive

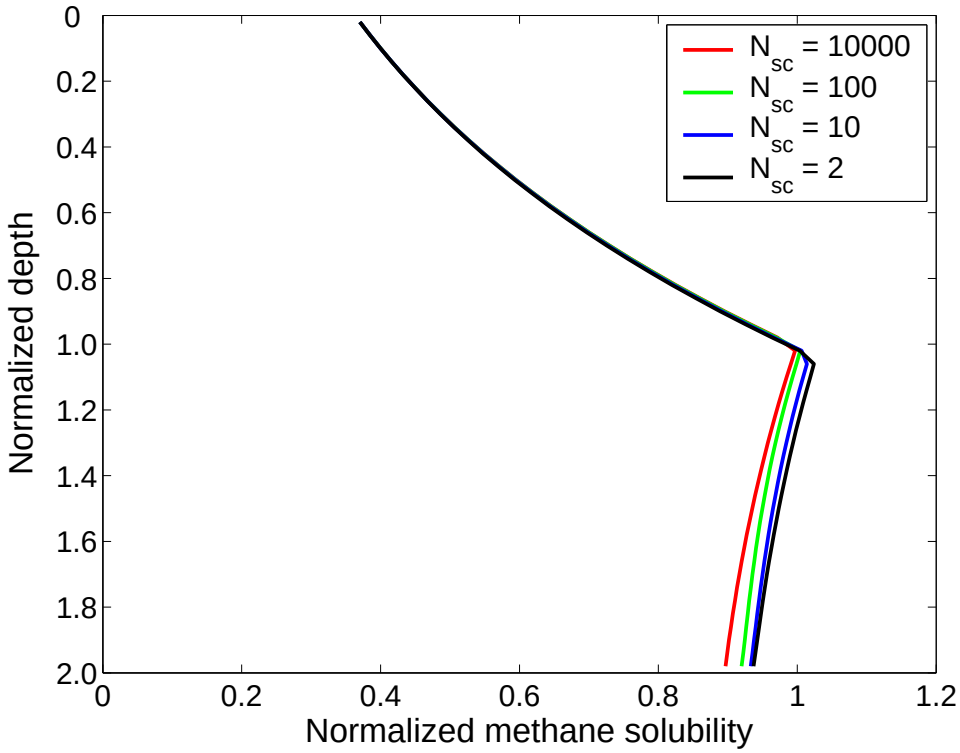

Figure 9.5: Effect of overpressure on methane solubility curves. Decreasing the value of N_{sc} from 10000 to 2 causes increasing overpressure within the sediment and results in a deeper base of the GHSZ. The magnitude of this downward shift is, however, negligible even when the pore pressure is close to lithostatic.

decrease in the values of N_{sc} lead to lower gas hydrate and free gas saturations due to compaction disequilibrium. As mentioned before, relatively lower values of N_{sc} lead to higher overpressures, higher sediment porosities and faster sediment velocities, which result in lower organic carbon decay within the GHSZ and shorter residence times of hydrate and free gas in the GHSZ.

However, it should be noted that hydrate and free gas saturation profiles do not give a complete picture of their amounts, because each value of N_{sc} results in a different porosity profile. Thus, although hydrate and free gas saturation within the pore space decrease on lowering N_{sc}, the corresponding increase in porosity

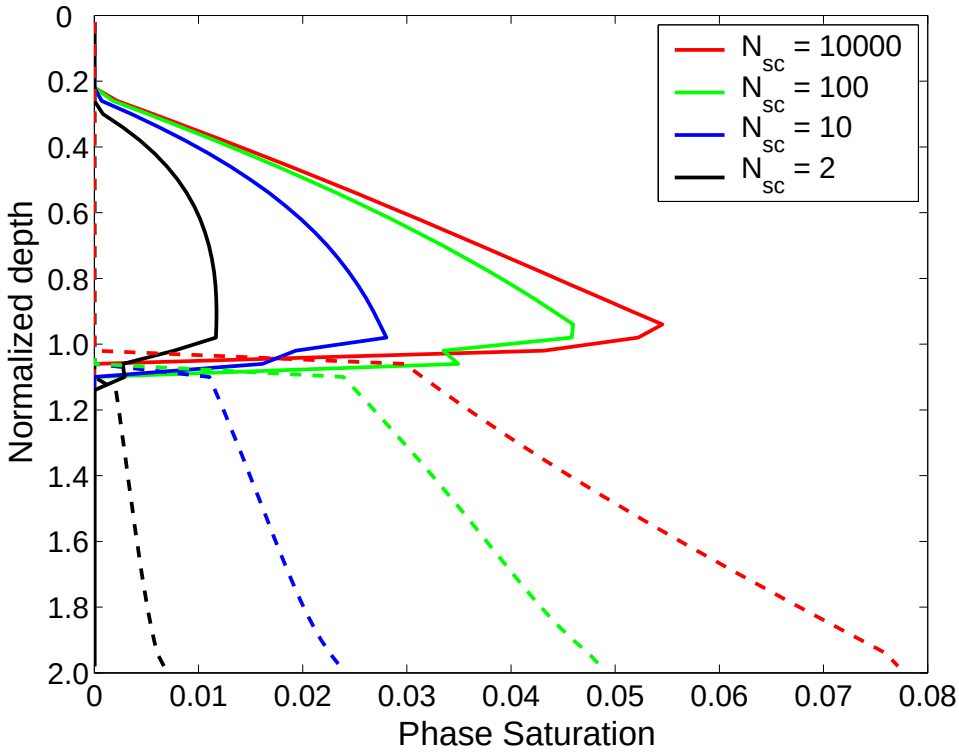

Figure 9.6: Effect of overpressure, characterized through N_{sc}, on steady-state gas hydrate saturation and free gas saturation profiles. Relatively smaller values of N_{sc} lead to overpressure development, higher porosities, higher sediment velocities, and lower net hydrate and free gas saturations.

might lead to net higher accumulation of hydrate or free gas within the sediment volume. To test this scenario, we plot the product of porosity and hydrate/free gas saturation (ϕS_j) to get the volume fraction of hydrate and free gas within the sediment. These profiles are plotted in Figure 9.7 and show that the net amount of gas hydrate or free gas saturation within the sediment also decreases on lowering N_{sc}. However, multiplying by porosity does reduce the magnitude of change observed between different cases. For example, peak hydrate saturation at the base of GHSZ decreases from about 6% to 1%, a factor of 6 change, on lowering N_{sc}

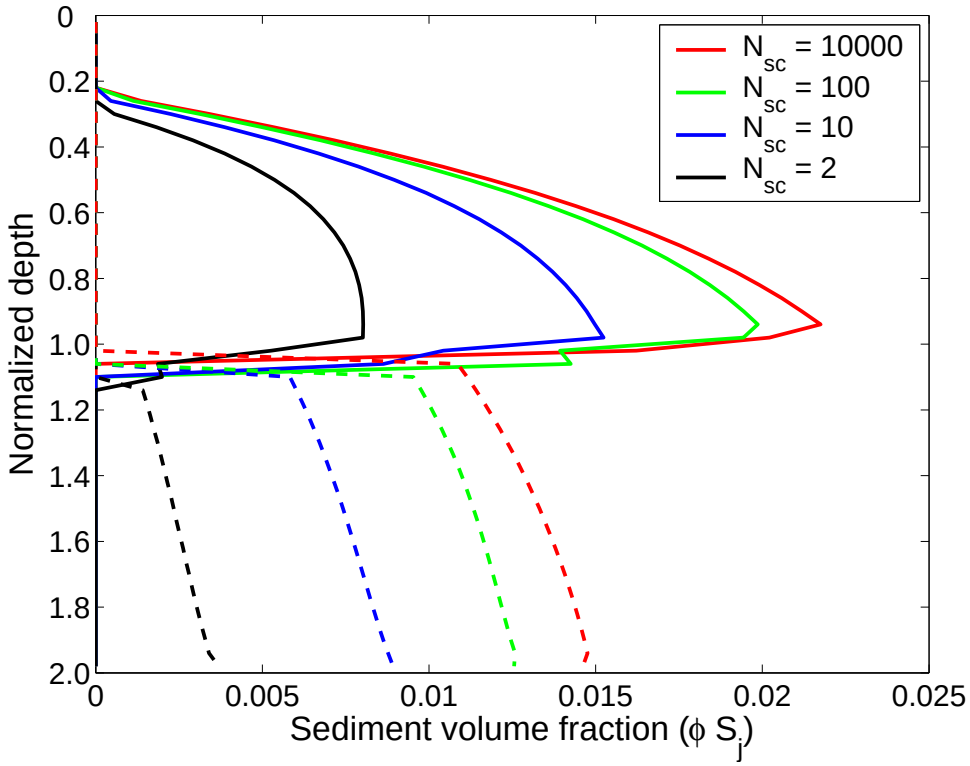

Figure 9.7: Effect of overpressure, characterized through N_{sc}, on steady-state gas hydrate and free gas sediment volume fraction.

from 10000 to 2. In contrast, peak change in sediment volume fraction of hydrate goes from about 2.2% to 0.7%, a factor of 3 change, for the same decrease in N_{sc}.

This validates our hypothesis that overpressure does lower the net amount of methane that accumulates in either hydrate or free gas phase. In other words, the decrease in hydrate and free gas saturation with increasing overpressure is not only a result of increased porosities. The effect of increased sediment and fluid velocities and lower organic carbon decay within the GHSZ has a much more significant impact on net gas hydrate and free gas accumulation.

9.3.1 Effect on free gas column thickness

Based on pressure profiles shown in Figures 9.1 and 9.2, it can be argued that deep connected free gas columns may result for settings characterized by high N_{sc}. In contrast, only short gas columns can form when N_{sc} is low before sediment fracture/failure occurs and vents the free gas into the ocean. Thus, from an exploration standpoint, geologic sites characterized by high permeability and low sedimentation rates (i.e., high N_{sc}) might be most suitable for targeting the free gas sealed by a hydrate layer.

9.4 Conclusions

A dimensionless numerical model for non-hydrostatic pressure compaction is developed to study the effect of overpressure on gas hydrate and free gas saturations. Non-dimensionalization of the equations lead to a sedimentation-compaction group, N_{sc}, defined as the ratio of sediment permeability to sedimentation rate. Simulations show that relatively high values of N_{sc} (close to 10^4) lead to systems close to hydrostatic pore pressure, while relatively low values of N_{sc} (about unity) lead to significant overpressure in the system. Overpressure development impacts this gas hydrate system by lowering effective stresses on the sediment, causing higher porosities. Higher sediment velocities achieved due to overpressure and high porosities ultimately lead to lesser organic carbon decay, resulting in lower hydrate and free gas saturations for our set of boundary conditions, i.e., fixed seafloor depth and constant geotherm.

Chapter 10

Modeling Two-Dimensional Heterogeneous Gas Hydrate Systems

10.1 Introduction

Gas hydrate modeling in homogeneous, one-dimensional (1-D) systems was discussed in previous chapters. This approach, although simple, allowed identification of key dimensionless groups controlling the system and helped in summarizing average gas hydrate saturation dependence on site-specific parameters using appropriate scaling schemes (Bhatnagar et al., 2007). However, natural gas hydrate systems are much more complex and heterogeneous than these simplified 1-D models. Some of the features missing in the 1-D model include:

- Free gas migration: Free gas is assumed to be immobile in most gas hydrate models. However, gas hydrate can become mobile if it exceeds the critical gas saturation, resulting in the build-up of connected gas columns. Development of thick gas columns can result in sediment failure and venting of free gas into the gas hydrate stability zone (GHSZ) or the ocean (Flemings et al., 2003; Hornbach et al., 2004; Liu and Flemings, 2007).

- Extension to two-dimensions (2-D): 2-D models depict natural systems more accurately by allowing lateral fluid migration and incorporating sediment het-

erogeneities. This can help predict high saturation hydrate/free gas accumulations within localized sediment layers or structures.

- Faulted or fractured systems: Fluid flow within natural gas hydrate systems can be dominated by local fault or fracture networks. These high permeability conduits can preferentially feed methane-charged water and gas to high permeability sand layers, resulting in concentrated hydrate deposits (Tréhu et al., 2004; Weinberger and Brown, 2006).

- Stratigraphy: Most gas hydrate systems are characterized by stratigraphic sequences of different permeabilities instead of a single, homogeneous sediment layer. Geochemical and geophysical proxy data often show relatively high gas hydrate saturation within local sand beds that alternate with silt or clay layers with little or no hydrate (Paull et al., 2000; Tréhu et al., 2003; Riedel et al., 2006; Weinberger and Brown, 2006). Effects of such parallel or dipping beds on gas hydrate distribution necessitates development of 2-D models.

To incorporate these features, we extend the previous 1-D model to 2-D systems with mobile free gas in this chapter. Heterogeneities, such as vertical fractures and parallel or dipping sediment layers are then added to this 2-D model to simulate complex and real-world gas hydrate settings. We start with component material balances in 2-D.

10.2 Mathematical Model

The two-dimensional material balances for water, sediment, organic carbon and methane are written as:

Water Balance

$$\frac{\partial}{\partial t}\left[\phi S_w c_w^l \rho_w + \phi S_h c_w^h \rho_h\right] + \nabla \cdot \left[\phi S_w c_w^l \rho_w \mathbf{v}_w + \phi S_h c_w^h \rho_h \mathbf{v}_s\right] = 0 \tag{10.1}$$

Sediment Balance

$$\frac{\partial}{\partial t}\left[(1-\phi)\,\rho_s\right] + \nabla \cdot \left[(1-\phi)\,\rho_s \mathbf{v}_s\right] = 0 \tag{10.2}$$

Organic Balance

$$\frac{\partial}{\partial t}\left[(1-\phi)\,\rho_s \alpha\right] + \nabla \cdot \left[(1-\phi)\,\rho_s \mathbf{v}_s \alpha\right] = -\rho_s \lambda\,(1-\phi)\,\alpha \tag{10.3}$$

Methane Balance

$$\begin{aligned} &\frac{\partial}{\partial t}\left[\phi S_w c_m^l \rho_w + \phi S_h c_m^h \rho_h + \phi S_g c_m^g \rho_g\right] + \\ &\nabla \cdot \left[\phi S_w c_m^l \rho_w \mathbf{v}_w + \phi S_h c_m^h \rho_h \mathbf{v}_s + \phi S_g c_m^g \rho_g \mathbf{v}_g\right] = \nabla \cdot \left[\phi S_w D_m \rho_w \nabla c_m^l\right] \\ &\qquad + \frac{M_{CH_4}}{M_{org}} \rho_s \lambda\,(1-\phi)\,\alpha \end{aligned} \tag{10.4}$$

where ϕ denotes porosity, c_i^j represents mass fraction of component i in phase j, S_j represents phase saturation, $\mathbf{v}_j$ denotes phase j velocity vector, ρ_j denotes phase

density, λ is the methanogenesis reaction rate constant, D_m denotes methane diffusivity, and α is organic carbon content in sediments. Subscripts m, w, s, h and g denote methane, water, sediment, hydrate, and free gas, respectively. Superscripts l, h and g represent water, hydrate and free gas phases, respectively.

10.2.1 Constitutive relationships

The following constitutive relationships are used in this formulation.

- Darcy's law for water flux in a compacting medium (Bear, 1988):

$$S_w\phi(\mathbf{v}_w - \mathbf{v}_s) = -\frac{kk_{rw}}{\mu_w}(\nabla p_w - \rho_w g \nabla z) \tag{10.5}$$

where k is the absolute permeability of the sediment, k_{rw} denotes relative permeability of water, μ_w is water viscosity, and p_w is water pressure.

- Darcy's law for free gas flux can be written as:

$$S_g\phi(\mathbf{v}_g - \mathbf{v}_s) = -\frac{kk_{rg}}{\mu_g}(\nabla p_g - \rho_g g \nabla z) \tag{10.6}$$

where k_{rg} denotes relative permeability of gas, μ_g is gas viscosity, and p_g is gas pressure.

- Absolute permeability of sediment is modeled as a power law function of porosity (Smith, 1971):

$$k = k_0\left(\frac{\phi}{\phi_0}\right)^8 \tag{10.7}$$

where k_0 and ϕ_0 are the initial sediment permeability and porosity at time of depo-

sition.

• Permeability reduction due to hydrate formation is modeled as (assuming pore-filling structure) (Kleinberg et al., 2003):

$$k = k_0 \left(1 - S_h^2 + \frac{2(1-S_h)^2}{\ln(S_h)}\right) \tag{10.8}$$

This function (k/k_0) is plotted in Figure 10.1 as a function of gas hydrate saturation, S_h. The ratio approaches unity at hydrate saturation close to zero and decreases monotonously as S_h increases. This decrease in sediment absolute permeability increases the capillary entry pressure for free gas, effectively making gas hydrate a seal for the connected gas column beneath the GHSZ.

• Water relative permeability model in the presence of free gas is (Bear, 1988):

$$k_{rw} = k_{rw}^0 (S_w^*)^4, \quad \text{where} \quad S_w^* = \frac{S_w - S_{wr}}{1 - S_{wr}} \tag{10.9}$$

where k_{rw}^0 is the end-point relative permeability and S_{wr} is the residual water saturation.

• Gas relative permeability in the presence of water is (Bear, 1988):

$$k_{rg} = k_{rg}^0 (S_g^*)^2, \quad \text{where} \quad S_g^* = \frac{S_g - S_{gr}}{1 - S_{wr} - S_{gr}} \tag{10.10}$$

where k_{rg}^0 is the end-point relative permeability and S_{gr} is the residual gas saturation.

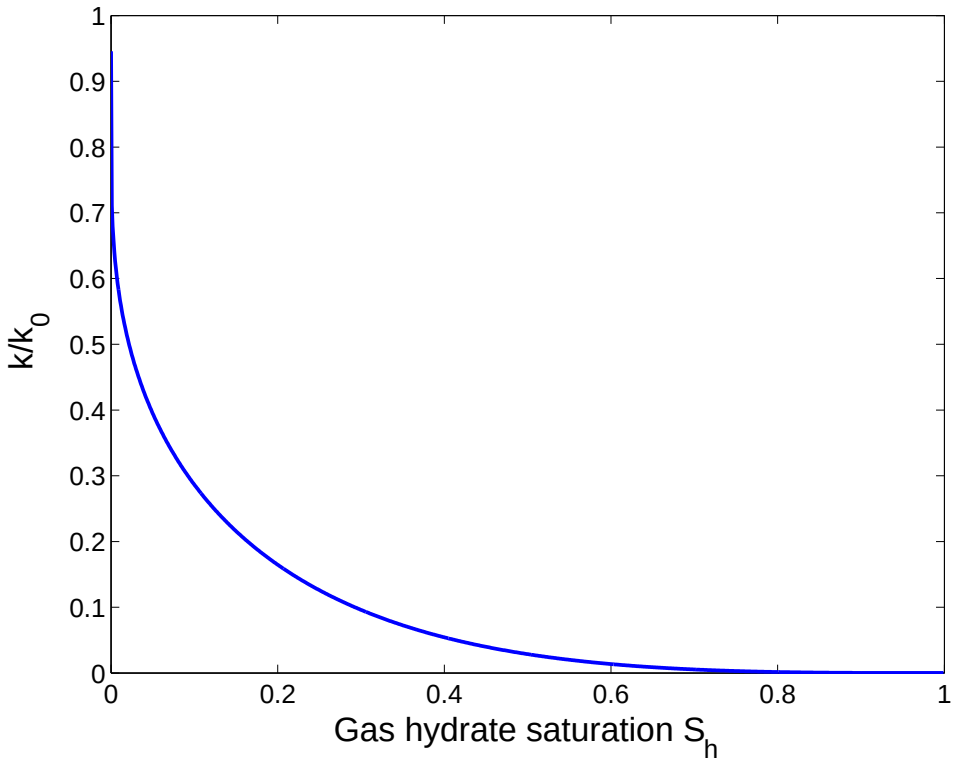

Figure 10.1: Decrease in sediment absolute permeability (k/k_0) due to gas hydrate precipitation and assuming it to be pore-filling. Permeability to flow rapidly decreases as hydrate saturation increases from zero.

- Capillary pressure (P_c) is the difference between gas and water pressure:

$$P_c = p_g - p_w \tag{10.11}$$

The Leverett J-function, $J(S_w)$, is used to normalize capillary pressure curves for lithologies with different porosities and permeabilities as:

$$J(S_w) = \frac{P_{c,0}(S_w)}{\sigma_{gw} \cos\theta} \sqrt{\frac{k_0}{\phi_0}} \tag{10.12}$$

where $P_{c,0}(S_w)$ is the capillary pressure curve at reference porosity ϕ_0 and absolute

permeability k_0, σ_{gw} is the gas-water interfacial tension and θ is the contact angle. Assuming constant σ_{gw} and θ, capillary pressure curve for any given porosity (ϕ) and permeability (k) can be evaluated from this J-function as:

$$P_c(S_w) = J(S_w)\sigma_{gw}\cos\theta\sqrt{\frac{\phi}{k}} = P_{c,0}(S_w)\sqrt{\frac{k_0\phi}{\phi_0 k}} \tag{10.13}$$

The Brooks-Corey model is used to define the capillary pressure curve as a function of normalized water saturation (S_w^*) (Bear, 1988):

$$P_{c,0}(S_w) = P_{ce,0}{S_w^*}^{-1/n}, \quad \text{where} \quad S_w^* = \frac{S_w - S_{wr}}{1 - S_{wr}} \tag{10.14}$$

where $P_{ce,0}$ is the capillary entry pressure at ϕ_0 and k_0, and n is the pore-size distribution index.

- Porosity-effective stress relationship is defined as (Rubey and Hubbert, 1959):

$$\phi = \phi_\infty + (\phi_0 - \phi_\infty)e^{-\frac{\sigma_v - p_w}{\sigma_\phi}} \tag{10.15}$$

where ϕ_∞ is minimum porosity achieved at great depth, σ_v is vertical effective stress, and σ_ϕ is a characteristic stress (constant).

- Lithostatic stress gradient as a function of densities and porosity is:

$$\frac{\partial\sigma_v}{\partial z} = [(1-\phi)\rho_s + \phi\rho_w]\, g \tag{10.16}$$

10.2.2 Normalized variables and dimensionless groups

The above equations are now written in dimensionless form according to the scaling schemes defined in section 9.2.3, but are repeated here for continuity. Reduced porosities are defined as:

$$\tilde{\phi} = \frac{\phi - \phi_\infty}{1 - \phi_\infty} \quad , \quad \eta = \frac{\phi_0 - \phi_\infty}{1 - \phi_\infty} \quad , \quad \gamma = \frac{1 - \phi_\infty}{\phi_\infty} \tag{10.17}$$

The dimensionless Peclet number, Damkohler number and the group quantifying sedimentation-compaction are defined as:

$$\mathrm{Pe}_1 = \frac{U_{f,sed} L_t}{D_m} \quad , \quad \mathrm{Da} = \frac{\lambda L_t^2}{D_m} \quad , \quad N_{sc} = \frac{k_0 \rho_w g}{\mu_w \dot{S}} \tag{10.18}$$

where $U_{f,sed}$ is the fluid flux due to sedimentation-compaction at hydrostatic pore pressure, L_t is depth to the base of the GHSZ, and $\dot{S}$ is the sedimentation rate at the seafloor. The ratio of the characteristic compaction depth to L_t is defined by $N_{t\phi}$:

$$N_{t\phi} = \frac{L_\phi}{L_t} = \frac{\sigma_\phi / (\rho_w g)}{L_t} \tag{10.19}$$

Normalized methane concentrations are defined as:

$$\tilde{c}_m^l = \frac{c_m^l}{c_{m,eqb}^l} \quad , \quad \tilde{c}_m^h = \frac{c_m^h}{c_{m,eqb}^l} \quad , \quad \tilde{c}_m^g = \frac{c_m^g}{c_{m,eqb}^l} \tag{10.20}$$

Lithostatic stress (σ_v), water pressure, gas pressure and capillary pressure are

normalized by hydrostatic water pressure at the base of the GHSZ:

$$\tilde{\sigma}_v = \frac{\sigma_v}{\rho_w g L_t} \quad , \quad \tilde{p}_w = \frac{p_w}{\rho_w g L_t} \quad , \quad \tilde{p}_g = \frac{p_g}{\rho_w g L_t} \quad , \quad \tilde{P}_c = \frac{P_c}{\rho_w g L_t} \tag{10.21}$$

Dimensionless distances and time are defined as:

$$\tilde{z} = \frac{z}{L_t} \quad , \quad \tilde{x} = \frac{x}{L_t} \quad , \quad \tilde{t} = \frac{t}{L_t^2 / D_m} \tag{10.22}$$

All phase densities are normalized by water density as:

$$\tilde{\rho}_h = \frac{\rho_h}{\rho_w} \quad , \quad \tilde{\rho}_g = \frac{\rho_g}{\rho_w} \quad , \quad \tilde{\rho}_s = \frac{\rho_s}{\rho_w} \tag{10.23}$$

Sedimentation and compaction in this 2-D model is assumed to be in 1-D, i.e., zero lateral strain. This causes the sediment to move only in the vertical direction, with no lateral movement. Consequently, gas hydrate within the matrix as well as immobile free gas (if it is below critical saturation) can only move downward with the sediment. Water and mobile gas, however, can move in vertical as well as horizontal directions. Hence, the sediment velocity vector $\mathbf{v}_s$ is replaced in the following equations by the z-direction velocity v_s. Further, sediment velocity v_s is normalized by the sedimentation rate at the seafloor $\dot{S}$:

$$\tilde{v}_s = \frac{v_s}{\dot{S}} \tag{10.24}$$

Finally, organic carbon content and initial TOC are scaled as:

$$\tilde{\alpha} = \frac{\alpha}{\alpha_0} \quad , \quad \beta = \frac{\alpha_0}{c^l_{m,eqb}} \tag{10.25}$$

where α_0 is TOC content at the seafloor and $c^l_{m,eqb}$ is methane solubility in water at the base of the GHSZ.

10.2.3 Dimensionless mass balances

The above scaling schemes lead to the following dimensionless form of the four mass balances, initial and boundary conditions.

Water Balance:

$$\frac{\partial}{\partial \tilde{t}}\left[\frac{1+\gamma\tilde{\phi}}{\gamma}\left(S_w c^l_w + S_h c^h_w \tilde{\rho}_h\right)\right] + \mathrm{Pe}_1\left(\frac{1+\gamma}{1-\eta}\right)\frac{\partial}{\partial \tilde{z}}\left[\left\{\left(\frac{1+\gamma\tilde{\phi}}{\gamma}\right)S_w\tilde{v}_s - N_{sc}\left(\frac{1+\gamma}{\gamma}\right)\left(\frac{1+\gamma\tilde{\phi}}{1+\gamma\eta}\right)^8 k_{rw}\left(\frac{\partial \tilde{p}_w}{\partial \tilde{z}} - 1\right)\right\}c^l_w + \left(\frac{1+\gamma\tilde{\phi}}{\gamma}\right)S_h\tilde{\rho}_h\tilde{v}_s c^h_w\right] + \mathrm{Pe}_1\left(\frac{1+\gamma}{1-\eta}\right)\frac{\partial}{\partial \tilde{x}}\left[-N_{sc}\left(\frac{1+\gamma}{\gamma}\right)\left(\frac{1+\gamma\tilde{\phi}}{1+\gamma\eta}\right)^8 k_{rw}\frac{\partial \tilde{p}_w}{\partial \tilde{x}}c^l_w\right] = 0 \tag{10.26}$$

The initial pressure profile is assumed to be hydrostatic. The boundary condition (B.C.) at the seafloor is hydrostatic pressure, left and right side boundaries of the 2-D domain are assumed to be no-flow boundaries, whereas the bottom boundary is maintained at hydrostatic pressure gradient. These initial and B.C.s are written as:

$$\text{I.C.} : \tilde{p}_w(\tilde{z}, \tilde{x}, 0) = \frac{\rho_w g D_0 + \rho_w g z}{\rho_w g L_t} = \frac{D_0}{L_t} + \tilde{z} \tag{10.27}$$

$$\text{B.C.}(1) : \tilde{p}_w(0, \tilde{x}, \tilde{t}) = \frac{D_0}{L_t} \quad , \quad (\text{Hydrostatic pressure}) \tag{10.28}$$

$$\text{B.C.}(2) : \frac{\partial \tilde{p}_w}{\partial \tilde{x}}(\tilde{z}, 0, \tilde{t}) = \frac{\partial \tilde{p}_w}{\partial \tilde{x}}(\tilde{z}, D_x, \tilde{t}) = 0 \quad , \quad (\text{No} - \text{flow}) \tag{10.29}$$

$$\text{B.C.}(3) : \frac{\partial \tilde{p}_w}{\partial \tilde{z}}(D_z, \tilde{x}, \tilde{t}) = 1 \quad , \quad (\text{Hydrostatic gradient}) \tag{10.30}$$

where D_0 is seafloor depth, D_x is the width of the domain, and D_z is bottom of the domain.

Sediment balance:

$$\frac{\partial}{\partial \tilde{t}} \left[1 - \tilde{\phi}\right] + \text{Pe}_1 \left(\frac{1+\gamma}{1-\eta}\right) \frac{\partial}{\partial \tilde{z}} \left[(1 - \tilde{\phi})\tilde{v}_s\right] = 0 \tag{10.31}$$

The initial velocity profile is obtained by assuming hydrostatic pressure, while the B.C. at the seafloor is the normalized sedimentation rate equal to unity:

$$\text{I.C.} : \tilde{v}_s(\tilde{z}, \tilde{x}, 0) = \frac{1-\eta}{1-\tilde{\phi}} \, , \, (\text{for hydrostatic compaction}) \tag{10.32}$$

$$\text{B.C.}(1) : \tilde{v}_s(0, \tilde{x}, \tilde{t}) = 1 \tag{10.33}$$

Organic balance:

$$\frac{\partial}{\partial \tilde{t}} \left[\left(1 - \tilde{\phi}\right) \tilde{\alpha}\right] + \text{Pe}_1 \left(\frac{1+\gamma}{1-\eta}\right) \frac{\partial}{\partial \tilde{z}} \left[(1 - \tilde{\phi})\tilde{v}_s\tilde{\alpha}\right] = -\text{Da} \left(1 - \tilde{\phi}\right) \tilde{\alpha} \tag{10.34}$$

Initially, no organic carbon is present within the sediment, whereas the seafloor

organic concentration is set to the normalized value of unity as a B.C.:

$$\text{I.C.} : \tilde{\alpha}(\tilde{z}, \tilde{x}, 0) = 0 \tag{10.35}$$

$$\text{B.C.}(1) : \tilde{\alpha}(0, \tilde{x}, \tilde{t}) = 1 \tag{10.36}$$

Methane balance:

$$\begin{aligned}
&\frac{\partial}{\partial \tilde{t}}\left[\frac{1+\gamma\tilde{\phi}}{\gamma}\left(S_w\tilde{c}_m^l + S_h\tilde{c}_m^h\tilde{\rho}_h + S_g\tilde{c}_m^g\tilde{\rho}_g\right)\right] + \mathrm{Pe}_1\left(\frac{1+\gamma}{1-\eta}\right)\\
&\frac{\partial}{\partial \tilde{z}}\left[\left\{\left(\frac{1+\gamma\tilde{\phi}}{\gamma}\right)S_w\tilde{v}_s - N_{sc}\left(\frac{1+\gamma}{\gamma}\right)\left(\frac{1+\gamma\tilde{\phi}}{1+\gamma\eta}\right)^8 k_{rw}\left(\frac{\partial\tilde{p}_w}{\partial\tilde{z}} - 1\right)\right\}\tilde{c}_m^l + \right.\\
&\left.\left\{\left(\frac{1+\gamma\tilde{\phi}}{\gamma}\right)S_g\tilde{v}_s - N_{sc}\left(\frac{1+\gamma}{\gamma}\right)\left(\frac{1+\gamma\tilde{\phi}}{1+\gamma\eta}\right)^8 k_{rg}\left(\frac{\mu_w}{\mu_g}\right)\left(\frac{\partial\tilde{p}_g}{\partial\tilde{z}} - \tilde{\rho}_g\right)\right\}\tilde{\rho}_g\tilde{c}_m^g + \right.\\
&\left.\left(\frac{1+\gamma\tilde{\phi}}{\gamma}\right)S_h\tilde{c}_m^h\tilde{\rho}_h\tilde{v}_s\right] + \mathrm{Pe}_1\left(\frac{1+\gamma}{1-\eta}\right)\frac{\partial}{\partial\tilde{x}}\left[-N_{sc}\left(\frac{1+\gamma}{\gamma}\right)\left(\frac{1+\gamma\tilde{\phi}}{1+\gamma\eta}\right)^8 k_{rw}\frac{\partial\tilde{p}_w}{\partial\tilde{x}}\tilde{c}_m^l - \right.\\
&\left.N_{sc}\left(\frac{1+\gamma}{\gamma}\right)\left(\frac{1+\gamma\tilde{\phi}}{1+\gamma\eta}\right)^8 k_{rg}\left(\frac{\mu_w}{\mu_g}\right)\frac{\partial\tilde{p}_g}{\partial\tilde{x}}\tilde{\rho}_g\tilde{c}_m^g\right] = \frac{\partial}{\partial\tilde{z}}\left[\frac{1+\gamma\tilde{\phi}}{\gamma}S_w\frac{\partial\tilde{c}_m^l}{\partial\tilde{z}}\right] + \\
&\frac{\partial}{\partial\tilde{x}}\left[\frac{1+\gamma\tilde{\phi}}{\gamma}S_w\frac{\partial\tilde{c}_m^l}{\partial\tilde{x}}\right] + \frac{M_{CH_4}}{M_{org}}\tilde{\rho}_s\mathrm{Da}(1-\tilde{\phi})\tilde{\alpha}\beta
\end{aligned} \tag{10.37}$$

At time $\tilde{t} = 0$, there is no methane in the system. Methane concentration at the seafloor is set to zero, while methane concentration gradient is set to zero at the other three boundaries:

$$\text{I.C.} : \tilde{c}_m^l(\tilde{z}, \tilde{x}, 0) = 0 \tag{10.38}$$

$$\text{B.C.}(1) : \tilde{c}_m^l(0, \tilde{x}, \tilde{t}) = 0 \tag{10.39}$$

$$\text{B.C.}(2) : \frac{\partial\tilde{c}_m^l}{\partial\tilde{z}}(D_z, \tilde{x}, \tilde{t}) = \frac{\partial\tilde{c}_m^l}{\partial\tilde{x}}(\tilde{z}, 0, \tilde{t}) = \frac{\partial\tilde{c}_m^l}{\partial\tilde{x}}(\tilde{z}, D_x, \tilde{t}) = 0 \tag{10.40}$$

10.2.4 Numerical Solution

The above equations (10.26, 10.31, 10.34 and 10.37) and boundary conditions form a set of highly coupled, non-linear equations that are solved using a fully-implicit finite-difference formulation. This ensures stability of the code, which is difficult to achieve using explicit schemes, especially during free gas migration and non-hydrostatic compaction. The equations are expressed in residual form and the Newton-Raphson method is used to iterate on them until convergence is achieved. Expansion of the time-derivative terms (to ensure material balance) is shown in Appendix A4, while phase-switching and choice of primary variables is discussed in Appendix A5.

10.3 Results

The general dimensionless equations derived in the previous section are now solved for different test cases. We start with simple, homogeneous, 2-D cases and progressively add heterogeneities to the system. Specifically, we first explain free gas migration in homogeneous, 2-D systems, which is followed by modeling high permeability fractures. We later include different permeability layers in 2-D and also simulate systems with combinations of fractures and heterogeneous permeability layers.

10.3.1 Free gas migration

Simulation results in previous chapters assumed free gas to be immobile, resulting in free gas being advected with the sediment. However, free gas becomes mobile if the critical gas saturation is exceeded. Mobile free gas can then rise buoyantly and move as a separate phase. This will lead to the build-up of free gas beneath the GHSZ, which may be sealed by the overlying low permeability hydrate layer.

We examine two cases of free gas migration in homogeneous, 2-D systems corresponding to different values of the sedimentation-compaction group (N_{sc}). All other parameters remain same for both cases, with the following values: $\mathrm{Pe}_1 = 0.1$, $\mathrm{Da} = 10$, $\beta = 10$, $\eta = 6/9$, $\gamma = 9$, $N_{t\phi} = 1$, seafloor temperature of 3°C, geotherm of 0.04°C/m, seafloor depth of 2700 mbsl, and salinity equal to that of standard seawater. Seawater density and viscosity are assumed to be 1030 kg/m^3 and 1 cp, respectively, while gas density and viscosity are calculated at the local temperature-pressure conditions (Selim and Sloan, 1989).

Capillary entry pressure ($p_{ce,0}$) at reference porosity and permeability is assumed to be 0.02 MPa (Liu and Flemings, 2007), pore size distribution index (n) is taken to be unity (Sun and Mohanty, 2006), and residual water saturation (S_{wr}) is assumed to be 10% (Liu and Flemings, 2007). Residual gas saturation values in the literature range from 4.5-17% (Schowalter, 1979) to more recent estimates of 2% (Moridis, 2003; Liu and Flemings, 2007) for gas hydrate systems. We choose a value of S_{gr}=3% for simulations shown in this section.

We now present simulation results for $N_{sc} = 1000$ and $N_{sc} = 10$. As shown

schematically in Chapter 9 (Figure 9.1), these two cases will explain how pore water overpressure due to sedimentation-compaction regulates the build-up of the connected free gas column. All simulation results are obtained for 2-D cases. However, since these systems are homogeneous in the lateral direction, we explain the results mostly using 1-D depth profiles. 2-D contour plots are shown for some specific cases only.

Case 1: $\mathbf{N_{sc} = 1000}$

We first simulate the case $N_{sc} = 1000$, which indicates that sediment permeability is large compared to the sedimentation rate. This will lead to overpressure due to sedimentation-compaction being close to zero, i.e., any overpressure that develops in this case will be caused by permeability reduction due to hydrate or free gas build-up only. Figure 10.2 shows the pore pressure, gas pressure and lithostatic stress profiles as a function of normalized depth at dimensionless time $\tilde{t} = 0.7$. The relatively large value of N_{sc} keeps water pressure close to hydrostatic.

Figure 10.3 shows the gas hydrate and free gas saturation at $\tilde{t} = 0.7$. Compared to gas saturation profiles shown previously, Figure 10.3 shows that gas in excess of the critical saturation migrates upwards buoyantly to the base of the GHSZ. Thus, maximum gas saturation occurs just below the GHSZ, while sediment sequences far below the GHSZ contain free gas close to the residual saturation. Peak hydrate saturation is about 25% at the base of the GHSZ, which reduces the absolute sediment permeability, increases the gas capillary entry pressure and seals the gas layer below. As more free gas accumulates beneath this hydrate layer, gas

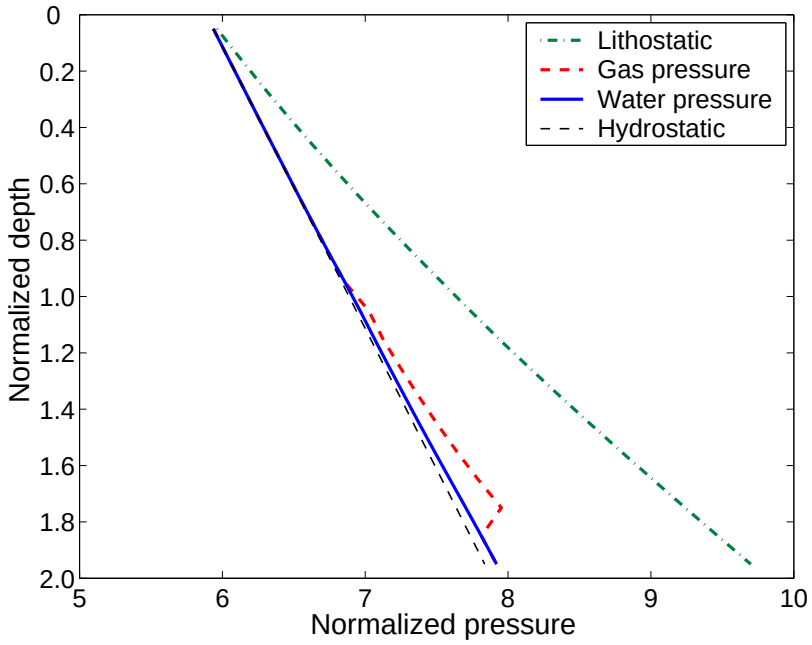

Figure 10.2: Lithostatic, gas pressure, water pressure, and hydrostatic pressure profiles at time $\tilde{t} = 0.7$ for $N_{sc} = 1000$. Gas pressure in excess of the water pressure is the capillary pressure.

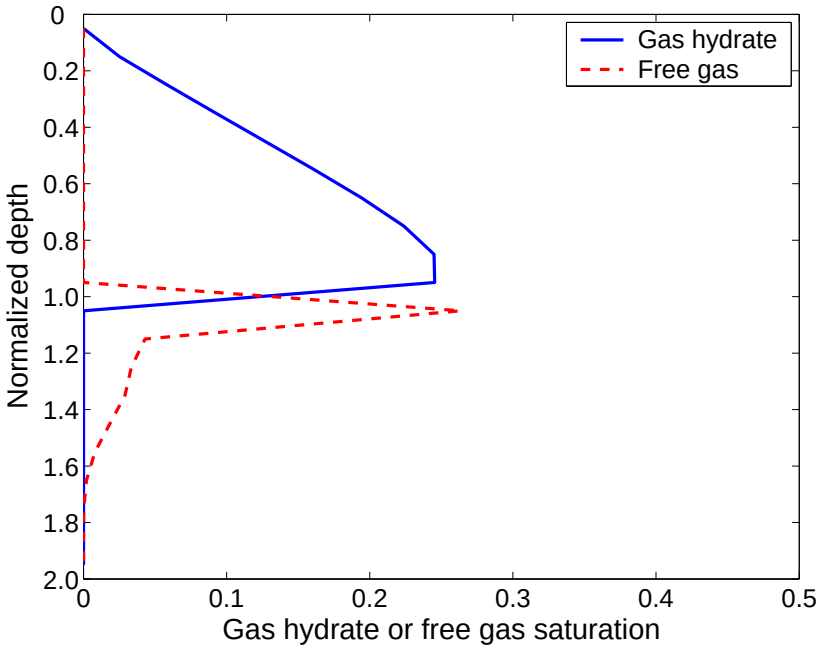

Figure 10.3: Gas hydrate and free gas saturation profiles at time $\tilde{t} = 0.7$ for $N_{sc} = 1000$. Gas starts to migrate to the base of the GHSZ when it exceeds the critical saturation.

pressure increases such that it exceeds the capillary entry pressure, causing free gas to migrate into the GHSZ. This results in increased gas hydrate saturation at the base of the GHSZ, thereby restricting further gas migration.

Figure 10.4 and 10.5 show this transient behavior at time $\tilde{t} = 1$. Water pressure starts to deviate from the hydrostatic profile due to relatively large hydrate and free gas saturations near the base of the GHSZ, which significantly reduce the relative permeability of water. More importantly, a sharp increase in gas hydrate saturation is seen just above the base of the GHSZ. This sharp increase is solely due to gas migration from beneath the GHSZ and causes a longer connected free gas column to build-up beneath the hydrate layer. At a later time, gas pressure exceeds the new capillary entry pressure and again enters the GHSZ, causing an even larger hydrate saturation at the base of the GHSZ. Thus, this process assumes a cyclical nature, whereby gas keeps on accumulating beneath the hydrate layer, which continually becomes more concentrated at the base of the GHSZ due to periodical upward gas migration. However, as the gas column (and saturation) builds up, gas pressure increases to a point where it exceeds the lithostatic stress. At this point, the vertical gas effective stress (defined as the difference between gas pressure and lithostatic stress) becomes zero, causing new or pre-existing fractures to dilate, thereby allowing sudden free gas migration into the GHSZ or to the ocean.

Following previous work (Flemings et al., 2003; Liu and Flemings, 2007), this state at which gas pressure becomes equal to the overburden (lithostatic stress) is termed 'critical-state'. This critical-state is shown in Figures 10.6, 10.7 and 10.8,

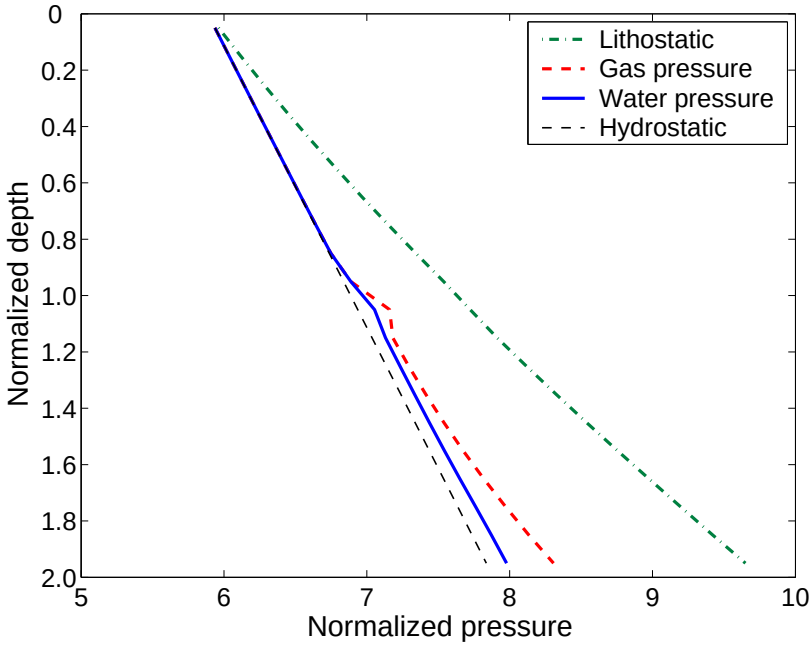

Figure 10.4: Lithostatic, gas pressure, water pressure, and hydrostatic pressure profiles at time $\tilde{t} = 1$ for $N_{sc} = 1000$.

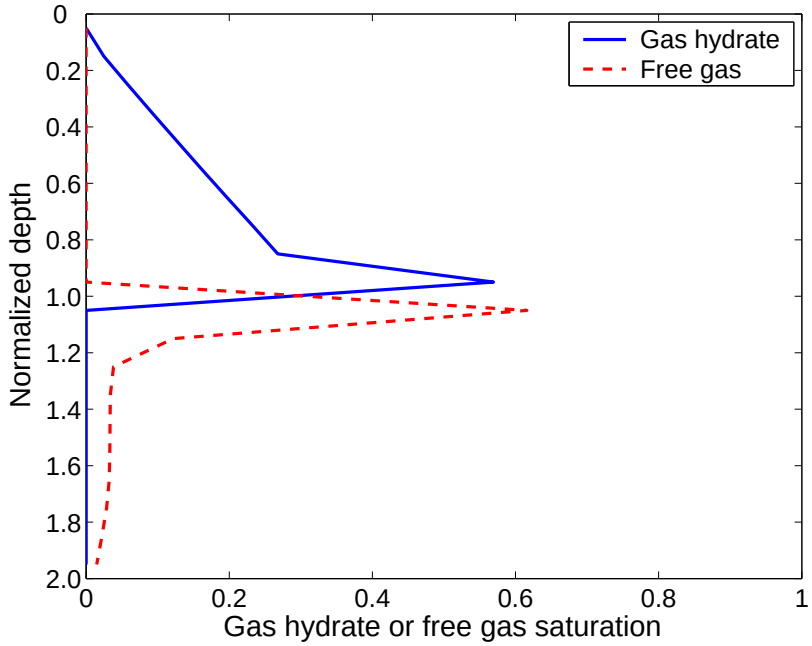

Figure 10.5: Gas hydrate and free gas saturation profiles at time $\tilde{t} = 1$ for $N_{sc} = 1000$.

which occurs at about $\tilde{t} \sim 2.5$. Figure 10.6 shows gas pressure just below the base of the GHSZ become equal to the overburden, causing vertical gas effective stress to be zero. Although we chose a relatively large value of N_{sc} for this simulation, the water pressure profile reveals large overpressure beneath the GHSZ. This occurs due to the low relative permeability of water caused by high hydrate and free gas saturations (∼80%) near the base of the GHSZ.

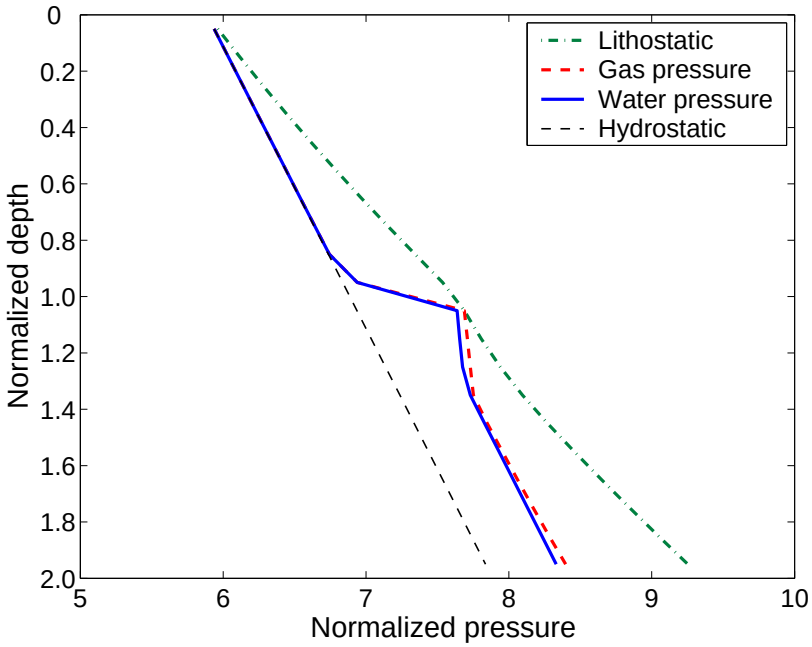

Figure 10.6: Lithostatic, gas pressure, water pressure, and hydrostatic pressure profiles for $N_{sc} = 1000$ when gas pressure becomes equal to the overburden at the critical-state ($\tilde{t} \sim 2.5$).

Hydrate and free gas saturation profiles at this critical-state are shown in Figure 10.7. Compared to previous transient results, this plot shows a much higher hydrate saturation at the base of the GHSZ, which is required to trap a much longer connected free gas column beneath the hydrate layer. The non-dimensional thick-

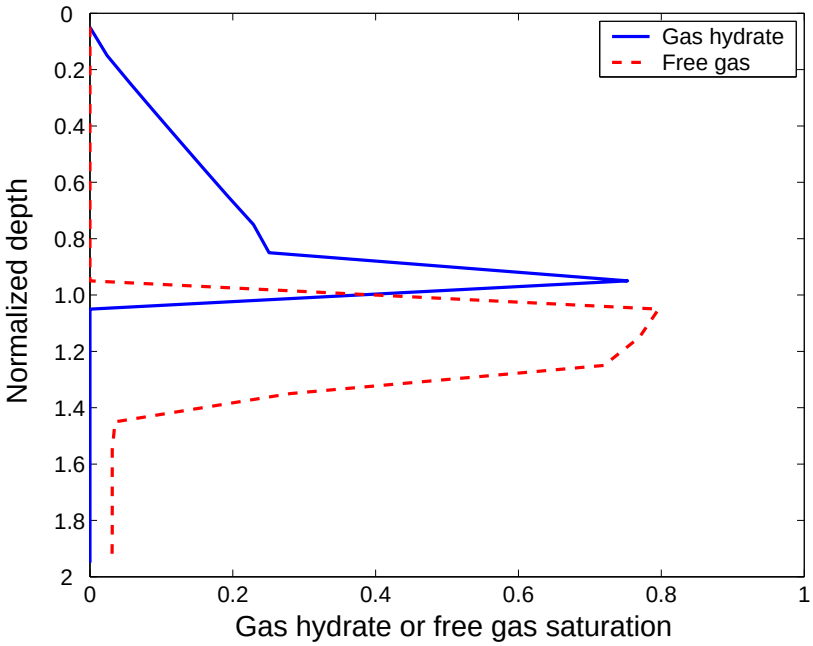

Figure 10.7: Gas hydrate and free gas saturation profiles at the critical-state for $N_{sc} = 1000$. A deep connected free gas column forms beneath the GHSZ and is trapped by the high saturation hydrate layer.

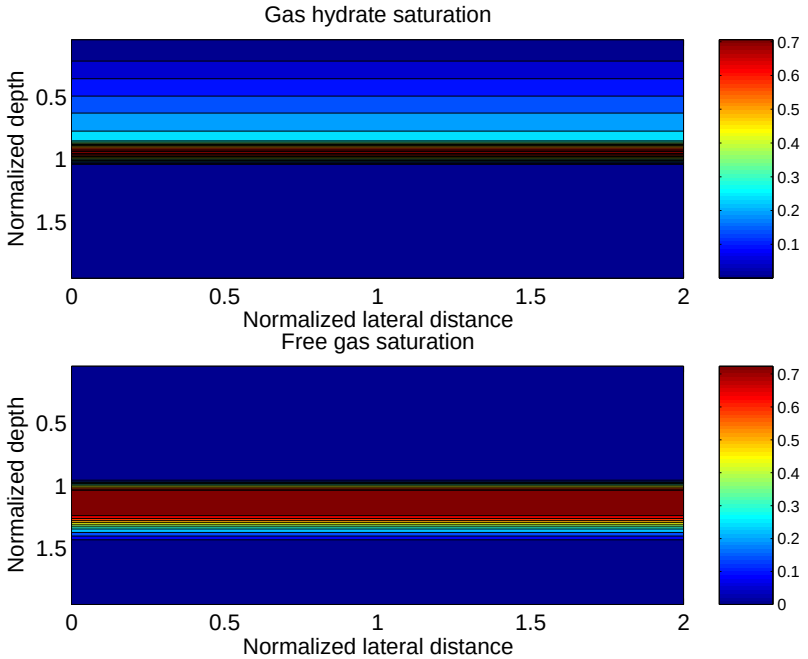

Figure 10.8: 2-D contour plot of hydrate and free gas saturations at the critical-state for $N_{sc} = 1000$.

ness of the free gas column from Figure 10.7 is about 0.4, which multiplied by the depth to the base of the GHSZ ($\sim$450 mbsf for Blake Ridge type seafloor conditions) yields a gas column about 180 meters thick. Finally, Figure 10.8 shows the 2-D contour plot of hydrate and free gas saturation at this critical-state.

Case 2: $\mathbf{N_{sc} = 10}$

Lowering N_{sc} from 1000 to 10 causes sediment permeability to decrease with respect to the sedimentation rate. This causes overpressure to develop in the system solely due to the effects of sedimentation-compaction, i.e., background pore water pressure becomes elevated even without any contribution from permeability reduction due to hydrate or free gas. Intuitively, this suggests that such systems would allow a relatively shorter gas column to develop before gas pressure exceeds the overburden and causes sediment failure (see Figure 9.1).

This hypothesis is confirmed by Figure 10.9, which shows different pressure profiles when gas pressure becomes equal to the overburden for $N_{sc} = 10$ (critical-state), at time $\tilde{t} \sim 1.5$. Compared to Figure 10.6 ($N_{sc} = 1000$), pore pressure profile in Figure 10.9 shows overpressure development throughout the sediment sequence. Because of this already elevated background water pressure, gas pressure does not has to increase much to exceed the overburden. Consequently, only a relatively thin free gas column develops before gas effective stress goes to zero, causing fractures to dilate.

Figure 10.10 shows the gas hydrate and free gas saturation profiles at this critical-state for $N_{sc} = 10$. Transient evolution of hydrate and free gas follows a pat-

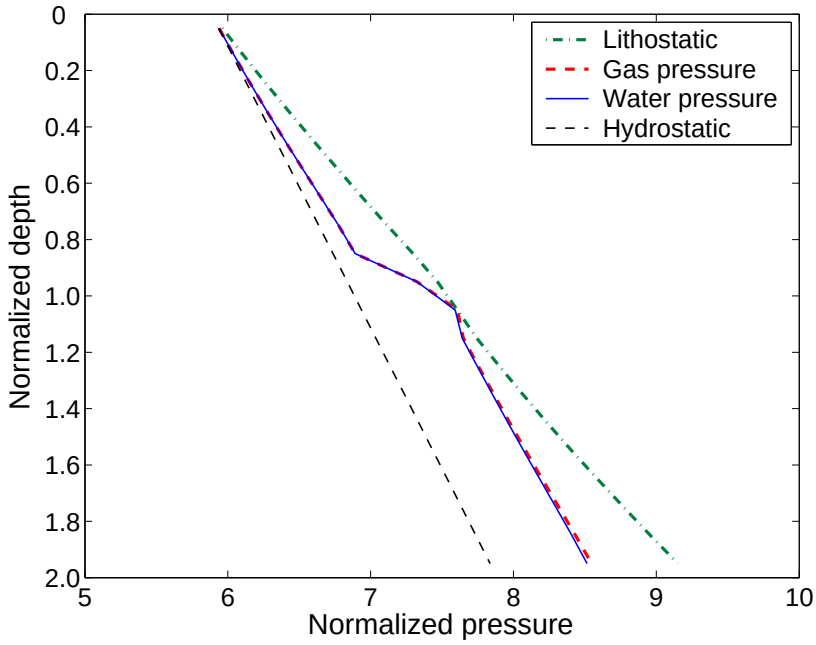

Figure 10.9: Lithostatic, gas pressure, water pressure, and hydrostatic pressure profiles for $N_{sc} = 10$ when gas pressure becomes equal to the overburden at the critical-state ($\tilde{t} \sim 1.5$).

tern similar to the previous case, whereby gas migrates buoyantly to the base of the GHSZ, causing a local spike in hydrate saturation at the base, which seals further gas migration. Since the gas saturation profile shows a relatively thin connected column, the peak hydrate saturation needed at the base to seal this column is also relatively low (~60%), compared to the 80% peak saturation in Figure 10.7. The dimensionless thickness of the free gas column in this case is about 0.1, which (assuming Blake Ridge type conditions, L_t = 450 mbsf) leads to a dimensional thickness of about 45 m.

Thus, the two cases shown above demonstrate that sediment permeability with respect to sedimentation rate and overpressure development play an important role

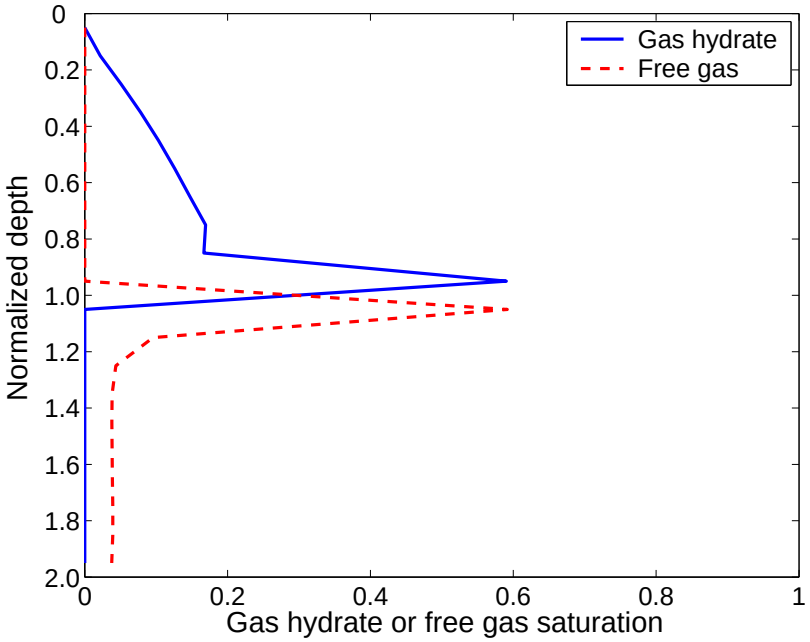

Figure 10.10: Gas hydrate and free gas saturation profiles at the critical-state for $N_{sc} = 10$ ($\tilde{t} \sim 1.5$). Compared to the thick gas column in Figure 10.7, only a relatively thin free gas column forms beneath the GHSZ in this case before gas pressure becomes equal to the overburden.

in determining the thickness of the connected free gas column beneath the GHSZ. Therefore, gas hydrate sites characterized by higher values of N_{sc} could have better exploration potential, if the associated free gas is taken into consideration.

10.3.2 Gas hydrate systems with fractures

Fracture networks can dominate fluid flow in gas hydrate systems, serving as high permeability conduits and causing localized high concentration of hydrate and free gas around these networks (Weinberger and Brown, 2006). Such networks might be especially important at settings such as Cascadia Margin (Hydrate Ridge), where gas hydrate is distributed very heterogeneously across varying length scales (Tréhu et al., 2004; Weinberger and Brown, 2006). Although several past studies have hypothesized the importance of fractures in gas hydrate systems, most of the current numerical models only simulate simple 1-D homogeneous sediment sequences. In comparison, our 2-D model offers the capability to assign different rock properties to different lithologies (such as sand, clay, fractures, etc.), thereby allowing us to study the effect of heterogeneities.

Vertical fractures are simulated in our model by assigning high permeabilities to gridblocks along a single column. Continuous sedimentation causes these fractures to move down with the sediment. We start with the case where a single vertical fracture is introduced in the system and follow transient gas hydrate and free gas accumulation as this fracture moves down with the sediment. Due to this downward motion, absolute permeability of any gridblock can change as a layer or fracture of different permeability passes through that gridblock. Hence, interfaces

between layers of different permeabilities are tracked in time. By knowing the interface position within any given gridblock, the horizontal and vertical permeabilities can be updated so that moving sediment layers of varying permeabilities can be simulated.

The permeability distribution for the vertical fracture is shown schematically in Figure 10.11. The vertical fracture has permeability 100 times higher than the surrounding sediment, i.e. $N_{sc} = 20$ for the sediment matrix and $N_{sc} = 2000$ for the fracture. The primary transport parameters are assigned the following values: $\mathrm{Pe}_1 = 0.1$, $\mathrm{Da} = 10$, $\beta = 6$, $\eta = 6/9$, $\gamma = 9$, $N_{t\phi} = 1$. Seafloor conditions and other parameters pertaining to relative permeabilities, capillary pressure, and physical properties of water, hydrate and gas remain the same as stated in section 10.3.1.

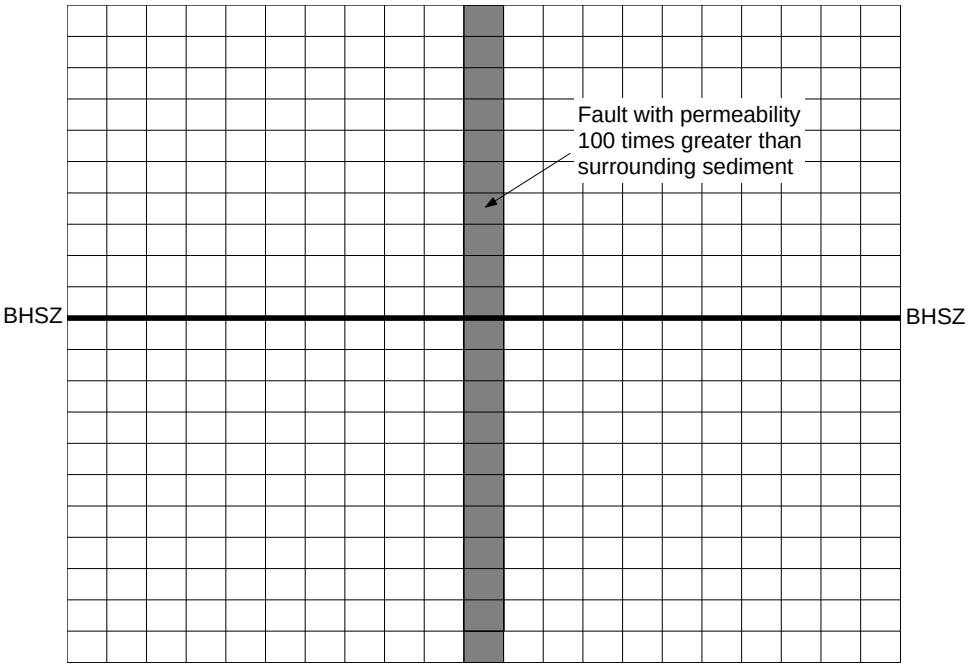

Figure 10.11: Permeability map showing initial location of a single, high permeability vertical fracture with permeability 100 times higher than the surrounding sediment.

Simulation results are now presented at different transient states. We first run the simulation with homogeneous sediment permeability to dimensionless time $\tilde{t} = 0.5$. At this time ($\tilde{t} = 0.5$) the fracture shown in Figure 10.11 is introduced. The system response to this fracture is now studied at later time values. Figure 10.12 shows the gas hydrate saturation contours at time $\tilde{t} = 0.6$ for this single vertical fracture system. The position of the fracture in this contour plot, and in subsequent plots, is shown through the set of dashed lines. The effect of the fracture in focusing flow along this high permeability conduit is clearly seen through the elevated hydrate saturations along and around the fracture. Peak gas hydrate saturation within the fracture is about 15%, while peak hydrate saturation in the surrounding sediments is about 7%. Free gas saturation contours at time $\tilde{t} = 0.6$, shown in 10.13, also depict maximum gas saturation along the fracture. However, free gas saturation at this time is too low to cause any lateral migration.

Figure 10.14 shows gas hydrate saturation contours at a later time ($\tilde{t} = 1.0$). Compared to Figure 10.12, peak hydrate saturation increases to $\sim$20% and occurs within the fracture just above the base of the GHSZ. This peak value is about twice the peak saturation in the surrounding sediments at the base of the GHSZ ($\sim$10%). As the fracture moves away from the seafloor, the shallower sediments are restored to the original lower permeability, causing them to have hydrate saturation equal to the surrounding sediments at similar depth. Figure 10.15 shows free gas saturation contours at $\tilde{t} = 1.0$. Buoyant free gas migrates upwards and gets sealed by the low permeability hydrate layer at the base of the GHSZ. Maximum free gas saturation occurs just below the GHSZ along the high permeability fracture ($\sim$50%). At this

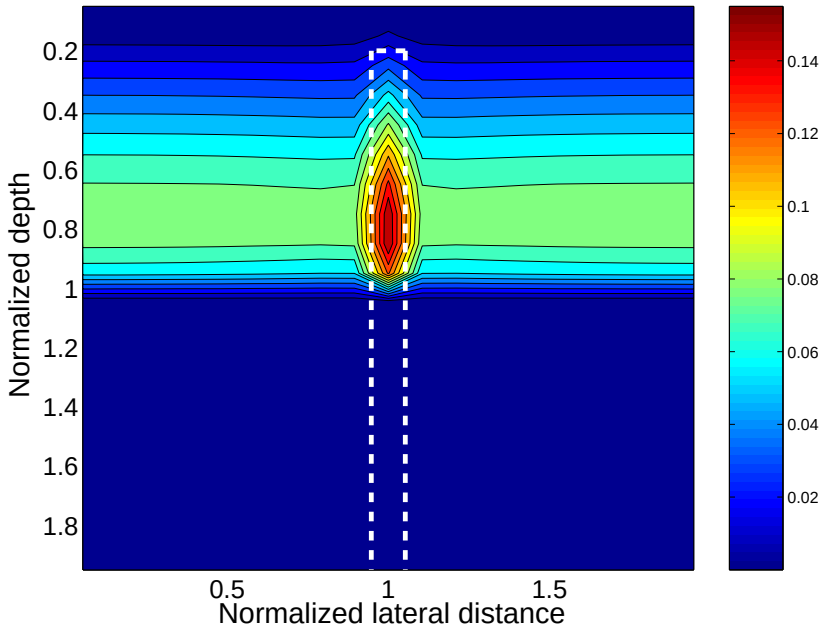

Figure 10.12: Gas hydrate saturation contours at time $\tilde{t} = 0.6$ for the vertical fracture system shown schematically in Figure 10.11. Dashed lines denote the position of the fracture.

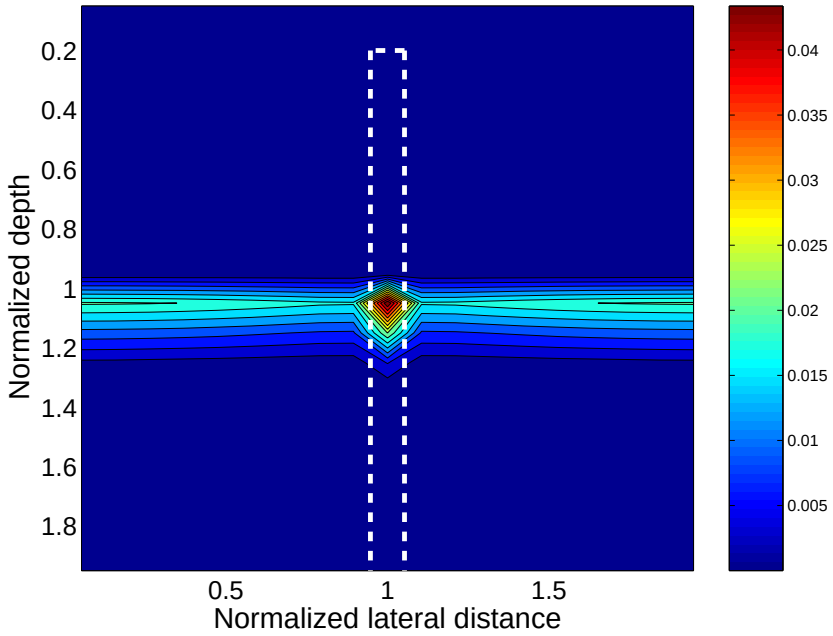

Figure 10.13: Free gas saturation contours at time $\tilde{t} = 0.6$ for the vertical fracture system shown schematically in Figure 10.11. Dashed lines denote the position of the fracture.

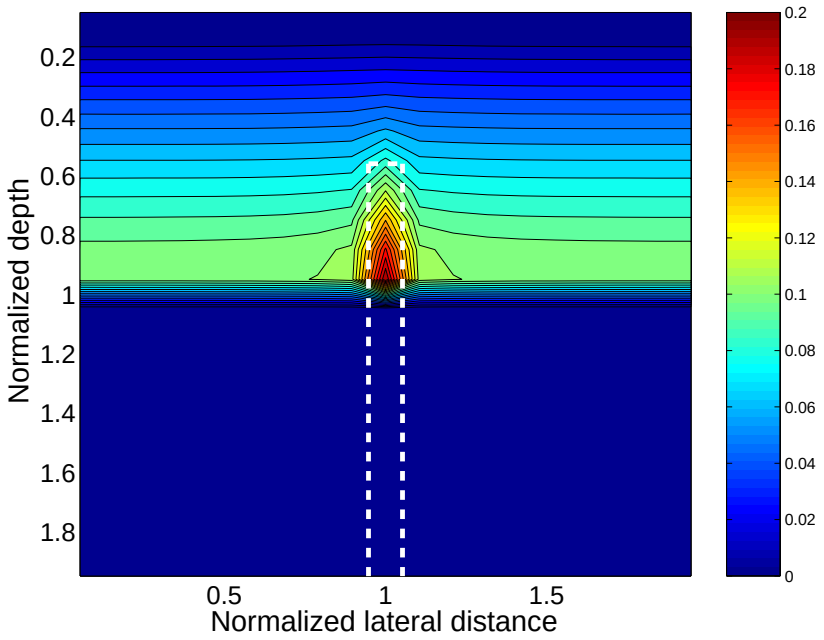

Figure 10.14: Gas hydrate saturation contours at time $\tilde{t} = 1.0$ for the vertical fracture system shown schematically in Figure 10.11. Peak gas hydrate saturation occurs at the base of the GHSZ within the fracture.

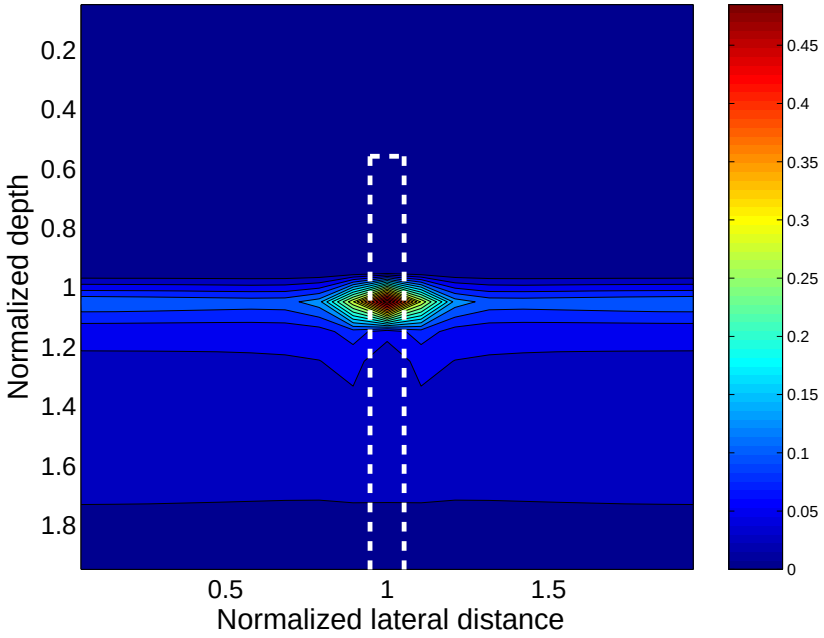

Figure 10.15: Free gas saturation contours at time $\tilde{t} = 1.0$ for the vertical fracture system shown schematically in Figure 10.11. Peak gas saturation is about 50% within the fracture, while lateral gas migration from the fracture causes gas saturation in neighboring gridblocks to increase to about 30%.

high saturation, free gas also migrates laterally, causing gridblocks just below the GHSZ and neighboring the fracture to also have relatively higher saturations.

Finally, we show gas hydrate saturation contours at time $\tilde{t} = 1.5$ in Figure 10.16, when the fracture has almost passed the GHSZ. The top of the fracture is very close to the base of the GHSZ, causing a relatively small increase in gas hydrate saturation within the fracture column. Peak hydrate saturation of about 12% within the fracture is marginally greater than the 10% saturation in sediments close to the base of the GHSZ but far away from the fracture. Overall, as the fracture moves out of the GHSZ, gas hydrate distribution becomes much more uniform along the lateral direction. Free gas saturation below the GHSZ at $\tilde{t} = 1.5$ (Figure 10.17) increases to a peak value of about 60% within the fracture and spreads out laterally away from the fracture. Similar to the region above the base of the GHSZ, free gas saturation also becomes more laterally uniform as the fracture is progressively buried deeper at later times.

Thus, presence of fractures can significantly affect gas hydrate and free gas distribution by focusing fluid flow along these conduits. This effect, however, is dynamic in nature. As these fractures move out of the GHSZ into deeper sediments, their effect on gas hydrate distribution becomes diminished.

10.3.3 Gas hydrate systems with different permeability layers/beds

Apart from vertical fractures, our model can also incorporate stratigraphy of varying permeabilities to simulate horizontal or dipping sand layers between low permeability clay layers. We first show pore pressure evolution for simple horizontal

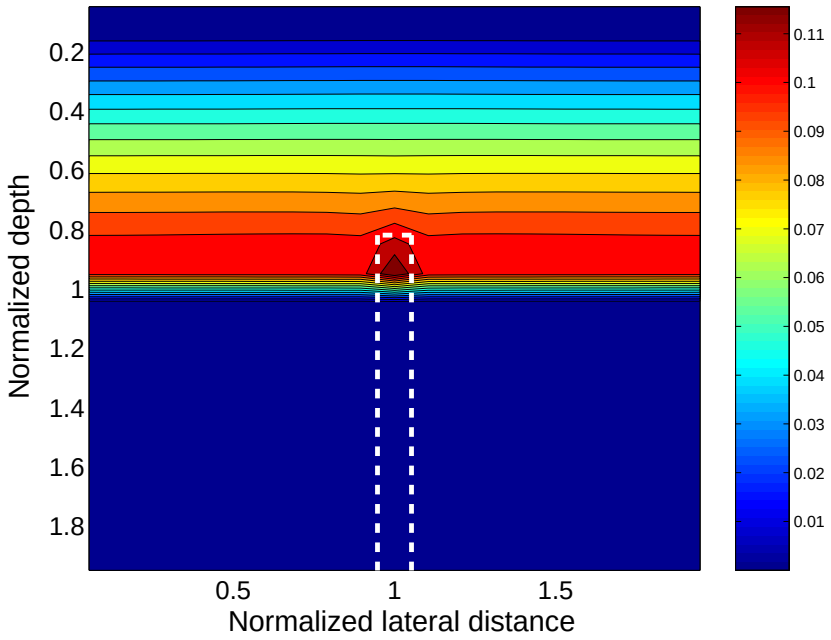

Figure 10.16: Gas hydrate saturation contours at time $\tilde{t} = 1.5$ for the vertical fracture system (Figure 10.11). Peak gas hydrate saturation within the fracture is almost equal to the value in surrounding sediment as the fracture moves out of the GHSZ.

beds and then move to more realistic cases of dipping sand layers.

Horizontal, high-permeability sand layer

We start with the simplest case of a horizontal high permeability sand layer deposited in low permeability clay sediments. This example is used to illustrate the downward movement of the high permeability sand layer and the corresponding pore pressure evolution. The parameter N_{sc} is 10 for the low permeability sediments and 1000 for the sand layer, i.e., the sand layer is 100 times more permeable than the surrounding sediments. Following values are assigned to the other transport parameters: : $\mathrm{Pe}_1 = 0.1$, $\mathrm{Da} = 10$, $\beta = 6$, $\eta = 6/9$, $\gamma = 9$, $N_{t\phi} = 1$, and

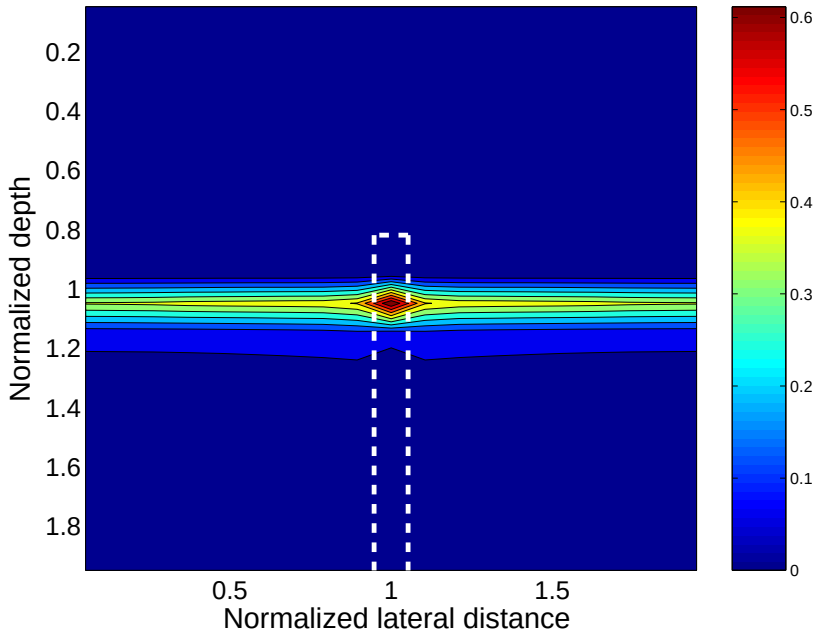

Figure 10.17: Free gas saturation contours at time $\tilde{t} = 1.5$ for the vertical fracture system shown schematically in Figure 10.11. Peak gas saturation is 67% within the fracture, while lateral gas migration from the fracture causes gas saturation in neighboring gridblocks to increase to about 40%.

critical gas saturation of 5%. Seafloor conditions and other parameters pertaining to relative permeabilities, capillary pressure, and physical properties of water, hydrate and gas remain the same as stated in section 10.3.1.

We start the simulation at time $\tilde{t} = 0$ with low permeability sediments and deposit the sand layer uniformly across the lateral section from time $\tilde{t} = 1.0$ to 1.5. Figure 10.18 shows various pressure profiles along the normalized depth at dimensionless times $\tilde{t} = 1.75$ and 2.25. The sand interval is marked by dotted lines in both plots. At time $\tilde{t} = 1.75$, the sand layer starts extends from $\tilde{z} = 0.25$ to $\tilde{z} = 0.6$ and the pore pressure gradient within this interval is almost hydrostatic due to its higher absolute permeability. Conversely, pore pressure gradient above and below

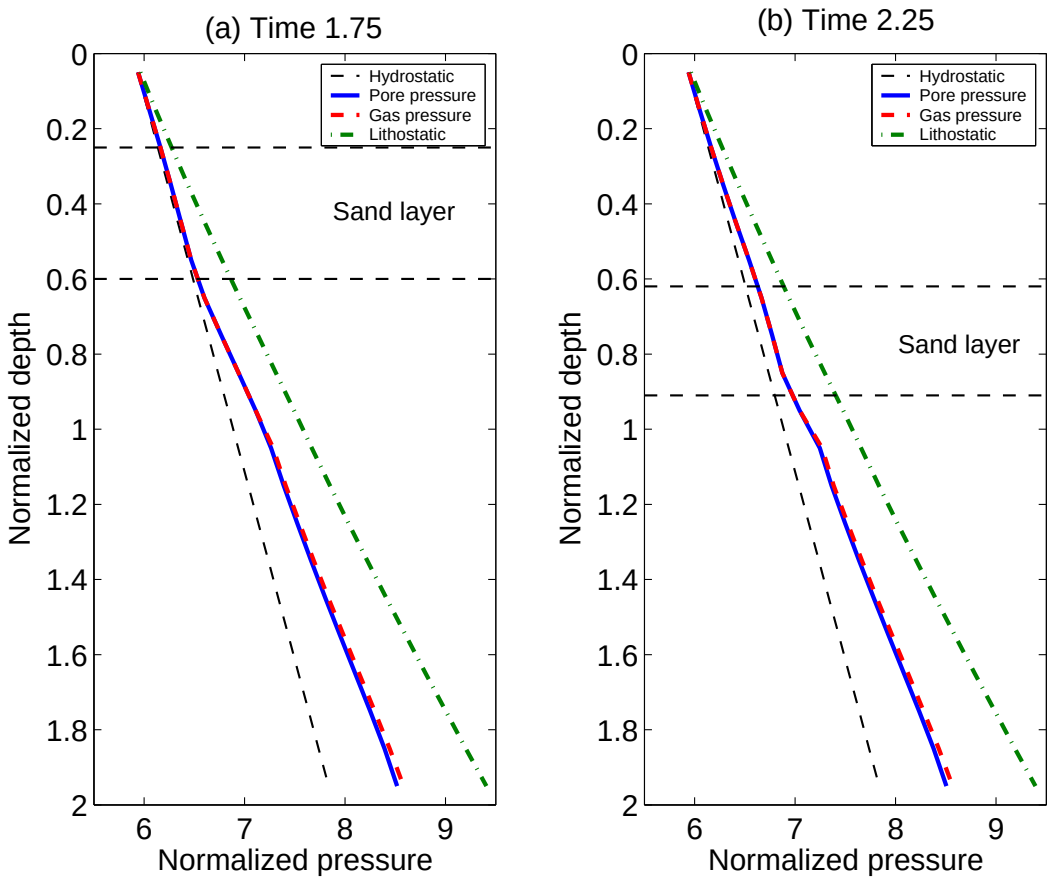

Figure 10.18: Pressure evolution for the case of a sand layer (high permeability) deposited in low permeability sediments uniformly across the lateral section. Sand layer is deposited from time $\tilde{t} = 1.0$ to 1.5. (a) Pore pressure, gas pressure and lithostatic stress profiles along depth at time $\tilde{t} = 1.75$. The dotted interval represents the sand layer and is characterized by pore pressure gradient that is close to the hydrostatic gradient. (b) At at later time, $\tilde{t} = 2.25$, the sand layer moves deeper and shrinks in thickness due to compaction.

the sand layer is greater than the hydrostatic gradient due to its lower absolute permeability. This change in pore pressure gradients across sediment interfaces is more clearly seen at time $\tilde{t} = 2.25$, when the sand layer moves further down into the sediment column and also shrinks in thickness due to compaction and porosity loss. This feature characterizes all simulations shown later, where the thickness

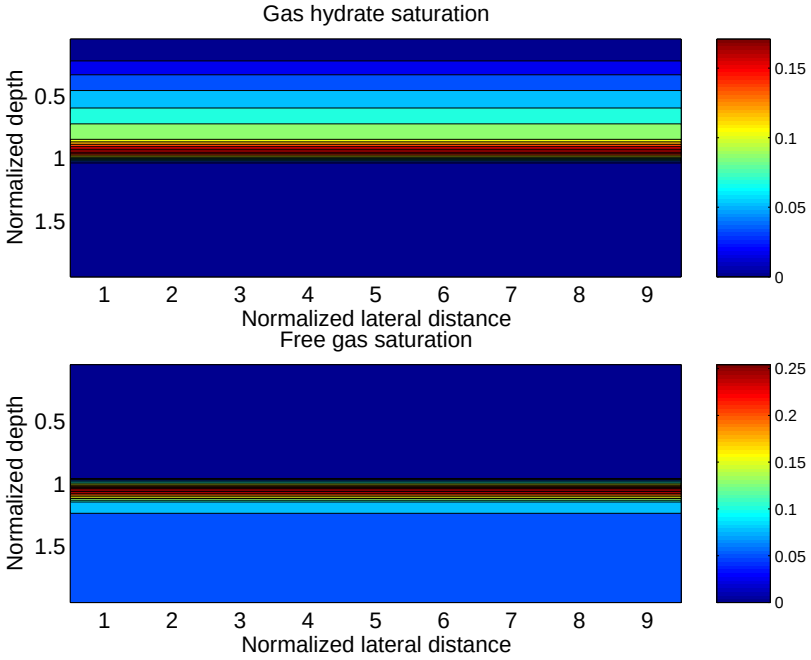

Figure 10.19: Gas hydrate and free gas saturation at time $\tilde{t} = 2.25$. Since the high permeability sand layer extends uniformly across the lateral section, hydrate and free gas saturation are also laterally homogeneous.

of the sand layer continuously decreases as it loses porosity and is buried deeper into the sediment column.

Gas hydrate and free gas saturation contours at $\tilde{t} = 2.25$ are shown in Figure 10.19. Due to the laterally uniform deposition of the sand layer, hydrate and free gas saturation also remain constant across the lateral section. Thus, this system

is essentially 1-D in nature and since the lateral ends of the domain are no-flow boundaries, there is no lateral fluid flow in this system. Consequently, there is no fluid focusing or enhanced concentration of hydrate or free gas within the high permeability sand layer. To introduce lateral heterogeneities in the system, we now model dipping sand layers as well as combinations of fractures and sand layers.

Dipping high permeability sand layers

To model a dipping sand layer, we start with a pre-existing sand layer at a given dip angle within the sediment and deposit low permeability clay on it. The downward movement of this sand layer and the corresponding transient hydrate/free gas evolution is then tracked through time. The permeability map, illustrated schematically in Figure 10.20, shows the initial position of of this sand layer. Similar to the case of the horizontal layer discussed above, the sand layer is assigned an absolute permeability 100 times greater than the surrounding sediments. The physical domain for all simulations in this section is $\tilde{z} \in [0, 2]$ and $\tilde{x} \in [0, 10]$. The parameter N_{sc} is 10 for the low permeability sediments and 1000 for the sand layer. The following values are assigned to the other transport parameters: $\mathrm{Pe}_1 = 0.1$, $\mathrm{Da} = 10$, $\beta = 6$, $\eta = 6/9$, $\gamma = 9$, $N_{t\phi} = 1$, and critical gas saturation of 5%. Seafloor conditions and other parameters pertaining to relative permeabilities, capillary pressure, and physical properties of water, hydrate and gas remain the same as stated in section 10.3.1. We now show results for two cases with different dip angles.

Case 1 - Low dip angle: In the first case, we start with a low dip angle of about 2 degrees. As mentioned previously, we start with a sand layer embedded in the

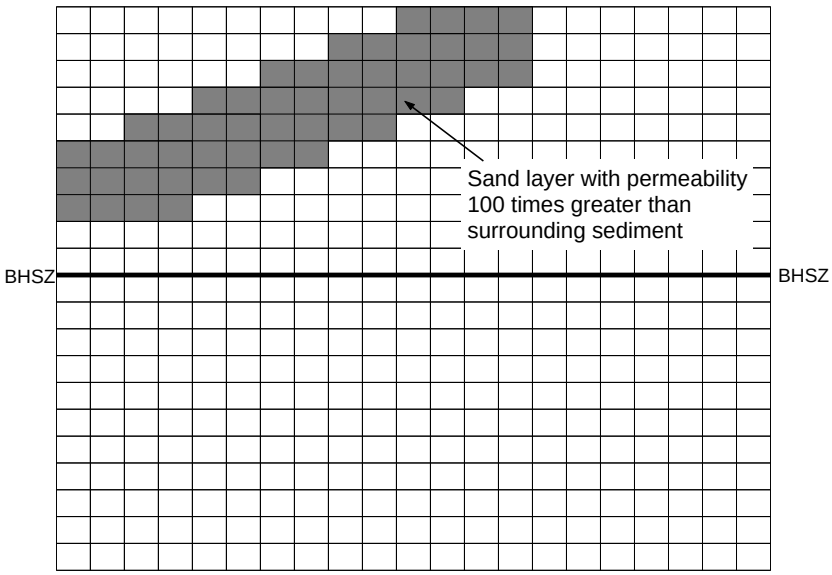

Figure 10.20: Schematic representation of the high permeability sand layer surrounded by low permeability clay sediments.

sediment matrix and start depositing low permeability clay at the seafloor at time $\tilde{t} = 0$. Gas hydrate saturation contours at time $\tilde{t} = 0.25$ are shown in Figure 10.21. Compared to the case of a horizontal layer, this plot shows significant concentration of hydrate within the sand layer. Peak gas hydrate saturation within the sand layer increases to about 30% but the color axis is scaled to a maximum of 15% to show the contours in the rest of the domain more clearly. However, the contour plot is not very convenient to look at because of the x-axis range being five time the z-axis range in Figure 10.21. Thus, gas hydrate and free gas saturations at time $\tilde{t} = 0.25$ are replotted in Figure 10.22 with the y-axis now rescaled to represent a vertical exaggeration (VE) of about 2:1.

The effect of fluid focusing through the high permeability sand layer is evident in the contour plots in Figure 10.22. As with Figure 10.21, the color axis for the

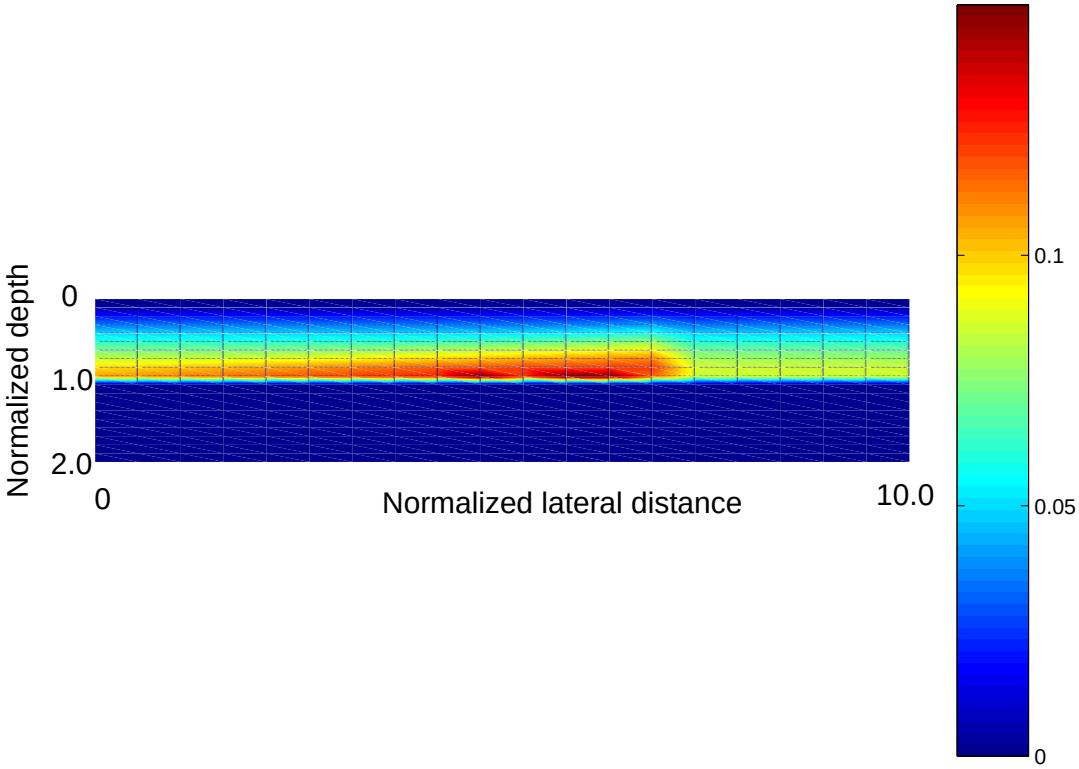

Figure 10.21: Gas hydrate saturation contours at $\tilde{t} = 0.25$ for the low dip angle with ”true” axis scale, i.e., no vertical exaggeration.

hydrate saturation contour plot in Figure 10.22 is scaled to a maximum of 15% to show the distribution in the rest of the GHSZ more clear, which otherwise gets dominated by the high saturation gridblocks only. The dashed lines in both contour plots denote the position of the sand layer that has moved away from the seafloor due to sedimentation. Peak gas hydrate saturation is about 30% within the sand layer and about 8% in the region close to the base of the GHSZ outside the sand layer. Free gas is also focused within the sand layer with saturations as high as 50%. Such high gas saturations cause it to migrate laterally out of the sand layer and into the low permeability sediments just below the GHSZ.

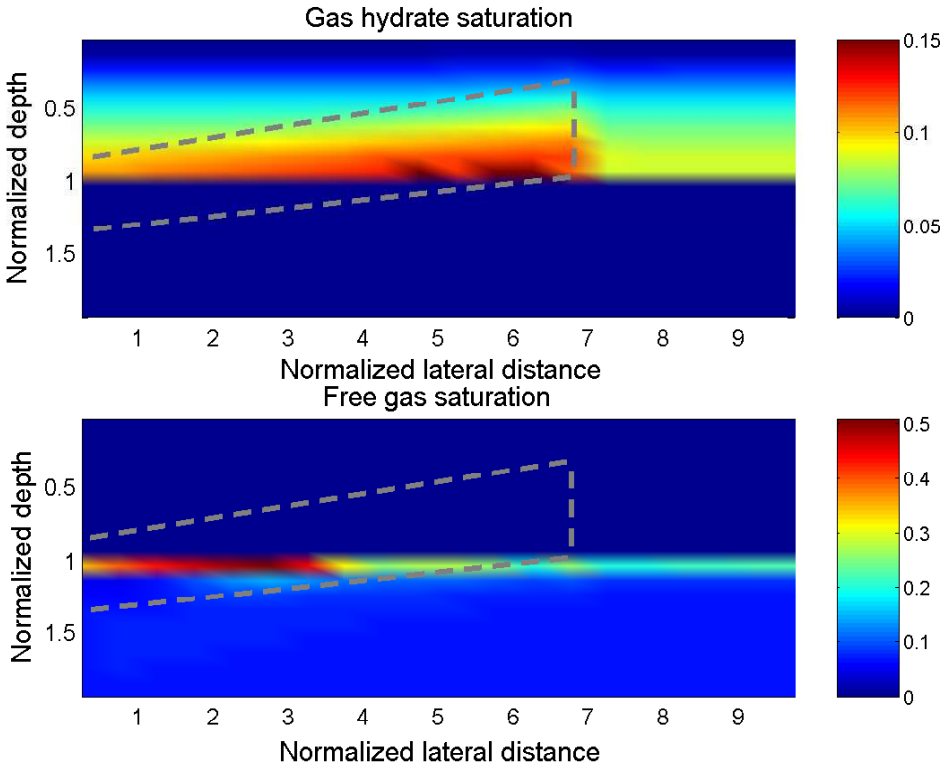

Figure 10.22: Gas hydrate and free gas saturation contours at $\tilde{t} = 0.25$ with a vertical exaggeration (VE) of about 2:1. Dashed lines denote the position of the sand layer within the low permeability sediment matrix.

At a later time, $\tilde{t} = 0.75$, the sand layer is buried even deeper into the sediments (Figure 10.23). Similar to the case of the fracture moving down (section 10.3.2), as the sand layer moves out of the GHSZ, its effect on gas hydrate saturation becomes diminished. Figure 10.23 shows the saturation contours for this case, where only a small section of the sand layer is present within the GHSZ. This small region within the sand layer is close to the base of the GHSZ and has hydrate saturation of about 12%, compared to about 8% saturation near the base on either side of the sand layer. Free gas saturation increases to about 67% within the sand layer just below the GHSZ with neighboring sediments outside the sand layer at about 30%. At an even later time, the sand layer moves completely out of the system causing hydrate saturation to become almost uniform laterally within the GHSZ.

Case 2 - High dip angle:

We next simulate a case with a dip of about 4 degrees to study the effect of the dip angle on hydrate saturation. All other parameters remain the same as the previous case. Compared to the previous case, which had a dip of about 2 degrees, Figure 10.24 shows much higher saturations within the sand layer at time $\tilde{t} = 0.3$. Peak hydrate saturation within the sand layer is about 45%, significantly higher than the 8% peak hydrate saturation in the low permeability sediments within the GHSZ. Free gas saturation is about 66% within the sand layer just below the GHSZ and, similar to previous figures, spreads laterally into the low permeability sediments outside the sand layer. Thus, keeping all other parameters same, higher dip angle leads to relatively higher fluid focusing and hydrate saturation within the GHSZ.

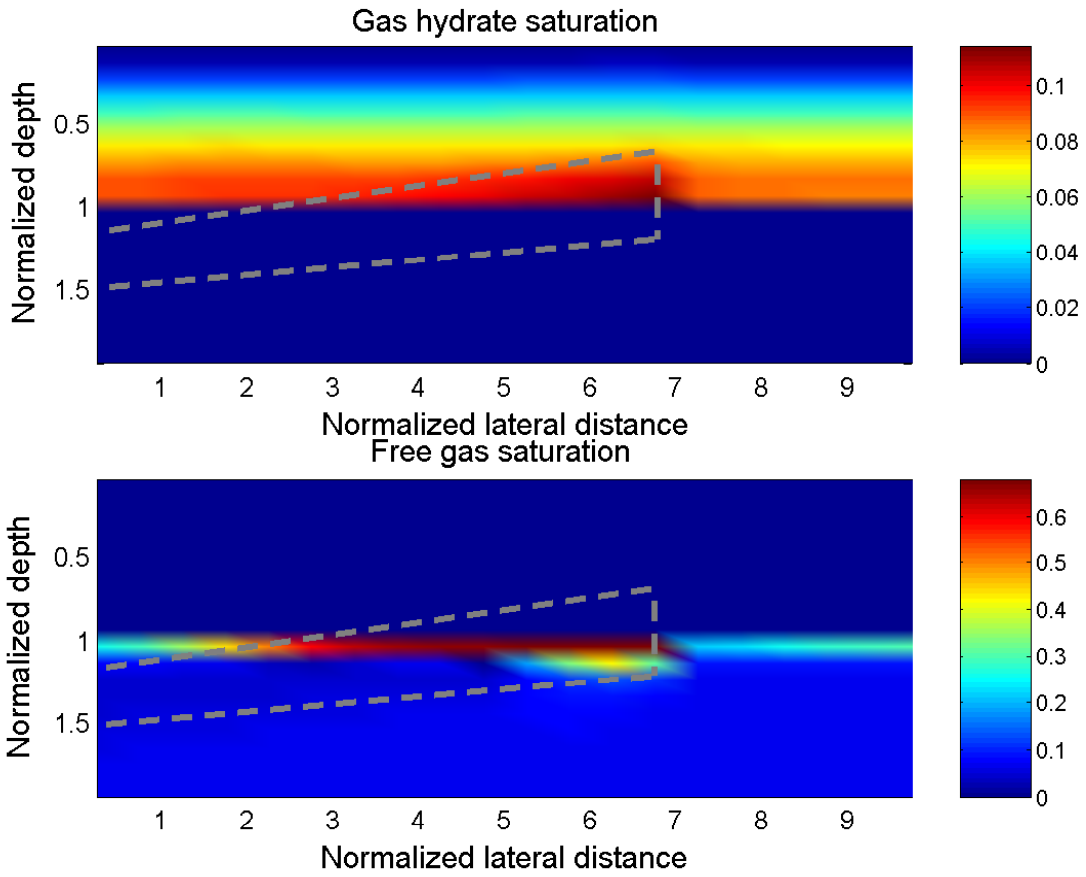

Figure 10.23: Gas hydrate and free gas saturation contours at $\tilde{t} = 0.75$ with a vertical exaggeration (VE) of about 2:1. Dashed lines denote the position of the sand layer within the low permeability sediment matrix.

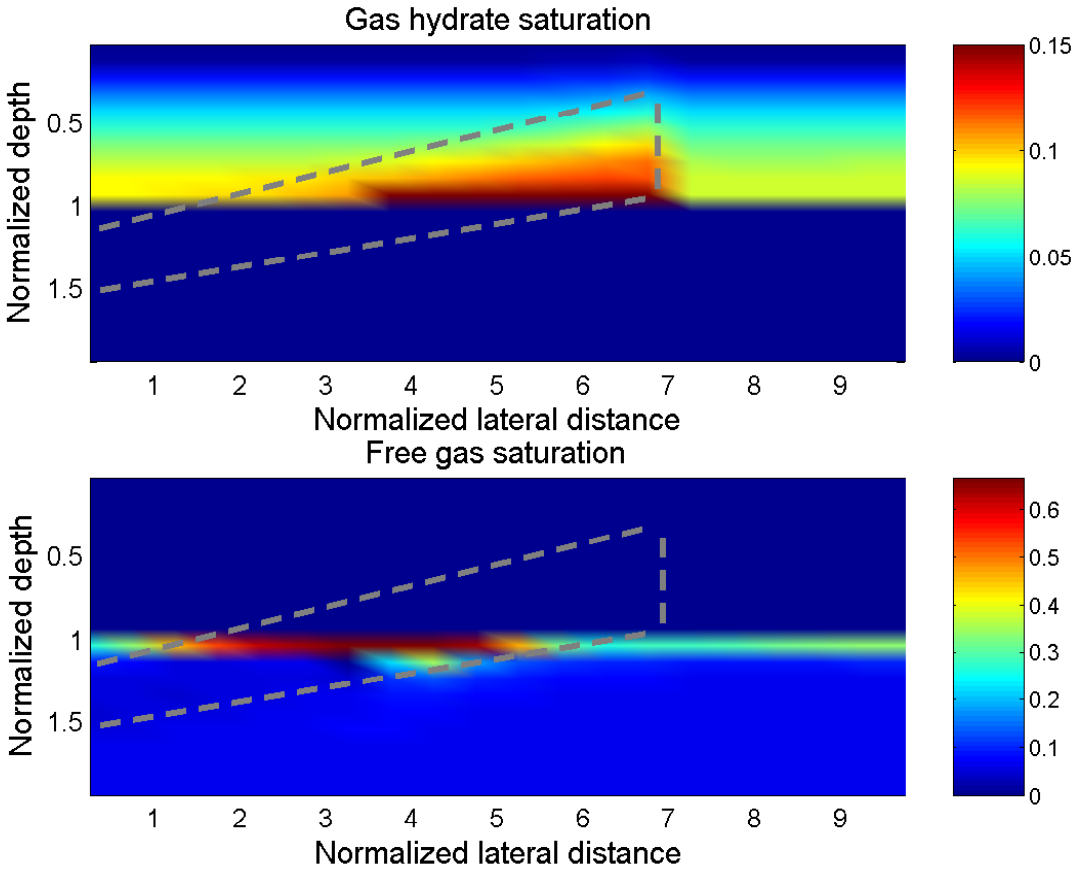

Figure 10.24: Gas hydrate and free gas saturation contours at $\tilde{t} = 0.3$ for the case of higher dip angle and with a vertical exaggeration (VE) of about 2:1. Color axis for the hydrate saturation contour plot is scaled to a maximum of 15%. Dashed lines denote the position of the sand layer within the low permeability sediment matrix.

10.3.4 Combination of fractures and dipping sand layers

After studying fractures and dipping sand layers in the previous two sections, we now combine these two features to simulate a more general setting where a fracture intersects a dipping sand layer. Following parameter values are used: $\mathrm{Pe}_1 = 0.1$, $\mathrm{Da} = 10$, $\beta = 6$, $\eta = 6/9$, $\gamma = 9$, $N_{t\phi} = 1$, and critical gas saturation of 5%. Seafloor conditions and other parameters pertaining to relative permeabilities, capillary pressure, and physical properties of water, hydrate and gas remain the same as stated in section 10.3.1. The initial system consists of a fracture located around the center of the grid and a dipping sand layer with a dip angle of about 2 degrees. Both the fracture and the sand layer have absolute permeabilities 100 times greater than that of the surrounding sediment.

Figure 10.25 shows gas hydrate and free gas saturation contours for this system after dimensionless time $\tilde{t} = 0.25$. This figure also has a VE of about 2:1, with the dashed lines indicating the location of the fracture and the dipping sand layer. It can be seen that gas hydrate is most concentrated near the intersection of the sand layer with the fracture, which has a peak saturation of about 48%. However, as before, the color axis for the hydrate saturation plot is scaled to a maximum of about 15% to show hydrate distribution in the rest of the GHSZ more clearly. Free gas saturation is maximum within the fracture, with peak saturation of 67% just below the GHSZ and about 40% within the sand layer around the region $\tilde{x} = 0$.

At a later time, $\tilde{t} = 0.75$, a significant portion of the sand layer moves out of the GHSZ, causing hydrate distribution to be more uniform laterally within the GHSZ

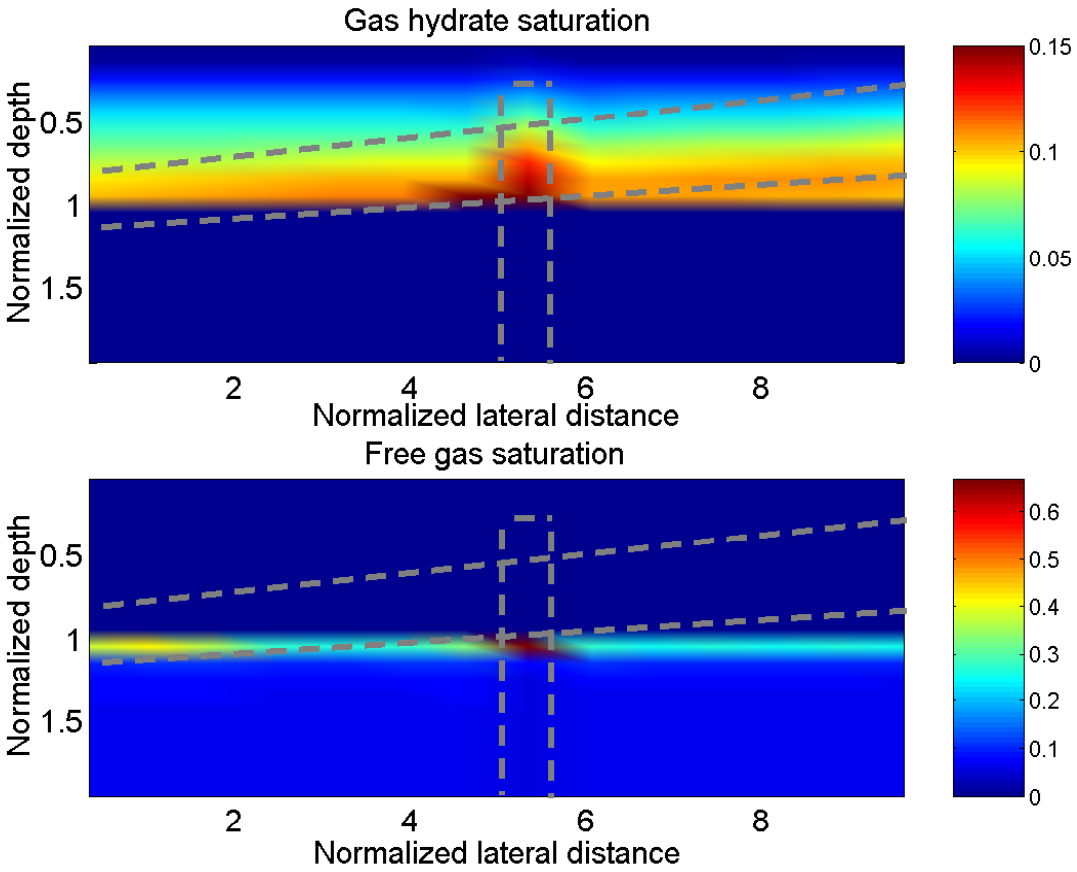

Figure 10.25: Gas hydrate and free gas saturation contours at $\tilde{t} = 0.25$ for the case of combined fracture and lower dip angle sand layer, with a vertical exaggeration (VE) of about 2:1. Color axis for the hydrate saturation contour plot is scaled to a maximum of 15%. Dashed lines denote the position of the fracture and the sand layer within the low permeability sediment matrix.

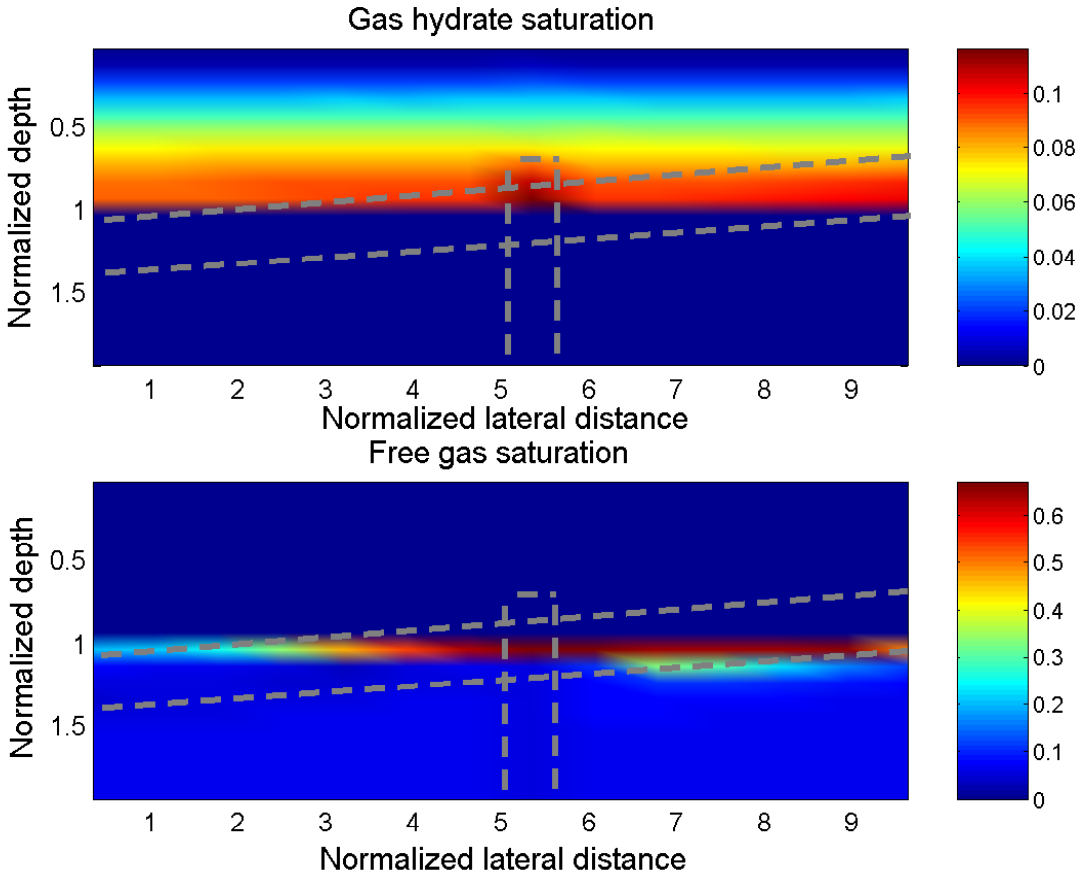

Figure 10.26: Gas hydrate and free gas saturation contours at $\tilde{t} = 0.75$ for the case of combined fracture and lower dip angle sand layer, with a vertical exaggeration (VE) of about 2:1. Dashed lines denote the position of the fracture and the sand layer within the low permeability sediment matrix.

(Figure 10.26). A small portion of the fracture still remains within the GHSZ, which causes a small increase in hydrate saturation ($\sim$12%) around that region. Free gas saturation is now about greater than 65% in a wide region within the sand layer and beneath the GHSZ. Both the fracture and the sand layer act as conduits to focus free gas within these more permeable sediments, which then rises buoyantly and migrates to the base of the GHSZ.

The simulation results presented above show that lithology plays an important role in producing heterogeneous gas hydrate/free gas accumulations. We simulated relatively simple systems with single fractures and/or dipping sand layers, whereas real geologic settings are characterized by much more heterogeneity in terms of fracture networks, multiple sand layers or isolated sand lenses. These preliminary simulations, however, serve as a starting point and demonstrate that the numerical model can be used in the future to simulate systems with considerable heterogeneity that mimic natural gas hydrate systems more accurately.

10.4 Conclusions

A general, dimensionless, two-dimensional (2-D) model was developed in this chapter to simulate gas hydrate and free gas accumulation in marine sediments over geologic timescales. Development of a 2-D model allows incorporation of sediment heterogeneity and lateral fluid flow in the system. Following conclusions can be drawn from the simulations:

- Free gas migrates buoyantly upwards into the GHSZ when its critical gas sat-

uration is exceeded. As free gas enters the GHSZ, gas hydrate precipitates at the base, causing an increase in the capillary entry pressure for the free gas. This restricts further gas entry into the GHSZ. Thus, free gas starts to accumulate beneath the GHSZ into a connected gas column. The thickness of this connected gas column is a function of the sedimentation-compaction group N_{sc}. Relatively higher values of N_{sc} lead to lower overpressure and development of a long gas column before gas pressure at the base of the GHSZ exceeds the lithostatic stress. At this point, fractures can dilate and vent the free gas below the hydrate, but we do not model this process in our simulations, i.e., our simulations are stopped whenever vertical gas effective stress becomes zero. Conversely, relatively lower values of N_{sc} leads to considerable overpressure in the system, which restricts the development of the gas column, i.e., fracturing can occur for a short gas column.

- Vertical fractures in the sediments focus fluid flow along this high permeability conduit causing relatively higher gas hydrate and free gas saturations within and around the fracture. However, as the fracture is progressively buried deeper into the sediments, hydrate saturation becomes more uniform laterally.

- Dipping high permeability sand layers surrounded by low permeability clay sediments are also simulated using our numerical model. Hydrate and free gas are concentrated within this sand layer due to fluid focusing. Higher dip angle leads to greater hydrate and free gas saturations within these sand

layers. However, similar to the case of fractures, the effect of these sand layers diminishes as it passes out of the GHSZ due to sedimentation.

Chapter 11

Conclusions and Future Work

11.1 Conclusions

General numerical models for simulating gas hydrate accumulation in marine sediments were developed in this thesis. In this chapter, we first summarize the conclusions from these models/theory and then present some future research directions. The overall conclusions are divided into the following three categories:

- **Gas hydrate accumulation in homogeneous 1-D systems**: For homogeneous, one-dimensional, hydrostatically-pressured systems, the key dimensionless groups controlling gas hydrate saturation at steady state are the two Peclet numbers (Pe_1 and Pe_2), the Damkohler number (Da), and the normalized organic carbon input at the seafloor (β). The type of gas hydrate accumulation, i.e., no hydrate and hydrate with or without free gas below, is a function of these parameters. Specifically, for biogenic in situ sources, average gas hydrate saturation is a function of Pe_1 and the organic carbon converted within the GHSZ. For deeper methane sources, average hydrate saturation depends on the net fluid flux ($\mathrm{Pe}_1 + \mathrm{Pe}_2$) and Pe_1. Further, settings dominated by in situ methane can be divided into diffusive and advective systems, with increase in sedimentation rates (Pe_1) causing higher hydrate sat-

urations in the former regime and lower hydrate saturation in the latter. For systems dominated by methane from depth, high saturations are obtained at high fluid flux ($\mathrm{Pe}_1 + \mathrm{Pe}_2$) and low sedimentation rates (Pe_1). Studying gas hydrate systems through these dimensionless groups helps in linking different geologic sites through a unified mechanism.

- **Sulfate-methane transition (SMT) as a gas hydrate proxy**: Pore water sulfate profile and depth of the SMT below the seafloor are shown to be functions of the net methane flux from depth for gas hydrate systems dominated by deeper sources. Since gas hydrate saturation and thickness of the gas hydrate layer within the GHSZ are also functions of net methane flux for this type of methane source, the scaled depth of the SMT becomes a fast and inexpensive proxy for quantifying hydrate saturation. Shallow SMT depths are shown through modeling and analytical theory to be indicative of high gas hydrate saturation. The depth to the first occurrence of gas hydrate below the seafloor is shown to be about 10-12 times the depth of the SMT for most gas hydrate settings. Finally, application of this new method to several sites along Cascadia Margin reveals a good match with saturations estimated from resistivity/chloride data and accurately predicts the lateral variability of hydrate saturation across these sites.

- **Effect of overpressure, free gas migration and sediment heterogeneity**: Overpressure development in the system is studied through the dimensionless group N_{sc}, which represents the ratio of sediment permeability to

seafloor sedimentation rate. Relatively large values of N_{sc} ($\sim$10,000) lead to near-hydrostatic pore pressures, while N_{sc} close to unity leads to near-lithostatic pore pressures. In general, overpressure development leads to faster sediment velocities through the GHSZ, causing a net decrease in the saturation as well as sediment volume fraction of hydrate as well as free gas for our set of boundary conditions. The depth of the GHSZ below the seafloor increases due to overpressure, but the magnitude of this increase is relatively small even for large overpressures. Overpressure also limits the thickness of the connected gas column beneath the GHSZ. This scenario is demonstrated by allowing free gas to migrate upwards buoyantly as soon as its critical gas saturation is exceeded. This gas column is sealed by high hydrate saturation at the base of the GHSZ, which restricts further gas migration into the GHSZ. The development of this free gas column is tracked through transient simulations, which show that high values of N_{sc} lead to deep connected gas columns, while low N_{sc} values yield shorter gas columns before fracturing occurs. Finally, several different cases are simulated that show the effect of fluid focusing within high permeability sediments. These include gas hydrate systems with vertical fractures, dipping sand layers and combinations of both. In general, these simulations show that hydrate as well as free gas become concentrated in greater amounts within these high permeability features.

11.2 Future Research Directions

This thesis incorporates most of the primary factors believed to control gas hydrate and free gas formation and distribution in marine sediments. However, some secondary factors and future tasks to be addressed include:

- **Dynamic effect of salinity on gas hydrate phase equilibrium**: Gas hydrate formation and dissociation affects the pore water salinity, which, in turn, changes the phase equilibrium of the system (Zatsepina and Buffett, 1998; Milkov et al., 2004; Liu and Flemings, 2006). A simple chloride balance was included in our 1-D model to study the effect of hydrate formation/dissociation on pore water salinity and its role as a gas hydrate proxy. However, the salinity change was not coupled to the thermodynamic and transport equations, so that changing salinity did not affect hydrate phase equilibrium. Although, for general cases, the change in salinity and its effect on phase equilibrium appears to be small from these preliminary simulations, such effects may become dominant in special sites characterized by high gas flux that can cause massive hydrate formation and large salinity anomalies (Milkov et al., 2004; Liu and Flemings, 2006, 2007)

- **Compositional effect on gas hydrate and free gas distribution**: All simulations and theory presented in this thesis assume methane to be the only hydrate former. However, at several gas hydrate settings (e.g., Gulf of Mexico) higher alkanes like ethane and propane can be present in amounts large enough to significantly alter the phase equilibrium and stability boundaries

(Milkov and Sassen, 2000). In such cases, gas hydrate may form sI or sII structures that can coexist with free gas over finite depths instead of a sharp boundary between hydrate and gas for methane hydrates. Thus, BSRs might not be easily seen on seismic profiles for such settings. Hence, the models developed in this thesis need to be extended to include multicomponent hydrates so that their effect on BSRs can be studied.

- **Blanking effect and chaotic zones**: Amplitude blanking refers to the attenuation of seismic amplitude and is believed to be caused by the reduction of impedance contrast in sediments containing gas hydrate (Lee and Dillon, 2001). In other words, gas hydrate preferentially forms in high porosity/permeability layers, which increases the acoustic impedance of hydrate bearing sediments to match the high impedance of low porosity/permeability, non-hydrate bearing sediments. This hypothesis about the lack of impedance contrast between different lithologies can be tested with our 2-D model in conjunction with a seismic and rock physics model. In addition to seismic blanking, chaotic zones may develop due to migration of free gas into the GHSZ. Conditions leading to such scenarios also need to be identified.

- **Concentrated hydrate/free gas accumulations**: Gas hydrate or free gas accumulations that are concentrated enough for economic production might form as a result of high permeability conduits and focused fluid flow. Some of the simple heterogeneous features are studied in this thesis, e.g., faults and dipping sand layers. However, more simulations need to be performed to

identify the factors and parameters controlling concentrated accumulations. Apart from the stratigraphic features, the potential of structural traps in focusing hydrate and free gas could also be studied.

Bibliography

Adisasmito, S., Frank, R. J., and Sloan, E. D., J. (1991). Hydrates of carbon dioxide and methane mixtures. *J. Chem. Eng. Data*, 36:68–71.

Archie, G. E. (1942). The electrical resistivity log as an aid in determining some reservoir characteristics. *Trans. Am. Inst. Min. Metall. Pet. Eng.*, 146:54–62.

Athy, L. F. (1930). Density, porosity and compaction of sedimentary rocks. *AAPG Bulletin*, 14(1):1–24.

Audet, D. M. and Fowler, A. C. (1992). A mathematical model for compaction in sedimentary basins. *Geophys. J. Int.*, 110:577–590.

Bear, J. (1988). *Dynamics of Fluids in Porous Media*. New York : Dover Publications Inc.

Bear, J. and Bachmat, Y. (1990). *Introduction to Modeling of Transport Phenomena in Porous Media*. Kluwer Academic Publishers, Dordrecht, The Netherlands.

Berner, R. A. (1980). *Early Diagenesis : A Theoretical Approach*. Princeton Univ. Press, Princeton, N.J.

Bethke, C. M. (1985). A numerical model of compaction-driven groundwater flow and heat transfer and its application to the Paleohydrology of intracratonic sedimentary basins. *J. Geophys. Res.*, 90:6817–6828.

Bhatnagar, G., Chapman, W. G., Dickens, G. R., Dugan, B., and Hirasaki, G. J. (2007). Generalization of gas hydrate distribution and saturation in marine sediments by scaling of thermodynamic and transport processes. *Am. J. Sci.*, 307:861–900.

Bhatnagar, G., Chapman, W. G., Dickens, G. R., Dugan, B., and Hirasaki, G. J. (2008). Sulfate-methane transition as a proxy for average methane hydrate saturation in marine sediments. *Geophys. Res. Lett.*, 35, L03611, doi:10.1029/2007GL032500.

Borowski, W. S. and Paull, C. K. (1997). The gas hydrate detection problem: Recognition of shallow-subbottom gas hazards in deep-water areas. In *Proceedings of the Offshore Technology Conference*, volume 1 OTC-8297, pages 211–216.

Borowski, W. S., Paull, C. K., and Ussler III, W. (1996). Marine pore-water sulfate profiles indicate in situ methane flux from underlying gas hydrate. *Geology*, 24(7):655–658.

Borowski, W. S., Paull, C. K., and Ussler III, W. (1999). Global and local variations of interstitial sulfate gradients in deep-water, continental margin sediments: Sensitivity to underlying methane and gas hydrates. *Mar. Geol.*, 159:131–154.

Boudreau, B. P. and Westrich, J. T. (1984). The dependence of bacterial sulfate reduction on sulfate concentration in marine sediments. *Geochim. Cosmochim. Acta*, 48:2503–2516.

Buffett, B. A. and Archer, D. (2004). Global inventory of methane clathrate: Sensitivity to changes in the deep ocean. *Earth Planet. Sci. Lett.*, 227:185–199.

Cao, Z. T., Tester, J. W., and Trout, B. L. (2002). Sensitivity analysis of hydrate thermodynamic reference properties using experimental data and ab initio methods. *J. Phys. Chem. B*, 106(31):7681–7687.

Castellini, D. G., Dickens, G. R., Snyder, G. T., and Ruppel, C. D. (2006). Barium recycling in shallow sediment above active mud volcanoes in the Gulf of Mexico. *Chem. Geol.*, 226:1–30.

Claypool, G. E. and Kaplan, I. R. (1974). *Natural Gases in Marine Sediments*, chapter Methane in marine sediments, pages 99–139. Plenum Press. New York.

Claypool, G. E. and Kvenvolden, K. A. (1983). Methane and other hydrocarbon gases in marine sediment. *Annu. Rev. Earth Planet. Sci.*, 11:299–327.

Clennell, M. B., Hovland, M., Booth, J. S., Henry, P., and Winters, W. J. (1999). Formation of natural gas hydrates in marine sediments 1. Conceptual model of gas hydrate growth conditioned by host sediment properties. *J. Geophys. Res.*, 104:22985–23003.

Coffin, R., Pohlman, J., Gardner, J., Downer, R., Wood, W., Hamdan, L., Walker, S., Plummer, R., Gettrust, J., and Diaz, J. (2007). Methane hydrate exploration on the mid Chilean coast: A geochemical and geophysical survey. *J. Petrol. Sci. Eng.*, 56(1):32–41.

Collett, T. S. (2000). *Quantitative well-log analysis of in-situ natural gas hydrates*. PhD thesis, Colorado School of Mines, Golden, CO.

Collett, T. S. (2002). Energy resource potential of natural gas hydrates. *AAPG Bull.*, 86:1971–1992.

Collett, T. S. and Ladd, J. (2000). Detection of gas hydrate with downhole logs and assessment of gas hydrate concentrations (saturations) and gas volumes on the Blake Ridge with electrical resistivity log data. In Paull, C. K., Matsumoto, R., Wallace, P. J., and Dillon, W. P., editors, *Proc. ODP, Sci. Results*, volume 164, pages 179–191, College Station, TX. Ocean Drilling Program.

Davie, M. K. and Buffett, B. A. (2001). A numerical model for the formation of gas hydrate below the seafloor. *J. Geophys. Res.*, 106:497–514.

Davie, M. K. and Buffett, B. A. (2003a). Sources of methane for marine gas hydrate: inferences from a comparison of observations and numerical models. *Earth Planet. Sci. Lett.*, 206:51–63.

Davie, M. K. and Buffett, B. A. (2003b). A steady state model for marine hydrate formation: Constraints on methane supplpy from pore water sulfate profiles. *J. Geophys. Res.*, 108, 2495, doi:10.1029/2002JB002300.

Davie, M. K., Zatsepina, O. Y., and Buffett, B. A. (2004). Methane solubility in marine hydrate environments. *Mar. Geol.*, 203:177–184.

de Caritat, P. P. (1989). Note on the maximum upward migration of pore water in response to sediment compaction. *Sediment. Geol.*, 65:371–377.

de Roo, J. L., Peters, C. J., Lichtenthaler, R. N., and Diepen, G. A. M. (1983). Occurrence of methane hydrate in saturated and unsaturated solutions of sodium chloride and water in dependence of temperature and pressure. *AICHE J.*, 29:651–657.

D'Hondt, S. L., Jørgensen, B. B., and Miller, et al., D. J., editors (2003). *Proc. ODP, Init. Repts.*, volume 201, College Station, TX. Ocean Drilling Program.

Dickens, G. R. (2001). The potential volume of oceanic methane hydrates with variable external conditions. *Org. Geochem.*, 32:11791193.

Dickens, G. R. (2003). Rethinking the global carbon cycle with a large, dynamic and microbially mediated gas hydrate capacitor. *Earth Planet. Sci. Lett.*, 213:169–183.

Dickens, G. R., Castillo, M. M., and Walker, J. C. G. (1997). A blast of gas in the latest Paleocene: Simulating first order effects of massive dissociation of oceanic methane hydrate. *Geology*, 25:259–262.

Dickens, G. R., O'Neil, J. R., Rea, D. K., and Owen, R. M. (1995). Dissociation of oceanic methane hydrate as a cause of the carbon isotope excursion at the end of the Paleocene. *Paleoceanography*, 10:965–971.

Dickens, G. R. and Quinby-Hunt, M. S. (1994). Methane hydrate stability in seawater. *Geophys. Res. Lett.*, 21:2115–2118.

Duan, Z., Moller, N., Greenberg, J., and Weare, J. H. (1992). The prediction of methane solubility in natural waters to high ionic strength from 0 to 250 c and from 0 to 1600 bar. *Geochim. Cosmochim. Acta*, 56:1451–1460.

Dugan, B. and Flemings, P. B. (2000). Overpressure and fluid flow in the New Jersey continental slope: implications for slope failure and cold seeps. *Science*, 289:288–291.

Egeberg, P. K. and Barth, T. (1999). Contribution of dissolved organic species to the carbon and energy budgets of hydrate bearing deep sea sediments (Ocean Drilling Program Site 997 Blake Ridge). *Chem. Geol.*, 149:25–35.

Egeberg, P. K. and Dickens, G. R. (1999). Thermodynamic and pore water halogen constraints on hydrate distribution at ODP Site 997 (Blake Ridge). *Chem. Geol.*, 153:53–79.

Einsele, G. (1992). *Sedimentary Basins: Evolution, Facies, and Sediment Budget*. Springer-Verlag, Berlin.

Falta, R. W., Pruess, K., Javandel, I., and Witherspoon, P. A. (1992). Numerical modeling of steam injection for the removal of nonaqueous phase liquids from the subsurface 1. Numerical formulation. *Water Resour. Res.*, 28(2):433–449.

Finkbeiner, T., Zoback, M., Flemings, P., and Stump, B. (2001). Stress, pore pressure, and dynamically constrained hydrocarbon columns in the South Eugene Island 330 field, northern Gulf of Mexico. *AAPG Bull.*, 85(6):1007–1031.

Flemings, P. B., Liu, X., and Winters, W. (2003). Critical pressure and multiphase flow in Blake Ridge hydrates. *Geology*, 31:1057–1060.

Floodgate, G. D. and Judd, A. G. (1992). The origins of shallow gas. *Cont. Shelf Res.*, 12:1145–1156.

Galloway, W. E. (1984). *Clastic Diagenesis*, volume 37, chapter Hydrogeologic regimes of sandstone diagenesis, pages 3–14. Am. Assoc. Petrol. Geol. Memoir.

Gering, K. L. (2003). Simulations of methane hydrate phenomena over geologic timescales. Part I : Effect of sediment compaction rates on methane hydrate and free gas accumulations. *Earth Planet. Sci. Lett.*, 206:65–81.

Gibson, R. E. (1958). The progress of consolidation in a clay layer increasing in thickness with time. *Geotechnique*, 8:171–182.

Giles, M. R. (1997). *Diagenesis: A Quantitative Perspective - Implications for Basin Modelling and Rock Property Prediction*. Kluwer Academic Publishing, Dordrecht.

Gutierrez, M. and Wangen, M. (2005). Modeling of compaction and overpressuring in sedimentary basins. *Marine and Petr. Geol.*, 22(3):351–363.

Haeckel, M., Suess, E., Wallman, K., and Rickert, D. (2004). Rising methane gas bubbles form massive hydrate layers at the seafloor. *Geochim. Cosmochim. Acta*, 68:4335–4345.

Handa, Y. P. (1990). Effect of hydrostatic pressure and salinity on the stability of gas hydrates. *J. Phys. Chem.*, 94:2652–2657.

Henrichs, S. M. and Reeburgh, W. S. (1987). Anaerobic mineralization of marine sediment organic matter: Rates and role of anaerobic processes in ocean carbon economy. *Geomicrobiol. J.*, 5:191–237.

Henry, P., Thomas, M., and Clennell, M. B. (1999). Formation of natural gas hydrates in marine sediments, 2, Thermodynamic calculations of stability conditions in porous sediments. *J. Geophys. Res.*, 104:2300523022.

Hensen, C. and Wallman, K. (2005). Methane formation at Costa Rica continental margin - constraints for gas hydrate inventories and cross-décollement fluid flow. *Earth Planet. Sci. Lett.*, 236:41–60.

Hesse, R. (2003). Pore water anomalies of submarine gas-hydrate zones as tool to assess hydrate abundance and distribution in subsurface: what have we learned in the past decade ? *Earth Sci. Rev.*, 61:149–179.

Hesse, R., Frape, S. K., Egeberg, P. K., and Matsumoto, R. (2000). Stable isotope studies (Cl, O, and H) of interstitial waters from Site 997, Blake Ridge gas hydrate field, West Atlantic. In Paull, C. K., Matsumoto, R., Wallace, P. J., and Dillon, W. P., editors, *Proc. ODP, Sci. Results*, volume 164, pages 129–137, College Station, TX. Ocean Drilling Program.

Holbrook, W. S., Hoskins, H., Wood, W. T., Stephen, R. A., Lizzaralde, D., and Leg 164 Science Party (1996). Methane hydrate and free gas on the Blake Ridge from vertical seismic profiling. *Science*, 273:1840–1843.

Holder, G. D., G., C., and Papadopoulos, K. D. (1980). Thermodynamic and molecular properties of gas hydrates from mixtures containing methane, argon and krypton. *Ind. Eng. Chem. Fundam.*, 19:282–286.

Hornbach, M. J., Holbrook, W. S., Gorman, A. R., Hackwith, K. L., Lizzaralde, D., and Pecher, I. (2003). Direct seismic detection of methane hydrate on the Blake Ridge. *Geophysics*, 68:92–100.

Hornbach, M. J., Saffer, D. M., and Holbrook, W. S. (2004). Critically pressured free-gas reservoirs below gas hydrate provinces. *Nature*, 427:142144.

Hutchison, I. (1985). The effect of sedimentation and compaction on oceanic heat flow. *Geophys. J. R. Astron. Soc.*, 82:439–459.

Hyndman, R. D. and Davis, E. E. (1992). A mechanism for the formation of methane hydrate and seafloor bottom-simulating reflectors by vertical fluid expulsion. *J. Geophys. Res. B*, 97:7025–7041.

Hyndman, R. D., Yuan, T., and Moran, K. (1999). The concentration of deep sea gas hydrates from downhole electrical resistivity logs and laboratory data. *Earth Planet. Sci. Lett.*, 172:167–177.

Iversen, N. and Jørgensen, B. B. (1993). Diffusion coefficients of sulfate and methane in marine sediments: Influence of porosity. *Geochim. Cosmochim. Acta*, 57:571–578.

Joye, S. B., Boetius, A., Orcutt, B. N., Montoya, J. P., Schulz, H. N., Erickson, M. J., and Lugo, S. K. (2004). The anaerobic oxidation of methane and sulfate reduction in sediments from Gulf of Mexico cold seeps. *Chem. Geol.*, 205:219–238.

Kastner, M., Kvenvolden, K. A., and Lorenson, T. D. (1998). Chemistry, isotopic composition, and origin of a methane-hydrogen sulfide hydrate at the Cascadia subduction zone. *Earth Planet. Sci. Lett.*, 28:337–344.

Kastner, M., Kvenvolden, K. A., Whiticar, M. J., Camerlenghi, A., and Lorenson, T. D. (1995). Relation between pore fluid chemistry and gas hydrates associated with bottom-simulating reflectors at the Cascadia Margin, Sites 889 and 892. In Carson, B., Westbrook, G. K., Musgrave, R. J., and Suess, E., editors, *Proc. ODP, Sci. Results*, volume 146 (pt. 1), pages 175–186, College Station, TX. Ocean Drilling Program.

Katz, M. E., Pak, D. E., Dickens, G. R., and Miller, K. G. (1999). The source and fate of massive carbon input during the Latest Paleocene Thermal Maximum. *Science*, 286:1531–1533.

Kennett, J. P., Cannariato, G., Hendy, I. L., and Behl, R. J. (2003). *Methane Hydrates in Quaternary Climate Change: The Clathrate Gun Hypothesis*. Am. Geophys. Union, Washington DC.

Kimura, G., Silver, E. A., and Blum, et al., P., editors (1997). *Proc. ODP, Init. Repts.*, volume 170, College Station, TX. Ocean Drilling Program.

Klauda, J. B. and Sandler, S. I. (2005). Global distribution of methane hydrate in ocean sediment. *Energ. Fuel.*, 19:459–470.

Kleinberg, R. L., Flaum, C., Griffin, D. D., Brewer, P. G., Malby, G. E., Peltzer, E. T., and Yesinowski, J. P. (2003). Deep sea NMR: Methane hydrate growth habit in porous media and its relationship to hydraulic permeability, deposit accumulation, and submarine slope stability. *J. Geophys. Res.*, 108, 2508, doi:10.1029/2003JB002389.

Kraemer, M., Owen, R. M., and Dickens, G. R. (2000). Lithology of the upper gas hydrate zone, Blake Outer Ridge: A link between diatoms, porosity, and gas hydrate. In Paull, C. K., Matsumoto, R., Wallace, P. J., and Dillon, W. P., editors, *Proc. ODP, Sci. Results*, volume 164, pages 229–236, College Station, TX. Ocean Drilling Program.

Kvenvolden, K. A. (1988). Methane hydrate - A major reservoir of carbon in the shallow geosphere ? *Chem. Geol.*, 71:41–51.

Kvenvolden, K. A. (1993). Gas hydrates: Geological perspective and global change. *Rev. Geophys.*, 31:173–187.

Kvenvolden, K. A. (1998). *Gas Hydrates: Relevance to World Margin Stability and Climate Change*, volume 137, chapter A primer on the geological occurence of gas hydrate, pages 9–30. Special Publications, Geological Society, London.

Kvenvolden, K. A. and Kastner, M. (1990). Gas hydrates of the Peruvian outer continental margin. In Suess, E. and von Heune, et al., R., editors, *Proc. ODP, Sci. Results*, volume 112, pages 517–526, College Station, TX. Ocean Drilling Program.

Lee, M. W. (2000). Gas hydrates amount estimated form acoustic logs at the Blake Ridge, Sites 994, 995, and 997. In Paull, C. K., Matsumoto, R., Wallace, P. J., and Dillon, W. P., editors, *Proc. ODP, Sci. Results*, volume 164, pages 193–198, College Station, TX. Ocean Drilling Program.

Lee, M. W. and Dillon, W. P. (2001). Amplitude blanking related to the pore-filling of gas hydrate in sediments. *Mar. Geophys. Res.*, 22(2):101–109.

Liu, X. and Flemings, P. B. (2006). Passing gas through the hydrate stability zone at southern Hydrate Ridge, offshore Oregon. *Earth Planet. Sci. Lett.*, 67:3403–3421.

Liu, X. L. and Flemings, P. B. (2007). Dynamic multiphase flow model of hydrate formation in marine sediments. *J. Geophys. Res.*, 112, B03101, doi:10.1029/2005JB004227.

Luff, R. and Wallman, K. (2003). Fluid flow, methane fluxes, carbonate precipitation and biogeochemical turnover in gas hydrate-bearing sediments at Hydrate Ridge, Cascadia Margin: Numerical modeling and mass balances. *Geochim. Cosmochim. Acta*, 67:3403–3421.

Luo, X., Vasseur, G., Pouya, A., Lamoureux-Var, V., and Poliakov, A. (1998). Elastoplastic deformation of porous media applied to the modeling of compaction at basin scale. *Marine and Petr. Geol.*, 15:145–162.

MacKay, M. E., Jarrard, R. D., Westbrook, G. K., Hyndman, R. D., and the Shipboard Scientific Party of Ocean Drilling Program Leg 146 (1994). Origin of bottom-simulating reflectors: Geophysical evidence from the Cascadia accretionary prism. *Geology*, 22:459–462.

Marshall, D. R., Saito, S., and Kobayashi, R. (1964). Hydrates at high pressure, part i: Methane-water, argon-water, and nitrogen-water system. *AICHE J.*, 10:202–205.

Martens, C. S. and Berner, R. A. (1977). Interstitial water chemistry of anoxic Long Island Sound sediments. 1. Dissolved gases. *Limnol. Oceanogr.*, 22:10–25.

McLeod, H. O. and Campbell, J. M. (1961). Natural gas hydrates at pressures to 10,000 psia. *J. Petrol. Tech.*, 13:590–595.

Milkov, A. V. (2004). Global estimates of hydrate-bound gas in marine sediments: how much is really out there? *Earth-Sci. Rev.*, 66:183–197.

Milkov, A. V., Claypool, G. E., Lee, Y. J., and R., S. (2005). Gas hydrate systems at Hydrate Ridge offshore Oregon inferred from molecular and isotopic properties of hydrate-bound and void gases. *Geochim. Cosmochim. Acta*, 69(4):1007–1026.

Milkov, A. V., Dickens, G. R., Claypool, G. E., Lee, Y. J., Borowski, W. S., Torres, M. E., Xu, W., Tomaru, H., Tréhu, A. M., and Schultheiss, P. (2004). Co-existence of gas hydrate, free gas, and brine within the regional gas hydrate stability zone at Hydrate Ridge (Oregon margin): evidence from prolonged degassing of a pressureized core. *Earth Planet. Sci. Lett.*, 222:829–843.

Milkov, A. V. and Sassen, R. (2000). Thickness of the gas hydrate stability zone, Gulf of Mexico continental slope. *Mar. Pet. Geol.*, 17:981–991.

Moridis, G. J. (2003). Numerical studies of gas production from methane hydrates. *SPE J*, 8(4):359–370.

Moridis, G. J. and Collett, T. S., editors (2003). *Strategies for gas production from hydrate accumulations under various geological and reservoir conditions*. Proceedings, TOUGH Symposium, Lawrence Berkeley National Laboratory, Berkeley, California.

Niewöhner, C., Hensen, C., Kasten, S., Zabel, M., and Schulz, H. D. (1998). Deep sulfate reduction completely mediated by anaerobic methane oxidation in sediments of the upwelling area off Namibia. *Geochim. Cosmochim. Acta*, 62:455–464.

Parrish, W. R. and Prausnitz, J. M. (1972). Dissociation pressures of gas hydrates formed by gas mixtures. *Ind. Eng. Chem. Proc. DD*, 11:26–35.

Paull, C. K., Matsumoto, R., Wallace, P. J., and Dillon, W. P., editors (2000). *Proc. ODP Sci. Results*, volume 164, College Station, TX. Ocean Drilling Program.

Paull, C. K., Matsumoto, R., and Wallace, et al., P. J., editors (1996). *Proceedings of the Ocean Drilling Program, Initial Reports*, volume 164, College Station, TX. Ocean Drill. Program.

Paull, C. K., Ussler, W. I., and Borowski, W. S. (1994). *Natural Gas Hydrates*, chapter Sources of biogenic methane to form marine gas hydrates, pages 392–409. Ann. N.Y. Acad. Sci., 715.

Paull, C. K., Ussler III, W., Lorenson, T., Winters, W., and Dougherty, J. (2005). Geochemical constraints on the distribution of gas hydrates in the Gulf of Mexico. *Geo. Mar. Lett.*, 25:273–280.

Peng, D. Y. and Robinson, D. B. (1976). A new two-constant equation of state. *Ind. Eng. Chem., Fundam.*, 1(15):59–64.

Piessens, R., de Doncker, E., Uberhuber, C. W., and Kahaner, D. K. (1983). *Quadpack: A subroutine package for automatic integration*. Springer-Verlag, New York.

Pitzer, K. S. and Mayorga, G. (1973). Thermodynamics of electrolytes. II. Activity and osmotic coefficients for strong electrolytes with one or both ions univalent. *J. Phys. Chem.*, 77(19):2300–2308.

Rempel, A. W. and Buffett, B. A. (1997). Formation and accumulation of gas hydrate in porous media. *J. Geophys. Res.*, 102:10151–10164.

Riedel, M., Collett, T. S., Malone, M. J., and the Expedition 311 Scientists, editors (2006). *Proc. IODP*, volume 311, Washington, DC. Integrated Ocean Drilling Program Management International Inc.

Rubey, W. W. and Hubbert, M. K. (1959). Role of fluid pressure in mechanics of over-thrust faulting; ii. Overthrust belt in geosynclinal area of western Wyoming in light of fluid pressure hypothesis. *Bull. Geol. Soc. Am.*, 70:167–206.

Schowalter, T. T. (1979). Mechanics of secondary hydrocarbon migration and entrapment. *AAPG Bulletin-american Association of Petroleum Geologists*, 63(5):723–760.

Selim, M. S. and Sloan, E. D. (1989). Heat and mass-transfer during the dissociation of hydrates in porous-media. *AICHE J.*, 35(6):1049–1052.

Seo, Y., Lee, H., and Ryu, B.-J. (2002). Hydration number and two-phase equilibria of CH_4 hydrate in the deep ocean sediments. *Geophys. Res. Lett.*, 29, 1244, doi:10.1029/2001GL014226.

Servio, P. and Englezos, P. (2002). Measurement of dissolved methane in water in equilibrium with its hydrate. *J. Chem. Eng. Data*, 47:87–90.

Sharp, J. M. (1976). Momentum and energy balance equations for compacting sediments. *Math. Geol.*, 8:305–332.

Sloan, E. D. (2003). Fundamental principles and applications of natural gas hydrates. *Nature*, 426(6964):353–359.

Sloan, E. D., J. and Koh, C. (2007). *Clathrate hydrates of natural gases*. CRC Press, third edition.

Smith, J. E. (1971). The dynamics of shale compaction and evolution of pore-fluid pressures. *Math. Geol.*, 3:239–263.

Snyder, G. T., Hiruta, A., Matsumoto, R., Dickens, G. R., Tomaru, H., Takeuchi, R., Komatsubara, J., Ishida, Y., and Yu, H. (2007). Pore water profiles and authigenic mineralization in shallow marine sediments above the methane-charged system on Umitaka Spur, Japan Sea. *Deep-Sea Res. II*, in press.

Subramanian, S., Ballard, A. L., Kini, R. A., Dec, S. F., and Sloan, E. D. (2000). Structural transitions in methane plus ethane gas hydrates - part i: upper transition point and applications. *Chem. Eng. Sci.*, 55(23):5763–5771.

Suess, E. and von Heune, et al., R., editors (1988). *Proceedings of the Ocean Drilling Program, Initial Reports*, volume 112, College Station, TX. Ocean Drilling Program.

Suetnova, E. and Vasseur, G. (2000). 1-D modeling rock compaction in sedimentary basins using a visocoelastic rheology. *Earth Planet. Sci. Lett.*, 178:373–383.

Sultan, N., Cochonat, P., Foucher, J.-P., and Mienert, J. (2004). Effect of gas hydrates melting on seafloor slope instability. *Mar. Geol.*, 213:379–401.

Sun, X., Nanchary, N., and Mohanty, K. K. (2005). 1-D modeling of hydrate depressurization in porous media. *Transp. Porous Med.*, 58:315–338.

Sun, X. F. and Mohanty, K. K. (2006). Kinetic simulation of methane hydrate formation and dissociation in porous media. *Chem. Eng. Sci.*, 61(11):3476–3495.

ten Haven, H. L., Littke, R., Rullkötter, J., Stein, R., and Welte, D. H. (1990). Accumulation rates and composition of organic matter in late Cenozoic sediments underlying the active upwelling area off Peru. In Suess, E. and von Heune, et al., R., editors, *Proc. ODP, Sci. Results*, volume 112, pages 591–606, College Station, TX. Ocean Drilling Program.

Terzaghi, K. (1943). *Theoretical Soil Mechanics*. New York, Wiley.

Tishchenko, P., Hensen, C., Wallman, K., and Wong, C. S. (2005). Calculation of the stability and solubility of methane hydrate in seawater. *Chem. Geol.*, 219:37–52.

Torres, M. E., Wallman, K., Tréhu, A. M., Bohrmann, G., Borowski, W. S., and Tomaru, H. (2004). Gas hydrate growth, methane transport, and chloride enrichment at the southern summit of Hydrate Ridge, Cascadia margin off Oregon. *Earth Planet. Sci. Lett.*, 226:225–241.

Tréhu, A. M., Bohrmann, G., Rack, F., and Torres, M. E., editors (2003). *Proceedings of the Ocean Drilling Program, Initial Reports*, volume 204, College Station, TX. Ocean Drill. Program.

Tréhu, A. M., Long, P. E., Torres, M. E., Bohrmann, G., Rack, F. R., Collett, T. S., Goldberg, D. S., Milkov, A. V., Riedel, M., Schultheiss, P., Bangs, N. L., Barr, S. R., Borowski, W. S., Claypool, G. E., Delwiche, M. E., Dickens, G. R., Gracia, E., Guerin, G., Holland, M., Johnson, J. E., Lee, Y. J., Liu, C. S., Su, X., Teichert, B., Tomaru, H., Vanneste, M., Watanabe, M., and Weinberger, J. L. (2004). Three-dimensional distribution of gas hydrate beneath southern Hydrate Ridge: Constraints from ODP Leg 204. *Earth Planet. Sci. Lett.*, 222:845–862.

Ussler, W. and Paull, C. K. (2001). Ion exclusion associated with marine gas hydrate deposits. In Paull, C. K. and Dillon, W. P., editors, *Natural Gas Hydrates: Occurrence, Distribution, and Detection*, volume 124 of *Geophys. Monogr. Ser.*, pages 41–51. AGU, Washington, D. C.

van der Waals, J. H. and Platteeuw, J. C. (1959). Clathrate solutions. *Adv. Chem. Phys.*, 2:1–57.

Wallman, K., Aloisi, G., Haeckel, M., Obzhirov, A., Pavlova, G., and Tishchenko, P. (2006). Kinetics of organic matter degradation, microbial methane generation, and gas hydrate formation in anoxic marine sediments. *Geochim. Cosmochim. Acta*, 70:3905–3927.

Wang, K., Hyndman, R. D., and Davis, E. E. (1993). Thermal effects of sediment thickening and fluid expulsion in accretionary prisms - model and parameter analysis. *J. Geophys. Res.*, 98(6):9975–9984.

Wangen, M. (1992). Pressure and temperature evolution in sedimentary basins. *Geophys. J. Intl.*, 110:601–613.

Weinberger, J. L. and Brown, K. M. (2006). Fracture networks and hydrate distribution at Hydrate Ridge, Oregon. *Earth Planet. Sci. Lett.*, 245(1):123–136.

Weinberger, J. L., Brown, K. M., and Long, P. E. (2005). Painting a picture of gas hydrate distribution with thermal images. *Geophys. Res. Lett.*, 32, L04609, doi:10.1029/2004GL021437.

Westbrook, G. K., Carson, B., and Musgrave et al., R. J., editors (1994). *Proc. ODP, Initial Reports*, volume 146 (Pt. 1), College Statiom, TX. Ocean Drilling Program.

Whiticar, M. J., Faber, E., and Schoell, M. (1986). Biogenic methane formation in marine and freshwater environments: CO_2 reduction vs. acetate fermentation - Isotope evidence. *Geochim. Cosmochim. Acta*, 50:693–709.

Xu, W., Lowell, R. P., and Peltzer, E. T. (2001). Effect of seafloor temperature and pressure variations on methane flux from a gas hydrate layer: Comparison between current and late Paleocene climate conditions. *J. Geophys. Res.*, 106:26413–26423.

Xu, W. and Ruppel, C. (1999). Predicting the occurrence, distribution, and evolution of methane gas hydrate in porous marine sediments. *J. Geophys. Res.*, 104:5081–5096.

Yang, S. O., Cho, S. H., Lee, H., and Lee, C. S. (2001). Measurement and prediction of phase equilibria for water + methane in hydrate forming conditions. *Fluid Phase Equil.*, 185:53–63.

Yang, X. S. (2001). A unified approach to mechanical compaction, pressure solution, mineral reactions and the temperature distribution in hydrocarbon basins. *Tectonophysics*, 330:141–151.

Yang, X. S. and Fowler, A. C. (1998). Fast and slow compaction in sedimentary basins. *SIAM J. Appl. Math.*, 59(1):365–385.

Yuan, T., Hyndman, R. D., Spence, G. D., and Desmons, B. (1996). Seismic velocity increase and deep-sea gas hydrate concentration above a bottom-simulating reflector on the northern Cascadia continental slope. *J. Geophys. Res.*, 101:13655–13671.

Zatsepina, O. Y. and Buffett, B. A. (1998). Thermodynamic conditions for the stability of gas hydrate in the seafloor. *J. Geophys. Res.*, 103:24127–24139.

Appendix A

Appendix

A.1 Non-dimensionalization of Sulfate Mass Balance

The net fluid flux in the system ($U_{f,tot}$) results from the combination of fluid flux due to continuous sedimentation and compaction of sediments ($U_{f,sed}$) and the external fluid flux ($U_{f,ext}$) (Davie and Buffett, 2003b; Bhatnagar et al., 2007):

$$U_{f,tot} = U_{f,sed} + U_{f,ext} \tag{A.1}$$

where $U_{f,sed}$ can be related to the sedimentation rate and porosities as (Davie and Buffett, 2003b):

$$U_{f,sed} = \frac{1-\phi_0}{1-\phi_\infty}\dot{S}\phi_\infty \tag{A.2}$$

In terms of Peclet numbers (8.4), the sum $U_{f,tot}$ can be written as:

$$\frac{U_{f,tot}L_t}{D_m} = \frac{U_{f,sed}L_t}{D_m} + \frac{U_{f,ext}L_t}{D_m} = \mathrm{Pe}_1 + \mathrm{Pe}_2 \tag{A.3}$$

Multiplying equation (8.3) by L_t/D_m and dividing by $c^0_{SO_4}$ gives:

$$(\mathrm{Pe}_1 + \mathrm{Pe}_2)\,\tilde{c}^l_s - \phi\frac{D_s}{D_m}\frac{\partial \tilde{c}^l_s}{\partial \tilde{z}} = \frac{F_{SO_4}}{\rho_f c^0_{SO_4}}\frac{L_t}{D_m} \tag{A.4}$$

We now model porosity loss by relating it to effective stress and assuming hydrostatic pressure (equilibrium compaction), which yields the following relationship between the reduced porosity and normalized depth (Bhatnagar et al., 2007):

$$\tilde{\phi} = \frac{\eta}{\eta + (1-\eta)e^{\tilde{z}}} \tag{A.5}$$

where $\tilde{\phi}$ and η are reduced porosities defined in terms of the maximum (ϕ_0) and minimum (ϕ_∞) porosities achieved during compaction:

$$\tilde{\phi} = \frac{\phi - \phi_\infty}{1-\phi_\infty} \quad , \quad \eta = \frac{\phi_0 - \phi_\infty}{1-\phi_\infty} \tag{A.6}$$

Dividing equation (A.4) by $(1-\phi_\infty)$ we obtain the dimensionless sulfate balance equation (8.5) of the main text:

$$\left(\frac{1+\gamma}{\gamma}\right)(\mathrm{Pe}_1 + \mathrm{Pe}_2)\,\tilde{c}_s^l - \left(\frac{1+\gamma\tilde{\phi}}{\gamma}\right)\frac{D_s}{D_m}\frac{\partial \tilde{c}_s^l}{\partial \tilde{z}} = \left(\frac{1}{1-\phi_\infty}\right)\frac{F_{SO_4}}{\rho_f c^0_{SO_4}}\frac{L_t}{D_m} \quad , \quad 0 < \tilde{z} < \tilde{L}_s \tag{A.7}$$

where γ was defined in the main text as $(\frac{1-\phi_\infty}{\phi_\infty})$

A.2 Non-dimensionalization of Methane Mass Balance

The steady-state water mass balance below the SMT can be written as:

$$\frac{\partial}{\partial z}\left[U_f c_w^l \rho_f + \frac{U_s}{1-\phi}\phi S_h c_w^h \rho_h\right] = 0 \ , \ L_s < z < L_t \tag{A.8}$$

where c_w^l and c_w^h are the water mass fractions in pore water and hydrate phase, respectively. Equation (A.8) can also be written in terms of the water flux (F_{H_2O}) as:

$$\begin{aligned} U_f c_w^l \rho_f + \frac{U_s}{1-\phi}\phi S_h c_w^h \rho_h &= F_{H_2O} \\ &= (U_{f,sed} + U_{f,ext})\rho_f \end{aligned} \tag{A.9}$$

Due to low methane solubility in water, we assume the mass fraction of water in aqueous phase to be unity. This gives us an expression for the water flux:

$$U_f = (U_{f,sed} + U_{f,ext}) - \frac{U_s}{1-\phi}\phi S_h c_w^h \frac{\rho_h}{\rho_f} \tag{A.10}$$

Substituting this expression for fluid flux into equation (9.25), we get:

$$\begin{aligned} &\left[(U_{f,sed} + U_{f,ext}) - \frac{U_s}{1-\phi}\phi S_h c_w^h \frac{\rho_h}{\rho_f}\right] c_m^l + \\ &\frac{U_s}{1-\phi}\phi S_h c_m^h \frac{\rho_h}{\rho_f} - \phi(1-S_h) D_m \frac{\partial c_m^l}{\partial z} = \frac{F_{CH_4}}{\rho_f} \end{aligned} \tag{A.11}$$

Similar to the sulfate mass balance, we multiply the above equation by (L_t/D_m) and divide by $c^l_{m,eqb}$ to get the following dimensionless form:

$$\left[(\mathrm{Pe}_1 + \mathrm{Pe}_2) - \frac{\mathrm{Pe}_1 \tilde{U}_s}{1-\phi}\phi S_h c^h_w \tilde{\rho}_h\right]\tilde{c}^l_m + \frac{\mathrm{Pe}_1 \tilde{U}_s}{1-\phi}\phi S_h \tilde{c}^h_m \tilde{\rho}_h - \phi(1-S_h)\frac{\partial \tilde{c}^l_m}{\partial \tilde{z}} = \frac{F_{CH_4}}{\rho_f c^l_{m,eqb}}\frac{L_t}{D_m} \tag{A.12}$$

where different scaled variables were defined in equation (8.26). Equation (A.13) can be rearranged as:

$$(\mathrm{Pe}_1 + \mathrm{Pe}_2)\,\tilde{c}^l_m + \frac{\mathrm{Pe}_1 \tilde{U}_s}{1-\phi}\phi S_h \tilde{\rho}_h\left(\tilde{c}^h_m - c^h_w \tilde{c}^l_m\right) - \phi(1-S_h)\frac{\partial \tilde{c}^l_m}{\partial \tilde{z}} = \frac{F_{CH_4}}{\rho_f c^l_{m,eqb}}\frac{L_t}{D_m} \tag{A.13}$$

Finally, dividing by ($1-\phi_\infty$) to express in terms of the reduced porosity, we get the dimensionless methane balance, equation (8.27).

A.3 Deriving Conditions for Maximum $\tilde{L}_s$ and Minimum $\tilde{L}_h$

The methane concentration profile in the absence of gas hydrate can be obtained using equation (8.28) along with the following boundary conditions:

$$\text{B.C.}(1) : \tilde{c}_m^l = 0 \quad \text{at} \quad \tilde{z} = \tilde{L}_s \tag{A.14}$$

$$\text{B.C.}(2) : \tilde{c}_m^l = \tilde{c}_{m,ext} \quad \text{at} \quad \tilde{z} = D \tag{A.15}$$

where D represents the bottom of the domain. These boundary conditions lead to the following methane concentration profile:

$$\tilde{c}_m(\tilde{z}) = \tilde{c}_{m,ext} \frac{1 - \exp\left[\frac{Q}{\tilde{D}_s}\left(g[\tilde{z}] - g[\tilde{L}_s]\right)\right]}{1 - \exp\left[\frac{Q}{\tilde{D}_s}\left(g[D] - g[\tilde{L}_s]\right)\right]} \ , \ \tilde{L}_s < \tilde{z} < D \tag{A.16}$$

If the depth of the external boundary condition (D) is sufficiently greater than unity, the exponential function in the denominator of the above expression approaches zero, simplifying the methane concentration profile and the methane flux as follows:

$$\tilde{c}_m(\tilde{z}) = \tilde{c}_{m,ext}\left(1 - \exp\left[\frac{Q}{\tilde{D}_s}\left(g[\tilde{z}] - g[\tilde{L}_s]\right)\right]\right) \ , \ \tilde{L}_s < \tilde{z} < D \ \text{and} \ D \gg 1 \tag{A.17}$$

$$f_{CH_4} = Q\tilde{c}_{m,ext} \ , \ \tilde{L}_s < \tilde{z} < D \ \text{and} \ D \gg 1 \tag{A.18}$$

Equating this methane flux to the sulfate flux at the SMT using equations (8.15) and (8.23) yields:

$$(-m)Q\tilde{c}_{m,ext} = \frac{Q}{1 - \exp\left[\frac{Q}{\tilde{D}_s}\left(g[0] - g[\tilde{L}_s]\right)\right]} \tag{A.19}$$

The above equation can be used to obtain the modified flux, Q, as a function of $\tilde{L}_s$:

$$Q = \frac{\tilde{D}_s \ln\left(\frac{1+m\tilde{c}_{m,ext}}{m\tilde{c}_{m,ext}}\right)}{g[0] - g[\tilde{L}_s]} \tag{A.20}$$

Finally, substituting the above relationship and equation (A.17) into the tangency conditions (8.45) and (8.46) gives the coupled set of equations (8.47) and (8.48).

A.4 Expansion of Time-derivative

The accumulation terms in the mass balance equations (10.26) or (10.37) contain products of primary variables such as porosity (ϕ), concentration ($\tilde{c}_m^l$) and saturation (S_w). Discretization of this time-derivative can be achieved in several ways. As an example, we use the following expansion for the product ($\phi S_w \tilde{c}_m^l$) to conserve mass:

$$\Delta_t(\phi S_w c_m^l) \equiv \phi^{n+1} S_w^{n+1} c_m^{l,n+1} - \phi^n S_w^n c_m^{l,n} \tag{A.21}$$

where Δ_t denotes the time change operator and superscripts $n+1$ and n represent time-levels. Adding an subtracting the terms $\phi^{n+1}(S_w^n c_m^{l,n})$ gives:

$$\Delta_t(\phi S_w c_m^l) \equiv \phi^{n+1}(S_w^{n+1} c_m^{l,n+1}) - \phi^n(S_w^n c_m^{l,n}) + \phi^{n+1}(S_w^n c_m^{l,n}) - \phi^{n+1}(S_w^n c_m^{l,n}) \tag{A.22}$$

which on rearranging yields:

$$\Delta_t(\phi S_w c_m^l) \equiv \phi^{n+1}(S_w^{n+1} c_m^{l,n+1} - S_w^n c_m^{l,n}) + S_w^n c_m^{l,n}(\phi^{n+1} - \phi^n) \tag{A.23}$$

The above equation can be rewritten in terms of the time change operator as:

$$\Delta_t(\phi S_w c_m^l) \equiv \phi^{n+1} \Delta_t(S_w c_m^l) + S_w^n c_m^{l,n} \Delta_t \phi \tag{A.24}$$

Porosity (ϕ) is a function of effective stress, which, in turn, is a function of the lithostatic stress and pore pressure. Hence, Δ_t can be written as a function of pore

pressure (p_w) as:

$$\Delta_t(\phi S_w c_m^l) \equiv \phi^{n+1}\Delta_t(S_w c_m^l) + S_w^n c_m^{l,n}\frac{\partial\phi}{\partial p_w}\Delta_t p_w \tag{A.25}$$

Using the porosity-effective stress relationship, equation (10.15), the derivative of porosity with respect to pressure is written as:

$$\Delta_t(\phi S_w c_m^l) \equiv \phi^{n+1}\Delta_t(S_w c_m^l) + S_w^n c_m^{l,n}\left(\frac{\phi-\phi_\infty}{\sigma_\phi}\right)\left(1-\frac{\sigma_v^{n+1}-\sigma_v^n}{p_w^{n+1}-p_w^n}\right)\Delta_t p_w \tag{A.26}$$

The lithostatic stress values are evaluated by integrating the sediment bulk density gradient, equation (10.16), and are updated during the iterations. Similar expansions of the time-derivative are applied to other mass balances.

A.5 Phase-switching of Primary Variables

The coupled equations (10.26), (10.31), (10.34) and (10.37) are solved numerically using a fully implicit formulation, with the primary variables being $\tilde{p}_w$, $\tilde{v}_s$, $\tilde{\alpha}$ and one of the following three ($\tilde{c}_m^l$,S_h, S_g). Choice between these last three primary variables is made according to the local thermodynamic conditions at any gridblock at any given timestep. Schemes for switching among different primary variables in similar problems have been proposed in the literature (Falta et al., 1992; Liu and Flemings, 2007). In our model, for example, if the gridblock is undersaturated with respect to methane, both hydrate and free gas saturations are zero and $\tilde{c}_m^l$ becomes the primary variable. If dissolved methane concentration within a gridblock becomes greater than the local solubility, $\tilde{c}_m^l$ becomes fixed, whereas S_h or S_g become the primary variable, depending on whether the gridblock is within the region of hydrate or stability or not.

A.5.1 New Phase Appearance

Three possible states are identified for switching between different primary variables ($\tilde{c}_m^l$,S_h, S_g) in the water and methane mass balances. Each gridblock is assigned a phase state, which can change in response to the local thermodynamic condition. These phase states are:

Phase state 1: Pore water is undersaturated with respect to methane at the previous time step and remains undersaturated at the new time step. Thus, if $\tilde{c}_{m,sol}^l$ is

methane solubility at any grid block (i, j), then for this phase state,

Phase (i, j) = 1 if $\tilde{c}_m^{l,n} < \tilde{c}_{m,sol}^{l}$ and $\tilde{c}_m^{l,n+1} < \tilde{c}_{m,sol}^{l} \Rightarrow S_h^{n+1}$ or $S_g^{n+1} = 0$

Phase state 2: Pore water is undersaturated with respect to methane at the previous time step but becomes saturated at the new time step.

Phase (i, j) = 2 if $\tilde{c}_m^{l,n} < \tilde{c}_{m,sol}^{l}$ but $\tilde{c}_m^{l,n+1} > \tilde{c}_{m,sol}^{l} \Rightarrow S_h^{n+1}$ or S_g^{n+1} becomes the new primary variable and $\tilde{c}_m^{l,n+1} = \tilde{c}_{m,sol}^{l}$

Phase state 3: Pore water is saturated with respect to methane at the previous time step and remains saturated at the new time step.

Phase (i, j) = 3 if $\tilde{c}_m^{l,n} = \tilde{c}_{m,sol}^{l}$ and S_h^{n+1} or $S_g^{n+1} > 0 \Rightarrow S_h^{n+1}$ or S_g^{n+1} remains the primary variable and $\tilde{c}_m^{l,n+1} = \tilde{c}_{m,sol}^{l}$

A.5.2 Phase Disappearance

Hydrate or free gas saturation going below zero during any iteration implies the disappearance of hydrate or free gas phases. This means that dissolved methane concentration can vary instead of being constrained by the solubility curve. Consequently, S_h^{n+1} or S_g^{n+1} is set to zero, $\tilde{c}_m^{l,n+1}$ becomes the primary independent variable and phase status of the gridblock is set equal to 1.

Proceedings of the 6th International Conference on Gas Hydrates (ICGH 2008), Vancouver, British Columbia, CANADA, July 6-10, 2008.

EFFECT OF OVERPRESSURE ON GAS HYDRATE DISTRIBUTION

Gaurav Bhatnagar, Walter G. Chapman, George J. Hirasaki*
Department of Chemical & Biomolecular Engineering
Rice University
6100 Main St., Houston, TX, 77005
USA

Gerald R. Dickens, Brandon Dugan
Department of Earth Science
Rice University
6100 Main St., Houston, TX, 77005
USA

ABSTRACT

The effect of overpressure on gas hydrate and free gas distribution in marine sediments is studied using a one-dimensional numerical model that couples sedimentation, fluid flow, and gas hydrate formation. Natural gas hydrate systems are often characterized by high sedimentation rates and/or low permeability sediments, which can lead to pore pressures higher than hydrostatic. To quantify the relative importance of these two factors, we define a dimensionless sedimentation-compaction group, N_{sc}, that compares the absolute permeability of the sediments to the sedimentation rate. Higher values of N_{sc} mean higher permeability or low sedimentation rate implying hydrostatic pore pressure. Conversely, lower values of N_{sc} indicate pore pressures greater than hydrostatic. Simulation results show that decreasing N_{sc} not only increases pore pressure from hydrostatic values, but also lowers the lithostatic stress gradient and gas hydrate saturation. This occurs because excess pore pressures result in smaller effective stress, causing high porosity and lower bulk density of the sediment. This leads to higher sediment velocity through the stability zone, thereby reducing the mass accumulation of methane and gas hydrate in the pore space. Effect of overpressure on depth of the gas hydrate stability zone is also studied.

Keywords: gas hydrates, overpressure, sedimentation-compaction, numerical modeling

NOMENCLATURE

c_i^j	Mass fraction of component i in phase j
$c_{m,eqb}^l$	Methane solubility at base of GHSZ
D_m	Methane diffusivity in seawater
Da	Damkohler number
g	Acceleration due to gravity
N_{sc}	Sedimentation-compaction group
k	Absolute sediment permeability
k_0	Absolute sediment permeability at seafloor
k_{rj}	Relative permeability of phase j
L_t	Depth to the base of the GHSZ
L_ϕ	Characteristic depth of compaction
M_i	Molecular weight of component i
Pe_1	Peclet number

* Corresponding author: Phone: +1 713 348 5416 Fax +1 713 348 5478 E-mail: gjh@rice.edu

p_j Pressure of phase j

S_j Saturation of phase j

$\dot{S}$ Sedimentation rate at the seafloor

t Time

$U_{f,sed}$ Fluid flux due to sedimentation

v_j Velocity of phase j

z Depth below seafloor

α Organic carbon content

α_0 Organic carbon content at seafloor

β Normalized organic content at seafloor

γ, η Reduced porosity parameters

λ Methanogenesis reaction rate

μ_j Viscosity of phase j

ρ_j Density of phase j

σ_v Vertical effective stress

σ_ϕ Characteristic stress for compaction

ϕ Porosity

ϕ_0 Porosity at seafloor

ϕ_∞ Porosity at great depths

Subscripts/superscripts:

g Gas phase

h Hydrate phase

l, w Water phase or component

m Methane component

s Sediment phase

INTRODUCTION

Gas hydrate systems can be characterized by overpressure, i.e. pore water pressures higher than hydrostatic. This is particularly evident at settings dominated by low permeability silts/clays, e.g., Blake Ridge [1,2]. Over geologic timescales, continuous sedimentation causes increase in the overburden, resulting in compaction of sediments [3,4,5]. Overpressure can develop in such systems if pore water cannot be expelled from the pore space fast enough and, instead, starts to support some of the overburden. Since permeability controls this rate of pore water expulsion, sediments with low permeability can develop overpressure [4,5]. Alternatively, overpressure can also develop in sediments with relatively high permeability if the sedimentation rate is fast, i.e. increase in overburden is faster than rate of pore water expulsion [3].

Overpressure impacts the behavior of gas hydrate systems in several ways. For example, the maximum thickness of the free gas layer below the base of the gas hydrate stability zone (GHSZ) depends on the magnitude of overpressure [2,6,7]. The length of a free gas column sealed by overlying gas hydrate is regulated by the difference between pore water pressure and lithostatic stress. Thus, higher pore water pressures imply that relatively short connected gas columns can develop before fracturing or shear failure occurs, thereby causing a sudden release of free gas [2,6,7]. Conversely, relatively long connected gas columns can form when water overpressure is zero.

Overpressure also affects sediment and gas hydrate velocity through the GHSZ. At hydrostatic pore pressures, sediments achieve maximum compaction due to relatively high effective stresses acting on them. Development of overpressure reduces the effective stress acting on the sediments, resulting in higher sediment porosity, which leads to faster sediment velocity through the GHSZ. In a gas hydrate system dominated by in-situ biogenic methane supply, this increase in sediment velocity curtails the amount of organic carbon converted within the GHSZ. This occurs because the organic carbon is also progressively buried deeper with the sediment. Additionally, increase in sediment velocity also reduces the residence time of gas hydrate in the GHSZ. These two mechanisms can cause overpressure to result in relatively lower gas hydrate and free gas saturations at steady-state.

Increase in pore pressure can also change the thermodynamic stability regime and extend the base of the GHSZ to greater depths below the seafloor. However, we show through numerical simulations that this increase in depth of the GHSZ due to overpressure is relatively small, even when pore pressures become close to lithostatic limits.

We have previously developed generalized dimensionless numerical models to study gas hydrate and free gas distribution in marine sediments [8,9]. However, in the previous work, pressure was assumed to be hydrostatic. In this

paper, we extend the previous dimensionless models to explicitly incorporate water pressure through the use of Darcy's law in a compacting medium. This allows us to model overpressure development in compacting sediments and study its effect on gas hydrate/free gas saturation.

NON-HYDROSTATIC COMPACTION IN GAS HYDRATE SYSTEMS

We now develop a one-dimensional numerical model to simulate overpressure generation in marine gas hydrate systems and study the parameters governing this process. Darcy's law is used to model fluid low relative to the compacting sediment. We only focus on the effects of overpressure due to sedimentation-compaction and sediment permeability in this paper. Consequently, we assume a relatively higher value of critical gas saturation of 10%. This ensures that free gas will remain immobile within the sediment matrix. We start with the mass balances for different system components.

Mass balances

The water, methane, sediment and organic mass balances are written as:

Water Balance:

$$\frac{\partial}{\partial t}\left[\phi S_w c_w^l \rho_w + \phi S_h c_w^h \rho_h\right] + \frac{\partial}{\partial z}\left[\phi S_w c_w^l \rho_w v_w + \phi S_h c_w^h \rho_h v_s\right] = 0 \quad (1)$$

Methane Balance:

$$\frac{\partial}{\partial t}\left[\phi S_w c_m^l \rho_w + \phi S_h c_m^h \rho_h + \phi S_g c_m^g \rho_g\right] + \frac{\partial}{\partial z}\left[\phi S_w c_m^l \rho_w v_w + \phi S_h c_m^h \rho_h v_s + \phi S_g c_m^g \rho_g v_s\right] = \frac{\partial}{\partial z}\left[\phi S_w D_m \rho_w \frac{\partial c_m^l}{\partial z}\right] + \frac{M_{CH_4}}{M_{org}} \rho_s \lambda (1-\phi)\alpha \quad (2)$$

Sediment Balance:

$$\frac{\partial}{\partial t}\left[(1-\phi)\rho_s\right] + \frac{\partial}{\partial z}\left[(1-\phi)\rho_s v_s\right] = 0 \quad (3)$$

Organic Balance:

$$\frac{\partial}{\partial t}\left[(1-\phi)\rho_s\right]\alpha + \frac{\partial}{\partial z}\left[(1-\phi)\rho_s v_s \alpha\right] = -\rho_s \lambda (1-\phi)\alpha \quad (4)$$

Constitutive relationships

We now list the constitutive relationships used in this formulation.

Darcy's law for water flux in a compacting medium [10]:

$$S_w \phi (v_w - v_s) = -\frac{k k_{rw}}{\mu_w}\left(\frac{\partial p_w}{\partial z} - \rho_w g\right) \quad (5)$$

Absolute permeability of sediment is modeled as a power law function of porosity [11]:

$$k = k_0 \left(\frac{\phi}{\phi_0}\right)^8 \quad (6)$$

Water relative permeability in the presence of gas hydrate is (assuming pore-filling structure) [12]:

$$k_{rw} = 1 - S_h^2 + \frac{2(1-S_h)^2}{\ln(S_h)} \quad (7)$$

Water relative permeability in the presence of free gas is [10]:

$$k_{rw} = k_{rw}^0 \left(S_w^*\right)^4, \text{ where } S_w^* = \frac{S_w - S_{wr}}{1 - S_{wr}} \quad (8)$$

Porosity-effective stress relationship is defined as [13]:

$$\phi = \phi_\infty + (\phi_0 - \phi_\infty) e^{-\frac{\sigma_v - p_w}{\sigma_\phi}} \quad (9)$$

Lithostatic stress gradient can be written as a function of densities and porosity as:

$$\frac{\partial \sigma_v}{\partial z} = \left[(1-\phi)\rho_s + \phi \rho_w\right] g \quad (10)$$

Normalized variables and dimensionless groups

The above equations are now written in dimensionless form. Reduced porosities are defined as:

$$\tilde{\phi} = \frac{\phi - \phi_\infty}{1 - \phi_\infty},\ \eta = \frac{\phi_0 - \phi_\infty}{1 - \phi_\infty},\ \gamma = \frac{1 - \phi_\infty}{\phi_\infty} \tag{11}$$

The dimensionless Peclet number and Damkohler number are defined as:

$$Pe_1 = \frac{U_{f,sed} L_t}{D_m},\ Da = \frac{\lambda L_t^2}{D_m} \tag{12}$$

We also define a dimensionless group corresponding to the ratio of the absolute sediment permeability and the sedimentation rate at the seafloor:

$$N_{sc} = \frac{k_0 \rho_w g}{\mu_w \dot{S}} \tag{13}$$

Large values of N_{sc} correspond to high sediment permeability and/or low sedimentation rate, implying hydrostatic pressures. Conversely, low values of N_{sc} imply low permeability and/or high sedimentation rate, thereby causing pore pressures higher than hydrostatic. Similar dimensionless groups have been used to model non-hydrostatic compaction in sedimentary basins [14,15].

The ratio of compaction depth to the base of GHSZ is defined by the dimensionless group, $N_{t\phi}$:

$$N_{t\phi} = \frac{L_\phi}{L_t} = \frac{\sigma_\phi / (\rho_w g)}{L_t} \tag{14}$$

The normalized methane concentrations are defined as:

$$\tilde{c}_m^l = \frac{c_m^l}{c_{m,eqb}^l},\ \tilde{c}_m^h = \frac{c_m^h}{c_{m,eqb}^l},\ \tilde{c}_m^g = \frac{c_m^g}{c_{m,eqb}^l} \tag{15}$$

Lithostatic stress (σ_v), water pressure and gas pressure are normalized by hydrostatic water pressure at the base of the GHSZ:

$$\tilde{\sigma}_v = \frac{\sigma_v}{\rho_w g L_t},\ \tilde{p}_w = \frac{p_w}{\rho_w g L_t},\ \tilde{p}_g = \frac{p_g}{\rho_w g L_t} \tag{16}$$

Dimensionless depth and time are defined as:

$$\tilde{z} = \frac{z}{L_t},\ \tilde{t} = \frac{t}{L_t^2 / D_m} \tag{17}$$

All phase densities are normalized by water density ($\tilde{\rho}_i = \rho_i / \rho_w$). Sediment velocity is normalized by the sedimentation rate at the seafloor:

$$\tilde{v}_s = \frac{v_s}{\dot{S}} \tag{18}$$

Finally, organic carbon content and initial carbon content at the seafloor are scaled as:

$$\tilde{\alpha} = \frac{\alpha}{\alpha_0},\ \beta = \frac{\alpha_0}{c_{m,eqb}^l} \tag{19}$$

The resulting dimensionless mass balances and constitutive relationships are given in the appendix.

NUMERICAL SOLUTION

The coupled dimensionless equations are solved numerically using a fully implicit finite difference formulation, with the primary variables being $\tilde{p}_w$, $\tilde{v}_s$, $\tilde{\alpha}$ and one of the following three ($\tilde{c}_m^l, S_h, S_g$). Choice between these last three primary variables is made according to the local thermodynamic conditions at any gridblock at any given time-step. All four mass balances are cast in residual form and the Newton-Raphson method is used to iterate on them to converge to the solution.

RESULTS

To study the effect of overpressure on gas hydrate and free gas saturation, we simulate cases with different values of the sedimentation-compaction

parameter N_{sc}. Apart from the parameter N_{sc}, other primary simulation parameters include the Peclet number, the Damkohler number, the normalized organic carbon input and the reduced porosity parameters. Values of these parameters used in the simulations shown in this paper are: $Pe_1 = 0.1$, $Da = 10$, $\beta = 3$, $N_{t\phi} = 1$, $\eta = 6/9$, and $\gamma = 9$. Seafloor parameters are chosen to be similar to the Blake Ridge region [16], with seafloor temperature of 3°C, seafloor depth of 2700 m, and geotherm of 0.04°C/m. We keep these parameters constant in simulations shown later and only vary N_{sc} from higher to progressively lower values.

Figure 1 shows steady-state pore pressure profiles versus depth below the seafloor for four different values of N_{sc}. Hydrostatic pressure profile and lithostatic stress profiles are also plotted for each case as minimum and maximum bounds to the pore pressure, respectively.

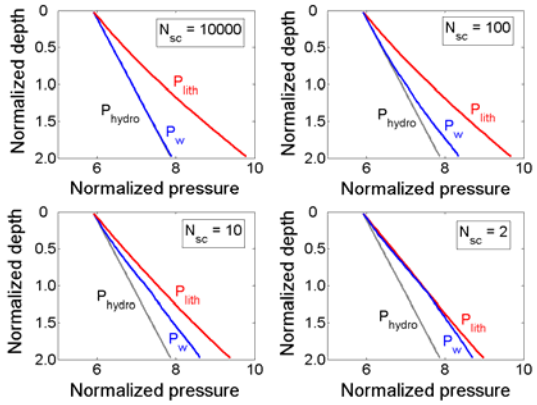

Figure 1: Effect of the sedimentation-compaction parameter, N_{sc}, on steady state pore pressure profiles. Each pore pressure curve is bounded by the hydrostatic pressure profile as the lower limit and the lithostatic stress profile as the upper limit.

Importantly, simulations (Figure 1) show that relatively higher values of N_{sc} (~10^4) lead to almost hydrostatic pore pressures, whereas relatively lower N_{sc} (of order unity) lead to pore pressures that are close to the lithostatic limit (Figure 1). This occurs because relatively low N_{sc} values imply lower sediment permeability and/or fast sedimentation rate. Either of these conditions can reduce the rate of expulsion of pore water in response to increasing overburden, leading to pore pressures higher than hydrostatic values. Conversely, relatively higher values of N_{sc} imply high sediment permeability and/or low sedimentation rate. This maintains equilibrium compaction and pore pressures that remain close to hydrostatic values.

Figure 1 also reveals that the lithostatic stress reduces as pore pressures increase. To illustrate this more clearly, we plot pore pressure and lithostatic stress profiles corresponding to the four cases together in Figure 2. Dashed set of curves in Figure 2 correspond to the lithostatic stress profiles, while solid curves denote pore pressure profiles. It can be seen from Figure 2 that pore pressure and lithostatic profiles remain separated from each other at large N_{sc}. However, on lowering N_{sc}, both pore pressure and lithostatic curves approach each other. Decrease in lithostatic stress on reducing N_{sc} occurs because increased porosities, resulting from lower effective stresses acting on the sediments, cause lower bulk densities of the sediment. Since the lithostatic stress gradient is a function of sediment bulk density, overpressure and higher porosities lead to lower lithostatic stress (Figure 2).

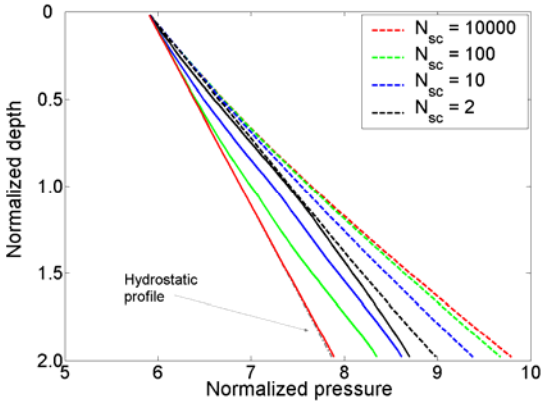

Figure 2: Pressure profiles shown in Figure 1 plotted together for all four cases. Lithostatic stress profiles (dashed curves) and the corresponding pore pressure profiles (solid curves) for the same value of N_{sc} are color-coded together.

As mentioned before, increase in pore pressure influences the thermodynamic stability of gas hydrates. Specifically, increase in pore pressure extends the depth to the base of the GHSZ deeper into the sediments. This change is shown through the methane solubility curves in Figure 3 for the same set of N_{sc} values simulated in the previous figures.

We start with the case N_{sc} = 10000, which corresponds to near-hydrostatic pore pressures. According to the scaling scheme defined previously, the solubility curve for this case has a peak methane solubility equal to unity at unit normalized depth. As pore pressure increases, i.e. N_{sc} decreases, we observe that the peak values of the solubility curves shift to higher values, with the peak itself occurring at slightly deeper depths. This demonstrates that the base of GHSZ is a dynamic boundary that moves in response to the pore pressure.

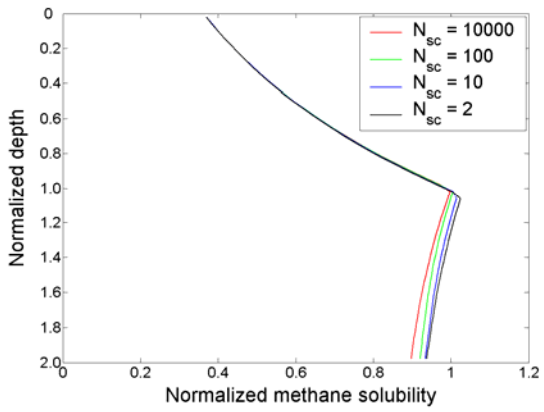

Figure 3: Effect of overpressure on methane solubility curves. Decreasing N_{sc} from 10000 to 2 causes increasing overpressure within the sediment and results in a deeper base of the GHSZ. The magnitude of this downward shift is, however, negligible even when the pore pressure is close to lithostatic.

But even when pore pressures are close to lithostatic, the downward shift in the base of the GHSZ is very small in the normalized form. When the normalized vertical depth scale (Figure 3) is converted back to the physical scale by multiplying with L_t, the depth to the base of GHSZ, this increase in the thickness of the GHSZ becomes larger, but is still relatively small. For example, for the case corresponding to almost lithostatic pore pressure, the downward shift in the base of the GHSZ is about 20 m, which, for Blake Ridge type seafloor conditions, is only about 0.7% of the water depth.

The effect of N_{sc} on steady-state gas hydrate and free gas saturation profiles is shown in Figure 4. Maximum gas hydrate and free gas saturation occur at the highest values of N_{sc}, which corresponds to hydrostatic pore pressure. Progressively decreasing N_{sc} leads to lower gas hydrate and free gas saturations due to compaction disequilibrium. As mentioned before, relatively lower values of N_{sc} lead to higher overpressures, higher sediment porosities and faster sediment velocities, which result in lower organic carbon decay within the GHSZ and shorter residence times of hydrate and free gas in the GHSZ.

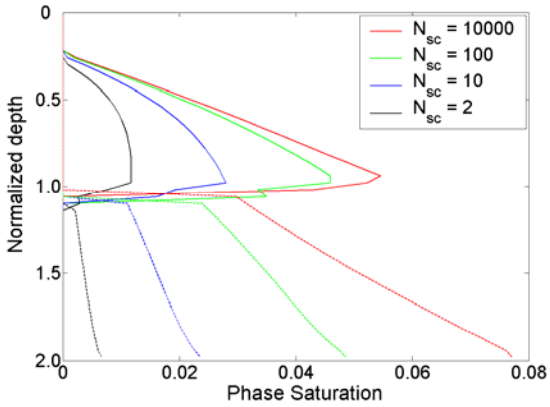

Figure 4: Effect of overpressure, characterized through N_{sc}, on steady-state gas hydrate saturation (solid curves) and free gas saturation profiles (dashed curves). Relatively smaller values of N_{sc} lead to overpressure development, higher porosities, higher sediment velocities, and lower net hydrate and free gas saturations.

However, it should be noted that hydrate and free gas saturation profiles do not give a complete picture of their amounts, because each value of N_{sc} results in a different porosity profile. Thus, although hydrate and free gas saturation within the pore space decrease on lowering N_{sc}, the corresponding increase in porosity might lead to

net higher accumulation of hydrate or free gas within the sediment volume. To test this scenario, we plot the product of porosity and hydrate/free gas saturation (ϕS_j) to get the volume fraction of hydrate and free gas within the sediment. These profiles are plotted in Figure 5 and show that the net amount of gas hydrate or free gas saturation within the sediment also decreases on lowering N_{sc}. However, multiplying by porosity does reduce the magnitude of change observed between different cases. For example, peak hydrate saturation at the base of GHSZ decreases from about 6% to 1%, a factor of 6 change, on lowering N_{sc} from 10000 to 2. In contrast, peak change in sediment volume fraction of hydrate goes from about 2.2% to 0.7%, a factor of 3 change, for the same decrease in N_{sc}.

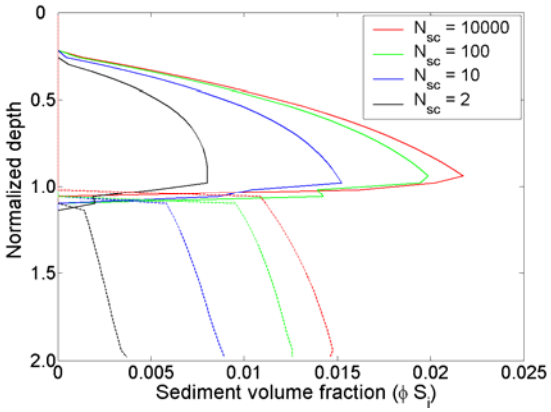

Figure 5: Effect of overpressure, characterized through N_{sc}, on steady-state gas hydrate (solid curves) and free gas (dashed curves) sediment volume fraction.

This validates our hypothesis that overpressure does lower the net amount of methane that accumulates in either hydrate or free gas phase. In other words, the decrease in hydrate and free gas saturation with increasing overpressure is not only a result of increased porosities. The effect of increased sediment and fluid velocities and lower organic carbon decay within the GHSZ has a much more significant impact on net gas hydrate and free gas accumulation.

Effect on free gas column thickness

Based on pressure profiles shown in Figures 1 and 2, it can be argued that deep connected free gas columns may result for settings characterized by high N_{sc}. In contrast, only short gas columns can form when N_{sc} is low before sediment fracture/failure occurs and vents the free gas into the ocean. Thus, from an exploration standpoint, geologic sites characterized by high permeability and low sedimentation rates (i.e., high N_{sc}) might be most suitable for targeting the free gas sealed by a hydrate layer.

CONCLUSIONS

A dimensionless numerical model for non-hydrostatic pressure compaction is developed to study the effect of overpressure on gas hydrate and free gas saturations. Non-dimensionalization of the equations lead to a sedimentation-compaction group, N_{sc}, defined as the ratio of sediment permeability to sedimentation rate. Simulations show that relatively high values of N_{sc} (about 10^4) lead to systems close to hydrostatic pore pressure, while relatively low values of N_{sc} (about unity) lead to significant overpressure in the system. Overpressure development impacts this gas hydrate system by lowering effective stresses on the sediment, causing higher porosities. Higher sediment velocities achieved due to overpressure and high porosities ultimately lead to lesser organic carbon decay, resulting in lower hydrate and free gas saturations for our set of boundary conditions, i.e., fixed seafloor depth and constant geotherm.

REFERENCES

[1] Winters WJ. *Stress history and geotechnical properties of sediment from the Cape Fear Diapir, Blake Ridge Diapir, and Blake Ridge*. In: Paull CK, Matsumoto R, Wallace PJ, Dillon WP, editors. Proceedings of the Ocean Drilling Program, Scientific Results, volume 164: College Station, Texas Ocean Drilling Program, 2000. p. 421-429.

[2] Flemings PB, Liu X, Winters WJ. *Critical pressure and multiphase flow in Blake Ridge gas hydrates*. Geology 2003; 31:1057-1060.

[3] Gibson RE. *The progress of consolidation in a clay layer increasing in thickness with time*. Geotechnique 1958; 8:171-182.

[4] Wangen M. *Pressure and temperature evolution in sedimentary basins*. Geophysical Journal International 1992; 110:601-613.
[5] Dugan B, Flemings PB. *Overpressure and fluid flow in the New Jersey continental slope: implications for slope failure and cold seeps*. Science 2000; 289:288-291.
[6] Hornbach MJ, Saffer, DM, Holbrook, WS. *Critically pressured free-gas reservoirs below gas-hydrate provinces*. Nature 2004; 427:142-144.
[7] Liu XL, Flemings PB. *Dynamic multiphase flow model of hydrate formation in marine sediments*. Journal of Geophysical Research 2007; 112:B03101, doi:10.1029/2005JB004227.
[8] Bhatnagar G, Chapman WG, Dickens GR, Dugan B, Hirasaki GJ. *Generalization of gas hydrate distribution and saturation in marine sediments by scaling of thermodynamic and transport processes*. American Journal of Science 2007; 307:861-900.
[9] Bhatnagar G, Chapman WG, Dickens GR, Dugan B, Hirasaki GJ. *Sulfate-methane transition as a proxy for average methane hydrate saturation in marine sediments*. Geophysical Research Letters 2008; 35:L03611, doi:10.1029/2007GL032500.
[10] Bear J. *Dynamic of fluids in porous media*. New York: Dover Publications Inc., 1988.
[11] Smith JE. *The dynamics of shale compaction and evolution of pore-fluid pressures*. Mathematical Geology 1971; 3:239-263.
[12] Kleinberg RL, Flaum C, Griffin DD, Brewer PG, Malby GE, Peltzer ET, Yesinowski JP. *Deep sea NMR: Methane hydrate growth habitat in porous media and its relationship to hydraulic permeability, deposit accumulation, and submarine slope stability*. Journal of Geophysical Research 2003; 108(B10):2508, doi:10.1029/2003JB002389.
[13] Rubey WW, Hubbert MK. *Role of fluid pressure in mechanics of over-thrust faulting; ii. Overthrust belt in geosynclinal area of western Wyoming in light of fluid pressure hypothesis*. Geological Society of America Bulletin 1959; 70:167-206.
[14] Yang XS, Fowler AC. *Fast and slow compaction in sedimentary basins*. SIAM Journal on Applied Mathematics 1998; 59(1):365-385.
[15] Gutierrez M, Wangen M. *Modeling of compaction and overpressuring in sedimentary basins*. Marine and Petroleum Geology 2005; 22(3):351-363.
[16] Paull CK, Matsumoto R, Wallace PJ, Dillon WP, editors. Proceedings of the Ocean Drilling Program, Scientific Results, volume 164: College Station, Texas Ocean Drilling Program, 2000. p. 421-429.

APPENDIX

Dimensionless mass balances

The scaling schemes defined in the main text lead to the following form of the four mass balances, initial conditions (I.C.) and boundary conditions (B.C.).

Water Balance:

$$\frac{\partial}{\partial \tilde{t}}\left[\frac{1+\gamma\tilde{\phi}}{\gamma}\left(S_w c_w^l + S_h c_w^h \tilde{\rho}_h\right)\right] + Pe_1\left(\frac{1+\gamma}{1-\eta}\right)\frac{\partial}{\partial \tilde{z}}\left[\begin{array}{l}\dfrac{1+\gamma\tilde{\phi}}{\gamma} S_w c_w^l \tilde{v}_s - N_{sc}\dfrac{1+\gamma}{\gamma}\left(\dfrac{1+\gamma\tilde{\phi}}{1+\gamma\eta}\right)^8 \\ k_{rw}\left(\dfrac{\partial \tilde{p}_w}{\partial \tilde{z}} - 1\right)c_w^l + \dfrac{1+\gamma\tilde{\phi}}{\gamma} S_h c_w^h \tilde{\rho}_h \tilde{v}_s\end{array}\right] = 0 \quad \text{(A1)}$$

$$\text{I.C.: } \tilde{p}_w\left(\tilde{z},0\right) = \frac{\rho_w g D_0 + \rho_w g z}{\rho_w g L_t} = \frac{D_0}{L_t} + \tilde{z} \quad \text{(A2)}$$

$$\text{B.C. (1): } \tilde{p}_w\left(0,\tilde{t}\right) = \frac{D_0}{L_t} \quad \text{(A3)}$$

$$\text{B.C. (2): } \frac{\partial \tilde{p}_w}{\partial \tilde{z}}\left(D,\tilde{t}\right) = 1 \quad \text{(A4)}$$

where D_0 is seafloor depth and D is the bottom of the domain.

Methane Balance:

$$\frac{\partial}{\partial \tilde{t}}\left[\frac{1+\gamma\tilde{\phi}}{\gamma}\left(S_w\tilde{c}_m^l+S_h\tilde{c}_m^h\tilde{\rho}_h+S_g\tilde{c}_m^g\tilde{\rho}_g\right)\right]+Pe_1$$

$$\left(\frac{1+\gamma}{1-\eta}\right)\frac{\partial}{\partial \tilde{z}}\left[\begin{array}{l}\frac{1+\gamma\tilde{\phi}}{\gamma}S_w\tilde{c}_m^l\tilde{v}_s-N_{sc}\frac{1+\gamma}{\gamma}\left(\frac{1+\gamma\tilde{\phi}}{1+\gamma\eta}\right)^8\\ k_{rw}\left(\frac{\partial\tilde{p}_w}{\partial\tilde{z}}-1\right)\tilde{c}_m^l+\frac{1+\gamma\tilde{\phi}}{\gamma}S_h\tilde{c}_m^h\tilde{\rho}_h\tilde{v}_s\\ +\frac{1+\gamma\tilde{\phi}}{\gamma}S_g\tilde{c}_m^g\tilde{\rho}_g\tilde{v}_s-N_{sc}\frac{1+\gamma}{\gamma}\\ \left(\frac{1+\gamma\tilde{\phi}}{1+\gamma\eta}\right)^8k_{rg}\left(\frac{\partial\tilde{p}_g}{\partial\tilde{z}}-\tilde{\rho}_g\right)\frac{\mu_w}{\mu_g}\tilde{\rho}_g\tilde{c}_m^l\end{array}\right]$$

$$=\frac{\partial}{\partial\tilde{z}}\left[\frac{1+\gamma\tilde{\phi}}{\gamma}S_w\frac{\partial\tilde{c}_m^l}{\partial\tilde{z}}\right]+\frac{M_{CH_4}}{M_{org}}\tilde{\rho}_sDa\left(1-\tilde{\phi}\right)\tilde{\alpha}\beta \quad (A5)$$

I.C.: $\tilde{c}_m^l\left(\tilde{z},0\right)=0$ (A6)

B.C. (1): $\tilde{c}_m^l\left(0,\tilde{t}\right)=0$ (A7)

B.C. (2): $\frac{\partial\tilde{c}_m^l}{\partial\tilde{z}}\left(D,\tilde{t}\right)=1$ (A8)

Sediment Balance:

$$\frac{\partial}{\partial\tilde{t}}\left[1-\tilde{\phi}\right]+Pe_1\left(\frac{1+\gamma}{1-\eta}\right)\frac{\partial}{\partial\tilde{z}}\left[\left(1-\tilde{\phi}\right)\tilde{v}_s\right]=0$$

I.C.: $\tilde{v}_s\left(\tilde{z},0\right)=\frac{1-\eta}{1-\tilde{\phi}}$ (A9)

B.C. (1): $\tilde{v}_s\left(0,\tilde{t}\right)=1$ (A10)

Organic Balance:

$$\frac{\partial}{\partial\tilde{t}}\left[\left(1-\tilde{\phi}\right)\tilde{\alpha}\right]+Pe_1\left(\frac{1+\gamma}{1-\eta}\right)\frac{\partial}{\partial\tilde{z}}\left[\left(1-\tilde{\phi}\right)\tilde{v}_s\tilde{\alpha}\right]$$
$$=-Da\left(1-\tilde{\phi}\right)\tilde{\alpha}$$

I.C.: $\tilde{\alpha}\left(\tilde{z},0\right)=0$ (A11)

B.C. (1): $\tilde{\alpha}\left(0,\tilde{t}\right)=1$ (A12)

Initial porosity profile

Reduced porosity ($\tilde{\phi}$) is related to the dimensionless lithostatic stress ($\tilde{\sigma}_v$) and dimensionless pore pressure ($\tilde{p}_w$):

$$\tilde{\phi}=\eta\exp\left[-\frac{\tilde{\sigma}_v-\tilde{p}_w}{N_{t\phi}}\right] \quad (A13)$$

At hydrostatic pressure, the porosity profile can be computed as an analytical expression to serve as an initial condition:

$$\tilde{\phi}=\frac{\eta}{\eta+\left(1-\eta\right)\exp\left[\frac{\gamma\tilde{z}\left(\tilde{\rho}_s-1\right)}{N_{t\phi}\left(1+\gamma\right)}\right]} \quad (A14)$$

The sulfate-methane transition as a proxy for average methane hydrate saturation in marine sediments

G. Bhatnagar[1], W. G. Chapman[1], G. R. Dickens[2], B. Dugan[2], G. J. Hirasaki[1*]

[1]*Department of Chemical & Biomolecular Engineering, Rice University, Houston, Texas*

[2]*Department of Earth Science, Rice University, Houston, Texas*

[*] *Corresponding author: gjh@rice.edu*

Abstract.

We develop a relationship between the sulfate-methane transition (SMT) and average gas hydrate saturation (AGHS) for systems dominated by methane migration from deeper sources. The relationship is explained by a one-dimensional numerical model that simulates gas hydrate accumulation in marine sediments. Higher methane fluxes result in shallow SMT depths and high AGHS, while lower methane fluxes result in deep SMTs and low AGHS. We also generalize the variation between AGHS and scaled SMT depth, a procedure that aids prediction of AGHS at different sites from observations of the SMT, such as along Cascadia Margin.

1. Introduction

Gas hydrates can form in the pore space of sediment along continental margins when methane and other low molecular weight gases combine with water at appropriate pressure, temperature and salinity conditions [*Kvenvolden*, 1993]. These hydrates are components of dynamic systems in which methane enters and leaves a gas hydrate stability zone (GHSZ) at variable rates [*Dickens*, 2003]. Based on the supply of methane, marine gas hydrate systems can be distinguished into two end-members: *in-situ* systems where microbes generate methane within the GHSZ [e.g., *Claypool and Kvenvolden*, 1983]; and deep-source systems where rising fluids bring methane from depth [e.g., *Hyndman and Davis*, 1992]. However, quantifying gas hydrate saturation in these systems remains a challenge. In this paper, we develop a model that relates average gas hydrate saturation (AGHS) to the depth of sulfate-methane transition (SMT) in deep-source systems. This facilitates prediction of AGHS at sites where SMT depth is known.

The SMT denotes a relatively thin zone near the seafloor where pore water sulfate and methane are depleted to zero concentration (Figure 1). This depletion occurs due to the anaerobic oxidation of methane reaction (AOM: $CH_4 + SO_4^{2-} \rightarrow HCO_3^- + HS^- + H_2O$) [*Borowski et al.*, 1999]. Although microbes can also consume sulfate using solid organic carbon [*Berner*, 1980], AOM can dominate overall sulfate depletion in sediments with gas hydrates and

modest methane fluxes [*Borowski et al.*, 1996; *Snyder et al.*, 2007]. Further, since we focus only on deep-source gas hydrate systems (i.e., sites with low organic carbon input), AOM becomes the only sulfate sink. The sulfate profile and SMT depth in such deep-source systems should depend on methane flux from below because of the simple 1:1 AOM reaction [*Borowski et al.*, 1996; *Snyder et al.*, 2007]. Additionally, the thickness of the gas hydrate zone and gas hydrate saturation are functions of upward methane flux [*Davie and Buffett*, 2003; *Bhatnagar et al.*, 2007]. Thus, SMT depth (L_s, Figure 1) should relate to gas hydrate saturation [*Borowski et al.*, 1999].

To study this relationship between SMT depth and AGHS, we expand the model of *Bhatnagar et al.* [2007] by including a sulfate balance for deep-source systems (Figure 1). We show that, at steady-state conditions, the depth of the SMT relates to net fluid flux in the system and to AGHS (volume fraction of pore space) within the GHSZ. Compared to previous site-specific studies, our model generalizes the relationship between SMT depth and AGHS at any gas hydrate setting dominated by methane flux from depth.

2. Mathematical Model for Gas Hydrate Accumulation and AOM

Gas hydrate accumulation in marine sediment is simulated using a numerical model that includes phase equilibrium, sedimentation, diffusion, compaction-driven fluid flow, and external fluid flow [*Bhatnagar et al.*, 2007]. Following *Bhatnagar et al.* [2007], the three-phase methane mass balance (liquid, gas hydrate and free gas) can be written to include the AOM reaction in dimensionless form as:

$$\begin{aligned}
&\frac{\partial}{\partial \tilde{t}}\left[\frac{1+\gamma\tilde{\phi}}{\gamma}\left(S_w\tilde{c}_m^w + S_h\tilde{c}_m^h\tilde{\rho}_h + S_g\tilde{c}_m^g\tilde{\rho}_g\right)\right] + \\
&\frac{1+\gamma}{\gamma}\frac{\partial}{\partial \tilde{z}}\left[\begin{array}{l}\left(\left(Pe_1+Pe_2\right) - Pe_1\tilde{U}_s\frac{(1+\gamma\tilde{\phi})}{\gamma(1-\tilde{\phi})}S_h c_w^h\tilde{\rho}_h\right)\tilde{c}_m^w \\ +Pe_1\tilde{U}_s\frac{(1+\gamma\tilde{\phi})}{\gamma(1-\tilde{\phi})}\left(S_h\tilde{c}_m^h\tilde{\rho}_h + S_g\tilde{c}_m^g\tilde{\rho}_g\right)\end{array}\right] = \\
&\frac{\partial}{\partial \tilde{z}}\left[\frac{1+\gamma\tilde{\phi}}{\gamma}S_w\frac{\partial\tilde{c}_m^w}{\partial\tilde{z}}\right] - Da_{AOM}\frac{M_{CH_4}c_{s,0}^w}{M_{SO_4}c_{m,eqb}^w}\left[\frac{1+\gamma\tilde{\phi}}{\gamma}S_w\right]\tilde{c}_m^w\tilde{c}_s^w
\end{aligned} \qquad (1)$$

where S_i represents saturation of phase i in pore space, $\tilde{\rho}_i$ is the density of phase i scaled by water density, M_j is molecular weight, and subscripts/superscripts w, h and g denote liquid water, hydrate and free gas phases, respectively. We normalize vertical depth as $\tilde{z} = z/L_t$, where L_t is depth to the base of GHSZ. Time is made dimensionless by a combination of L_t and methane diffusivity D_m ($\tilde{t} = t/(L_t^2/D_m)$).

Methane mass fraction in phase i (c_m^i) is scaled by methane solubility in the liquid phase at the base of GHSZ ($c_{m,eqb}^w$), c_w^h is mass fraction of water in hydrate phase ($c_w^h = 1 - c_m^h$), while sulfate mass fraction in pore water (c_s^w) is scaled by the seawater value ($c_{s,0}^w$), to get the corresponding normalized variables:

$$\tilde{c}_m^i = \frac{c_m^i}{c_{m,eqb}^w} \quad \text{for} \quad i \in \{w, h, g\} \quad , \qquad \tilde{c}_s^w = \frac{c_s^w}{c_{s,0}^w} \tag{2}$$

Reduced porosity parameters, $\tilde{\phi}$ and γ, and normalized sediment flux, $\tilde{U}_s$, are defined as:

$$\tilde{\phi} = \frac{\phi - \phi_\infty}{1 - \phi_\infty}, \qquad \gamma = \frac{1 - \phi_\infty}{\phi_\infty}, \qquad \tilde{U}_s = \frac{U_s}{U_{f,sed}} \tag{3}$$

where ϕ is sediment porosity, ϕ_∞ is the minimum porosity at great depth, U_s is sediment flux, and $U_{f,sed}$ is the fluid flux resulting from sedimentation and compaction. Porosity loss is related to depth using a constitutive relationship between porosity and vertical effective stress assuming hydrostatic pressure [*Bhatnagar et al.*, 2007]:

$$\tilde{\phi} = \frac{\eta}{\eta + (1 - \eta) e^{\tilde{z}}}, \qquad \eta = \frac{\phi_0 - \phi_\infty}{1 - \phi_\infty} \tag{4}$$

where η and ϕ_0 are the reduced and actual porosities at the seafloor, respectively. $U_{f,sed}$ is related to seafloor sedimentation rate ($\dot{S}$) and porosities as follows [*Berner*, 1980]:

$$U_{f,sed} = \frac{1 - \phi_0}{1 - \phi_\infty} \dot{S} \phi_\infty \tag{5}$$

The two Peclet numbers Pe_1, Pe_2 and the Damkohler number Da_{AOM} are defined as:

$$Pe_1 = \frac{U_{f,sed} L_t}{D_m}, \qquad Pe_2 = \frac{U_{f,ext} L_t}{D_m}, \qquad Da_{AOM} = \frac{\rho_w c_{m,eqb}^w}{M_{CH_4}} \frac{\lambda_{AOM} L_t^2}{D_m} \tag{6}$$

where $U_{f,ext}$ is the upward fluid flux due to external sources and has negative value (due to opposite direction to $U_{f,sed}$), and λ_{AOM} is the second order rate constant for AOM. Thus, Pe_1 has positive value, while Pe_2 becomes negative. Since we focus on deep-source systems, results shown later are relevant for cases where $|Pe_2| > |Pe_1|$. Importantly, Pe_1 characterizes the ratio of compaction-driven fluid flux to methane diffusion, while Pe_2 represents the ratio of external

fluid flux to methane diffusion. The Damkohler number compares AOM rate to methane diffusion. Finally, we complete the system by formulating the dimensionless sulfate mass balance:

$$\frac{\partial}{\partial \tilde{t}}\left[\frac{1+\gamma\tilde{\phi}}{\gamma}S_w\tilde{c}_s^w\right]+\frac{1+\gamma}{\gamma}\frac{\partial}{\partial \tilde{z}}\left[\left(\left(Pe_1+Pe_2\right)-Pe_1\tilde{U}_s\frac{(1+\gamma\tilde{\phi})}{\gamma(1-\tilde{\phi})}S_h c_w^h\tilde{\rho}_h\right)\tilde{c}_s^w\right]=$$
$$\frac{\partial}{\partial \tilde{z}}\left[\frac{1+\gamma\tilde{\phi}}{\gamma}S_w\left(\frac{D_s}{D_m}\right)\frac{\partial \tilde{c}_s^w}{\partial \tilde{z}}\right]-Da_{AOM}\left[\frac{1+\gamma\tilde{\phi}}{\gamma}S_w\right]\tilde{c}_m^w\tilde{c}_s^w \quad (7)$$

where D_s denotes sulfate diffusivity. The initial and boundary conditions for the two mass balances are written as:

I.C.: $\tilde{c}_s^w(\tilde{z},0)=\tilde{c}_m^w(\tilde{z},0)=0$ (8)

B.C. (1): $\tilde{c}_s^w(0,\tilde{t})=1$, $\tilde{c}_m^w(0,\tilde{t})=0$ (9)

B.C. (2): $\frac{\partial \tilde{c}_s^w}{\partial \tilde{z}}(D,\tilde{t})=0$, $\tilde{c}_m^w(D,\tilde{t})=\tilde{c}_{m,ext}^w=\frac{c_{m,ext}^w}{c_{m,eqb}^w}$ (10)

where $c_{m,ext}^w$ is the methane concentration in the external flux, $\tilde{c}_{m,ext}^w$ is the normalized value, and *D* denotes the bottom of the model domain.

3. Results

Equations (1) and (7) are solved numerically to obtain steady-state profiles for methane, gas hydrate saturation, and pore water sulfate concentration. For results shown later, we assume seafloor temperature (T_0) to be 3°C, geothermal gradient (G) to be 0.04°C/m, and pore water salinity representative of standard seawater. Changing T_0 or G results in methane solubility curves that are similar in the normalized form [*Bhatnagar et al.*, 2007], causing AGHS to be relatively insensitive to changes in T_0 or G. However, the normalized solubility curves are more sensitive to seafloor depth. Thus, we use a seafloor depth of 1000 m for results shown in Figures 2 and 3, whereas Figure 4 generalizes the relationship between AGHS and SMT depth for multiple seafloor depths. Porosity at the seafloor (ϕ_0) and at depth (ϕ_∞) are assumed to be 0.7 and 0.1, respectively. Diffusivities D_s and D_m are taken to be 0.56×10^{-9} and 0.87×10^{-9} m^2/s, respectively [*Iversen and Jørgensen*, 1993], c_m^h is set to 0.134, seawater sulfate concentration equals 28 mM, and ρ_h and ρ_f equal 930 and 1030 kg/m^3, respectively. At steady state, $\tilde{c}_{m,ext}^w$ is not significant, provided it exceeds the minimum required to form hydrate [*Bhatnagar et al.*, 2007]. Consequently, we assume in all simulations here that $\tilde{c}_{m,ext}^w$ equals unity.

We first study the effect of Da_{AOM} on steady-state profiles. For fixed Pe_1 and Pe_2, decreasing Da_{AOM} results in a thickening of the SMT zone (Figure 2a). Higher Da_{AOM} implies faster consumption of methane and sulfate compared to diffusion, causing a relatively sharp SMT. The thickness of the SMT zone is usually less than a few meters at most gas hydrate settings, so we use a large value of Da_{AOM} (10^8) in further simulations.

Concentration profiles simulated for three different sets of Pe_1 and Pe_2, but with the sum $Pe_1 + Pe_2$ held constant at -10, are shown in Figure 2b. Overlap of these profiles demonstrates that neither Pe_1 nor Pe_2 individually controls the concentration profiles, but that their sum determines the concentrations and the scaled SMT depth, $\tilde{L}_s = L_s / L_t$. This sum, $Pe_1 + Pe_2$, represents the net fluid flux through the system. Hydrate saturation profiles, however, depend on more than the sum of the Peclet numbers (Figure 2c). The AGHS ($\langle S_h \rangle$) for each of the three cases is about 0.2%, 0.5% and 2%, with the highest value corresponding to the smallest Pe_1 (0.1) and largest Pe_2 (-10.1). Small Pe_1 and large Pe_2 correspond to low sedimentation rate and high methane flux, respectively, resulting in higher AGHS. However, for all three cases, the product $Pe_1 \langle S_h \rangle$ is the same. Thus, Figure 2c demonstrates that $Pe_1 \langle S_h \rangle$, which characterizes the flux of gas hydrate through the GHSZ, is controlled by the net fluid flux, $Pe_1 + Pe_2$ [*Bhatnagar et al.*, 2007].

Increasing net methane flux from depth (i.e., raising the magnitude of $Pe_1 + Pe_2$) results in a shallow scaled SMT depth (Figure 3a), as proposed by *Borowski et al.* [1996, 1999]. Increasing Pe_2, with Pe_1 held constant, increases gas hydrate saturation (Figure 3b) due to higher methane input to the system. Consequently, $Pe_1 \langle S_h \rangle$ also increases. Hence, the scaled depth to the SMT, $\tilde{L}_s$, and $Pe_1 \langle S_h \rangle$ both depend on the sum $Pe_1 + Pe_2$. As a consequence, scaled SMT depth and $Pe_1 \langle S_h \rangle$ become correlated. This correlation, shown in Figure 4 for three seafloor depths, indicates that average gas hydrate flux, $Pe_1 \langle S_h \rangle$, increases as $\tilde{L}_s$ decreases. Thus, AGHS can be estimated for any system dominated by methane flux from depth if $\tilde{L}_s$ and Pe_1 are known (Figure 4).

4. Application to Cascadia Margin Sites

Sites drilled by Ocean Drilling Program (ODP) Leg 146 and Integrated Ocean Drilling Program Expedition (IODP) 311 penetrate gas hydrate accumulations along Cascadia Margin [*Westbrook et al.*, 1994; *Riedel et al.*, 2006]. The low organic carbon content of sediment and pervasive upward fluid migration at these sites suggests that gas hydrate in the Cascadia Margin is

controlled by methane supplied from depth [*Riedel et al.*, 2006]. We now summarize calculation of AGHS from site-specific data at Cascadia Margin Sites 889, U1325, U1326 and U1328 (Table 1):

- Use sedimentation rate ($\dot{S}$) to calculate Pe_1 from equations (5) and (6);
- Calculate the scaled SMT depth $\tilde{L}_s$ using the dimensional depths L_s and L_t;
- For given seafloor depth and $\tilde{L}_s$, obtain gas hydrate flux $Pe_1 \langle S_h \rangle$ from Figure 4;
- Divide this gas hydrate flux by Pe_1 to yield AGHS, $\langle S_h \rangle$ (Table 1)

At Site 889 (ODP Leg 146), pore water chloride profile indicates a peak hydrate saturation close to 2% at the base of GHSZ, and AGHS <1% within the GHSZ [*Davie and Buffett*, 2003]. This result agrees favorably with our simulation that shows peak saturation of about 2.2 % at the base of GHSZ and AGHS of 0.4% across the entire GHSZ (Table 1). *Hyndman et al.* [1999] calculated gas hydrate saturation between 25-30% of pore space in the 100 m interval above the base of GHSZ at Site 889 using resistivity log data. Subsequent calculations using a different set of Archie parameters revise this estimate to 5-10% in that 100 m interval [*Riedel at al.,* 2006]. Further, *Ussler and Paull* [2001] show that a smoothly decreasing chlorinity profile at Site 889 yields hydrate saturation of 2-5% within discrete layers. Although several parameter uncertainties confront such estimates [*Egeberg and Dickens*, 1999; *Riedel et al*., 2006], AGHS predicted using our SMT model concurs with the lower estimates at Site 889.

For the IODP Expedition 311 sites, drilled along the northern Cascadia Margin, we compare our predictions with AGHS computed from chloride anomalies and resistivity log data (Table 1). AGHS is calculated from chloride data by assuming a background *in situ* chloride profile and attributing the relative pore water freshening to gas hydrate dissociation [e.g., *Egeberg and Dickens*, 1999]. AGHS is obtained from resistivity data using the Archie equation and parameters given in *Riedel et al.* [2006]. AGHS at Sites U1325 and U1326 estimated from resistivity and chlorinity are similar and our predictions based on SMT depth are close to these estimates (Table 1). At Site U1328, our predicted AGHS is distinctly lower than resistivity-based estimate (Table 1). Site U1328 is a cold vent characterized by focused fluid and gas flow that causes high gas hydrate saturations close to the seafloor [*Riedel et al*., 2006]. Such local heterogeneities that might enhance methane flux from depth are not included in our simple 1-D model, thereby causing greater deviation between predicted and estimated AGHS.

Overall, we get good first order agreement between AGHS derived from chloride anomalies/resistivity logs and those predicted using our model, although our simulations consistently show lower AGHS at these sites. A possible explanation for this general deviation is that interpretations of resistivity logs

depend on knowledge of formation water resistivity and three empirical constants, which are hard to constrain in clay-rich sediments. Additionally, our simulations (Figures 2 and 3) and previous models [e.g., *Davie and Buffett*, 2003] predict gas hydrate to first occur well below the seafloor. In contrast, log-based results often predict hydrate starting immediately below the seafloor, causing AGHS to be higher than that predicted from simple transport models. Apart from the small deviations between model and chloride/resistivity log predictions, our model captures the trend in the lateral variation of AGHS correctly and likely provides a lower bound on AGHS. Hence, our model and generalized results (Figure 4) provide a simple and fast technique to constrain AGHS in deep-source gas hydrate systems.

5. Conclusions

We show that scaled depth to the SMT ($\tilde{L}_s$) can be used to estimate AGHS for deep-source gas hydrate systems. Simulation results demonstrate that the net fluid flux controls $\tilde{L}_s$ and the average gas hydrate flux ($Pe_1 \langle S_h \rangle$) through the GHSZ, thereby allowing us to correlate $\tilde{L}_s$ and $Pe_1 \langle S_h \rangle$. Results also show that conditions that create shallow $\tilde{L}_s$ and low Peclet number (Pe_1) lead to higher AGHS. Application of this method to sites along Cascadia Margin reveals a good match with saturations estimated from chloride/resistivity log data and accurately predicts the lateral variability in AGHS.

Acknowledgments. We acknowledge financial support from the Shell Center for Sustainability, the Kobayashi Graduate Fellowship, and the Department of Energy (DE-FC26-06NT42960). We thank Janice Hewitt for help with editing this manuscript. Comments from anonymous reviewers improved this manuscript.

References

Berner, R. A. (1980), *Early Diagenesis : A Theoretical Approach*, Princeton Univ. Press, Princeton, N.J.

Bhatnagar, G., W. G. Chapman, G. R. Dickens, B. Dugan, and G. J. Hirasaki (2007), Generalization of gas hydrate distribution and saturation in marine sediments by scaling of thermodynamic and transport processes, *Am. J. Sci.*, *307*, 861-900.

Borowski, W. S., C. K. Paull, and W. Ussler III (1996), Marine pore-water sulfate profiles indicate in situ methane flux from underlying gas hydrate, *Geology*, *24(7)*, 655-658.

Borowski, W. S., C. K. Paull, and W. Ussler III (1999), Global and local variations of interstitial sulfate gradients in deep-water, continental margin sediments: Sensitivity to underlying methane and gas hydrates, *Mar. Geol.*, *159*, 131-154.

Claypool, G. E., and K. A. Kvenvolden (1983), Methane and other hydrocarbon gases in marine sediment, *Annu. Rev. Earth Planet. Sci.*, *11*, 299-327.

Davie, M. K., and B. A. Buffett (2003), Sources of methane for marine gas hydrate: inferences from a comparison of observations and numerical models, *Earth Planet. Sci. Lett.*, *206*, 51-63.

Dickens, G. R. (2003), Rethinking the global carbon cycle with a large, dynamic and microbially mediated gas hydrate capacitor, *Earth Planet. Sci. Lett.*, *213*, 169-183.

Hyndman, R. D., and E. E. Davis (1992), A mechanism for the formation of methane hydrate and seafoor bottom-simulating reflectors by vertical fluid expulsion, *J. Geophys. Res. B*, *97*, 7025-7041.

Hyndman, R. D., T. Yuan, and K. Moran (1999), The concentration of deep sea gas hydrates from downhole electrical resistivity logs and laboratory data, *Earth Planet. Sci. Lett.*, *172*, 167-177.

Iversen, N., and B. B. Jørgensen (1993), Diffusion coefficients of sulfate and methane in marine sediments: Influence of porosity, *Geochim. Cosmochim. Acta*, *57*, 571-578.

Kvenvolden, K. A. (1993), Gas hydrates: Geological perspective and global change, *Rev. Geophys.*, *31*, 173-187.

Riedel, M., T. S. Collett, M. J. Malone, and the Expedition 311 Scientists (Eds.) (2006), *Proc. IODP*, vol. 311, Integrated Ocean Drilling Program Management International Inc., Washington, DC.

Snyder, G. T., A. Hiruta, R. Matsumoto, G. R. Dickens, H. Tomaru, R. Takeuchi, J. Komatsubara, Y. Ishida, and H. Yu (2007), Pore water profiles and authigenic mineralization in shallow marine sediments above the methane-charged system on Umitaka Spur, Japan Sea, *Deep-Sea Res. II*, *54*, 1216-1239.

Ussler, W., and C. K. Paull (2001), Ion exclusion associated with marine gas hydrate deposits, in *Natural Gas Hydrates: Occurrence, Distribution, and Detection*, *Geophys. Monogr. Ser.*, vol. 124, edited by C. K. Paull and W. P. Dillon, pp. 41{51, AGU, Washington, D. C.

Westbrook, G. K., B. Carson, and R. J. Musgrave et al. (Eds.) (1994), *Proc. ODP, Initial Reports*, vol. 146 (Pt. 1), Ocean Drilling Program, College Statiom, TX.

Table 1. Site-specific parameters and calculated AGHS for Cascadia Margin sites compared with estimates from resistivity log data and chloride anomalies

Site	$\dot{S}$ (cm/k.y.)	Pe_1	Seafloor depth (m)	L_s / L_t (m/m) = $\tilde{L}_s$	$Pe_1 \langle S_h \rangle$ (Figure 4)	$\langle S_h \rangle$ (calc.)	$\langle S_h \rangle$ (res. log)	$\langle S_h \rangle$ (Cl^-)
889[a]	25	0.07	1311	10/225 = 0.044	0.03	0.4%	-	<1% [b]
U1325[c]	38.3	0.11	2195	4.5/230 = 0.02	0.22	2%	3.7%[e]	5.3%[f]
U1326[c]	38.3[g]	0.11	1828	2.5/230 = 0.011	0.46	4.2%	6.7%[e]	5.5%[f]
U1328[c]	34.3	0.09	1267	1.5/219 = 0.007	0.67	7.4%	12.6%[e]	-

[a] ODP Leg 146 [*Westbrook et al.*, 1994]

[b] Taken from numerical model of *Davie and Buffett*, 2003

[c] IODP Expedition 311 [*Riedel et al.*, 2006]

[e] Calculated from Archie equation using resistivity log data [*Riedel et al.*, 2006]

[f] Calculated using relative freshening of pore water chloride profiles [*Riedel et al.*, 2006]

[g] $\dot{S}$ was not available, hence assumed equal to rate at nearest site U1325

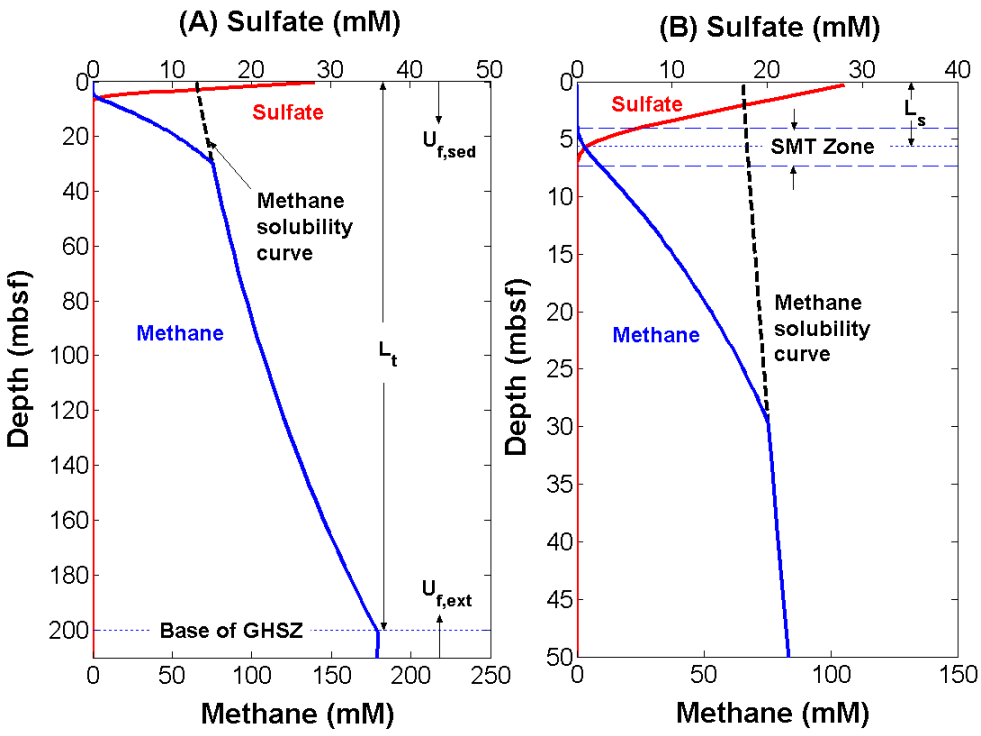

Figure 1. (A) Schematic representation of a gas hydrate system showing pore water sulfate and methane concentrations, which go to zero at some shallow depth because of anaerobic oxidation of methane (AOM). Also shown are methane solubility in water, the two fluid fluxes ($U_{f,sed}$ and $U_{f,ext}$), and depth to the base of the gas hydrate stability zone (L_t). (B) Close-up of the sulfate-methane transition (SMT) showing overlap of sulfate and methane profiles, and its depth below the seafloor (L_s).

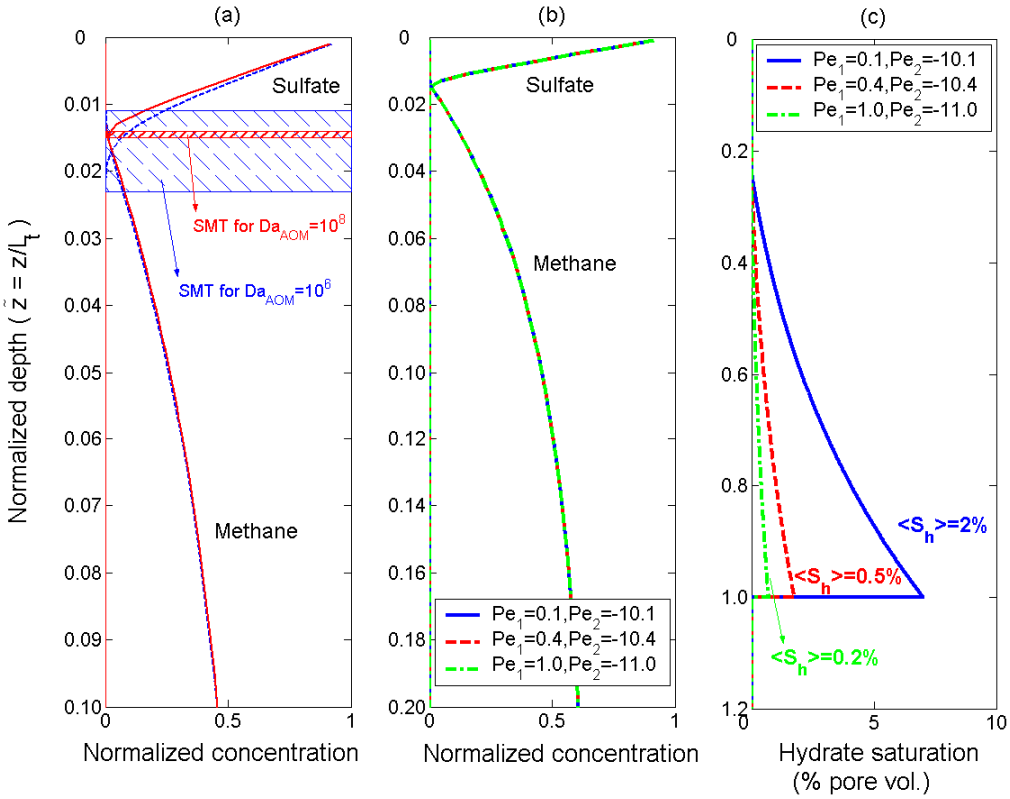

Figure 2. Effect of Damkohler number (Da_{AOM}) and Peclet numbers (Pe_1 , Pe_2) on steady-state profiles. $Pe_1 + Pe_2 = -10$ for all cases. Note different y-axis scale for each plot. (a) Sulfate and methane profiles for Da_{AOM} = 10^8 (solid curves) and Da_{AOM} = 10^6 (dashed curves). Hatched regions compare the thickness of the SMT for the two cases. (b) Simulations for different sets of Pe_1 and Pe_2 , with $Pe_1 + Pe_2 = -10$. Overlap of methane and sulfate profiles shows that $Pe_1 + Pe_2$ controls the concentrations. (c) The product $Pe_1 \langle S_h \rangle$ depends on $Pe_1 + Pe_2$, but hydrate saturation profiles are a function of Pe_1 .

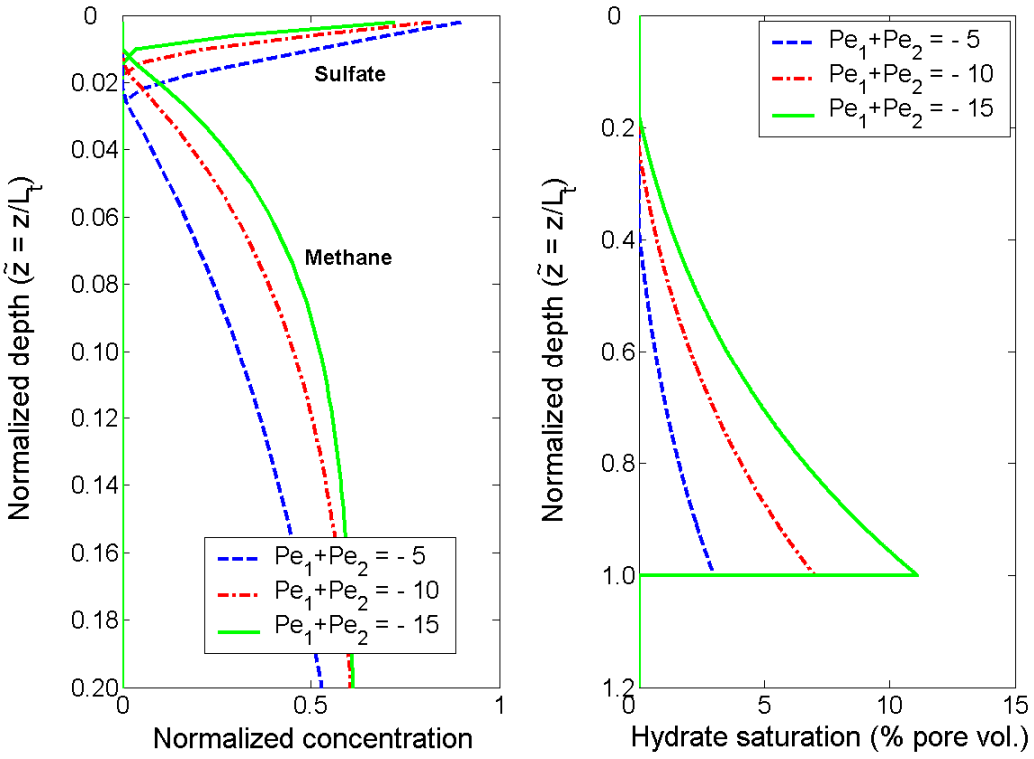

Figure 3. Effect of net fluid flux ($Pe_1 + Pe_2$) on steady-state concentrations. Pe_1 equals 0.1 for all simulations. (a) High magnitude of $Pe_1 + Pe_2$ defines higher net methane fluxes, resulting in shallower SMT zones. (b) Gas hydrate saturation at steady state increases as magnitude of $Pe_1 + Pe_2$ increases.

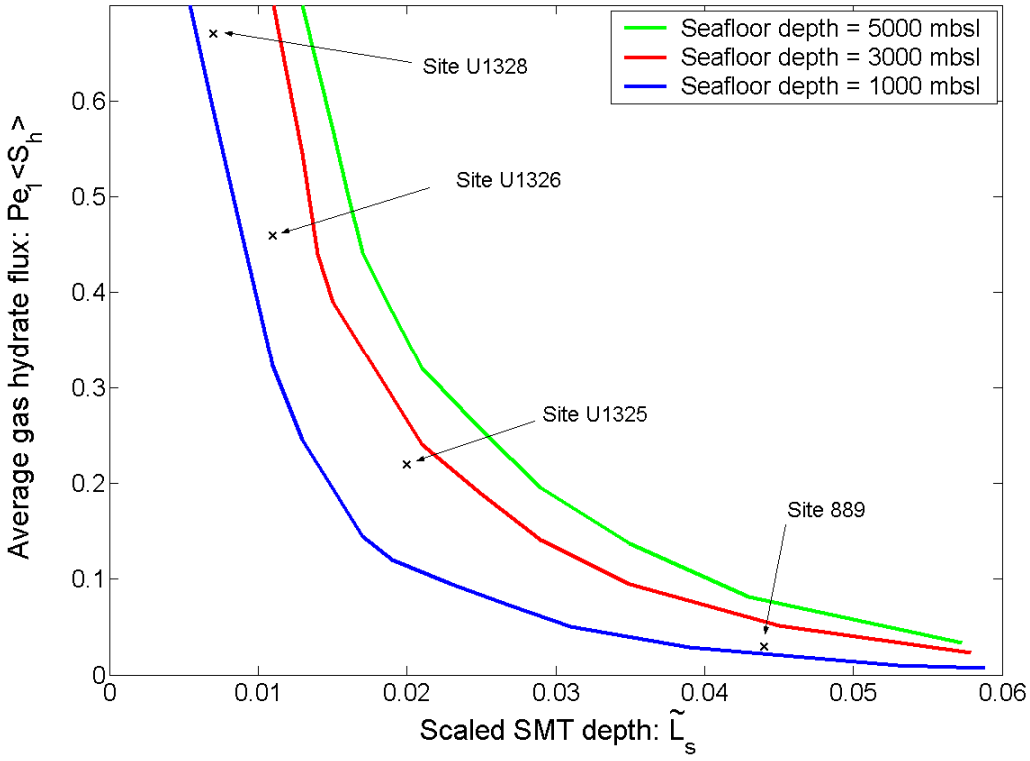

Figure 4. Relationship between average gas hydrate flux $Pe_1\langle S_h\rangle$ and scaled SMT depth ($\tilde{L}_s = L_s / L_t$) for several seafloor depths. Points corresponding to four Cascadia Margin sites are plotted to show how AGHS is estimated from $\tilde{L}_s$ using this plot (Table 1).

National Energy Technology Laboratory

626 Cochrans Mill Road
P.O. Box 10940
Pittsburgh, PA 15236-0940

3610 Collins Ferry Road
P.O. Box 880
Morgantown, WV 26507-0880

One West Third Street, Suite 1400
Tulsa, OK 74103-3519

1450 Queen Avenue SW
Albany, OR 97321-2198

539 Duckering Bldg./UAF Campus
P.O. Box 750172
Fairbanks, AK 99775-0172

Visit the NETL website at:
www.netl.doe.gov

Customer Service:
1-800-553-7681